A fundamental study of spray drying fluid catalytic cracking catalyst

A FUNDAMENTAL STUDY OF SPRAY DRYING FLUID CATALYTIC CRACKING CATALYST

PROEFSCHRIFT

ter verkrijging van de graad van doctor aan de
Technische Universiteit Eindhoven, op gezag van de
Rector Magnificus, prof.dr. R.A. van Santen, voor een
commissie aangewezen door het College voor
Promoties in het openbaar te verdedigen
op maandag 16 juni 2003 om 16.00 uur

door

Stefan Cornelis Theodorus van der Sanden

geboren te Drunen

Dit proefschrift is goedgekeurd door de promotoren:

prof.dr.ir. P.J.A.M. Kerkhof
en
prof.dr. J. Andrieu

Copromotor:
dr.ir. W.J. Coumans

CIP-DATA LIBRARY TECHNISCHE UNIVERSITEIT EINDHOVEN

Sanden, Stefan C.T. van der

A fundamental study of spray drying fluid catalytic cracking catalyst / by Stefan C.T. van der Sanden – Eindhoven: Technische Universiteit Eindhoven, 2003.
Proefschrift. - ISBN 90-386-2575-8
NUR 913
Trefwoorden: sproeidrogen / slurries / poreuze materialen; diffusie / aardolietechnologie; kraken / FCC katalysatoren / fysisch-chemische simulatie en modellering.
Subject headings: spray drying / slurries / porous materials; diffusion / petroleum cracking catalysts; FCC catalysts / physicochemical simulation and modeling.

Omslag: Martine de Rooy
Foto: Kees van Weert
Druk: Universiteitsdrukkerij, Technische Universiteit Eindhoven

Het werk in dit proefschrift is ondersteund door Akzo-Nobel Chemicals BV.

Rerum novarum cupidus

Samenvatting

In dit onderzoek zijn verschillende fundamentele aspecten van het sproeidrogen van *fluid catalytic cracking* (FCC) katalysator bestudeerd. Het FCC proces is een belangrijke technologie voor olieraffinage en is verantwoordelijk voor ca. 40% van de totale benzine-productie. FCC katalysator is een fijn poreus poeder van ronde deeltjes met een gemiddelde diameter van 60 micron. FCC katalysator bestaat uit verschillende componenten bij elkaar gehouden door een bindmiddel. In dit onderzoek is een typische FCC katalysator gebruikt die bestaat uit zeoliet Y, een matrix van klei en alumina en een silica bindmiddel. De invloed van procescondities op eigenschappen van de FCC katalysator heeft centraal gestaan. Het drooggedrag is experimenteel bestudeerd door laagjes te drogen onder goed gedefinieerde omstandigheden en middels sproeidroog-experimenten op proeffabriek schaal. Eveneens zijn de transportverschijnselen en de vorming van de interne morfologie tijdens het drogen beschreven met een wiskundig model voor een enkele druppel in een sproeidroog proces. De invloed van de droogcondities en de materiaaleigenschappen op de concentratieverdelingen in de druppels is bestudeerd.

Het drooggedrag en de droogsnelheid van FCC katalysator zijn bestudeerd door desorptie isothermen en droogcurven van laagjes te meten van de enkelvoudige componenten en mengsels daarvan. De krimpcurve van FCC katalysator is ook gemeten. Met mengregels en de gegevens van de enkelvoudige componenten zijn de desorptie-isotherm en de diffusiecoëfficiënt in het reguliere regime van mengsels en FCC katalysator berekend. De desorptie-isotherm van FCC katalysator en van mengsels van de

componenten kunnen goed voorspeld worden met een massa gewogen gemiddelde. Het initieel drooggedrag van de FCC katalysator wordt voornamelijk bepaald door het drooggedrag van het bindmiddel. Het volume van de FCC katalysator neemt lineair af met het vochtgehalte tot de krimpgrens. De krimpgrens is afhankelijk van de droogcondities: hogere droogsnelheden leiden tot lagere porositeiten. Dit is een gevolg van het complex drooggedrag van het silica bindmiddel. De vorming van kleine poriën door het silica bindmiddel verlaagt de grensvlakactiviteit en droogsnelheid in de beginfase met ca. 10% van de initiële droogsnelheid. Netwerkvorming vergroot de weerstand tegen deformatie en uiteindelijk krimpt het materiaal niet verder. Deze fase van krimp wordt opgevolgd door een niet-krimpende fase, die is opgedeeld in een penetratie-periode en een regulier regime. In de penetratie-periode kan de droogsnelheid analytisch beschreven worden en de overgang naar het regulier regime is bij een constant vochtgehalte van ongeveer 0.4 kg_w/kg_{ds}. De diffusiecoëfficiënt van FCC katalysator wordt het nauwkeurigst voorspeld met een parallel transportmodel: de totale weerstand tegen watertransport is bepaald door de component met de laagste weerstand. Dit geeft de mogelijkheid het drooggedrag van FCC katalysator met een bepaalde samenstelling te beschrijven met een redelijke nauwkeurigheid.

Met een proeffabriek schaal sproeidroger zijn experimenten gedaan om de invloed van de procescondities op de FCC katalysator eigenschappen te bestuderen. De FCC katalysator is onderzocht op: eindvochtgehalte, deeltjesgrootte en deeltjesgrootteverdeling, bulk dichtheid, oppervlak, porositeit en poriegrootteverdeling. De morfologie is bestudeerd met elektronenmicroscopie. De procescondities, die zijn gevarieerd, zijn de luchttemperatuur, luchtdebiet en druppelgrootteverdeling (verstuiver configuratie). De materiaaleigenschappen, die zijn gevarieerd, zijn het watergehalte van de voeding en de tijd tussen het bereiden van de voeding en het versproeien. Eén van de belangrijkste

resultaten is dat, voor een standaard samenstelling van de FCC katalysator, de onderzochte eigenschappen vrijwel constant blijven binnen de toegepaste sproeidroog-condities. Blijkbaar beïnvloedt het drooggedrag van het silica bindmiddel niet de porositeit van de gesproeidroogde FCC katalysator. De gemiddelde deeltjesgrootte kan worden berekend met het vochtgehalte van de voeding en de initiële (gemiddelde) druppelgrootte. Deze laatste is sterk afhankelijk van de keuze van de verstuiver configuratie.

Twee wiskundige modellen zijn ontwikkeld voor een enkele druppel in een sproeidroogproces. Het eerste model beschrijft de ontwikkeling van de interne morfologie tijdens krimp en beschrijft het (effectieve) transport van zeoliet en matrix deeltjes als één vaste fase. Het transport van de vaste fase is verdeeld in twee regimes: voor hoge watergehaltes bewegen de deeltjes met Brownse beweging en wanneer ze contact maken, pakken de deeltjes samen in een koek. De koek wordt gecomprimeerd door de capillairdruk aan het grensvlak van de druppel. De deformatie-eigenschappen van de koek en de procescondities bepalen de hoeveelheid krimp en daarmee de relatieve deeltjesgrootte, de dichtheid en porositeit. Voor de vaste stof deeltjesgrootte van FCC katalysator wordt de Brownse beweging reeds bij lage vaste stofconcentraties opgevolgd door de koek compressie. De schijnbare diffusiecoëfficiënt in de koek is erg hoog en resulteert in vlakke concentratieprofielen in de koek. Een grotere compressibiliteit van de koek en lagere droogsnelheden vergroten de hoeveelheid krimp en resulteren in kleinere deeltjes met lagere porositeit en grotere dichtheid. De eigenschappen van de gesproeidroogde FCC katalysator kunnen slechts gesimuleerd worden als de koek compressie bij een lagere vaste stofconcentratie begint dan de initiële concentratie. Dit is een sterke aanwijzing dat het regime van de Brownse beweging erg beperkt is of dat het

contact tussen de vaste stofdeeltjes plaatsvindt bij relatief lage concentraties. Dit kan ook een effect zijn van het bindmiddel.

Het tweede model is voornamelijk ontwikkeld om de segregatie van bindmiddel te beschrijven tijdens het krimpen. De basis van dit model is de impulsbalans voor een binair mengsel in een inerte porie zoals beschreven in het *velocity profile model*. De transportvergelijkingen zijn gekoppeld aan de deformatievergelijking van de koek zoals beschreven in het eerste model. In het model is het Brownse beweging regime achterwege gelaten. Het model beschrijft zowel de ontwikkeling van de interne morfologie als het transport van de binder in de vloeistof. Sproeidroogcondities, eigenschappen van de koek en het bindmiddel bepalen de morfologie en segregatie. De frictie van water en bindmiddel met de wand van de koek is vergelijkbaar en de segregatie van het bindmiddel wordt voornamelijk bepaald door diffusie van het bindmiddel in water: een hogere diffusiecoëfficiënt resulteert in minder segregatie. Voor de erg deformeerbare FCC katalysator accentueert dit het belang om de diffusie van het bindmiddel te beheersen.

Summary

In this research several fundamental aspects of spray drying fluid catalytic cracking (FCC) catalyst have been studied. The FCC process is a major technology in oil refining and produces about 40% of the total gasoline. FCC catalyst is a fine porous powder of spherical particles with an average diameter of 60 micron. FCC catalyst consists of different components that are held together by a binder material. In this work a typical FCC catalyst is used that consists of zeolite Y, a matrix of clay and alumina and a silica binder. The central point of the study was the influence of process conditions on FCC catalyst properties. The drying behaviour has been studied experimentally by drying layers under well-defined conditions and performing spray drying experiments on a pilot-plant scale. In addition, the transport phenomena and development of the internal morphology during drying have been described mathematically for a single droplet in a spray drying process. The influence of various drying conditions and material parameters on the concentration distributions in the droplet has been studied.

The drying behaviour and kinetics of FCC catalyst have been studied by measuring desorption isotherms and drying curves of layers for the single components and mixtures thereof. In addition, the shrinkage curve of FCC catalyst has been measured. With mixing rules and the data of the single components the desorption isotherm and regular regime diffusion coefficient of mixtures and FCC catalyst have been calculated. The desorption isotherms of FCC catalyst and mixtures of the components are well predicted with a mass weighing averaging model. The initial drying behaviour of FCC catalyst is mainly controlled by the drying behaviour of the binder material. The volume of FCC catalyst

decreases linearly with the water content until the shrinkage limit. However, the shrinkage limit depends on the drying conditions: higher drying rates result in lower porosities. This is a result of the complex drying behaviour of the silica binder material. The formation of small pores by the silica binder decreases the interface activity and drying rate in the initial period with ca. 10% of the initial drying rate. Network formation increases the resistance to deformation and finally the material shrinks no further. This shrinking period is followed by a non-shrinking period that can be subdivided in a penetration period and a regular regime. In the penetration period the drying kinetics can be described analytically and the transition to the regular regime is at a constant water content of ca. 0.4 kg_w/kg_s. The diffusion coefficient of FCC catalyst is most accurately predicted with a parallel transport model: the total resistance to transport is controlled by the component with the lowest resistance. This enables the description of the drying behaviour of a certain FCC catalyst composition with a reasonable accuracy.

With a pilot-plant scale spray drying experiments have been done to investigate the influence of the process conditions on the properties of FCC catalyst. The FCC catalyst has been analysed on moisture content, particle size distribution, bulk density, surface area, porosity and pore size distribution. The morphology has been studied with electron microscopy. The varied process conditions are the air temperature, airflow and droplet size distribution (nozzle configuration). The varied material properties are the feed water content and the batch aging time (time between preparation of the feed and spray drying). A major result is that, for a standard formulation of FCC catalyst, the properties remain almost constant within the applied spray drying process conditions. Apparently, the silica binder drying behaviour does not influence the porosity of spray dried FCC catalyst. The average particle size can be calculated from the water content of the feed and the initial

(average) droplet size. The latter depends largely on the choice of the nozzle configuration.

Two mathematical models have been developed for a single droplet in a spray drying process. The first model describes the development of the internal morphology during shrinkage and describes the (effective) transport of zeolite Y and matrix particles as one solid phase. The transport of the solid phase is divided in two regimes: for higher water contents the particles move according to Brownian motion and upon contact the particles compact into a cake. The cake is compressed under the capillary pressure at the interface of the droplet. The deformation properties of the cake and the process conditions determine the shrinkage of the droplet and by that the relative particle size, the density and porosity. For the particle sizes of FCC catalyst components the initial Brownian motion regime is followed by the cake compression regime at relatively low solids concentration. The apparent diffusion coefficient in the cake is very high and results in flat concentration profiles in the cake. A higher compressibility of the cake and lower drying rates increase the amount of shrinkage and result in smaller particles with lower porosity and higher density. The properties of spray dried FCC catalyst can only be simulated if the cake formation starts at a lower solids concentration than the initial concentration. This strongly indicates that the Brownian motion regime is very limited or that the contact between the solid particles occurs at relatively low volume fraction solids. The latter could be an effect of the binder material.

The second model is mainly developed to describe the binder segregation during the shrinkage period. The basis of this model is the momentum balance for a binary liquid in an inert pore as described in the velocity profile model. The transport equations are coupled to the deformation of the cake as described by the first model. In the model the Brownian motion regime is omitted. The model describes both the development of the

internal morphology and the transport of the binder in the liquid. Spray drying conditions, properties of the cake and the binder determine the morphology and segregation. The friction with the cake wall for both water and binder is comparable and the segregation of the binder is controlled mainly by diffusion of the binder in the water: a higher diffusion coefficient results in less segregation. For FCC catalyst, which is highly deformable, this accentuates the importance of controlling diffusion of the binder material.

Contents

3 The influence of spray drying conditions on FCC catalyst properties

4 Modelling droplets of particulate slurries: drying behaviour and morphology

5 Modelling binder segregation during spray drying of slurries

6 Evaluation

7 Appendices

Chapter 1
Introduction

The globally increasing consumption of mineral oil and the limit of its natural reserves will have far-reaching effects on human society in the 21st century. Scientists and engineers are trying for more than one and a half century to increase the production of fuel and chemicals from crude oil, which has led to many technological developments. Nevertheless, the combustion of mineral oil and its derivatives contribute to the global warming.

Fluid catalytic cracking (FCC) is a central technology in modern oil refining and is responsible for about 40 % of the total gasoline production. In the FCC process heavy residues from distillation are cracked into lighter fractions with the aid of a catalyst, the FCC catalyst. At present, there are more than 300 fluid cracking units available worldwide and over 200 types of FCC catalysts.

1.1 Fluid catalytic cracking process

The modern FCC unit has a riser-regenerator technology, as schematically depicted in figure 1.1. In the riser reactor, FCC catalyst is mixed with atomised oil. The cracking reactions cause expansion and the mixture moves upwards, hence the process name. The residence time is only several seconds and at the top of the riser, the catalyst is separated from gas in a cyclone. After stripping of residual hydrocarbons with steam, the FCC catalyst is regenerated: the deposited coke, which results from the cracking reactions, is burned off with hot air. The energy produced from the regeneration is used to heat the riser reactor. During the regeneration process the catalyst loses activity and about 1 percent is lost through fines (Harding, 2001). Therefore, regenerated FCC catalyst is continuously mixed with fresh catalyst.

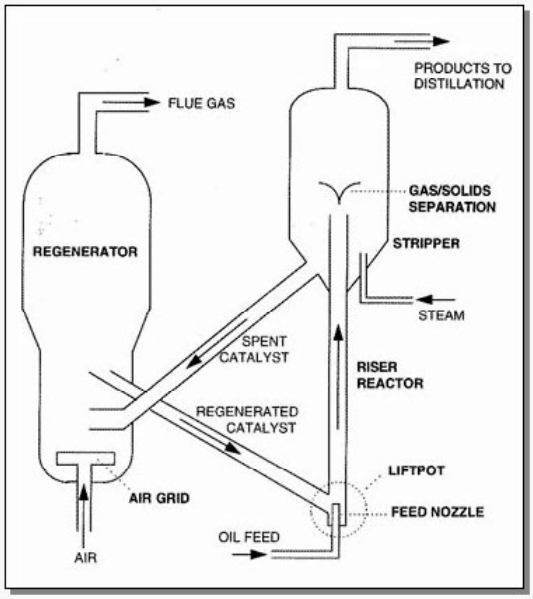

Figure 1.1. Schematic overview of FCC unit.

1.2 FCC catalyst properties

In commercial applications both chemical and physical properties of FCC catalyst are of importance (Magee, 1976). The short contact time requires a high catalytic activity. Changes in feed stock quality or environmental constraints require a specific selectivity to modify the product composition. However, these properties have not been studied in this thesis, as the focus is on the physical properties. The physical properties are important for process operation and durability of the FCC catalyst and these properties may also affect the chemical properties. The physical properties that are studied here are: particle size distribution, particle shape, density, surface area, pore volume and pore size distribution. Other physical properties, which have not been measured, are: attrition resistance, thermal and hydrothermal stability.

Particle size and density are important factors for attrition resistance and fluidisability. The optimum particle size distribution for fluidisation is specific for each FCC unit. Small particles are undesirable because of fines loss. Particle shape is another important factor for attrition resistance, because particles that are more spherical will have less attrition.

1.3 FCC catalyst composition

A modern FCC catalyst consists of a zeolite component, incorporated in a matrix. In addition, additives are used to improve the performance, for example to promote the combustion of coke, capture contaminants (metals) and reduce emissions. The zeolite and matrix components and their properties will be described briefly.

1.3.1 Zeolite component

The most common zeolite in modern FCC catalysts is the Y type. The zeolite can be dealuminated with steam to increase the silica/alumina ratio and can contain rare earth ions to increase stability. Examples of other zeolites that are used in combination with zeolite Y are: ZSM-5, Beta zeolite, MCM-22 and ITQ-7 (Corma, 1995, 2001).

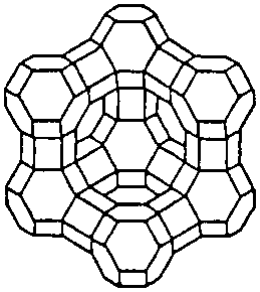

Figure 1.2. Zeolite framework structure.

Zeolite Y is a faujasite type zeolite having a framework structure as depicted in figure 1.2. The pore opening consists of a twelve ring with a pore-entrance diameter of $7.4 \cdot 10^{-10}$ m (figure 1.3). The pores in the centre of the zeolite have a diameter of approx. $1.2 \cdot 10^{-9}$ m. The atomic composition is $(Na_2,Ca,Mg)_{29}[Al_{58}Si_{134}O_{384}] \cdot 240H_2O$, which corresponds to a water content of 0.29 kg_w/kg_s (Meier, 1996). A zeolite crystal consists of a regular array of framework units and the shape is normally cubic. A zeolite particle is a single crystal or an agglomerate of crystals. The average particle size is of the order magnitude of a micrometer, although much smaller zeolites can also be synthesized (e.g. Rajagopalan, 1986). The true density of the skeletal is approximately 2500 kg/m^3.

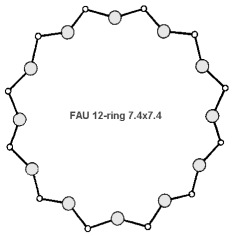

Figure 1.3. Pore opening.

The high activity of the zeolite could be utilised only when the zeolite particles were diluted in a matrix (Plank, 1976). Typically, about 35 wt.% of the FCC catalyst is zeolite, while a range between 5 and 50 wt.% is applied (Sullivan, 1995).

1.3.2 Matrix component

Besides diluting the activity of the zeolite, the matrix has several functions to enhance the performance of the FCC catalyst. As a co-catalyst, the matrix interacts with the zeolite to increase activity and selectivity (Hayward, 1990). The matrix further supplies strength and attrition resistance, reduces emissions and the effects of contaminating metals. The matrix is usually a combination of a binder, clay and an active material (Woltermann, 1993).

Binder

Binders are mainly used in FCC catalysts to increase the attrition resistance. The most common are silica sol, aluminium chlorhydrol and peptised alumina. However, FCC catalyst is also produced without binder material (Woltermann, 1993).

In this study only the silica sol binder is used. The formed clear and low viscosity sol is meta-stable: particle growth and network formation take place and depend on temperature, pH and silica concentration of the sol (see for example Brinker, 1990;

Sullivan, 1995). The size and form of the silica particles depend on the state of polymerisation, and thus on temperature, concentration and pH. The polymerisation occurs in three stages (Iler, 1979):

1. Polymerisation of monomer to form particles.
2. Growth of particles.
3. Linking of particles into clusters and subsequent network formation. The network can extend throughout the liquid, thereby increasing the viscosity, and finally result in a gel.

When a gel is formed, it ages and several processes of change are categorised (Brinker, 1990). It was found that primary silica binder particles grow from ca. $2 \cdot 10^{-9}$ to $4 \cdot 10^{-9}$ m in diameter during a sol ageing time of one to several hours (the time between preparation and spray drying). The cluster size was approximately $2 \cdot 10^{-8}$ m (Sullivan, 1995). The skeletal density of silica is also about 2500 kg/m^3.

The neutralisation step in the preparation of the silica sol controls the bulk of the pore structure in the catalyst (Magee, 1976). In addition, the ageing time of the sol and the temperature influence the surface area and pore size distribution. The amount of binder is often related linearly to the strength of the catalyst particle. However, Bergna was the first to demonstrate the effect of a binder-enriched shell near the surface of a particle (Bergna, 1989). This resulted in a large decrease of the amount of binder necessary. Longer sol ageing times increase the attrition resistance, which was explained with the formation of a finely textured, fibrillar structure (Pederson, 1989).

Active matrix

An active matrix enables the pre-cracking of high molecular weight hydrocarbons, which would normally not be able to diffuse in the zeolite micro-pores (Hayward, 1990). The matrix also enables passivation of metals, thereby preventing poisoning and high regeneration temperatures (Woltermann, 1993). Alumina is the most commonly used active matrix component and fulfils the above-mentioned functions. In some cases silica is included to stabilise the surface of alumina and to increase the activity of the surface area. Pseudo-boehmite alumina is peptised with an acid to create small particles, which increases the attrition resistance (Pedersen, 1989). The peptisation is found to be dependent on the nature and concentration of the electrolyte, temperature and pressure

(Zakharchenya, 1996). The average particle size of peptised boehmite alumina is in the range of $2.0 \cdot 10^{-8} \pm 1.5 \cdot 10^{-8}$ m and is narrowly distributed, although few larger particles have been observed. Reversible gelling of alumina occurs, although the formed gel is less strong than the silica gel. The alumina gel can be dissolved in water and, if severe stirring is applied, a suspension will appear again. The density of alumina is ca. 3990 kg/m^3 (Perry's, 1999).

Clay

Clays used in catalysts may be thermally or chemically treated and usually constitutes 10 – 65 wt.% of the catalyst. Clays used are kaolin, halloysite and montmorillonite (Woltermann, 1993). Kaolin clay is used because its ability to form pumpable slurries of high solids content. The clay particles are platelets and have no internal pores. Clay is added to increase density without affecting catalytic properties and surface area. The large clay particles also create large pores. The apparent particle size has to be small enough to result in good bulk density and attrition resistance. Average platelet lengths of $3 \cdot 10^{-7}$ m are normal and 60 – 80 wt.% is smaller than $2 \cdot 10^{-6}$ m. Kaolin has a low surface area and contains low amounts of metal, such as iron and titanium, which influence selectivity by secondary reactions. The skeletal density of kaolin is about 2500 kg/m^3.

1.4 Internal structure and FCC catalyst properties

The choice of the FCC catalyst components and the arrangement thereof (the internal structure) has a large influence on the activity and selectivity. The diffusion of hydrocarbons in the catalyst can be divided in two regions: diffusion in the matrix and diffusion in the zeolite particles.

Besides the type and treatment of the zeolite component, the particle size and dispersion of the zeolite influence activity, selectivity and stability of the catalyst. Activity and selectivity increase with decreasing crystal size (Rajapagolan, 1986). The increase in activity is due to the larger surface area. The better selectivity is ascribed to the differences in diffusivity of the reactants and intermediates.

As mentioned before, the distribution of the binder has a large influence on the attrition resistance. However, an enriched-shell of binder particles will decrease the porosity (accessibility) of the surface and hence the transport rate. Thus, a formed shell

should be permeable enough for hydrocarbon molecules to reach the zeolite crystals in the catalyst. An optimal combination of nano-sized (binder) particles and micron-sized (zeolite and clay) particles would result in accessible macro pores.

Pedersen found silica-alumina regions in the interior of commercial FCC catalysts, which increase density and attrition resistance (Pedersen, 1989). However, if the regions are located in the enriched-shell, attrition resistance is supposed to decrease. Also, if these regions encapsulate zeolite crystals, the overall activity and selectivity will be reduced.

Particles that are hollow or show major cracks and crevices will have lower density and attrition resistance.

A high surface area is thought to decrease the attrition resistance, to increase the activity but also coke formation and metal poisoning. The matrix surface area plays a minor role in the conversion of n-hexane (Brait, 1998). During the first few cycles the surface area and the activity decrease considerably.

The total porosity and pore size distribution mainly influence the transport properties. A wide pore size distribution enables a broad range of hydrocarbon sizes to diffuse into the catalyst particle. Large pores increase the rate of regeneration and decrease the effect of coke deposition. In addition, the risk of over-cracking is higher when large molecules are cracked and diffusion is slow. The hydrothermal stability is directly related to the pore size distribution. Hydrothermal collapse is related to the presence of small pores ($< 3 \cdot 10^{-9}$ m diameter), which are unstable in steam in the presence of alkali oxides (Magee, 1976). A higher porosity usually decreases the attrition resistance. A high surface area and small pores will hold hydrocarbons and leads to higher regeneration temperatures and increased degradation.

1.5 FCC catalyst manufacture

Four major categories of manufacturing routes are documented: 1) in-situ formation, 2) gel based matrix method, 3) sol based matrix method, and 4) core and shell technology (Sullivan, 1995). These production processes involve at least the mixing of components followed by spray drying.

For the experimental work, the sol based matrix method is applied to prepare the FCC catalyst feed. This method replaced the older gel matrix method, due to improved attrition

resistance and selectivity. Sol based FCC catalysts have a higher bulk density and are able to bind a higher concentration of zeolite (Sullivan, 1995).

1.5.1 FCC catalyst feed preparation

The preparation method is based on the patent of Elliot (Elliot, 1975). Sulphuric acid is mixed with sodium silicate at low pH (1.8 – 3.0) to form a silica sol. At lower pH, a sol of poor quality is formed, and at higher pH, thickening and gelling will occur faster. A dispersed aluminium source may be added to the silica sol. Then clay is added. Because zeolite is alkali, it must be added to a liquid with a pH in the range of 3.0 – 4.5. The spray drier feed should have a pH in the range of 2.8 – 4.0, because at pH lower than 2.8 the zeolite will be destructed and above 4.0 the slurry will be too thick. Rigorous mixing during feed preparation is essential to obtain a hard, dense and homogeneous catalyst (Woltermann, 1993). Insufficient mixing can influence attrition resistance, density and morphology as well as activity and selectivity of the FCC catalyst. Further, it is common to add fines to the feed before spray drying. The solids content of the feed affects the particle diameter: a higher solids concentration increases the particle diameter (Magee, 1976). A higher viscosity of the feed also increases the particle diameter, due to increased energy necessary for atomisation.

1.5.2 Spray drying

Spray drying is the transformation of a liquid containing suspended and/or dissolved solids into a powder by atomising the liquid into a hot drying medium (usually air). The principle of spray drying is extensive contacting of liquid with air. The air transfers heat to the droplet and takes up the evaporated water. The spray drying process is complex due to the simultaneous exchange of momentum, heat and mass. In addition, the properties of the dried material depend strongly on temperature and water content. Furthermore the spray drying process is large and expensive. The spray drying process is said to control the fluidisation and circulation properties of the catalyst in an FCC unit (Woltermann, 1993).

The spray drying process is usually divided in four stages: 1) atomisation of the feed into a spray of droplets, 2) dispersion of the spray in the air (spray-air contact), 3) drying of the droplets, and 4) product-air separation (Masters, 1985). Together with the feed properties, each of these stages determine the drying history of the droplet and hence the

final properties. A schematic picture of the spray drier used in this research is given in picture 1.4.

Atomisation

Atomisation is the process that transforms the liquid feed into droplets with a high specific surface area. Commonly used atomisers are pressure nozzles, rotating disc atomisers and two-fluid nozzles. In this research a pressure nozzle is used of Spraying Systems[I]. Pressure forces the liquid through a core and a small orifice. The core swirls the liquid and the after the orifice, a thin conical sheet is formed that disintegrates into small droplets. The spray angle, droplet size distribution and droplet velocity are determined by feed properties (concentration, temperature, viscosity) and operating parameters (pressure and the nozzle type).

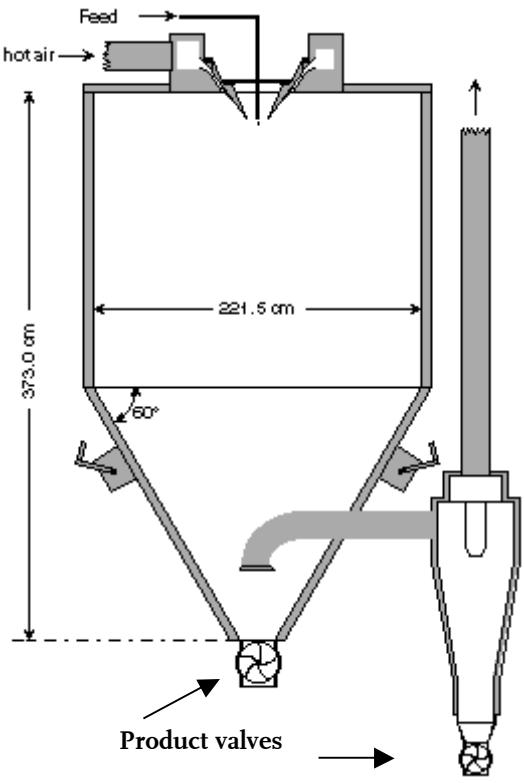

Figure 1.4. **Schematic representation of the used spray drier.**

Spray-air contact

The liquid sheet and atomised droplets come in contact with the air and the droplets, which have a high velocity, are dispersed. The airflow direction with respect to the droplet motion can be co-current, counter-current or mixed-flow.

Drying

The drying process in a spray drier is complex because millions of individual droplets experience different drying histories. The properties of the dried material are made up of the properties of these dried particles. The description of the drying process varies from simplified, engineering models to sophisticated theoretical models and numerical

[I] See www.spray.com.

methods (see for example Kerkhof, 1974; Kerkhof, 1975; Van der Lijn, 1976; Masters, 1985; Coumans, 1987 and Kieviet 1997, 1997a, 1997b). In *chapter 2* the drying kinetics are discussed generally and in *chapters 4* and *5* specific attention is given to the drying kinetics of shrinking droplets in a spray drier. In all the models the diffusion equation is at the basis of the description.

Product air separation

Product that hits the wall of the drying chamber usually slides down and is collected via a valve at the bottom of the drier. Sometimes the accumulated powder has to be removed from the wall: the used spray drier has two hammers at the conical part of the drying chamber. The product is separated from the exhaust air by cyclones.

Spray driers are built with different drying chamber shapes, air inlet geometries and flow direction. The spray drier used in this research has a co-current airflow, supplied by two ventilators, one in the inlet and one in the outlet duct. The pressure nozzle atomiser is placed in the centre of the inlet airflow.

1.6 FCC catalyst characterisation and evaluation methods

The choice of a suitable FCC catalyst is an important factor for the performance of a specific FCC unit. In the industry, the micro activity test is widely used to specify the catalysts cracking quality and attrition tests are used to evaluate the strength.

In this thesis the focus is on the physical properties of FCC catalyst. The particle size distribution is measured with laser scattering and the particle shape by electron microscopy. The skeletal density is measured with helium picnometry and the bulk density with a Stampfvolumeter (tapping a certain amount of powder). The surface area, porosity and pore size distribution are measured with incipient wetness impregnation, nitrogen sorption and mercury porosimetry. Pore sizes can be divided into three regions: micro-pores with diameter $< 2 \cdot 10^{-9}$ m, meso-pores with a diameter between $2 \cdot 10^{-9}$ and $5 \cdot 10^{-8}$ m and macro-pores, with a diameter $> 5 \cdot 10^{-8}$ m.

1.7 Outline

The impulse for this research was the question how FCC catalyst properties are influenced by spray drying conditions. For a manufacturer it would be profitable if

properties, such as surface area and pore size distribution, could be tuned with process conditions, independent of the FCC catalyst formulation. The wide variety of FCC catalyst formulations initiated to study the drying kinetics as function of the composition.

In this thesis various fundamental aspects of drying of FCC catalyst are described. Both experimental and theoretical/numerical methods are applied to study the (spray) drying and properties of a typical FCC catalyst. It is possible to read the chapters separately, although some procedures and methods are described only once.

In *chapter 2* the drying behaviour of FCC catalyst is studied. Because FCC catalyst is a multi component material, mixing rules are used to describe the drying behaviour with properties of the single components. Layer drying experiments are done to describe the drying kinetics. In addition, the shrinkage behaviour and sorption isotherms are measured. The diffusion coefficient and sorption isotherm are calculated with single component properties.

Chapter 3 deals with spray drying experiments on pilot-plant scale. The influence of spray drying conditions on FCC catalyst properties is studied for a typical formulation. Process variables are batch ageing time, air temperature, feed flow (or nozzle pressure), airflow and feed water content.

Then, in *chapter 4*, a model is derived to describe the spray drying of particulate materials. The model describes the formation and shrinkage of crust forming droplets using a constitutive equation and diffusion equations as basis. The model predicts the final particle size, density and porosity as function of spray drying conditions, feed and particulate material properties. Results are compared with spray dried FCC catalyst and literature data.

The spray drying model is extended in *chapter 5* to describe the segregation of the binder material, because the distribution of binder is important for the attrition resistance. The transport of the binder and water mixture through the porous matrix (including zeolite) is based on the velocity profile model, which describes the transport of a binary mixture in an inert pore (Kerkhof, 2001). The shrinkage and transport of the matrix (including zeolite) is described similarly to the model in *chapter 4*. The influence of spray drying conditions and material properties on the binder segregation is studied numerically.

In *chapter 6* the work is evaluated.

References

Bergna, H.E., 1989, Attrition-resistant porous particles produced by spray drying, Characterization and Catalyst Development: an Interactive Approach, Ed. Bradley, S.A., Gattuso, M.J., Bertolacini,R.J., ACS Symposium Series 411, chapter 7, Washington D.C., USA.

Brait, A., Seshan, K. and Lercher, J.A., 1998, Evaluation of commercial FCC catalysts for hydrocarbon conversion I. Physicochemical characterization and n-hexane conversion, Applied Catalysis A: General, 169, 299-313.

Brinker, C.J. and Scherer, G.W., 1990, Sol-gel science: the physics and chemistry of sol-gel processing, Academic Press, San Diego, USA.

Corma, A., Gonzalez-Alfaro, V. and Orchilles, A.V., 1995, Catalytic cracking of alkanes on MCM-22 zeolite. Comparison with ZSM-5 and beta zeolite and its possibility as an FCC cracking additive, Applied Catalysis A: General, 129, 203-215.

Corma, A., Martinez-Triguero, J. and Martinez, C., 2001, The use of ITQ-7 as FCC zeolitic additive, Journal of Catalysis, 197, 151-159.

Coumans, W.J., Kerkhof, P.J.A.M. and Bruin, S., 1987, Theoretical and practical aspects of aroma retention in spray drying and freeze drying, Drying Technology, 12, 1&2, 99-149.

Elliot, C.H. Jr., 1975, Process for preparing a petroleum cracking catalyst, Patent No. US3867308.

Harding, R.H., Peters, A.W. and Nee, J.R.D., 2001, New developments in FCC catalyst technology, Applied Catalysis, A: General, 221(1-2), 389-396.

Hayward, C.M.T. and Winkler, W.S., 1990, FCC: matrix/zeolites interactions, Hydrocarbon Processing, 69(2), 55-56.

Iler, R.K., 1979, The chemistry of silica: solubility, polymerization, colloid and surface properties, and biochemistry, Wiley, New York, USA.

Kerkhof, P.J.A.M. and Schoeber, W.J.A.H., 1974, Theoretical modelling of the drying behaviour of droplets in spray dryers, Advances in preconcentration and dehydration of foods, Editors: A. Spicer, Applied Science Publishers Ltd., London, UK, 349-397.

Kerkhof, P.J.A.M., 1975, A quantative study of the effect of process variables on the retention of volatile trace components in drying, Ph.D. thesis, Eindhoven University of Technology, Eindhoven, The Netherlands.

Kerkhof, P.J.A.M., Geboers, M.A.M. and Ptasinksi, K.J., 2001, On the isothermal binary mass transport in a single pore, Chemical Engineering Journal, 83, 107-121.

Kieviet, F.G., 1997, Modelling quality in spray drying, Ph.D. thesis, Eindhoven University of Technology, Eindhoven, The Netherlands.

Kieviet, F.G., Raaij, J. van, Moor, P.P.E.A. de and Kerkhof, P.J.A.M., 1997a, Measurement and modelling of the air flow pattern in a pilot plant spray dryer, Transactions of the Institution of Chemical Engineers, Part A. Chemical Engineering Research, 75, 321-328.

Kieviet, F.G. and Kerkhof, P.J.A.M., 1997b, Airflow, temperature, and humidity patterns in a co-current spray dryer: modelling and measurements, Drying Technology, 15, 6-8, 1763-1773.

Lijn, J. van der, 1976, The 'constant rate period' during the drying of shrinking spheres, Chemical Engineering Science, 31, 929-935.

Magee, J.S. and Blazek, J.J., 1976, Preparation and performance of zeolites cracking catalyst, in Rabo, J.A. ed., Zeolite Chemistry and Catalysis, ACS Monograph, No. 171, American Chemical Society, Washington, D.C., 615-679

Masters, K., 1985, Spray drying handbook, Longman Scientific & Technical, Essex, UK.

Meier, W.M., Olson, D.H. and Baerlocher, Ch., 1996, Atlas of zeolite structure types, 4th rev. ed., Elsevier, London, UK.

Pedersen, L.A., Lowe, J.A. and Matocha, C.K. Sr., 1989, Attrition- and metal-resistant fluid cracking catalyst prepared with alumina powder in the matrix, in: Characterization and Catalyst Development: an Interactive Approach, Ed. Bradley, S.A., Gattuso, M.J., Bertolacini, R.J., ACS Symposium Series 411, Chapter 38, 414-429, Washington D.C., USA.

Perry's Chemical Engineering Handbook, Electronic release edition 1999.

Plank, C.J. and Rosinski, E.J., 1976, Method for fluid cracking with a composite catalyst, Patent No. US3939058.

Radford, 1997, A model of particulate drying in pneumatic conveying systems, Powder Technology, 93, 109-126.

Rajagopalan, K., Peters, A.W. and Edwards, G.C., 1986, Influence of zeolite particle size on selectivity during fluid catalytic cracking, Applied Catalysis, 23, 69-80.

Sullivan, C.E., 1995, Binder kinetics and FCC catalyst microstructure, Ph.D. thesis, University of Wisconsin-Madison, Wisconsin, USA.

Woltermann, G.M., Magee, J.S. and Griffith, S.D., 1993, Commercial preparation and characterization of FCC catalysts, in: Fluid Catalytic Cracking: Science and Technology, Ed. Magee, J.S., Mitchell, M.M. Jr., Elsevier, Amsterdam, The Netherlands.

Zakharchenya, R.I., 1996, Influence of peptization on the properties of alumina produced from boehmite sols, Journal of Sol-Gel Science and Technology, 6, 179-186.

Chapter 2

Drying kinetics of fluid catalytic cracking catalyst

ABSTRACT

Desorption isotherms, drying curves and a shrinkage curve have been measured for a typical fluid catalytic cracking (FCC) catalyst at several temperatures. In addition, mixing rules have been applied to predict the desorption isotherms and diffusion coefficients based on the measured properties of the single components of the FCC catalyst.

The predicted desorption isotherms show good agreement with the experimental isotherms for lower water activities; for higher water activities the water content is over predicted. The drying behaviour of the binder component strongly dominates the initial drying behaviour of the FCC catalyst. The transition to the 'falling rate period' depends on the initial drying conditions; the transition from the penetration period to the regular regime is at a constant water content. The diffusion coefficient of the FCC catalyst is most accurately predicted with the parallel model.

2.1 Introduction

In the field of industrial catalysis, fluid catalytic cracking (FCC) is one of the largest heterogeneous catalysis processes. The variety in FCC units, changing feed stock quality and increasing environmental demands, require a wide range of FCC catalysts formulations. FCC catalysts usually consist of a type of zeolite, the main cracking component, embedded in a catalytically active matrix. A binder component is important to increase attrition resistance and prevent the loss of fines. In the manufacture of FCC catalyst, spray drying is the common technique to form micro-spherical particles (Woltermann, 1993). To design a spray drying process or to optimise an existing one, a good knowledge of the drying behaviour and drying kinetics of FCC catalyst is essential.

FCC catalyst is regarded as a multi-component material: zeolite Y, clay, alumina and silica. Zeolite Y is the main cracking component and consists of micron-sized, aggregated crystals, which contain micro-pores (Meier, 1996). Clay is used as an inert densifier and consists of platelets with a width of about a micrometer. Pseudo-boehmite alumina is an active matrix element and is peptised with an acid to produce a sol with a particle size of several hundred nanometers. The binder material is a silica sol, of which the properties depend strongly on the pH, concentration and solution temperature of the prepared sol. The silica sol is in a meta-stable state: polymerisation of the silicic acid forms particles, which grow and finally link to form a network and thicken to a gel (Scherer, 1990, 1997; Brinker, 1990).

The drying curve is used to investigate the different drying stages and regular regime analysis is applied to calculate the concentration dependent diffusion coefficient. The diffusion coefficient includes all contributing mechanisms for mass transport and is for a given material dependent on temperature and water content.

The aim of this chapter is to describe the drying kinetics of FCC catalyst using properties of the single components. This allows prediction of drying kinetics for any given composition. Various drying stages are being discussed and the desorption isotherms and diffusion coefficients are determined at different temperatures. In addition, the interaction between the single components is studied from binary mixtures.

2.2 Drying theory

2.2.1 Sorption isotherms

The sorption isotherm of a material is the relation between the equilibrium water content and the water activity at a certain temperature. For porous materials like FCC catalyst, the adsorption mechanism is different from the desorption mechanism, which results in a hysteresis loop for the isotherm (Sing, 1982). In this study the desorption isotherm, being more relevant for the drying process, is measured. The desorption isotherm shows to which equilibrium water content the material may dry once the air conditions are known. The desorption isotherm is also used to calculate the water vapour pressure at the interface, which is needed to find the drying rate. Numerous models for the sorption isotherm have been published (e.g. Papadakis, 1993).

With respect to the sorption isotherm, it is assumed that the components in the mixture do not interact and that thermodynamic equilibrium exists, i.e. each phase in the mixture has the same water activity. The water content of a given multi-component mixture $u_{mixture}$ at a certain water activity a_w is then calculated by means of mass weighted averaging of water contents:

$$u_{mixture}(a_w) = \sum_{j=1}^{n} \omega_j u_j(a_w) \tag{2.1}$$

in which ω_j is the mass fraction of species j on dry solids basis.

The water content u_j (kg_w/kg_s) is based on dry solids:

$$u_j = \frac{\rho_{w,j}}{\rho_s} \tag{2.2}$$

in which $\rho_{w,j}$ is the water concentration of species j (kg_w/m^3)and ρ_s the solids concentration.

2.2.2 Shrinkage

Drying processes are often accompanied by shrinkage. The shrinkage behaviour of a material is characterised with a shrinkage or volume curve, which gives the material volume as a function of the water content. From the shrinkage limit and the skeletal density, the porosity and apparent density of the material can be calculated.

2.2.3 Drying kinetics and regular regime analysis

In drying processes three drying stages can be distinguished. In a convective drying process the evaporation energy is supplied by heated air and in the beginning a material will tend to wet-bulb conditions (first stage). When the heat transfer from the air to the material is equal to the (latent) heat needed for evaporation, the second stage is defined as the 'constant activity period' (CAP). The water activity of the interface is nearly constant and has a value close to one (Kerkhof, 1975). When the surface area for evaporation is constant, which is the case for a layer, the drying rate is also constant, and therefore this stage is usually called the 'constant rate period'. In the CAP the external mass transfer resistance controls the drying process and the drying flux $j_w^{\,i}$ is controlled by external conditions (air temperature, air humidity in the bulk and at the interface and the relative velocity). It is assumed that the resistance to mass (and heat) transfer is located in a thin film at the interface through which the transport can be described as quasi-stationary. At the interface exists a thermodynamic equilibrium. The effect of net mass transfer on heat and mass transfer rates is given in (Bird, 1960) and is, for the applied drying conditions, negligible (Kerkhof, 1974). The drying flux $j_w^{\,i}$ is related linearly to the mass transfer coefficient in the film layer, k_f:

$$j_w^i = k_f\left(\rho_{vi} - \rho_{v\infty}\right) \tag{2.3}$$

in which ρ_{vi} is the water vapour density in the gas phase at the interface and $\rho_{v\infty}$ the water vapour density in the bulk.

The mass transfer coefficient is calculated with film conditions and the correlation for the Sherwood number (Krischer, 1978):

$$Sh = 0.664\, Re^{0.5} Sc^{0.33} \tag{2.4}$$

According to the sorption isotherm, the interface water activity starts to decrease significantly at a certain water content, and hence the humidity at the interface decreases as well. The lower activity causes the drying rate to decrease. This period is defined as the falling rate period (FRP, third stage). The water concentration profiles inside the material become steeper and the mass transfer becomes internally limited. Finally, the drying process stops when the water activity of the material is in equilibrium with the activity in the gas phase (water vapour pressure).

The water transport in the material is described with a diffusion process, in which all contributing mechanisms for water transport are combined into one parameter: the diffusion coefficient. The drying kinetics for both shrinking and non-shrinking layers can be described with a diffusion equation on solid basis (Kerkhof, 1975):

$$\left(\frac{\partial u}{\partial t}\right)=\frac{\partial}{\partial \sigma}\left(\rho_s^2 D\left(\frac{\partial u}{\partial \sigma}\right)\right) \tag{2.5}$$

in which D is the diffusion coefficient

The transformed space co-ordinate, σ, for a layer is defined as:

$$\sigma \equiv \int_0^r \rho_s dr \tag{2.6}$$

The initial conditions are:

$$t=0 \quad 0\le\sigma\le\sigma^{\max} \quad u=u_0 \tag{2.7}$$

in which u_0 is the initial water content.

The boundary conditions are given by:

$$\begin{aligned} t>0 \qquad \sigma=0 \qquad & \frac{\partial u}{\partial \sigma}=0 \\ \sigma=\sigma^{\max} \quad & -\rho_s^2 D\frac{\partial u}{\partial \sigma}=j_w^i \end{aligned} \tag{2.8}$$

The FRP is divided into two sub stages: a penetration period (PP) and a regular regime (RR). The concentration profiles and drying stages for a zero concentration at the external boundary are schematically depicted in figure 2.1. In the PP the water content at the centre equals the initial value, while the surface water content is equal to the equilibrium value. In the RR the water content at the internal boundary changes significantly. The shape of the water concentration profiles becomes independent of the initial water content and initial drying flux. The RR drying curve depends only on the geometry and the diffusion coefficient.

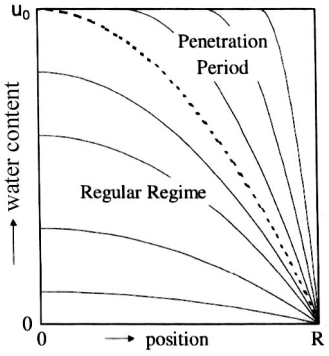

Figure 2.1. Concentration profiles and drying stages, from Coumans, 2000.

Schoebers method

Schoeber developed a method to calculate the diffusion coefficient in the RR from an experimental drying curve (Schoeber, 1976; Coumans, 1987; Liu, 1993; Coumans, 2000). In the measured drying curve the drying flux $j_w^{\ i}$ is given as a function of the average water content $\overline{u}$ or time. The drying flux is an important parameter for the calculation of the diffusion coefficient and can be obtained from the overall mass balance over the layer:

$$j_w^i = -L\overline{\rho}_s \frac{d\overline{u}}{dt} \tag{2.9}$$

in which L is the layer thickness.

The flux parameter, F, is defined as:

$$F = \frac{j_w^i L}{\overline{\rho}_s} = -L^2 \frac{d\overline{u}}{dt} \tag{2.10}$$

Schoeber defined a parameter X, which for a zero interface water content u_i is given by:

$$X = \frac{d \ln F}{d \ln \overline{u}} \tag{2.11}$$

From the experimental drying curve (-d$\overline{u}$/dt versus $\overline{u}$), the flux parameter F and parameter X can be calculated at any value of $\overline{u}$.

In the PP the diffusion process can be regarded as taking place in a semi-infinite layer, hence the following relation is valid (Schoeber, 1976; Coumans, 1987; Liu, 1993):

$$F\,(u_\circ - \overline{u}) = \text{constant} \tag{2.12}$$

By using equation 2.11 and assuming a zero interface water content u_i, the following equation for parameter X of the PP can be derived:

$$X_{PP} = \frac{\overline{u}}{u_\circ - \overline{u}} \tag{2.13}$$

The transition point from the PP to the RR is found from the intersection of the X versus $\overline{u}$ curves defined in equations 2.11 and 2.13. The diffusion coefficient follows from the RR-part of the experimental drying curve with the equation:

$$D = \frac{d}{d\overline{u}}\left(\frac{2F}{\mathrm{Sh}_d}\right) \quad \text{at } u = \overline{u} \tag{2.14}$$

For a layer the Sherwood number of the dispersed phase Sh_d is given by:

$$\mathrm{Sh}_d = \frac{\pi^2}{2}\left(1 + \frac{1}{2}\cdot\frac{X-1}{X+1}\right) \tag{2.15}$$

The procedure to calculate the diffusion coefficient from experimental drying curves may be carried out as follows:

1. Obtain the drying curve: -d$\overline{u}$/dt versus $\overline{u}$.
2. Calculate X versus $\overline{u}$ from equation 2.11.
3. Calculate X_{PP} versus $\overline{u}$ from equation 2.13.
4. Find the transition point of the PP to the RR from the intersection of the X-curves.
5. For $\overline{u} < \overline{u}_{\text{transition}}$:
    a. Calculate Sh_d versus $\overline{u}$ from equation 2.15.
    b. Calculate D versus $\overline{u}$ from equation 2.14.

2.2.4 Diffusion coefficient of mixtures

The diffusion coefficient of a mixture $D_{mixture}$ will depend on those of the single components D_j and on the volume fraction φ_j of each component. In the mixture a local thermodynamic equilibrium is assumed and the values of the diffusion coefficients D_j are based on the local equilibrium values for the water content in each phase. For a given water activity the sorption isotherm determines the water content of each component u_j. The water concentration of component j, $\rho_{w,j}$ is related to the water content u_j via the density. The water concentrations are related to a chosen reference phase n via an equilibrium partition coefficient $K_{j,n}$:

$$K_{j,n} = \frac{\rho_{w,j}}{\rho_{w,n}} \tag{2.16}$$

Note that the n^{th} equilibrium partition coefficient equals one and is included in the equations for convenience. The water concentration of component j is related to the average water concentration $\overline{\rho}_w$ by:

$$\rho_{w,j} = \frac{K_{j,n}\overline{\rho}_w}{\sum_{k=1}^{n}\varphi_k K_{k,n}} \tag{2.17}$$

The diffusion coefficient in phase *j* at average water concentration is given by (Kroes, 1999):

$$D'_j(\overline{\rho}_w) = \frac{K_{j,n} D_j(\rho_{w,j})}{\sum_{k=1}^{n} \varphi_k K_{k,n}} \tag{2.18}$$

2.2.4.1 Series and parallel models

For FCC catalyst only the series and parallel models are studied. Regarding these limit situations, the actual diffusion coefficient of the mixture is expected to be within these bounds. The series model gives the lower boundary:

$$\frac{1}{D_{mixture}(\overline{\rho}_w)} = \sum_{j=1}^{n} \frac{\varphi_j}{D'_j(\overline{\rho}_j)} \tag{2.19}$$

and the parallel model the upper boundary:

$$D_{mixture}(\overline{\rho}_w) = \sum_{j=1}^{n} \varphi_j D'_j(\overline{\rho}_j) \tag{2.20}$$

As an extra parameter, one may introduce the volume fraction ψ of the material for which the pure series model applies, and the volume fraction $1-\psi$ for which the pure parallel model applies (Krischer, 1978).

2.2.4.2 Clausius-Mossotti model

For binary mixtures equations 2.19 and 2.20 can also be used. In addition, the Clausius-Mossotti model is applied to predict diffusion coefficients (e.g. Maxwell, J.C., 1904; Hashin, 1962; and Kroes, 1999). This model was originally derived for electrical conductivity and considers the binary mixture as a dispersion of spheres in a continuum. The Clausius-Mossotti model is applied to binary mixtures of clay and the results were comparable to the parallel model (Kroes, 1999). The diffusion coefficient of a binary mixture is given by:

$$D_{mixture}(\overline{\rho}_w) = D'_i(\overline{\rho}_w)\left(\frac{2D'_i(\overline{\rho}_w) + D'_j(\overline{\rho}_w) - 2\phi_j\left(D'_i(\overline{\rho}_w) - D'_j(\overline{\rho}_w)\right)}{2D'_i(\overline{\rho}_w) + D'_j(\overline{\rho}_w) - \phi_j\left(D'_i(\overline{\rho}_w) - D'_j(\overline{\rho}_w)\right)}\right) \tag{2.21}$$

Although the Clausius-Mossotti model can be extended to multi component mixtures, this is not studied here.

2.2.5 Temperature dependence of the diffusion coefficient

The influence of the temperature on the diffusion coefficient is described with an Arrhenius type of equation:

$$D(T) = D_{\infty} \exp\left(-\frac{E_a}{RT}\right) \tag{2.22}$$

in which R is the gas constant, and T the absolute temperature.

The activation energy, E_a, is calculated from two measured diffusion coefficients at different temperatures.

2.2.6 The drying behaviour of a silica sol

The binder material is made by mixing water glass and an acid to produce a silicic acid solution. Silicic acid ($Si(OH)_4$) is a tetra functional monomer and polymerises to form primary particles of several nanometers diameter. The further particle growth and network formation depends on the solution temperature, pH and concentrations of the species (Brinker, 1990). For a solution pH < 7 or if salts are present, the primary particle growth is limited, the particles stay small and tend to from aggregates, which combine to a network, the silica gel. Because of the long drying times compared to spray drying, there will be simultaneous evaporation of water and the development of a silica gel. This complicated interaction of phenomena is not studied, though the drying of the silica sol is treated in the same way as the other components.

A short phenomenological description is given and a comprehensive review can be found in (Scherer, 1990).

The curvature of the liquid meniscus in the nano-sized pores at the surface may decrease the drying rate in the CAP by vapour pressure reduction. The liquid tension compresses the solid phase and the material shrinks. For a gel, the force to submerge the solid phase is low and the radius of the meniscus is larger than the pore radius of the gel. The shrinkage continues until the radius of the meniscus is approximately equal to the radius of the pores. Then the FRP begins and the interface recedes in the pores.

2.3 Experimental

2.3.1 Materials and formulations

2.3.1.1 Materials

Sodium zeolite Y and kaolin clay have been purchased from Sigma-Aldrich[1]. Disperal® alumina has been obtained from Condea Chemie and was dispersed with nitric acid. Sodium silicate (water glass) has been obtained from Akzo-Nobel Chemicals. The silica sol is prepared by mixing sodium silicate, water and sulphuric acid in a vessel at constant pH.

2.3.1.2 Mixture formulation and preparation

All formulations are based on dry solids basis. Binary mixtures have been made in 1:3, 1:1, and 3:1 mass ratios. In addition, zeolite and clay mixtures have been made in 1:4, 2:3, 3:2 and 4:1 mass ratios. Samples are prepared by blending the amounts of dry solids and subsequently adding water under mixing until a homogeneous slurry is obtained.

2.3.1.3 FCC catalyst formulation and preparation

The FCC catalyst formulation is a mixture of 21 wt.% zeolite Y, 42 wt.% clay, 15 wt.% alumina and 22 wt.% silica. FCC catalyst feed is made by gradual addition of clay to the silica sol under mixing. Subsequently dispersions of zeolite Y and alumina have been added. The water content of the slurry is approximately 3.6 kg_w/kg_{ds}, which is equal to 21.7 wt.% dry solids. One sample has been made in which silica binder is omitted.

2.3.2 Drying experiments

Drying curves are measured by weighing a sample in the experimental set-up, which is developed in our laboratory (Kroes, 1999; Coumans, 1987). The drying apparatus consists of two cylindrical chambers, connected via a small tube (figure 2.2). In the upper chamber an electronic precision balance (resolution 1 mg) is placed and the temperature is kept constant. In the lower chamber a Teflon sample holder is placed, which is attached to the balance via the connection tube. The sample holder has a cylindrical shape with a diameter of 6 cm and a sample height of 3 mm. A Pt-100 temperature sensor is placed in the bottom of the sample holder to register the sample temperature. The covered sample

[1] See www.sigmaaldrich.com; www.condea.de; www.akzonobel.com

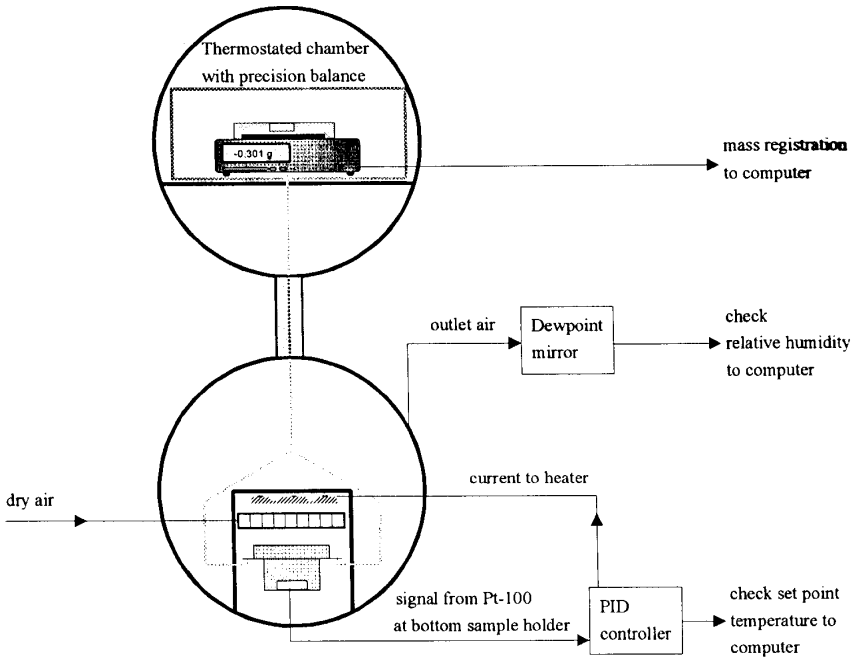

Figure 2.2. Schematic overview of the drying apparatus, from Kroes, 1999.

is heated before the measurement. During the experiment the temperature of the sample is kept constant with a PID controlled infrared heater, while dry air is led over the sample with an adjustable velocity between 0 and 0.8 m/s. The mass and temperature of the sample are recorded by a computer. In addition, the temperature and humidity of the outgoing air and the temperature of the chamber are recorded. Some samples were pre-treated by drying in a stove at the experimental temperature to achieve a lower initial water content. The drying curves were measured at sample temperatures between 30 and 70 °C.

2.3.3 Characterisation methods

2.3.3.1 Water content

The initial and final water contents of a sample are measured with a precision balance (±0.1 mg) after drying at least 48 hours at 200 °C in a stove.

2.3.3.2 Density

The skeletal density is measured with a helium stereopicnometer (Quantachrome). The skeletal volume of the material is measured with helium, because helium is assumed

to fill the small pores of the zeolite Y. The bulk density is measured with a Stampfvolumeter (Engelsmann) with a graduated cylinder of 250 ml and tapping a thousand times.

2.3.3.3 Porosity

The total pore volume is determined with incipient wetness impregnation of water: water is added to the powder until it sticks to a spoon (Leofanti, 1998). The porosity is calculated using the skeletal density of the material. This method gives a fair indication of the total porosity and, since results vary from person to person, it is used qualitatively.

2.3.3.4 Shrinkage curve

The FCC catalyst feed was placed in a Perspex cylinder (3 cm height, 2 cm diameter) and degassed under vacuum in a desiccator. Subsequently the samples are slowly dried at 25 °C above a saturated LiCl solution (a_w = 0.11). At certain time intervals, a sample is coated with paraffin to prevent further evaporation. Then the volume is determined via measuring the apparent weight above and under water and correcting for the paraffin volume (Van Es, 1990).

2.3.3.5 Desorption isotherms

About 3 g of (over) hydrated sample is placed in a glass holder of 2.5 cm radius and 1 cm depth. The holder is placed above a saturated salt solution in a plastic container and kept at constant temperature. Equilibrium is defined when the mass of the sample no longer changed significantly (± 1%). Water activities of the saturated solutions are taken from Greenspan (Greenspan, 1977). Desorption isotherms are measured between 25 and 70 °C.

2.4 Results and discussion

2.4.1 Density

The measured skeletal and bulk densities are summarised in table 2.1. The calculated skeletal density of FCC catalyst equals $2.53 \cdot 10^3$ kg/m^3, which agrees very well with the measured value: the difference is ca. 4%, which indicates that the interaction between the components is small. The difference can be explained by the inaccuracy of the

measurement. Accordingly, the skeletal density of FCC catalyst can be predicted well with the single component densities.

Table 2.1. Skeletal and bulk densities of single components and FCC catalyst

Material	*Skeletal density (kg/m³)*	*Bulk density (kg/m³)*	*Void fraction*
Zeolite Y	$2.42 \cdot 10^3$	$5.0 \cdot 10^2$	0.79
Clay	$2.62 \cdot 10^3$	$9.6 \cdot 10^2$	0.64
Alumina	$2.84 \cdot 10^3$	$9.5 \cdot 10^2$	0.66
Silica	$2.27 \cdot 10^3$	$8.6 \cdot 10^2$	0.62
FCC catalyst	$2.44 \cdot 10^3$	$9.6 \cdot 10^2$	0.61

The bulk densities of the materials are comparable, except for zeolite Y. The larger volume fraction voids for the zeolite Y is explained by the presence of the micro-pores.

2.4.2 Shrinkage curve

The shrinkage curve of FCC catalyst is measured, where slow drying took place at 25 °C above saturated LiCl (a_w = 0.11). The volume decreases linearly with decreasing water content until the shrinkage limit, as shown in figure 2.3. The average volume at low water contents equals $9.46 \cdot 10^{-4}$ m^3/kg_s. The apparent density, calculated with this volume, equals 1056 kg/m^3, which is higher than the measured bulk density. The intercept of the linear fit is a measure for the skeletal density and equals $3.36 \cdot 10^{-4}$ m^3/kg_s. The corresponding skeletal density equals 2974 kg/m^3, which is substantially higher than the measured value from picnometry (2440 kg/m^3). The water content at the shrinkage limit is 0.59 kg_w/kg_s and corresponds to a porosity of 0.59. The measured skeletal density (i.e. 2440 kg/m^3) and the density of water have been used to reconstruct the linear part of the shrinkage curve. This linear part is agrees very well with the linear fit. When the apparent density of the FCC catalyst is also known, the shrinkage curve can be predicted.

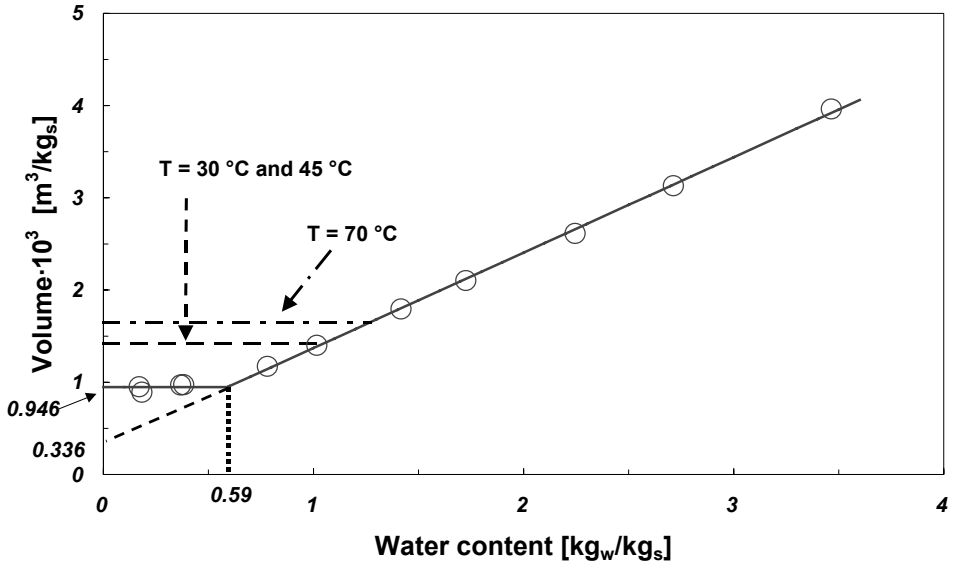

Figure 2.3. Shrinkage curve of FCC catalyst dried at 25 °C above a saturated LiCl solution. The dotted lines are measured final volumes for drying experiments at 30, 45 and 70 °C.

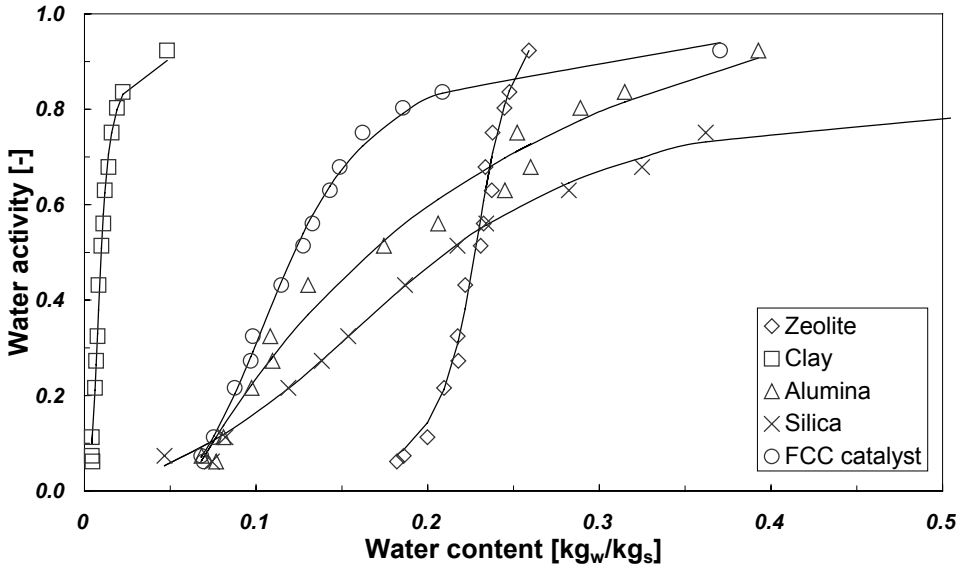

Figure 2.4. Desorption isotherms of single components and FCC catalyst at 30 °C

2.4.3 Water desorption isotherms

An equation and the parameters to fit the desorption isotherms of the components is given in appendix A.

2.4.3.1 Single components

Figure 2.4 shows the desorption isotherms of the single components and FCC catalyst at 30 °C. The desorption isotherms of components at 30, 45 and 70 °C are given in appendix B. In general, temperature effects are small and become more pronounced at higher water activity (a_w).

Comparing the single components, the water content of clay is very low, silica has the largest water content at high a_w and zeolite Y at low a_w. For zeolite Y it can be observed that, at higher a_w, the water content of the material decreases rather slightly as a_w decreases; at low values for a_w the water content decreases strongly with decreasing values for a_w. This behaviour is typical for micro-porous materials. The zeolite Y sample is composed of many particles and each particle consists of an agglomerate of zeolite Y crystals with micro-pores. For higher a_w the larger pores between the crystals and the surface area of the crystals determine the sorption behaviour. The water activity changes strongly as the water content decreases slightly. At lower a_w the micro-porous crystals dominate the sorption behaviour very strongly and the water activity does not change very much due to the uniform size of the pores. Apparently, the size distributions of the pores between the crystals and the agglomerates are relatively broad and show some overlap. It appeared that for alumina the dispersion technique has a large influence on the position of the sorption isotherm. There is probably a direct relation with the particle size. The water content of silica increases significantly for a small change in a_w at high a_w. The temperature effect on the silica sorption isotherm is very limited. This is remarkable considering the variation in the silica concentration and pH during the drying process. Apparently, the differences in polymerisation behaviour do not affect the sorption isotherm significantly.

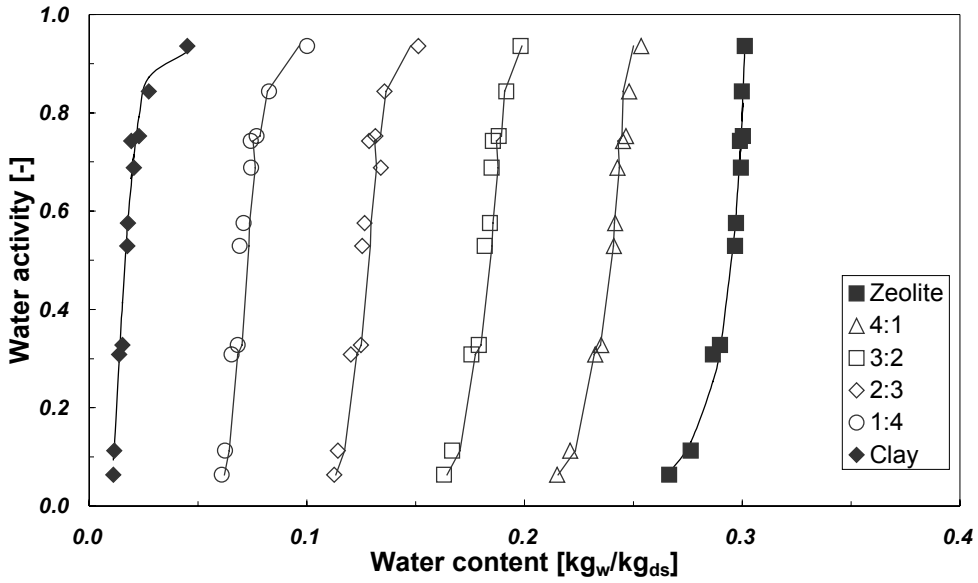

Figure 2.5. Desorption isotherms of zeolite - clay mixtures and single components at 25 °C. The lines represent the predicted values of the mixtures.

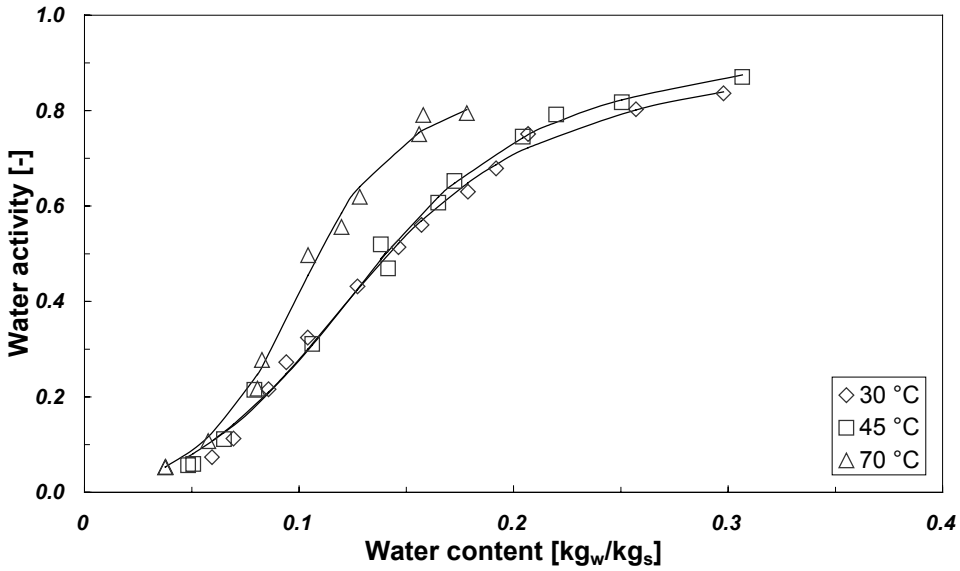

Figure 2.6. Desorption isotherm of FCC catalyst at 30, 45 and 70 °C. Lines are calculated with the equations and parameters given in appendix A.

2.4.3.2 Binary mixtures

The sorption isotherms of zeolite Y and clay mixtures at 25 °C are shown in figure 2.5. The measured values are in very good agreement with the predicted values. In general, the predicted isotherms of the binary mixtures at higher temperatures have the correct shape, although their values are less accurate. The deviations are the largest for mixtures with alumina, which is partly due to the dispersion technique. The sorption isotherms and the predicted values of the binary mixtures at 45 °C are also given in appendix B. The differences between the measured and predicted values are probably caused by experimental errors.

2.4.3.3 FCC catalyst

The desorption isotherms of the FCC catalyst at 30, 45 and 70 °C are given in figure 2.6. Considering the results for the single components, it can be concluded that the water content of FCC catalyst at low a_w is mainly determined by zeolite Y and at high a_w by silica. The shape of the desorption isotherm of FCC catalyst is similar to those of clay, silica and alumina. The catalyst consists of ca. 80 wt.% of these components. Figure 2.7 shows the predicted versus the measured water content. For a water content < 0.1 kg_w/kg_s

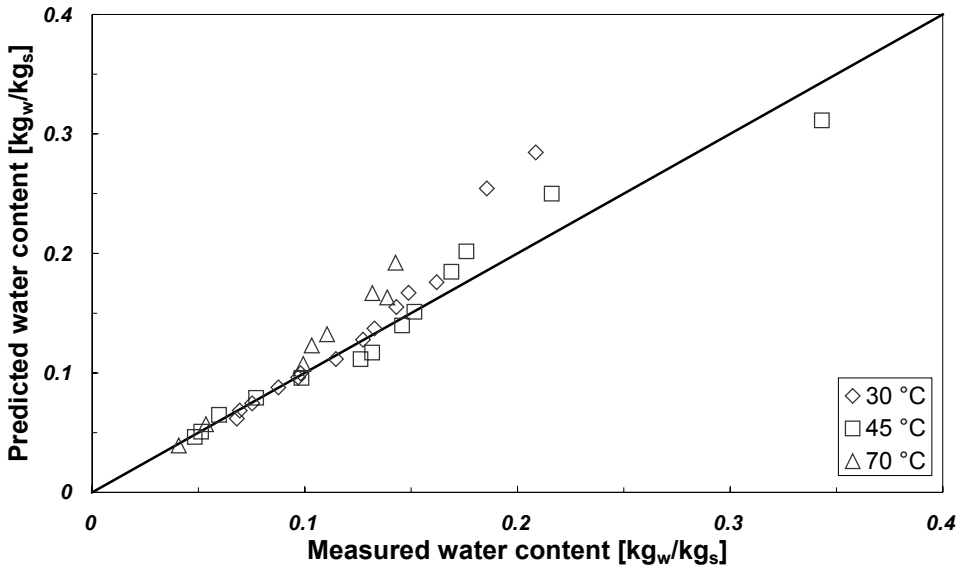

Figure 2.7. Measured and predicted water contents of desorption isotherms of FCC catalyst at 30, 45 and 70 °C.

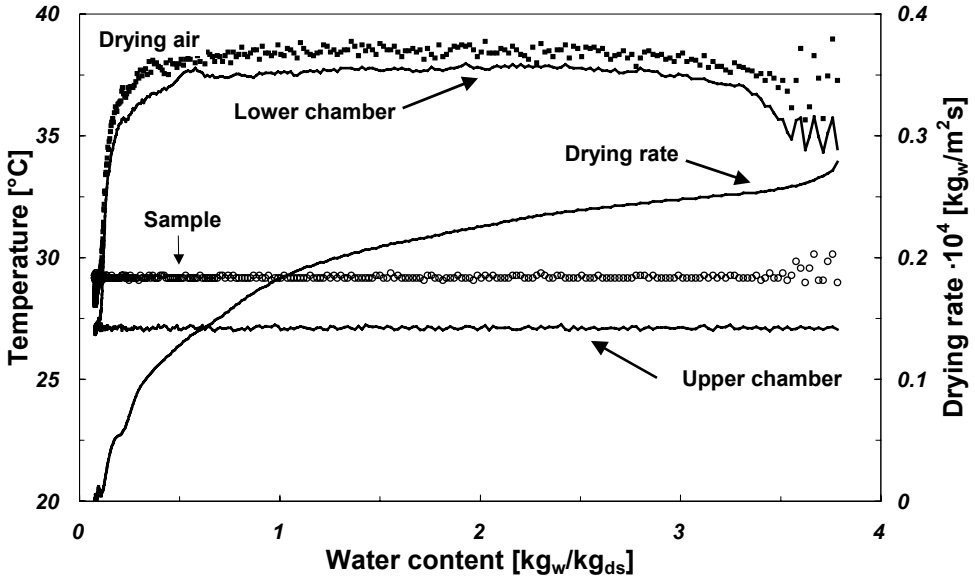

Figure 2.8. Drying rate and temperatures during drying of FCC catalyst at 30 °C.

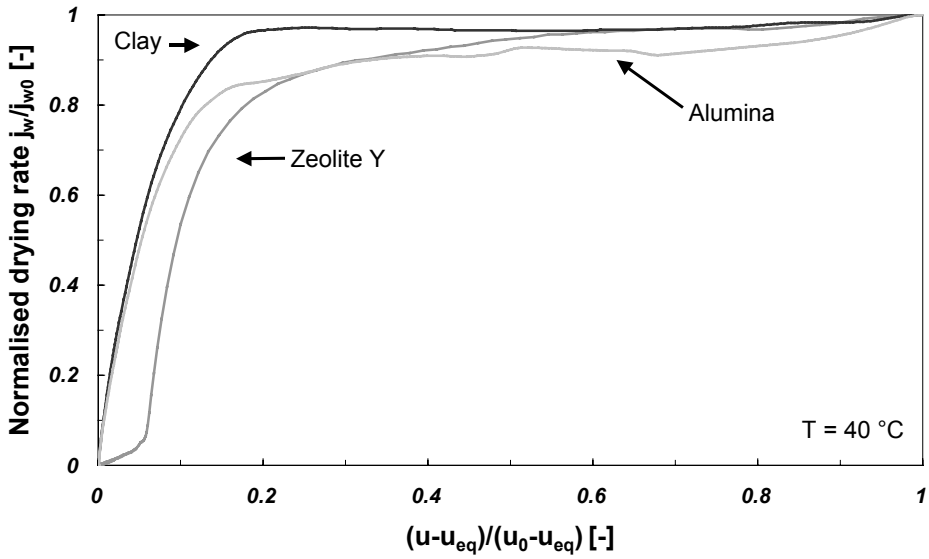

Figure 2.9. Characteristic drying curves of zeolite Y, clay and alumina at 40 °C. Other characteristic parameters are given in table 2.2.

the predicted values are in good agreement with the measured values, but deviate in the higher region. At 70 °C the deviations are larger and start at a lower water content. Presumably the deviations are caused by experimental errors.

2.4.4 Drying experiments

In figure 2.8 a typical drying curve of FCC catalyst and the measured temperatures during the experiment are shown. After the heating period the temperatures attain a constant value until the FRP is entered. When the drying rate decreases substantially, the air and lower chamber temperatures also decrease. The initial water content, the initial drying flux and the equilibrium water content of the drying experiments are given in table 2.2. The equilibrium water contents are not equal to zero. Although dry air is used in the experiment, the residual water evaporated very slowly, indicating a very low diffusion coefficient (which includes all contributing mechanisms to mass transfer).

2.4.4.1 Characteristic drying curves

Figure 2.9 shows the characteristic drying curves of zeolite Y, clay and alumina. The drying rate decreases gradually from the beginning and occurred for most of the experiments. Because it is also found for pure water, the effect is due to the experimental conditions and cannot be attributed to the material. The decrease could be caused by the increased air humidity in the drying chamber, or by shrinkage of the material, which increases the external mass transfer resistance.

Silica and FCC catalyst did not shrink uniformly during drying: the layers cracked, what resulted in many small islands. Various stages of the drying process of silica at 40 °C are visualised in figures 2.10 a – h. Also it is observed that the preparation of the silica sol has a large influence on the drying kinetics. Even with exactly the same concentrations and drying conditions, the drying curves were not reproducible. The polymerisation behaviour of silica is a complex phenomenon since it involves many reactions. The polymerisation behaviour and its influence on the drying kinetics were beyond the scope of this study (see for example Scherer, 1990; Brinker, 1990).

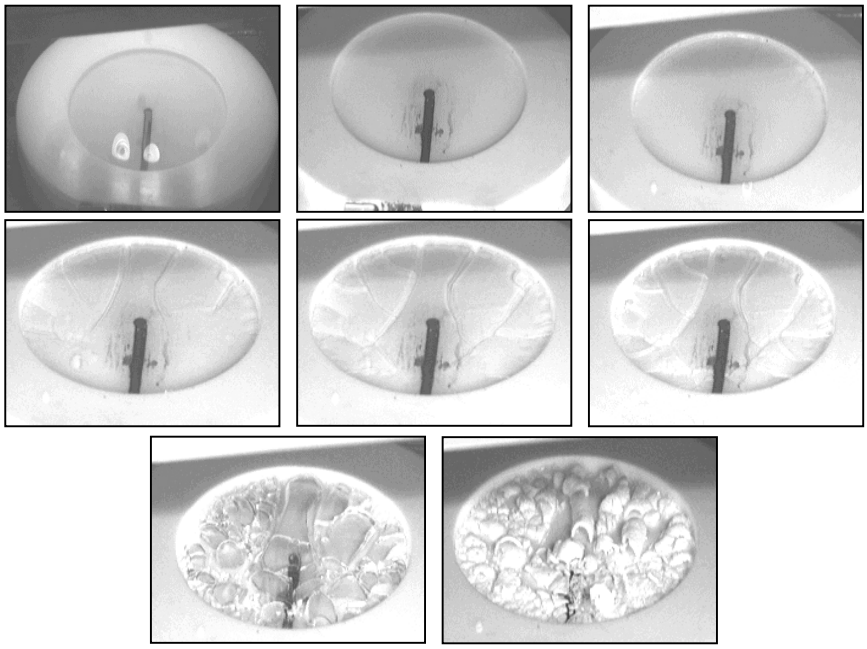

Figure 2.10 a – h. Pictures of the morphology of silica during a drying experiment at 40 °C. Water contents are respectively: 5.1, 4.0, 3.5, 3.0, 2.4, 1.9, 1.4 (FRP) and 0.3 kg_w/kg_s.

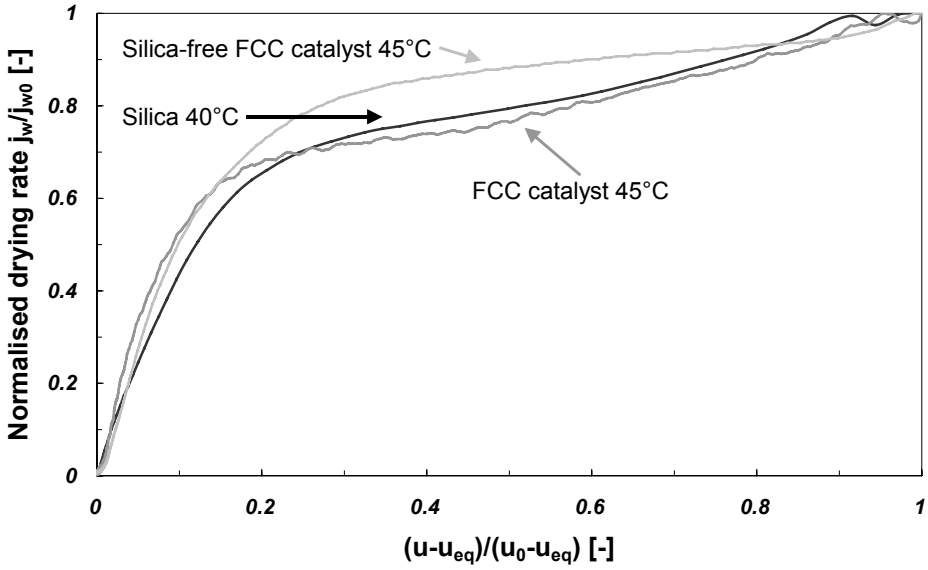

Figure 2.11. Characteristic drying curves of silica at 40 °C and FCC catalyst and silica free FCC catalyst at 45 °C. Other characteristic parameters are given in table 2.2.

Table 2.2. Experimental data for the characteristic drying curves.

Material	*T (°C)*	j_{wo}^{i} *(kg$_w$/m^{2}s)*	u_o *(kg$_w$/kg$_s$)*	u_{eq} *(kg$_w$/kg$_s$)*
Zeolite	40	$4.32 \cdot 10^{-4}$	2.61	0.06
Clay	40	$4.10 \cdot 10^{-4}$	4.67	0.005
Alumina	40	$4.31 \cdot 10^{-4}$	10.5	0.06
Silica	40	$3.63 \cdot 10^{-4}$	6.87	0.15
FCC catalyst	45	$4.44 \cdot 10^{-4}$	3.58	0.09
Binder free catalyst	45	$4.14 \cdot 10^{-4}$	2.02	0.08

The period of gradually decreasing drying rate is still considered as the CAP and is rather long. This is caused by the high initial water contents (table 2.2). The CAP is followed by a rapidly decreasing drying rate in the falling rate period. The transition from the CAP to the FRP is not at a well-defined water content, but occurs in a range of water contents. The CAP of zeolite Y is rather short: the drying rate decreases slowly until the water content is ca. 0.5 kg_w/kg_s and then decreases much faster. An additional transition is observed at u = 0.2 kg_w/kg_s, which is due to the micro-pores of the material.

The characteristic drying curves of silica, FCC catalyst and silica free FCC catalyst (at different temperatures) are depicted in figure 2.11. The initial water contents are given in table 2.2. The drying rate of silica free FCC catalyst is higher than of the other two. This shows the influence of silica on the drying rate. For silica and FCC catalyst there is no CAP observed: after the initial heating period the drying rate decreases gradually. This decrease is higher than observed for the other materials. This is probably due to the effect of the water activity reduction from the curvature of the liquid meniscus at the surface. A pore radius of $1 \cdot 10^{-8}$ m would result in a relative water activity of 0.9. The monotonous decrease indicates that the radius of meniscus becomes smaller as the material shrinks during the drying process. When about 80 % of the water has evaporated, the drying rate decreases faster. The transition to the FRP is between a water content of 1.1 and 1.6 kg_w/kg_s. The similarity of the drying curves points out that, at high water contents, the drying rate of FCC catalyst is determined by the silica component. This is in agreement with the results found for the desorption isotherms.

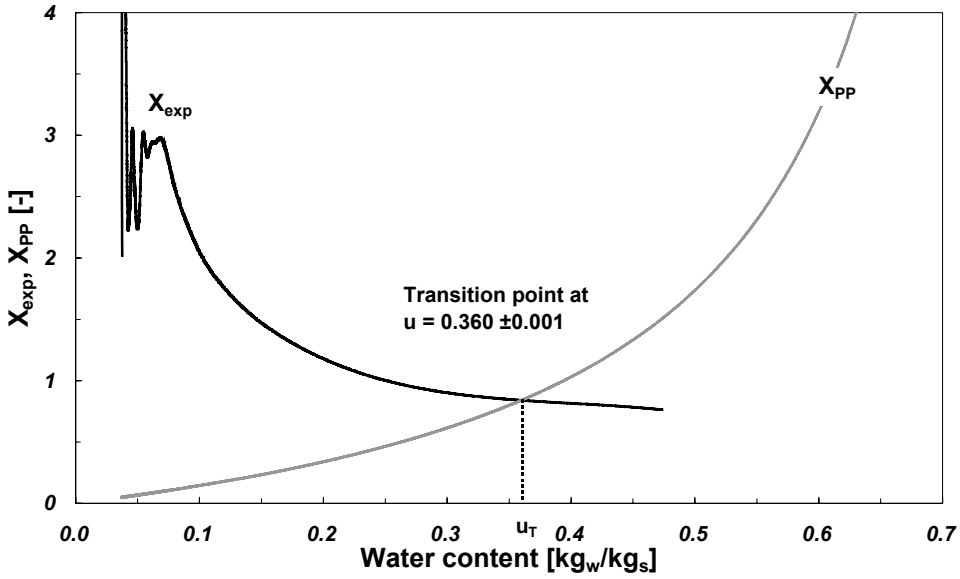

Figure 2.12. X parameter curve for the penetration period (X_{PP}) and the experimental parameter (X_{exp}) for FCC catalyst at 45 °C. Drying parameters are given in table 2.2.

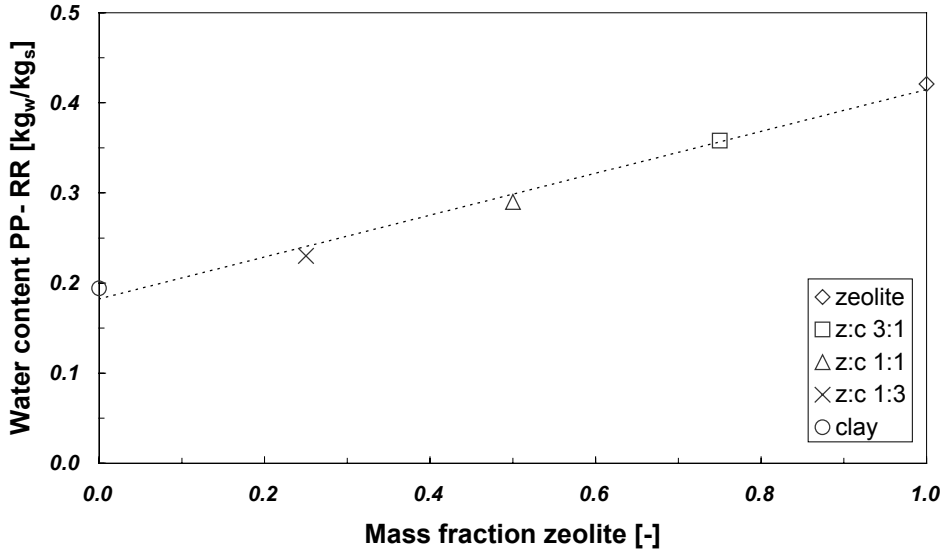

Figure 2.13. Water content at PP – RR transition of zeolite – clay mixtures and single components at sample temperature of 45 °C.

2.4.4.2 Transition of the penetration period to the regular regime

The transitions of the penetration period to the regular regime of a material are at almost the same water contents for the different sample temperatures: differences are within 17 %. In table 2.3 the water contents at the transition of the PP to the RR are given. Silica has a transition point at the highest water content and clay at the lowest. The value for FCC catalyst is in between these values. An example of the determination of the transition point of FCC catalyst at 45 °C is given in figure 2.12. The transition points for mixtures of zeolite Y and clay at a sample temperature of 45 °C are depicted in figure 2.13. The transition point increases linearly with the mass fraction. The mixture of zeolite Y and alumina has comparable results, although the deviations from the linear relation are somewhat larger. In figure 2.14, the different stages of drying are indicated in the drying curve of FCC catalyst.

Table 2.3. Transition points from PP to RR.

Material	*PP – RR transition water content (kg_w/kg_s)*		
Sample temperature (°C)	30	45	70
Zeolite	0.459	0.421	0.377
Clay	0.127	0.161	0.154
Alumina	0.314	0.337	0.361
Silica	0.547	0.545	0.479
FCC catalyst	0.384	0.360	0.393

2.4.4.3 Diffusion coefficients

The diffusion coefficients have been fitted and the fit equations and parameters are given in appendix C.

Single components

The diffusion coefficients of zeolite Y at three different temperatures are given in figure 2.15. The scattering at low water content is due to the inaccuracy of the experiment: the change of mass at low water contents becomes very small. The diffusion coefficient of zeolite Y shows a clear transition to a lower value at a relatively high water content. The water content of the transition point decreases with increasing temperature. The transition is caused by a change of the transport mechanism. A possible explanation is

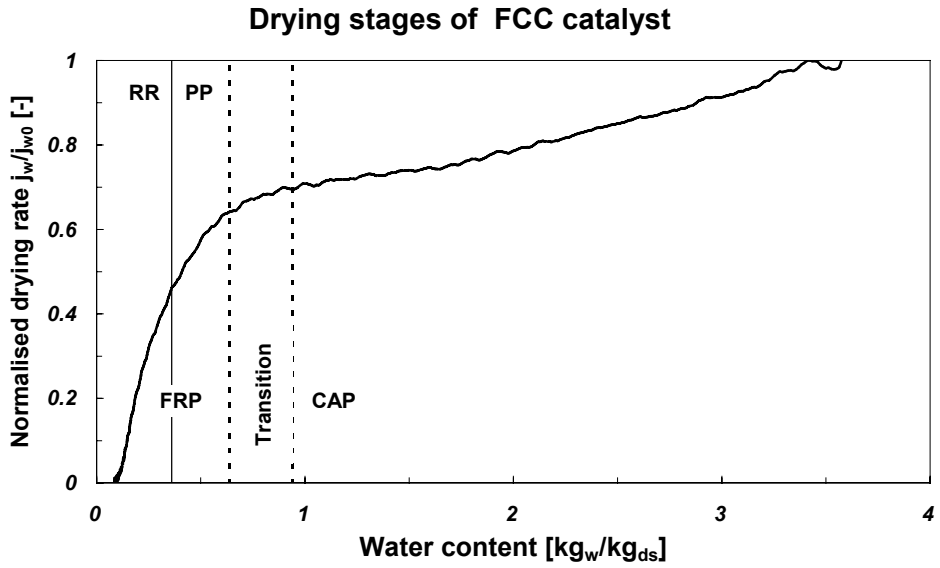

Figure 2.14. Drying stages of FCC catalyst at 45 °C.

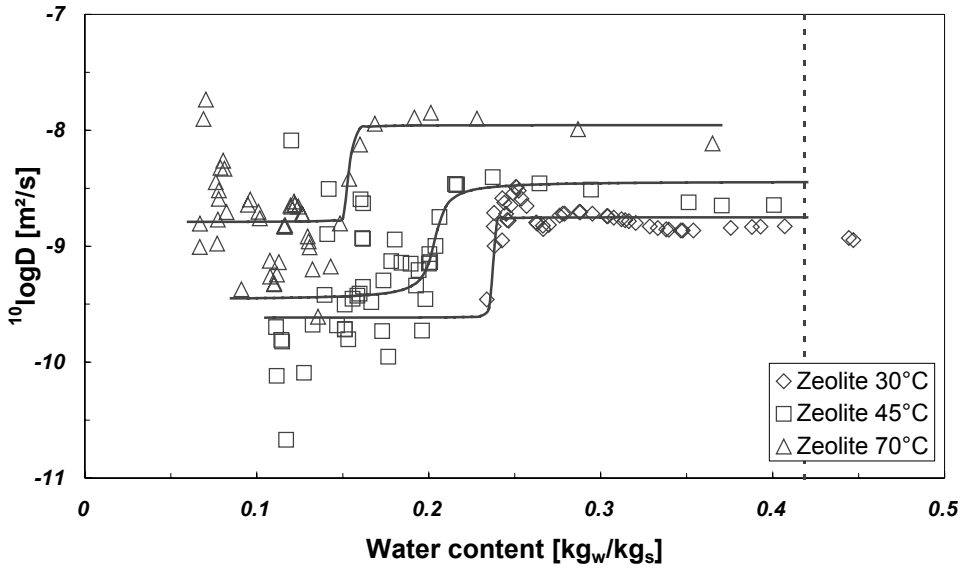

Figure 2.15. Diffusion coefficients of water in zeolite at three sample temperatures.

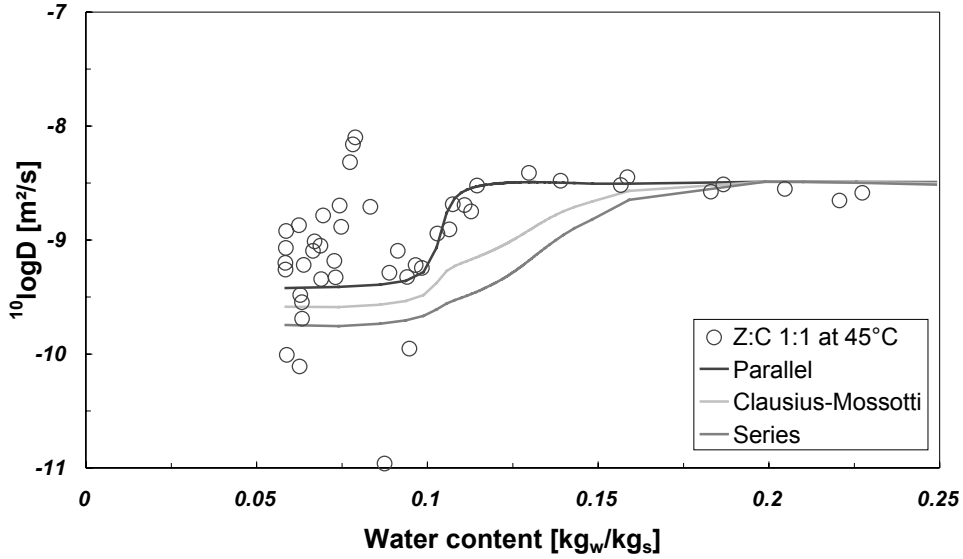

Figure 2.16. Diffusion coefficient of water in a 1:1 zeolite – clay mixture at 45 °C and predicted values.

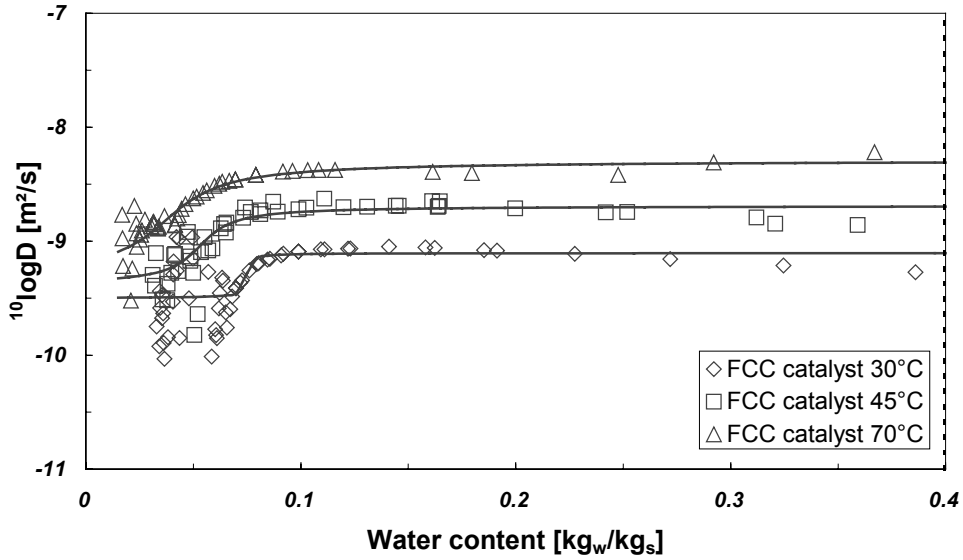

Figure 2.17. Diffusion coefficient of water in FCC catalyst for three sample temperatures.

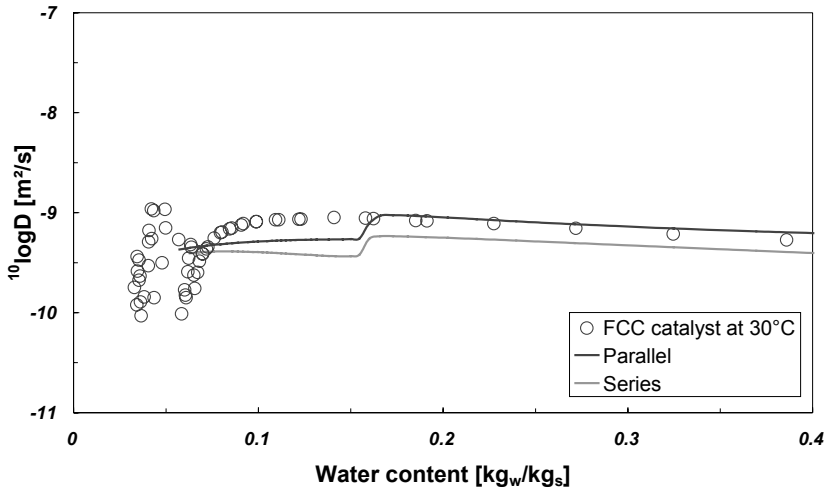

Figure 2.18. Diffusion coefficient of water in FCC catalyst at 30 °C and predicted values.

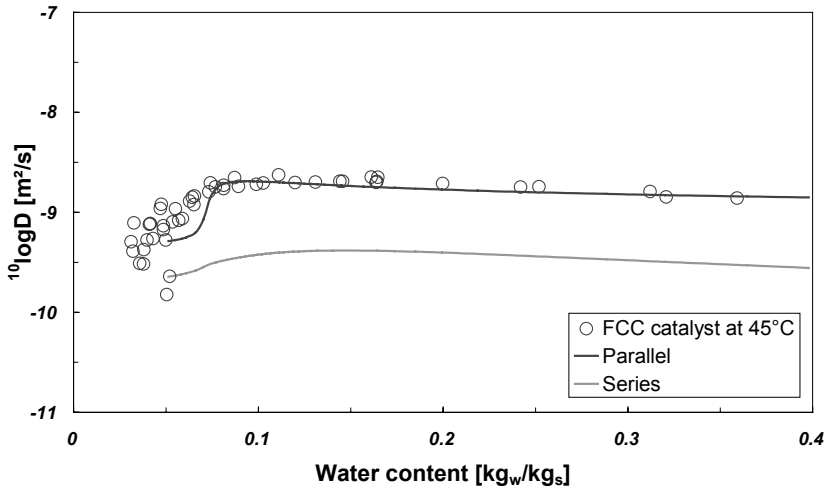

Figure 2.19. Diffusion coefficient of water in FCC catalyst at 45 °C and predicted values.

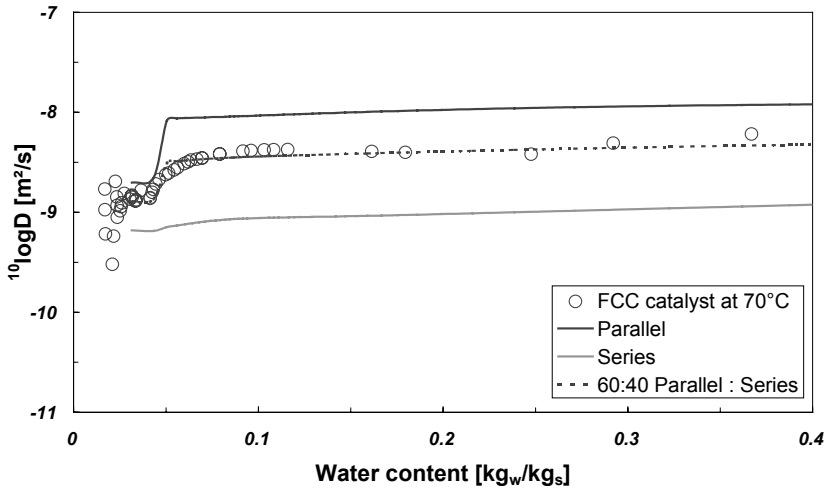

Figure 2.20. Diffusion coefficient of water in FCC catalyst at 70 °C and predicted values.

that when the water between the crystals has evaporated, only the micro-pores remain filled. The water transport from the micro-pores controls the overall drying rate. Considering the theoretical pore diameter of $7.4 \cdot 10^{-10}$ m, the water activity at the interface would be about 0.08. However, the water content where the diffusion coefficient increases is lower than the equilibrium water content at low a_w. This indicates that pores larger than the well-defined micro-pores contribute significantly to the equilibrium water content. The value of the measured diffusion coefficient at lower water contents and the apparent constant value are in reasonable agreement with self-diffusivity data from NMR measurements for water in a NaX zeolite at 298 K (Kaerger, 1992).

The values of the diffusion coefficient of the other components show an approximately constant value. At very low water contents the evaluation method becomes quite sensitive to small experimental errors and a large scattering of the results is observed. The diffusion coefficients of the other components are given in appendix B.

Binary mixtures

The results of the measurement and the predicted values from the series, parallel and Clausius-Mossotti models for the 1:1 zeolite Y – clay mixture at 45 °C are given in figure 2.16. The parallel model most accurately predicts the diffusion coefficient. The results of diffusion coefficients of the other mixtures and temperatures are given in appendix B. For all mixtures, the parallel model predicts the diffusion coefficient the most accurate.

FCC catalyst

The diffusion coefficients of FCC catalyst at different temperatures are shown in figure 2.17. It seems that the diffusion coefficient increases at low water content and becomes more or less constant after the transition point. The transition point, which is due to the zeolite Y, becomes less distinct at higher temperatures. The measured and predicted values are shown in figures 2.18 – 2.20. The experimental diffusion coefficient of FCC catalyst at 30 °C is out of the limiting bounds of the models at low water content, which is probably a result of the measured diffusion coefficient of zeolite Y. At 30 and 45 °C the parallel model is suitable to describe the diffusion coefficient. At 70 °C the parallel model over-predicts the diffusion coefficient and a 60% parallel and 40% series combination gives the best result. The parameters of the model are the volume fractions of the single components and the ratio parallel to series model. The used volume

fractions are based on bulk densities of the single components. However, it is not certain that after mixing the bulk densities are still valid. In addition, because the FCC catalyst layer cracked at low water content and formed several small parts, the results should be interpreted with caution.

2.4.4.4 Temperature dependence of the diffusion coefficient

The diffusion coefficients of the measured materials increase with increasing temperature, as does the diffusion coefficient of FCC catalyst (figure 2.17). The calculated activation energies of diffusion are depicted in figure 2.21. The mountain in the activation energy of the zeolite Y is caused by the shift of the transition point with the temperature (figure 2.15). These high values of the activation energy are not realistic because the transport mechanism is changing at lower water contents, and two mechanisms are compared. This mountain is also observed for FCC catalyst at a water content that matches with the mass fraction zeolite Y. The measured values at higher water contents are somewhat lower than the activation energy for long-range self-diffusion of water in zeolite NaX, which is 50 – 65 kJ/mol (Kaerger, 1992). The other components show a slight increase in activation energy with increasing water content. The values are comparable to the evaporation heat of water, which suggests that the water in the materials is present as free water and adsorption is not strong for these water contents.

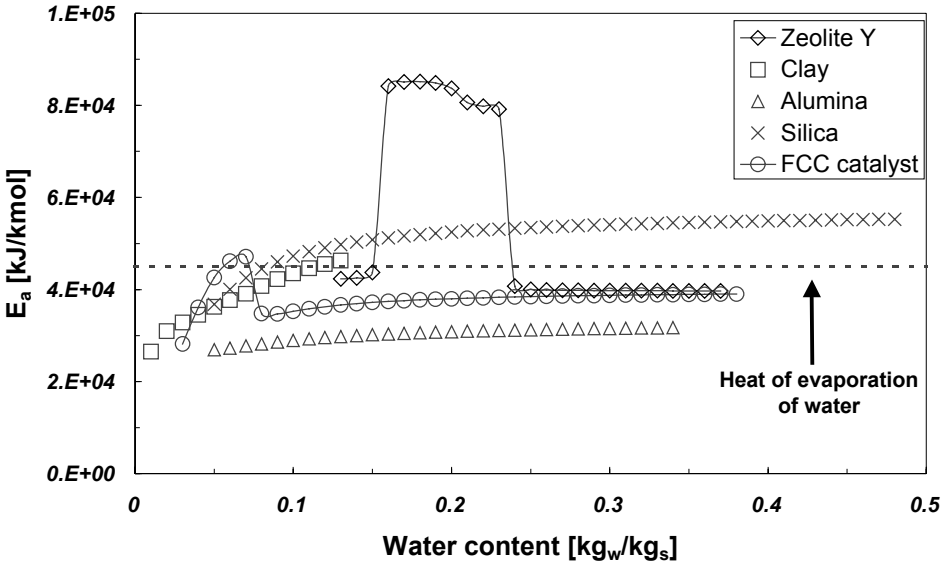

Figure 2.21. Activation energy of diffusion for the single components and FCC catalyst as function of water content.

The lower values at low water contents indicate that the diffusion coefficient is less temperature dependent.

2.5 Conclusions

The description of the drying behaviour of FCC catalyst using the properties of the single components is studied. The mixing rule for the desorption isotherm reasonably predicts the values for FCC catalyst. In the CAP, the silica binder determines the drying behaviour: the drying flux depends on both the external conditions and the meniscus radius at the surface. The transition to the FRP depends on the initial drying flux and depends mainly on the silica component. The transition from the PP to the RR is at a constant water content of ca. 0.4 kg_w/kg_s. The diffusion coefficient of FCC catalyst is most accurately predicted with the parallel model. This implies that, for a FCC catalyst mixture, the water transport is controlled by the material with the highest diffusivity.

For layer drying experiments the gelling of silica influences the shrinkage of FCC catalyst. In case of spray drying FCC catalyst, it is not certain whether gelling occurs. The drying behaviour of silica depends on the preparation of the silica sol. This implies that this also influences the drying behaviour of the FCC catalyst. The sorption isotherm of alumina is influenced by the dispersion method.

Notation

Roman

a_w	Water activity	[-]
D	Diffusion coefficient	$[m^2/s]$
E_a	Activation energy	[J/kg]
F	Flux parameter	$[kg_w\ m^2/kg_s\ s]$
H	Absolute humidity of air	$[kg_w/kg_{da}]$
j	Drying flux	$[kg_w/m^2\ s]$
k	Mass transfer coefficient	[m/s]
K	Equilibrium partition coefficient	[-]
L	Layer thickness	[m]
r	space co-ordinate	[m]
R	Gas constant	[J/kg K]
t	time	[s]
T	Temperature	[K]
u	Water content	$[kg_w/kg_s]$
X	Parameter	[-]

Greek

φ	Volume fraction	[-]
ρ	Concentration	$[kg/m^3]$
σ	Transformed space co-ordinate	$[kg_s/m^2]$
ω	Mass fraction	[-]

Subscript

d	Dispersed phase
da	Dry air
f	Film
i	Interface
s	Solids
w	Water
o	Initial
∞	Infinite

References

Bird, R.B., Stewart, W.E. and Lightfoot, E.N., 1960, Transport Phenomena, J. Wiley & Sons, New York, USA.

Brinker, C.J. and Scherer, G.W., 1990, Sol-gel science: the physics and chemistry of sol-gel processing, Academic Press, San Diego, USA.

Coumans, W.J., 1987, Power law diffusion in drying processes, Ph.D. thesis, Eindhoven University of Technology, Eindhoven, The Netherlands.

Coumans, W.J., 2000, Models for drying kinetics based on drying curves of slabs, Chemical Engineering and Processing, 39, 53-68.

Es, M.A.L.J. van, 1990, Krimpgedrag van klei (shrinkage behaviour of clay), Masters thesis, Eindhoven University of Technology, Eindhoven, The Netherlands.

Gregg, S.J. and Sing, K.S.W., 1982, Adsorption, surface area and porosity, 2nd ed., Academic Press, London, UK.

Greenspan, L., 1977, Humidity fixed points of binary aqueous solutions, Journal of Research of the National Bureau of Standards, 81A, 89-96.

Hashin, Z. and Shtrikman, S., 1962, Journal of Applied Physics, 33, 3125.

Kaerger, J. and Ruthven, D.M., 1992, Diffusion in zeolites and other microporous solids, J. Wiley & Sons, New York, USA.

Kerkhof, P.J.A.M., 1975, A quantative study of the effects of process variables on the retention of volatile trace components in drying, Ph.D. thesis, Eindhoven University of Technology, Eindhoven, The Netherlands.

Krischer, O. und Kast, W., 1978, Die wissenschaftlichen Grundlagen der Trocknungstechnik, 1er Band, 3rd Ed., Springer-Verlag, Berlin, Germany.

Kroes, B., 1999, The influence of material properties on drying kinetics, Ph.D. thesis, Eindhoven University of Technology, Eindhoven, The Netherlands.

Leofanti, G., Padovan, M., Tozzola, G. and Venturelli, B., 1998, Surface area and pore texture of catalysts, Catalysis Today, 41, 207-219.

Liu, T. and Coumans, W.J., 1993, Regular regime analysis and moisture diffusivity in wood, Drying Technology, 11, 5, 977-1003.

Maxwell, J.C., 1904, A treatise on electricity and magnetism, 3rd Ed., Clarendon Press, Oxford, U.K.

Meier, W.M., Olson, D.H. and Baerlocher, Ch., 1996, Atlas of zeolite structure types, 4th rev. ed., Elsevier, London, UK.

Papadakis, S.E., Bahu, R.E., McKenzie, A., and Kemp, I.C., 1993, Correlations for the equilibrium moisture content of solids, Drying Technology, 11, 3, 543-553.

Scherer, G.W., 1990, Theory of drying, Journal of the American Ceramic Society, 73, 1, 3-14.

Scherer, G.W., 1997, Effect of drying on properties of silica gel, Journal of Non-Crystalline Solids, 215, 155-168.

Schoeber, W.J.A.H., 1976, Regular regimes in sorption processes, Ph.D. thesis, Eindhoven University of Technology, Eindhoven, The Netherlands.

Woltermann, G.M., Magee, J.S., Griffith, S.D., 1993, Commercial Preparation and Characterization of FCC Catalysts, in: Fluid Catalytic Cracking: Science and Technology, Ed. Magee, J.S., Mitchell, M.M.Jr., Elsevier, Amsterdam.

Chapter 3

The influence of spray drying conditions on fluid catalytic cracking catalyst properties

ABSTRACT

Fluid catalytic cracking (FCC) is a major process in oil refining. The process conditions in the FCC unit, different feed stocks and increasing environmental demands, require very specific FCC catalyst properties. In the production of FCC catalyst, spray drying is an important process to shape micro-spherical particles. The influence of spray drying conditions on FCC catalyst properties is studied. Measured FCC catalyst properties are: particle size distribution, particle shape, density, pore volume and pore size distribution. The studied spray drying conditions are: batch ageing time, nozzle configuration, air temperature, airflow, feed flow and feed water content. The macroscopic properties are related to a shrinkage-coefficient, which has been calculated for the experiments. The spray drying conditions mainly influence the morphology.

3.1 Introduction

Spray drying is an important operation in the manufacture of catalytic supports and catalysts, such as fluid catalytic cracking (FCC) catalysts. FCC catalysts are used in oil refineries to convert distillates and residues into lighter fractions. In a riser reactor the FCC catalyst particles are mixed with atomised oil. During the upward fluidisation the evaporated oil is cracked. At the top of the reactor the deactivated FCC catalyst is separated from the product stream, stripped and regenerated by burning off the deposited coke.

A modern FCC catalyst consists of zeolite, the major cracking component, embedded in a matrix. In addition, one or more additives are added. The severe process conditions, different feed stocks and product demands require very specific product properties for the FCC catalyst: such as particle size distribution, shape, density and strength. The particle size distribution and density are essential for fluidisation properties and separation of catalyst from the product stream. The strength and shape are important parameters for the attrition resistance. FCC catalyst components with a particle size smaller than 10^{-6} m decrease the attrition resistance (Woltermann, 1993). For the cracking process, important properties are selectivity, activity and thermal stability. Although the activity and selectivity depend mainly on the chosen materials, the pore structure will also contribute to these properties. Generally, larger surface areas are thought to favour the activity. However, it has been found that the matrix surface area also plays a minor role in the conversion of n-hexane (Brait, 1998). Larger surface areas would also increase attrition and coke deposition. The pore structure or pore size distribution influences the accessibility of and transport pathways in the interior. Larger molecules may be pre-cracked by an active matrix component into smaller ones, which are then transported to the zeolite particles and further cracked inside the micro-pores. Larger pores allow faster transport, although they also tend to decrease the stability and mechanical strength. It is thought that presence of meso-pores increases olefin and liquid yields, decreases coke formation, and increases attrition (Sullivan, 1995).

The use of a relative small amount of sub-colloidal binder resulted in the formation of an enriched shell that improved the attrition resistance (Bergna, 1989). Instead of using colloidal silica of $2.2 \cdot 10^{-8}$ m diameter, poly silicic acid particles of $2 - 3 \cdot 10^{-9}$ m diameter

were used. FCC catalyst with alumina in the matrix showed improved attrition resistance at comparable conversion and selectivity, and better activity after metal poisoning (Pedersen, 1989).

In the manufacture of FCC catalyst, the spray drying process produces particles with a size of ca. $6 \cdot 10^{-5}$ m and enables the control of the particle size distribution, density and, to some extent, the particle shape. The influence of spray drying conditions on product properties has been subject of several studies (e.g. Meenan, 1997; Meerdink, 1995, Kerkhof, 1975; Crosby, 1958, Lebeis, 1955). However, for catalytic materials literature is rare, mainly due to proprietary knowledge. For the drying of spheres of silica-alumina gels, it has been found that the drying rate in the falling rate period was the major determinant of the density (Lebeis, 1955). Much later the drying kinetics and particle size distribution of a cracking catalyst have been modelled and experimentally validated using a rotary atomiser and different operation variables (Andrieu, 1992). The particle size distribution could accurately be predicted.

This study was initiated by the fact that no literature is found that discusses the influence of spray drying conditions on FCC catalyst properties, other than (Andrieu, 1992). In other references, it is mentioned that spray drying is an art or that knowledge is proprietary (Magee, 1976; Woltermann, 1993). A typical FCC catalyst formulation has been spray dried at pilot-plant scale (evaporation rate ≈ 50 kg_w/hr). The varied process conditions are: air temperature, airflow and feed flow. In addition, the influence of the initial water content, the batch ageing time and the droplet size distribution are studied. The relative particle size, density and porosity are related to the amount of shrinkage.

3.2 Spray drying and product properties

The spray drying process is usually divided into four stages; atomisation, spray-air contact, drying, and separation of the dried product from the air (Masters, 1985). Although all four stages influence the final particle properties, only the atomisation and drying stages are considered, since these are thought to be the most important. The atomisation process has a large influence on the initial droplet size distribution. The shrinkage during the drying process then determines the final particle size distribution.

3.2.1 Atomisation and droplet size distribution

Atomisation is the transformation of a bulk liquid into a spray with high specific surface area. This results in short drying times and small particles. Different types of atomisers are used in practise, of which the most common are pressure nozzles and rotating disc atomisers (Masters, 1985). In the experiments, a centrifugal pressure nozzle is used. Kinetic energy from the applied pressure forms a spray. A rotating motion is given to the liquid by the core. Subsequently the liquid passes an orifice, which results in the formation of a conical, hollow film that disintegrates into a spray. The combination of the nozzle type, feed properties and applied pressure determines the droplet size distribution and flow. The nozzle pressure varies with the square of the flow rate. The mean particle diameter d_p is proportional to the nozzle pressure P_n by (Trullinger, 1997; and Masters, 1985):

$$\overline{d}_p \propto P_n^{-0.3} \tag{3.1}$$

The particle size distribution becomes narrower for higher nozzle pressures.

In general, the mass flow rate is proportional to the liquid density. A higher liquid viscosity uses more energy to break up the film, which results in an increased droplet diameter. The mean droplet diameter is proportional to the viscosity by the power of 0.25 (Trullinger (1997)). The temperature and surface tension are parameters that can be changed to influence the droplet size.

For a constant flow rate the pressure can be influenced by changing the nozzle configuration: the orifice size or the core slot diameter. A larger orifice or slot diameter will decrease the mean particle size at equal flow rate. Changing the nozzle will necessarily influence the spray angle of the film.

3.2.2 Shrinkage model and FCC catalyst properties

The amount of shrinkage can be related to the relative diameter, average porosity and density of the particle by means of a volume balance. During drying, water evaporates and the droplet (or particle) volume V_p decreases. It is assumed that the droplet remains spherical and shrinks uniformly. The shrinkage is ideal, i.e. there is no gas phase present in the droplet, and the shrunk volume equals the liquid volume of the evaporated water. The catalyst components are considered as the solid phase with a constant volume V_s. The

micro-pore volume of the zeolite is not influenced by the shrinkage. The densities of the solid, ρ_s, and water, ρ_w, are constant, and it is assumed that there is no interaction between the components and water. When the droplet has stopped shrinking the volume of the remaining water ($V_p - V_s$), including the water in the micro-pores, equals the total pore volume, V_{pore}.

3.2.2.1 Shrinkage-coefficient

The shrinkage-coefficient, S, is defined as the ratio of the actual amount of shrinkage to the maximum possible amount of shrinkage:

$$S = \frac{V_\circ - V_p}{V_\circ - V_s} \tag{3.2}$$

3.2.2.2 Physical properties related to the shrinkage-coefficient

The amount of shrinkage can be calculated from measured properties. In addition, the initial droplet diameter $d_{d\circ}$ and the bed porosity ε_{bed} are calculated from the shrinkage-coefficient.

The particle porosity, ε_p, is defined as:

$$\varepsilon_p = \frac{V_{pore}}{V_{pore} + V_s} \tag{3.3}$$

The shrinkage-coefficient can be calculated from the measured particle porosity ε_p and initial water content $u_\circ$ via:

$$S = 1 - \frac{\varepsilon_p \rho_w}{u_\circ (1 - \varepsilon_p) \rho_s} \tag{3.4}$$

in which ρ_w is the density of water and ρ_s the density of the solids.

The micro-pore volume of the zeolite component does not shrink during the drying process. Hence, the maximum shrinkage-coefficient for FCC catalyst S^{max} is not equal to one and can be calculated with the minimum particle porosity.

The initial mean droplet radius d_{do} can be calculated with the measured mean particle diameter d_p and the particle porosity ε_p:

$$\overline{d}_{do} = \overline{d}_p \left[(1-\varepsilon_p)\left(1+\frac{\rho_s}{\rho_w}u_\circ\right)\right]^{1/3} \tag{3.5}$$

The bed porosity can be calculated with the bulk density, ρ_{bulk}:

$$\varepsilon_{bed} = 1-\frac{\rho_{bulk}}{\rho_s(1-\varepsilon_p)} \tag{3.6}$$

The particle porosity, relative particle size and bulk density for constant bed porosity are given as function of the shrinkage-coefficient in figure 3.1 for a standard FCC catalyst formulation. The vertical line equals the maximum shrinkage-coefficient, calculated from the used FCC catalyst composition.

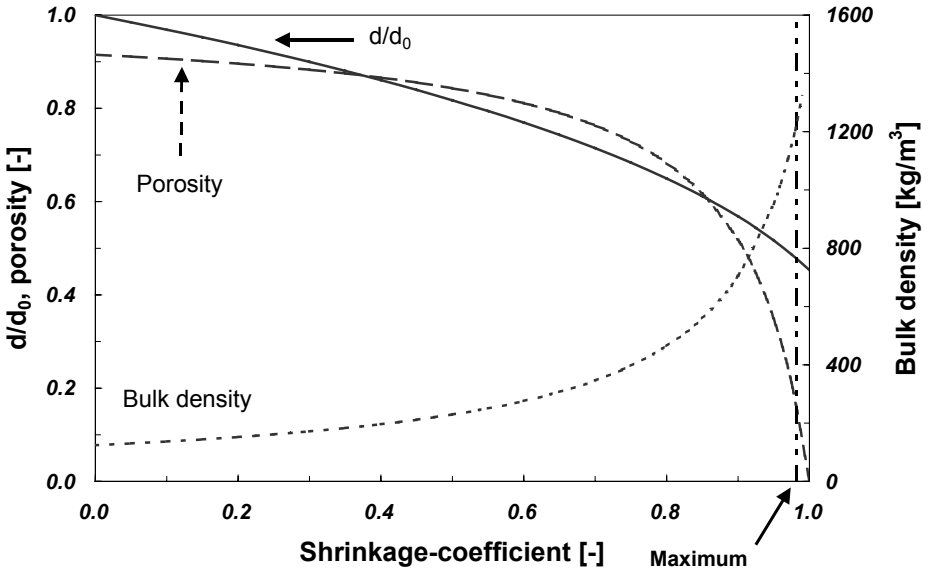

Figure 3.1. Relative particle diameter, porosity and bulk density as function of the shrinkage-coefficient.

3.3 Experimental

3.3.1 FCC catalyst formulation and feed preparation

The same FCC catalyst formulation has been used in all experiments. The FCC catalyst formulation is a mixture of 24 wt.% zeolite Y, 47 wt.% clay, 15 wt.% alumina and 14 wt.% silica. Dry solids contents are based on 48 hours drying at 200 °C. A silica sol was prepared by vigorously mixing sodium silicate, water and sulphuric acid in a vessel at constant pH. Kaolin clay was added gradually to the sol. Subsequently zeolite Y and dispersed alumina were added. For standard experiments the water content of the feed, u_o, was circa 3.6 kg_w/kg_s (solids content 21.8 wt.%). Other experiments had initial water contents of 4.6 (17.9 wt.%) and 7.3 kg_w/kg_s (12.0 wt.%). The preparation of the silica sol and the dispersion of alumina results in the presence of salts in the feed. These salts will crystallise during the drying process. The amount of salts is 10.2 wt.% of the dry catalyst weight, which corresponds to 9.3 wt.% of total dry solids. In the manufacture of FCC catalyst the salts are washed out, however, in this thesis FCC catalyst characterisation is done with the salts present.

3.3.2 Spray drier

The feed is pumped to a pilot plant scale co-current spray drier with a three-plunger pump. The feed is atomised by a Spraying Systems SK pressure nozzle, producing a hollow conical spray with a spray angle of ca. 80°. The diameter of the drying chamber is 2.20 m and the total height is 3.70 m with a conical angle of 60° at 2.0 m from the top (see figure 1.4). The electrically heated air enters the drying chamber via an annulus and the nozzle is placed in the centre. The air exits the drier via a horizontal pipe, which is placed about 0.5 m above the bottom and has a downward opening in the centre of the chamber. The airflow then passes a cyclone where particles are separated. Product was both collected from a valve at the bottom of the drying chamber (tower product) and a valve at the bottom of the cyclone (cyclone product).

3.3.3 Drying conditions

The feed flow is mass flow controlled and can be varied between 30 and 80 kg/hr, with corresponding nozzle pressures between 10 and 59 bars. The airflow was about 600

m^3/hr and the air inlet humidity, H_{in}, varied between ca. $6.0 \cdot 10^{-3}$ and $1.0 \cdot 10^{-2}$ kg_w/kg_{da}. One set of experiments is done with airflow of ca. 1200 m^3/hr. The air inlet temperature was varied between 220 and 497 °C.

3.3.4 Characterisation methods

Mass balance over the spray drier

The residual water content of the product, u_p, is determined after 48 hours drying at 200 °C. The experiments are checked with a mass balance for the dry solids:

$$G_s = G_{total} \frac{1}{(1+u_o)} = G_s u_p\Big|_{tower} + G_s u_p\Big|_{cyclone} + G_s\Big|_{loss} \tag{3.7}$$

in which G_s is the dry solids flow and G_{total} the total feed flow.

The accumulation of water in the lost product is neglected. The solids flow is composed of a tower and cyclone product flow and the tower-to-cyclone ratio equals $G_{s,tower}/G_{s,cyclone}$. The tower-to-cyclone ratio is used to produce a mixture of the tower and cyclone product: the total product. Some samples were washed at elevated temperature to remove the salts. These samples will be referred to as washed product, in contrary to unwashed product.

Particle size distribution

The particle size distribution is measured of the tower, cyclone and total product. The particle size distribution is measured with laser scattering (Coulter LS-130 and Malvern Mastersizer S). The results are presented as the volume mean particle diameter (Masters, 1985). The smallest measurable particle size is about 10^{-6} m, and the largest $9 \cdot 10^{-4}$ m.

Bulk density

The tapped bulk density, ρ_{bulk}, is measured using a Stampfvolumeter (Engelsmann) with a graduated cylinder of 250 ml after tapping a thousand times.

Pore volume

The total pore volume, V_{wi}, is determined with incipient wetness impregnation of water: water is added to the sample until it sticks to a spoon (Leofanti, 1998). The particle porosity is calculated using the skeletal density of the catalyst, which is measured with helium picnometry. This method gives a fair indication of the total porosity.

Surface area and pore size distribution

Nitrogen adsorption and desorption isotherms are measured with a Coulter Omnisorp 100 at liquid nitrogen temperature (-196 °C). Prior to measurement the samples are stored under vacuum at 200 °C overnight. For porous materials the adsorption and pore filling mechanism is different from the desorption and pore emptying mechanism. This usually results in a small parallel hysteresis loop of the isotherm. This is typical for solids that contain slit-shaped meso-pores resulting from the presence of kaolin platelets. Pores are usually divided into three groups, depending on the pore diameter. Micro-pores have diameters smaller than $2 \cdot 10^{-9}$ m, macro-pores larger diameters than $5 \cdot 10^{-8}$ m, and the meso-pore range lies in between. Standard textbook methods are applied to compare the results.

The total surface area, A_{BET}, is determined with the Brunauer, Emmett and Teller (BET) method (Brunauer, 1938; Gregg, 1982) with sorption data from relative pressures between 0.05 – 0.21 (Johnson, 1978). The micro-pore surface area, A_{mipore}, can be calculated by subtracting the macro- and meso-pore surface area, A_{mapore}, from the BET surface area (Andersson, 1998).

The *t*-plot analysis is based on the Harkins and Jura adsorption layer thickness, *t*, (Harkins, 1944; Gregg, 1982). The micro-pore volume, V_{mipore}, and surface area, A_{mipore}, are calculated from respectively the intercept and slope of fitted data for a layer thickness between $3.54 \cdot 10^{-10}$ and $5.6 \cdot 10^{-10}$ m. The V_{mipore} of FCC catalyst is usually attributed to micro-pores of the zeolite component (Brait, 1998). Because the amount of zeolite in the feed was constant, it is expected that V_{mipore} remains the same.

The Barrett, Joyner and Halenda (BJH) method with layer thickness *t* is used to calculate the pore size distributions from the desorption isotherm (Barrett, 1951; Gregg, 1982). The average pore diameter equals four times the total pore volume divided by the total surface area, both from the desorption isotherm. The pore diameter is calculated with the Kelvin equation (Gregg, 1982). The contact angle is taken 0°, the surface tension is $8.86 \cdot 10^{-3}$ N/m and the molar volume of liquid nitrogen $3.46 \cdot 10^{-2}$ m^3/kmol.

Mercury porosimetry is based on the intruded mercury volume as function of applied pressure. Because mercury has a large contact angle with most solid materials, penetration of pores occurs only under pressure and not by capillary forces. The cylindrical pore model is used to relate the pore diameter to the pressure, via the

Washburn equation. The pore volume distribution is obtained directly from the intrusion volume versus pressure data. The pore surface area results from dividing the pore volume by the pore diameter and multiply by four. The volume of pores, with a diameter larger than 10^{-6} m, is omitted. These larger pores are present between the catalyst particles and are not part of the internal structure. The contact angle of mercury is taken 140° and the surface tension $4.8 \cdot 10^{-1}$ N/m, although these values have a rather large uncertainty (Leofanti, 1998). Mercury porosimetry is used to investigate the influence of the drying conditions and has a qualitative function.

Particle shape

Scanning electron microscopy (SEM) is done with an ETEC Omniscan and a JEOL JSM-5600. With SEM, the shape (sphericity), surface morphology (for example smoothness, dimples and cracks) and the interior of the catalyst particles is studied.

3.4 Results and discussion

An overview of the process conditions and measured FCC catalyst properties is given in appendix D. The used abbreviations are summarised in table 3.1.

Table 3.1. Abbreviations for pore volume and surface area properties.

Property	*Abbreviation*	*Pore range*
Pore volume from incipient wetness impregnation	V_{wi}	All
Pore volume from nitrogen adsorption	V_{mipore}	Micro-pore
Pore volume from nitrogen desorption	$V_{maporeN2}$	Macro- and meso-pores
Pore volume from mercury porosimetry	$V_{maporeHg}$	Macro- and meso-pores
Surface area from nitrogen adsorption (BET)	A_{BET}	All
Surface area from nitrogen adsorption (t-plot)	$A_{maporeN2t}$	Macro- and meso-pores
Surface area from nitrogen desorption	$A_{maporeN2d}$	Macro- and meso-pores
Surface area from mercury porosimetry	$A_{maporeHg}$	Macro- and meso-pores

3.4.1 Effect of batch ageing time

The batch ageing time is the time between preparation of the feed and atomisation into the drying chamber. From the moment of producing the silica sol, the binder primary particles grow, form agglomerates and may even gel into an interconnected network (Brinker, 1990). A study of the kinetics of binder particle growth showed that the primary particle diameter increased from ca. $2 \cdot 10^{-9}$ to $4 \cdot 10^{-9}$ m and agglomerate sizes grew to approximately $2 \cdot 10^{-8}$ m in about 5 hours (Sullivan, 1995).

The batch ageing time is studied to exclude possible differences between batches that are spray dried from the same feed batch under different conditions. The effect of ageing is studied by spray drying half the batch after preparation and spray drying the other half of the same batch, which was kept under vigorous mixing, 3.5 hours later.

During the experiment with the fresh batch the solids accumulation in the drier was 2 wt.% of the total solids flow. The accumulation for the experiment with the aged batch was zero. Hence the tower-to-cyclone ratio decreased 2 %. The final water content was equal for both experiments: ca. $3.3 \cdot 10^{-2}$ kg_w/kg_s.

The nozzle pressure was 19.4 and 19.0 bar for the fresh and aged batch experiment respectively. This pressure difference would theoretically result in a less than 1 % smaller mean droplet diameter for the aged batch. The particle size distributions are shown in figure 3.2. The mean particle diameter d_p of the total product increased from $6.9 \cdot 10^{-5}$ to $7.2 \cdot 10^{-5}$ m (5 %) after ageing. The variance increased from $2.5 \cdot 10^{-5}$ to $2.8 \cdot 10^{-5}$ m. After washing the samples, the measured d_p's were $7.0 \cdot 10^{-5}$ and $7.1 \cdot 10^{-5}$ m respectively. The differences are within measurement accuracy. The washing of the samples, which excludes effects of the presence of the salts, does not influence the measurement of the particle size distribution. The analysis is done in an aqueous environment and the salts are probably dissolved prior to the measurement.

After ageing the tapped bulk density (ρ_{bulk}) of the unwashed tower and cyclone products decreased about 4 %. Although the differences are small, they are consistent with the increased d_p. From figure 3.1 it becomes clear that a small change in particle size has large influence on the porosity and ρ_{bulk} when the shrinkage-coefficient is almost equal to one. The decrease in ρ_{bulk} can be explained by a ca. 1.5 % increased d_p.

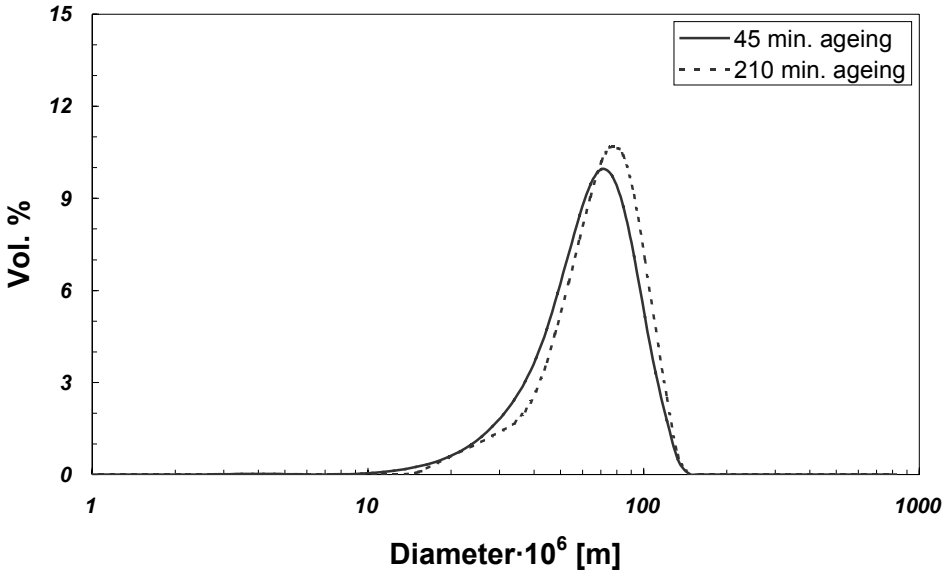

Figure 3.2. Particle size distribution of total product after 45 and 210 minutes ageing.

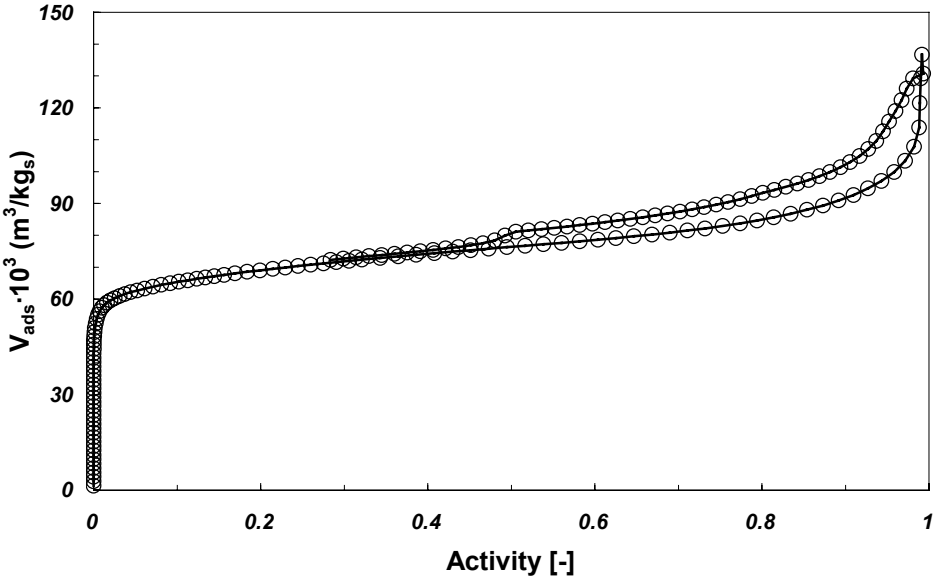

Figure 3.3. Nitrogen sorption isotherm of washed FCC catalyst.

Pore volume

The total pore volume from incipient wetness impregnation (V_{wi}) increased from $1.9 \cdot 10^{-4}$ to $2.0 \cdot 10^{-4}$ m^3/kg (2 %) after ageing. Both values correspond to a total porosity of ca. 0.32 m^3/m^3. The V_{wi} of the washed product increased from $3.3 \cdot 10^{-4}$ to $3.5 \cdot 10^{-4}$ m^3/kg (6 %) after ageing, which corresponds to porosities equal to 0.45 and 0.46 m^3/m^3 respectively. The particle density, calculated with V_{wi}, decreased less than 1 %.

The micro-pore volume (V_{mipore}) for both samples was ca. $5.7 \cdot 10^{-5}$ m^3/kg. After washing, V_{mipore} increased from $7.1 \cdot 10^{-5}$ to $7.3 \cdot 10^{-5}$ m^3/kg (3 %) with batch ageing time. Nevertheless, the difference is within measuring accuracy.

An example of the nitrogen sorption isotherm is given in figure 3.3. The small parallel hysteresis loop is typical for solids that contain slit-shaped meso-pores resulting from the presence of kaolin platelets. The macro- and meso-pore volume from nitrogen desorption ($V_{maporeN2}$) increased from $5.2 \cdot 10^{-5}$ to $8.0 \cdot 10^{-5}$ m^3/kg (54 %) after ageing. $V_{maporeN2}$ of the washed product showed an increase of 10 %: from $1.0 \cdot 10^{-4}$ to $1.1 \cdot 10^{-4}$ m^3/kg. This indicates that the presence of salts accounts for a large part of the difference.

The macro- and meso-pore volume from mercury porosimetry ($V_{maporeHg}$) of the washed samples increased from $2.4 \cdot 10^{-4}$ to $3.0 \cdot 10^{-4}$ m^3/kg (21 %). About 65 % of the increase of $V_{maporeHg}$ is found in the meso pore region, between $3.7 \cdot 10^{-9}$ and $2.4 \cdot 10^{-8}$ m and the rest for pores with a diameter of ca. $1.0 \cdot 10^{-7}$ m. $V_{maporeHg}$ for pores with a diameter between $2.4 \cdot 10^{-8}$ and $6.0 \cdot 10^{-8}$ is ca. 5 % smaller for the aged batch. However, the accuracy of the mercury porosimetry analysis is not very high and the results indicate the effects of the increased binder particle and agglomerate size.

Surface area

The BET surface area (A_{BET}) increased from $1.38 \cdot 10^5$ to $1.48 \cdot 10^5$ m^2/kg after ageing (7 %). The standard deviation of the determination of A_{BET} was $6 \cdot 10^3$ m^2/kg, determined with a quadruple measurement. After washing, A_{BET} increased from $2.26 \cdot 10^5$ to $2.50 \cdot 10^5$ m^2/kg (11 %). The increase of the BET surface area is unexpected considering the growth of particles. The absence of salts apparently increases A_{BET}.

The macro- and meso-pore surface area (A_{mapore}) is calculated from both the t-plot analysis ($A_{maporeN2t}$) and from the desorption isotherm ($A_{maporeN2d}$). $A_{maporeN2t}$ increased from $2.3 \cdot 10^4$ to $2.4 \cdot 10^4$ m^2/kg (4 %) and $A_{maporeN2d}$ increased from $2.0 \cdot 10^4$ to $2.6 \cdot 10^4$ m^2/kg (41

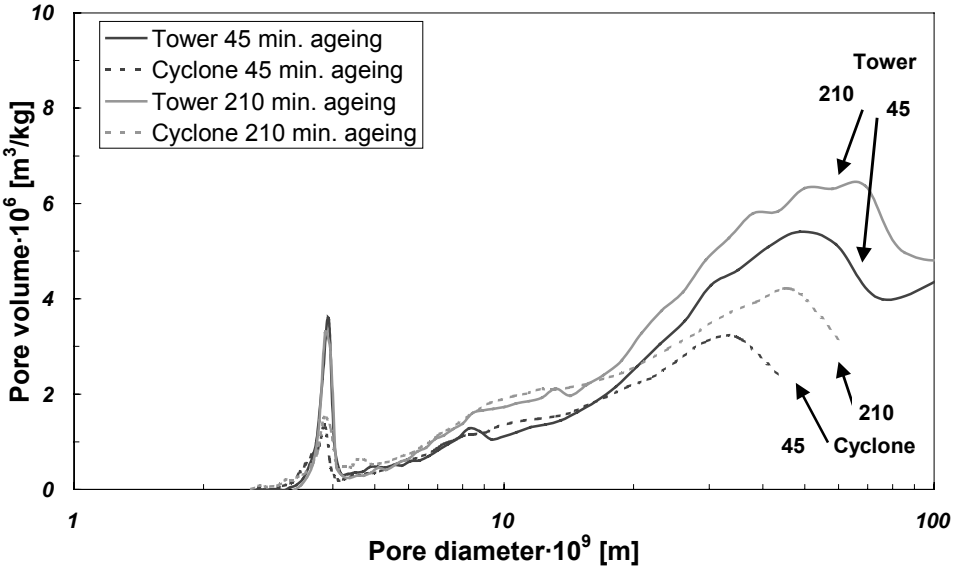

Figure 3.4. Pore volume distribution from N_2-desorption of unwashed tower and cyclone product after 45 and 210 minutes ageing.

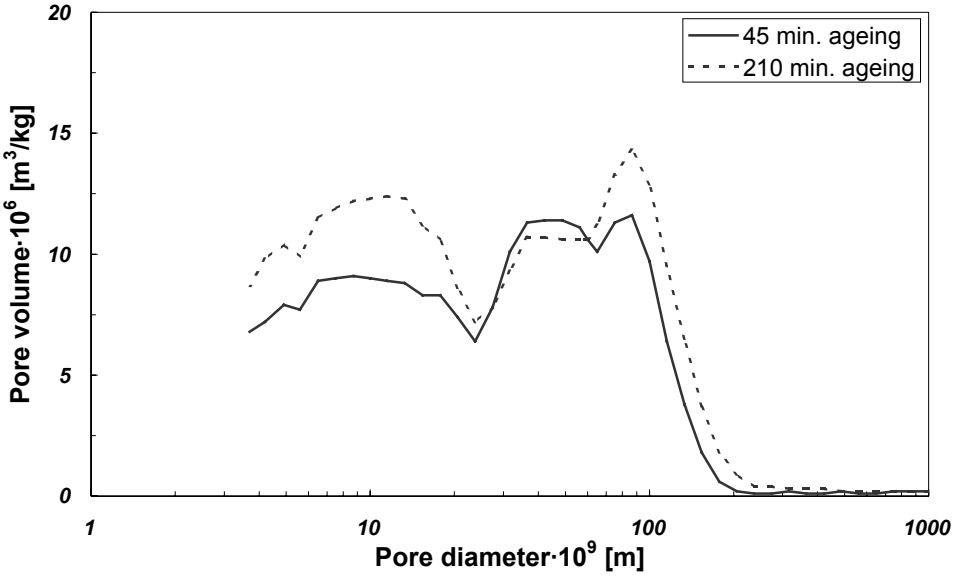

Figure 3.5. Pore size distribution from mercury intrusion of total product after 45 and 210 minutes ageing.

%). After washing, the respective surface areas from the t-plot were $9.0 \cdot 10^4$ and $9.2 \cdot 10^4$ m^2/kg and from desorption $8.9 \cdot 10^4$ and $9.1 \cdot 10^4$ m^2/kg. Although the increase of A_{mapore} with increasing batch ageing time is consistent, the differences after washing are within measuring accuracy. The macro- and meso-pore surface area from mercury porosimetry ($A_{macroHg}$) increased from $6.7 \cdot 10^4$ to $8.4 \cdot 10^4$ m^2/kg (25 %). The increase is due to the larger pore volume for small pores (see $V_{maporeHg}$) and is not consistent with the other results.

Pore size and distribution

Attention is drawn to figure 3.4, where the incremental pore volume distributions of the unwashed tower and cyclone products are presented. The average pore diameter of the unwashed product increased from $1.1 \cdot 10^{-8}$ to $1.2 \cdot 10^{-8}$ m after ageing (17 %). For the washed product, the average pore diameter increased from $4.6 \cdot 10^{-9}$ to $5.0 \cdot 10^{-9}$ m (9 %). The difference is attributed to the absence of salts.

The incremental $V_{maporeN2}$ increases with increasing pore diameter. The difference with ageing time is found in the macro- and meso pore region (diameter > $2 \cdot 10^{-8}$ m). The peak at $4 \cdot 10^{-9}$ m diameter is due to the hysteresis closure of the desorption mechanism. The surface area distributions also exhibit a peak at $4 \cdot 10^{-9}$ m pore diameter. The differences in surface area distribution are smaller, because larger pores contribute less to the surface area.

The incremental pore volume distributions of the washed product, measured with mercury porosimetry, are shown in figure 3.5. The average pore diameter decreased from $2.5 \cdot 10^{-8}$ to $2.4 \cdot 10^{-8}$ m (4 %).

Particle shape

Scanning Electron Microscopy (SEM) scans show wrinkles and dimples at the surface of particles from both experiments (figure 3.6). Although not very clear on the scans, the particles spray dried with the aged batch seem to show more wrinkles. The right figure shows more the presence of small particles, which could explain the lower tower-to-cyclone ratio. However, the presence of small particles could also be caused by sample preparation for the SEM, because the particle size distribution does not show the small particles.

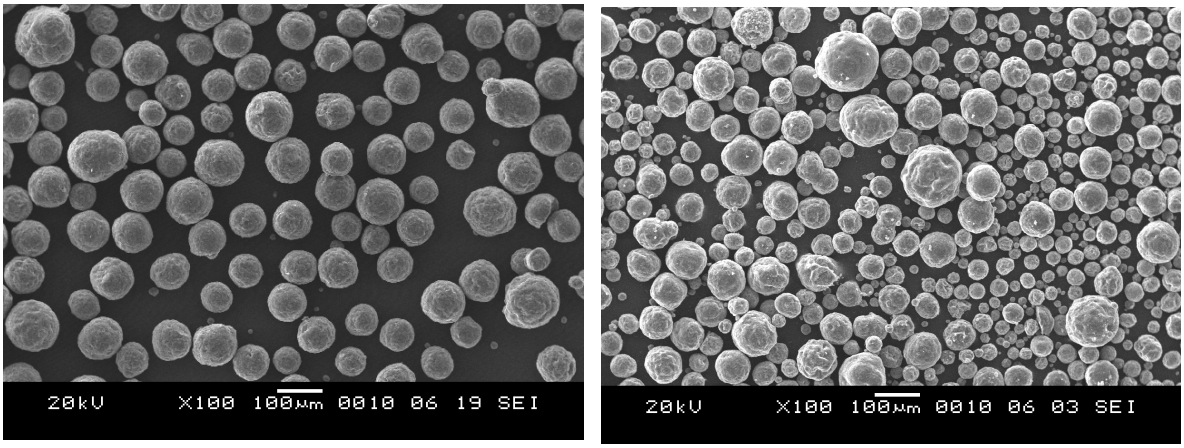

Figure 3.6. SEM scans of spray dried FCC catalyst. Left is from a fresh batch and right from an aged batch.

Discussion

The effects of the batch ageing time are small and on the limit of the measuring accuracy. The results of the particle size distribution, the tapped bulk density and total pore volume, all indicate a slight decrease in the amount of shrinkage after ageing. Also the surface of the particles from the aged batch shows more wrinkles. During ageing the agglomeration of primary binder particles causes the viscosity of the feed to increase. This could possibly change both the surface liquid behaviour and crust deformation resistance during shrinkage.

The increase in pore volume after batch ageing is consistent with the nitrogen and mercury analyses. However, the results do not unambiguously point at a certain pore size (range) of which the pore volume increased. Both methods show an increased pore volume for pores with a diameter larger than $2 \cdot 10^{-8}$ m, which is probably caused by the increased agglomerate size. It is remarkable that only the mercury porosimetry shows an increased pore volume for the smallest pores and not the nitrogen analysis, which is thought more accurate for the small pores. Probably growth of the primary binder particles results in a larger pore volume.

3.4.2 Effect of nozzle pressure/particle size distribution

The same feed is atomised using smaller slot diameters in the nozzle core to obtain a different droplet size distribution for the same feed flow rate. The pressure increased from 26 to 39 bar (53 %). For the higher pressure experiment, the air outlet temperature was 165 °C instead of 169 °C and the outlet humidity was $6.44 \cdot 10^{-2}$ instead of $6.13 \cdot 10^{-2}$

kg_w/kg_s. The other process conditions were comparable. The accumulation and/or loss were 13 % and 7 % of the total dry solids flow for the lower and higher pressure experiment respectively. Consequently, the tower-to-cyclone ratio decreased from 0.56 to 0.24. The dry solids content of the higher pressure product was 96.6 compared to 96.3 wt.% for the lower pressure product. The cyclone product was about 1 % drier than the tower product. Both results confirm that smaller particles are drier than larger particles. The differences are very small and, considering the sorption isotherm (see §2.4.3), the water content is near the equilibrium value.

The particle size distributions of the total product are given in figure 3.7. The d_p decreased from $7.1 \cdot 10^{-5}$ to $5.7 \cdot 10^{-5}$ m and the standard deviation from $2.5 \cdot 10^{-5}$ to $2.2 \cdot 10^{-5}$ m. Although the shape of the distribution is comparable, the slope of the distribution changes more abruptly for the lower pressure. The d_p of the washed product decreased from $7.3 \cdot 10^{-5}$ to $6.0 \cdot 10^{-5}$ m with increasing nozzle pressure.

The bull density of the higher pressure product was only 1 % lower.

Pore volume

The V_{wi} of the unwashed powders did not change and the V_{wi} of the washed product increased from $3.2 \cdot 10^{-4}$ to $3.3 \cdot 10^{-4}$ m^3/kg (3 %) with increasing pressure. The calculated particle density would decrease 1.4%, which is consistent with the result for ρ_{bulk}. It is remarkable that for both experiments the tower product V_{wi} is ca. 15% higher than the V_{wi} of the cyclone product, while there is no difference between the total products. Apparently, the incipient wetness impregnation method is influenced by the absolute particle size. This is possibly due to the formation of menisci between the particles, which increases the measured pore volume.

The V_{mipore} of the unwashed tower product decreased 4 % and the V_{mipore} of the unwashed cyclone product increased 9 % comparing the higher pressure to the lower pressure products.

The $V_{maporeN2}$ decreased for the tower product and increased for the cyclone product, comparing the higher pressure to the lower pressure. $V_{maporeHg}$ increased from $2.2 \cdot 10^{-4}$ to $2.5 \cdot 10^{-4}$ m^3/kg (11 %) with increasing the nozzle pressure.

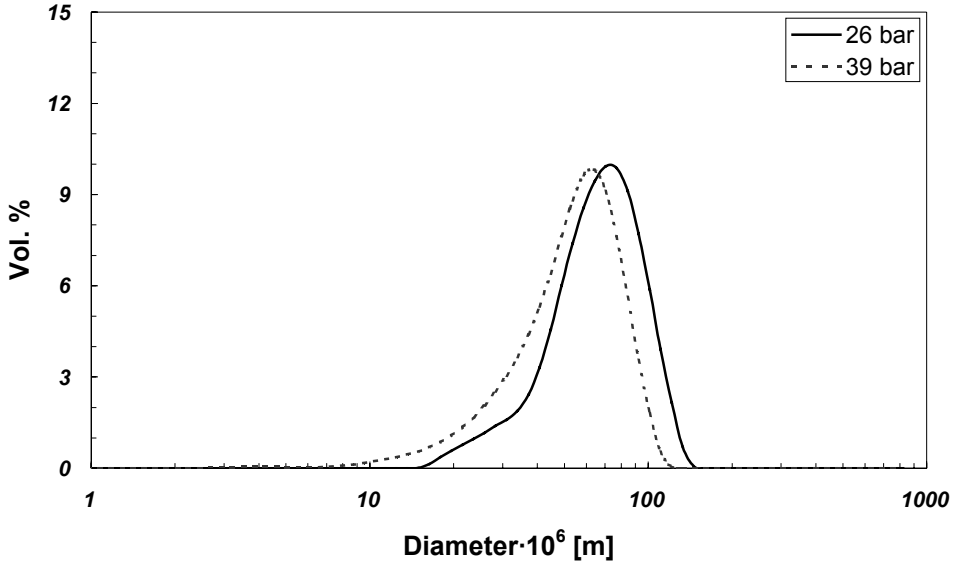

Figure 3.7. Particle size distribution of total product for different nozzle pressures.

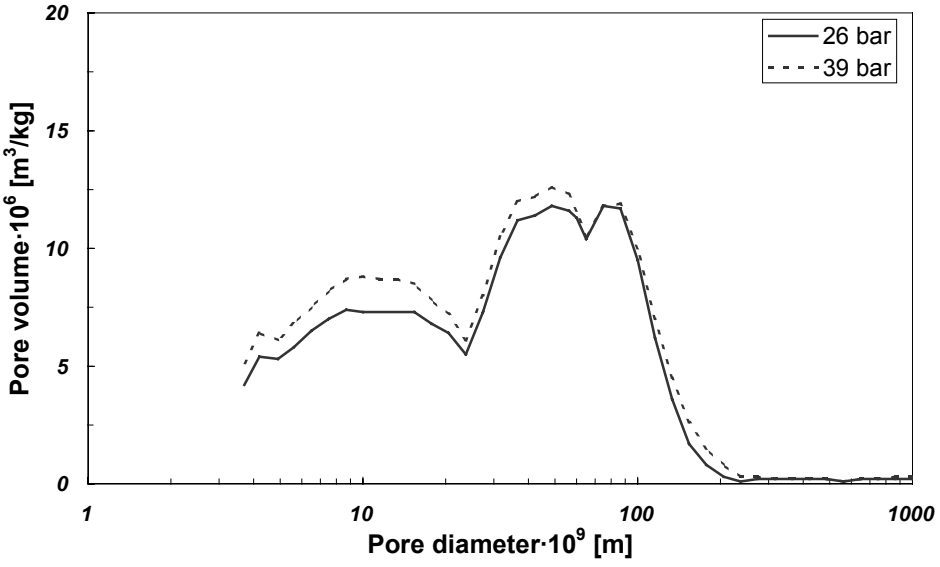

Figure 3.8. Pore volume distribution of washed total product for different nozzle pressures.

Surface area

The A_{BET} decreased about 10 % with increasing nozzle pressure. The tower product shows a smaller decrease than the cyclone product. In addition, the cyclone product usually has a lower A_{BET} than tower product.

The $A_{maporeN2d}$ decreased 8 % for the unwashed tower product and increased 14 % for the unwashed cyclone product comparing the higher pressure to the lower pressure experiments. The $A_{maporeN2t}$ showed a decrease of ca. 15 % for both the unwashed tower and cyclone product with increasing nozzle pressure.

The $A_{maporeHg}$ increased from $4.9 \cdot 10^4$ to $5.6 \cdot 10^4$ m²/kg (16 %) for the higher nozzle pressure experiment.

Pore size and distribution

The pore volume distribution for the tower product was almost identical. For the cyclone product the pore volume of the higher pressure product increased for pores larger than $7 \cdot 10^{-9}$ m diameter. Because both the pore volume and surface area increased the average pore diameter remained almost constant.

Figure 3.8 shows that the increase of the $V_{maporeHg}$ mainly results from pores with diameters between $3.7 \cdot 10^{-9}$ and $2.0 \cdot 10^{-8}$ m.

Particle shape

SEM scans are shown in figure 3.9. The particles all have a spherical shape, and the product for the higher pressure contains more small particles, as expected. The particles for a lower nozzle pressure are more wrinkled, indicating that this phenomenon occurs more often for larger particles.

Discussion

Changing the nozzle configuration is a suitable method to change the mean particle diameter and size distribution, without changing the physical properties largely. However, the SEM scans indicate that larger particles have more wrinkles than smaller ones. Producing more small particles decreases the tower-to-cyclone ratio, though the differences for ρ_{bulk} and V_{wi} are small. The absolute particle size influences the method of incipient wetness impregnation. The results from the nitrogen and mercury analyses are not consistent: both increasing and decreasing values are measured.

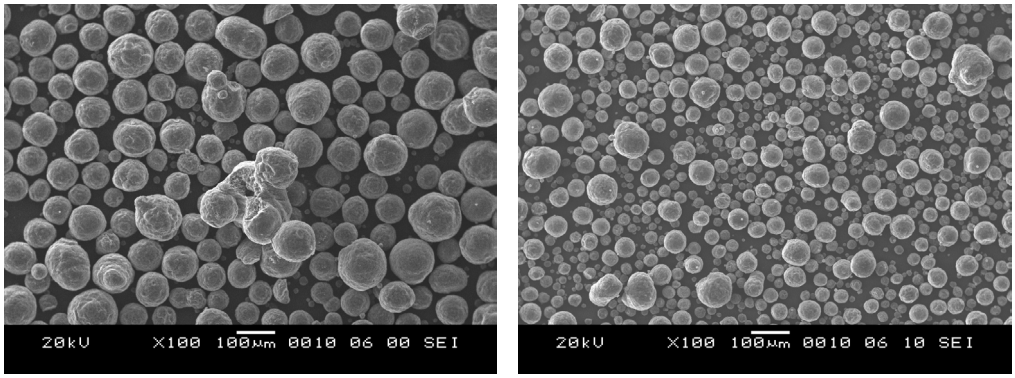

Figure 3.9. SEM scans of the total unwashed FCC catalyst. Left is at lower pressure and right at higher pressure.

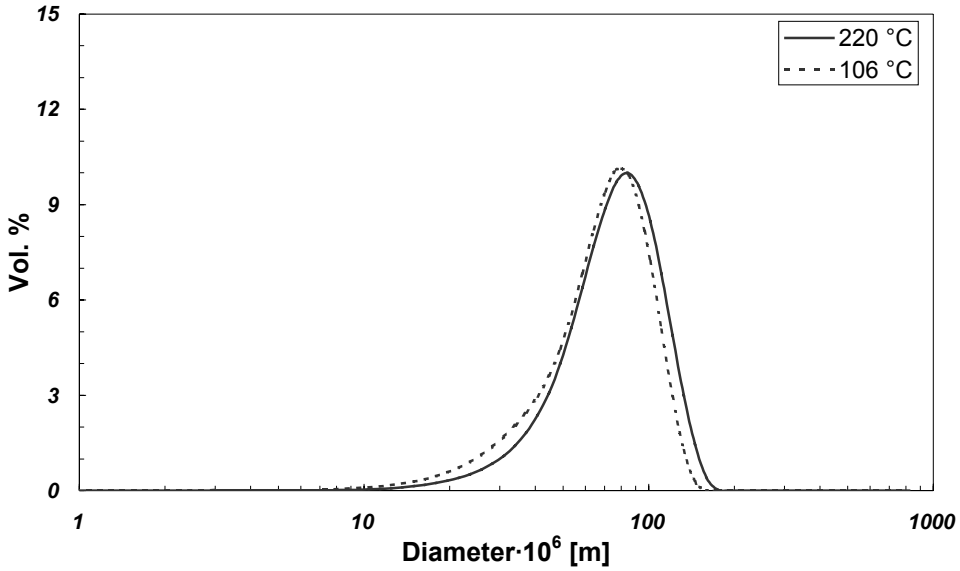

Figure 3.10. Particle size distribution of total FCC catalyst product for different air outlet temperatures.

3.4.3 Effect of air temperature

Spray drying experiments were done with several feed flows and air inlet temperatures. The feed flow was varied between 30 and 80 kg/h and the air inlet temperature was varied between 302 and 393 °C for the first series[1]. A second series was done with a constant feed flow of 50 kg/h and air inlet temperatures of 220, 357 and 497 °C respectively. The air outlet temperatures were between 122 and 184 °C for the first series and between 106 and 228 °C for the second series. The aim of the second series experiments was to study the influence of extreme air temperatures.

The experiments are categorised in three major groups; 1) experiments with a constant feed flow and different air inlet and outlet temperatures, 2) experiments with constant air inlet temperature and different feed flows and air outlet temperatures, and 3) experiments with (approximately) constant air outlet temperature and different feed flows and air inlet temperatures. The experiments of the last group are taken from experiments of the first two groups.

The differences in the mass balance were between -10 wt.% and + 13 wt.%, with an exception of –28 wt.%, which cannot be explained in another way than by a mistake of sample collection.

For a constant feed flow of 50 kg/h the final water content decreases from $6.3 \cdot 10^{-3}$ to $2.8 \cdot 10^{-3}$ kg_w/kg_s (dry solids content increases from 94 to 97%) increasing the air outlet temperature from 106 to 228 °C. The same result is observed for experiments of the first series, though the values are in between. The cyclone product is about 1 % (relative percentage) drier than the tower product. The maximum increase of the dry solids content for a constant air inlet temperature is 2 % and for a constant air outlet temperature the final water content remains constant. The water content of the product is near equilibrium.

The particle size distributions of FCC catalyst from 106 and 228 °C air outlet temperature are given in figure 3.10. The d_p increased from $7.4 \cdot 10^{-5}$ to $8.2 \cdot 10^{-5}$ m (10 %) with increasing air temperature, while the nozzle pressure difference was only 0.5 bar.

[1] The experiments have been done in two series. During the project the spray drier was moved within the Masterplan of the TU/e. The process control and the heater were renewed.

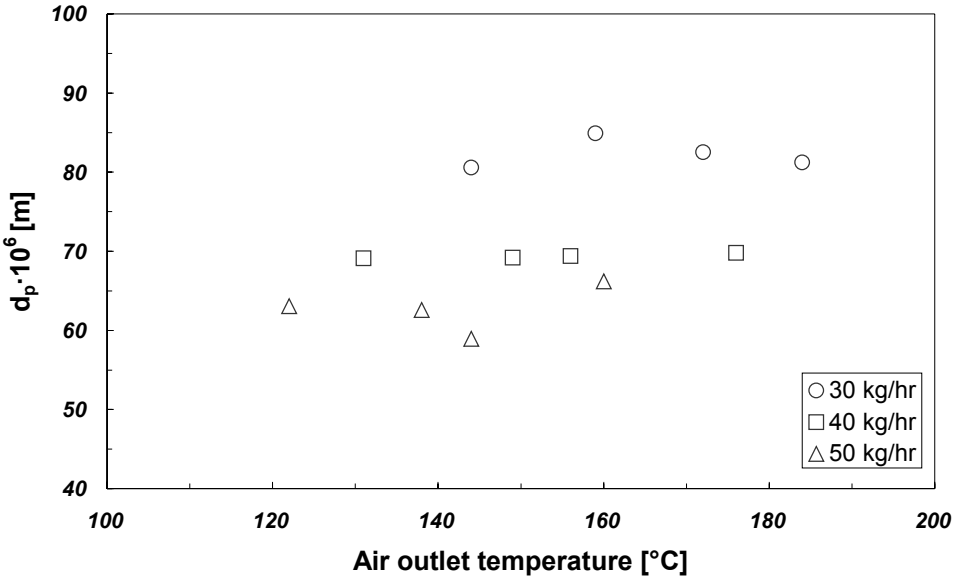

Figure 3.11. Mean particle diameter of FCC catalyst as function of air outlet temperature for different feed flows.

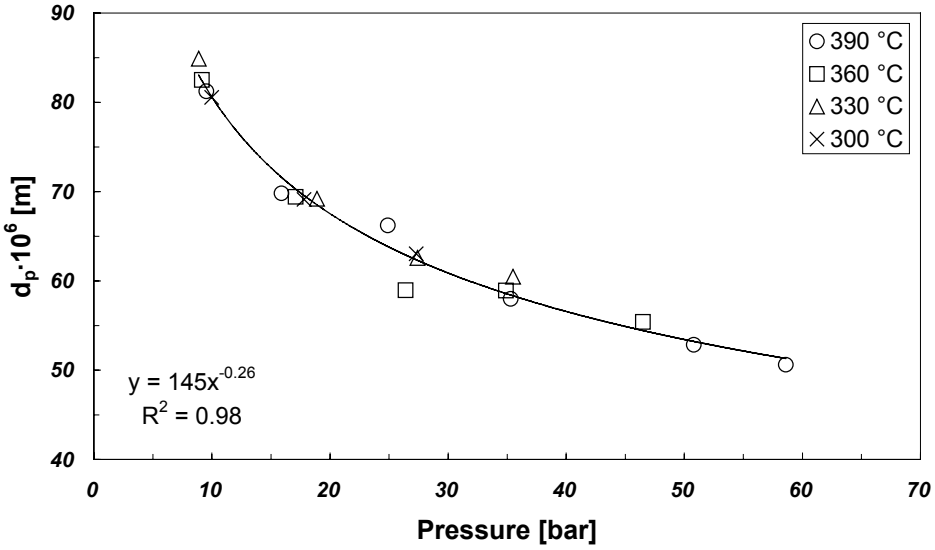

Figure 3.12. Mean particle diameter of FCC catalyst as function of nozzle pressure for different air inlet temperatures.

However, an increasing d_p with air temperature is not observed for other experiments, as shown in figure 3.11. Moreover, from figure 3.12 can be concluded that the nozzle pressure mainly determines the d_p. The value of the power constant in equation 4.1 equals -0.26, which is smaller than reported in literature. The difference in d_p for the extreme air temperatures could be due to several mechanisms. It is possible that at very high temperatures the formed crust is able to stop shrinkage or that only at such an extreme temperature particles inflate due to internal pressure generated from boiling phenomena. The tower product, with an air outlet temperature of 106 °C, contained particles larger than $2.0 \cdot 10^{-4}$ m diameter. These agglomerates were separated prior to further analysis. For this experiment, the difference in the mass balance for the solids was 10 wt.% of the total dry solids flow. Probably the surface of the particles was stickier, caused by a lower drying flux, and agglomerates were formed when collisions occurred. In addition, the large, sticky agglomerates are more likely to hit the wall and accumulate there.

The ρ_{bulk} decreases on average 2 % when the outlet temperature increases 40 °C at a constant feed flow (figure 3.13). Increasing the air outlet temperature from 106 to 228 °C decreases ρ_{bulk} from $1.13 \cdot 10^3$ to $1.04 \cdot 10^3$ kg/m^3 (8 %). The difference is ascribed to the particle density, because the shape of the particle size distribution is identical and the standard deviations are $2.8 \cdot 10^{-5}$ and $3.0 \cdot 10^{-5}$ m respectively. Increasing the feed flow results in a maximum decrease of 5 % for ρ_{bulk}, while the air outlet temperature decreases 55 °C. The ρ_{bulk} is approximately constant for constant air outlet temperature. Apparently, the air outlet temperature has a larger influence than the air inlet temperature, which is consistent with the results earlier obtained with the same spray drier (Kieviet, 1997). The particles experience a rather steep gradient of temperature and humidity in the beginning of the drying process and then the drying process continues in approximately constant air conditions.

Pore volume

In figure 3.14, the V_{wi} of the unwashed product is given as function of air outlet temperature for constant feed flow. The V_{wi} increases on average 8 % when the air outlet temperature increases 40 °C. The V_{wi} of the washed product increases from $3.0 \cdot 10^{-4}$ to $3.3 \cdot 10^{-4}$ m^3/kg (10 %) increasing the air outlet temperature 45 °C for the largest air outlet temperature difference V_{wi} increased from $3.1 \cdot 10^{-4}$ to $3.5 \cdot 10^{-4}$ m^3/kg (13 %). The particle

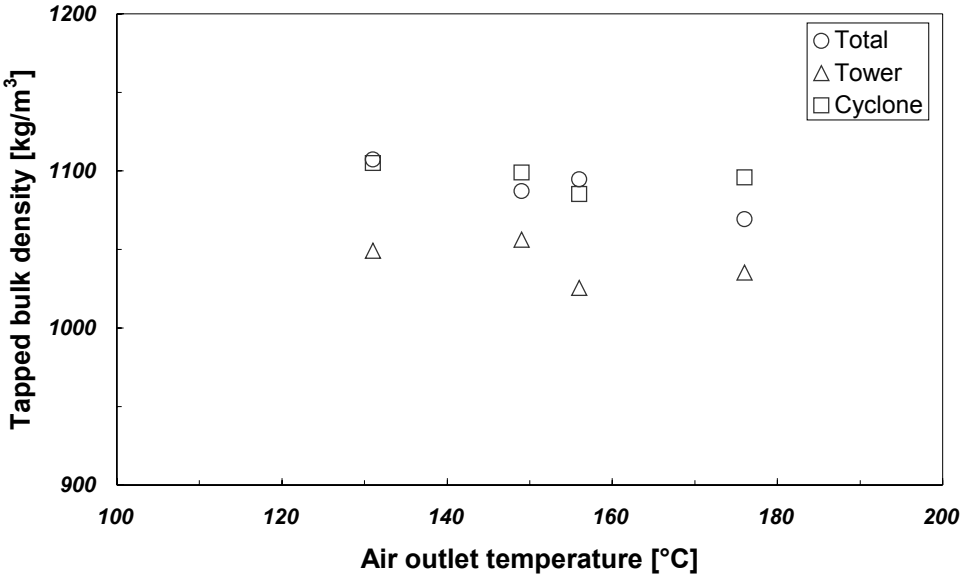

Figure 3.13. Tapped bulk density of total, tower and cyclone FCC catalyst product as function of air outlet temperature for a feed flow of 40 kg/h.

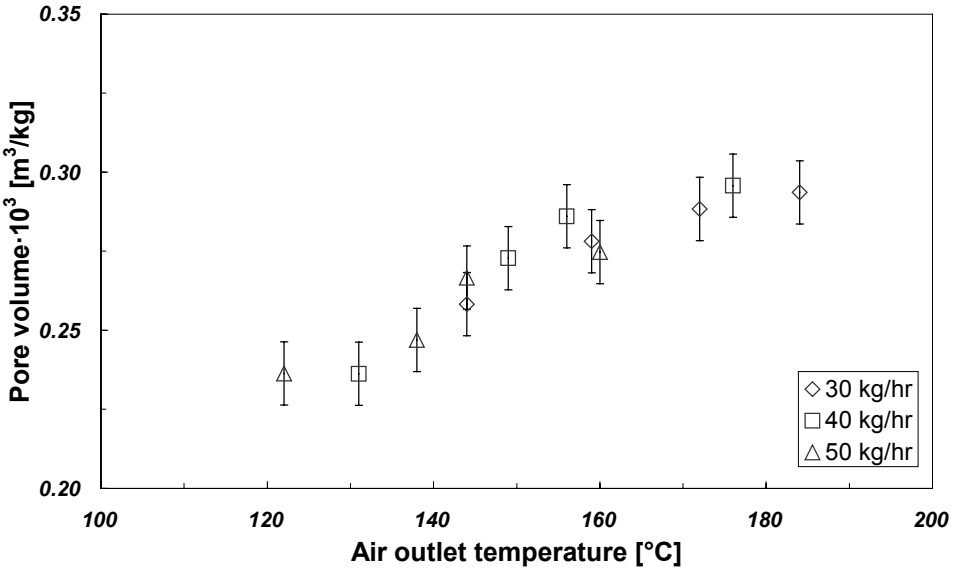

Figure 3.14. Total pore volume of unwashed FCC catalyst as function of air outlet temperature for three different constant feed flows.

density, calculated with the porosity, decreases 5 %, slightly less than the difference in ρ_{bulk}. The difference between the two series is caused by the modification of the spray drier. For a constant air inlet temperature, V_{wi} of the washed samples decreases about 10 %, while the air temperature decreases approx. 25 °C. For a constant air outlet temperature, the V_{wi} of the washed product shows no systematic relation. This indicates as well that the air outlet temperature mainly determines the pore volume.

The V_{wi} of the washed product is on average 32% higher than the V_{wi} of the unwashed product. The difference tends to be somewhat larger for bigger particles. This shows the influence of the salts on the measurement of the V_{wi} by incipient wetness impregnation. In addition, the V_{wi} of the tower product was on average 6 % higher than of the cyclone product (see also §*3.4.2*).

The V_{mipore} of the unwashed product increased on average 18 % increasing the air outlet temperature with 40 °C. The V_{mipore} of the washed product has a constant value of ca. $7.2 \cdot 10^{-5}$ m^3/kg. The standard deviation for a quadruple measurement was $5.4 \cdot 10^{-6}$ m^3/kg. The other experiments do not show differences in V_{mipore} for washed product.

A constant V_{mipore} is expected from the constant zeolite content. The differences for the unwashed samples indicate that salts form micro pores as well. In literature is was found that subsequent hydration and dehydration cycles result in a highly porous, high surface area salt structure consisting of sub-micron salt particles (Doehne, 1994). Higher drying temperatures probably enhance this mechanism.

At 300 °C air inlet temperature, the $V_{maporeN2}$ of the washed samples decreased from $1.9 \cdot 10^{-4}$ to $1.7 \cdot 10^{-4}$ m^3/kg (9 %) increasing the feed flow with 20 kg/h. The air outlet temperature decreased 24 °C. The $V_{maporeN2}$ of the other experiments have constant values.

The $V_{maporeHg}$ shows a maximum increase from $2.1 \cdot 10^{-4}$ to $2.5 \cdot 10^{-4}$ m^3/kg (18 %) when the air outlet temperature increased 40 °C. Experiments with constant feed flow and decreasing air outlet temperature also show a decreasing $V_{maporeHg}$. The $V_{maporeHg}$ does not change when the air outlet temperature is kept constant.

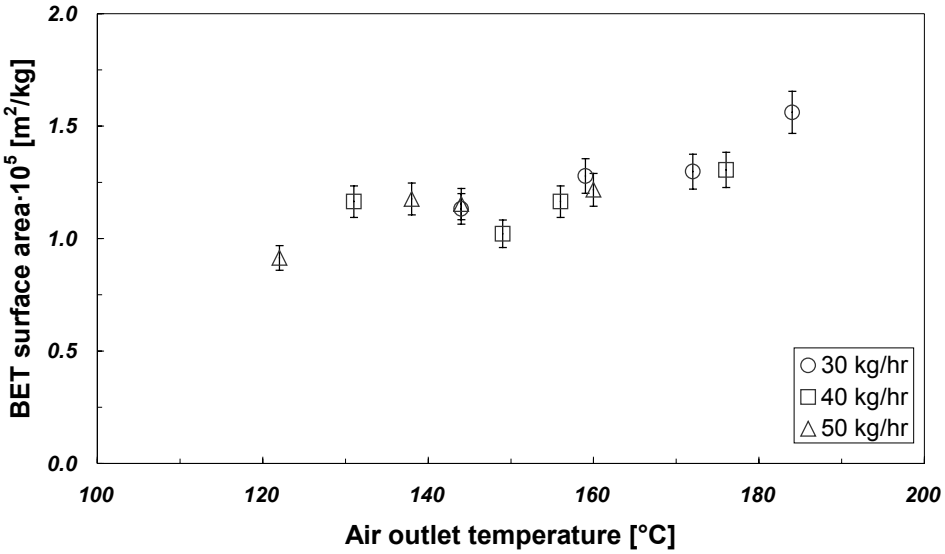

Figure 3.15. BET surface area of unwashed FCC catalyst as function of air outlet temperature for three different feed flows.

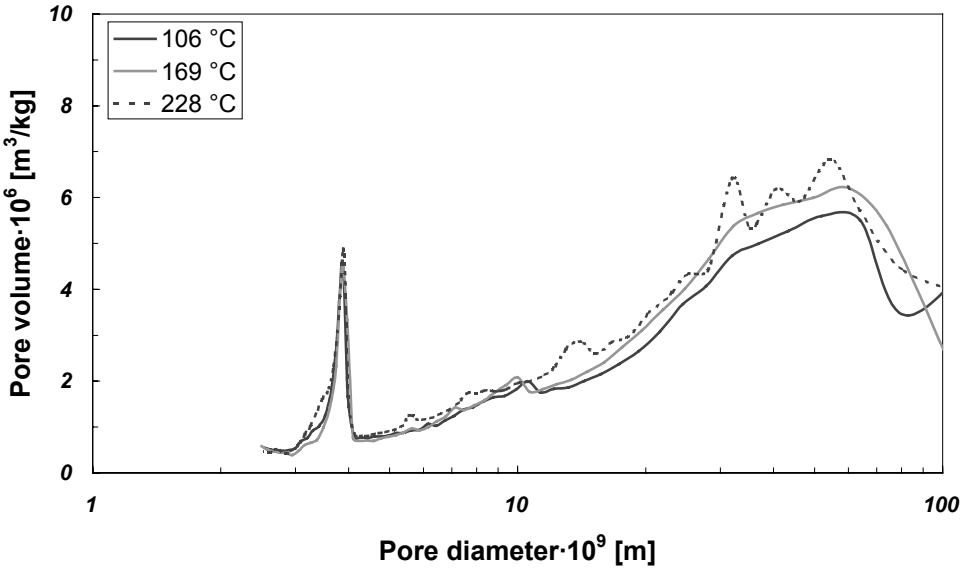

Figure 3.16. Pore volume distribution of washed total FCC catalyst product for a feed flow of 50 kg/h and three different air outlet temperatures.

Surface area

The A_{BET} of the unwashed product increases on average 28 % when the air outlet temperature increases 40 °C (figure 3.15) and increases from $1.17 \cdot 10^5$ to $1.72 \cdot 10^5$ m²/kg (47 %) when the air outlet temperature increases 122 °C. After washing the A_{BET} is at most 6 % higher for a temperature difference of 122 °C. For the other experiments, the differences are within measuring accuracy as well. There was no trend found comparing the surface areas of the tower and cyclone product. Obviously, the salts also influence the BET analysis.

Increasing the air outlet temperature 122 °C increases the $A_{maporeN2t}$ 10 %: from $7.1 \cdot 10^4$ to $7.8 \cdot 10^4$ m²/kg. The $A_{maporeN2t}$ of the unwashed samples shows a large data variability. The $A_{maporeN2t}$ also increases with increasing air outlet temperature for a constant air inlet temperature and remains equal for a constant air outlet temperature.

The $A_{maporeN2d}$ increases 6 % for the first series and has a constant value of ca. $9.0 \cdot 10^4$ m²/kg for the second series experiments with constant feed flow and increasing air temperature. The other experiments indicate that the air outlet temperature determines the $A_{maporeN2d}$ as well.

The results from mercury porosimetry show no trend, while the results for the second series are in contradiction with the nitrogen analysis. The values from mercury porosimetry are lower than from nitrogen analysis, which is due to the contribution of the smallest pores to the surface area.

Pore size and distribution

The pore volume distributions for constant feed flow, measured with nitrogen desorption, show no differences (figure 3.16). Accordingly, the average pore diameters are comparable: the average pore diameter decreases from $1.1 \cdot 10^{-8}$ to $9.9 \cdot 10^{-9}$ m increasing the air outlet temperature 122 °C. Consequently the surface area distributions are also comparable. The pore volume distributions of washed and unwashed product of the same experiment are shown in figure 3.17. The increase in pore volume is measured for the total range of pore sizes, though it is more profound for pores larger than $2.0 \cdot 10^{-8}$ m. This is a strong indicative that salt blocks pores of all sizes.

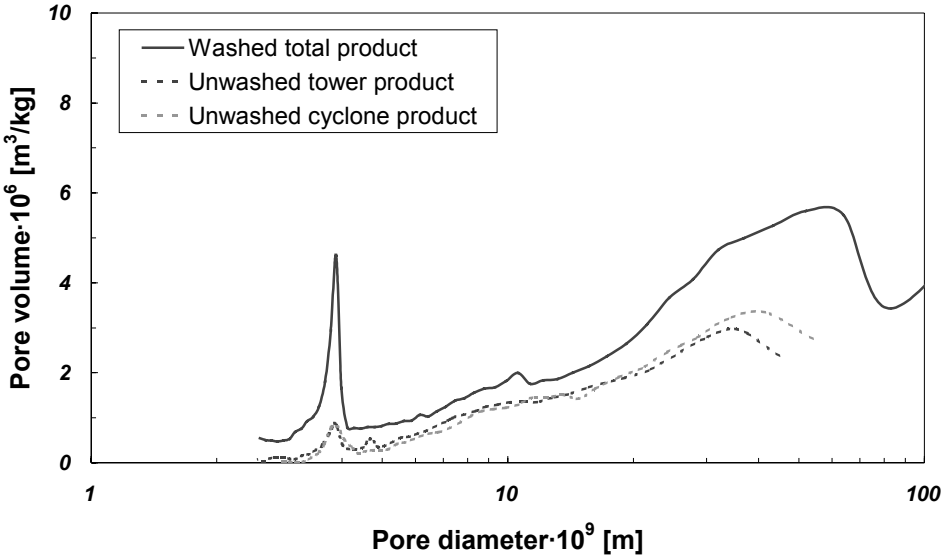

Figure 3.17. Pore volume distributions of washed and unwashed FCC catalyst product.

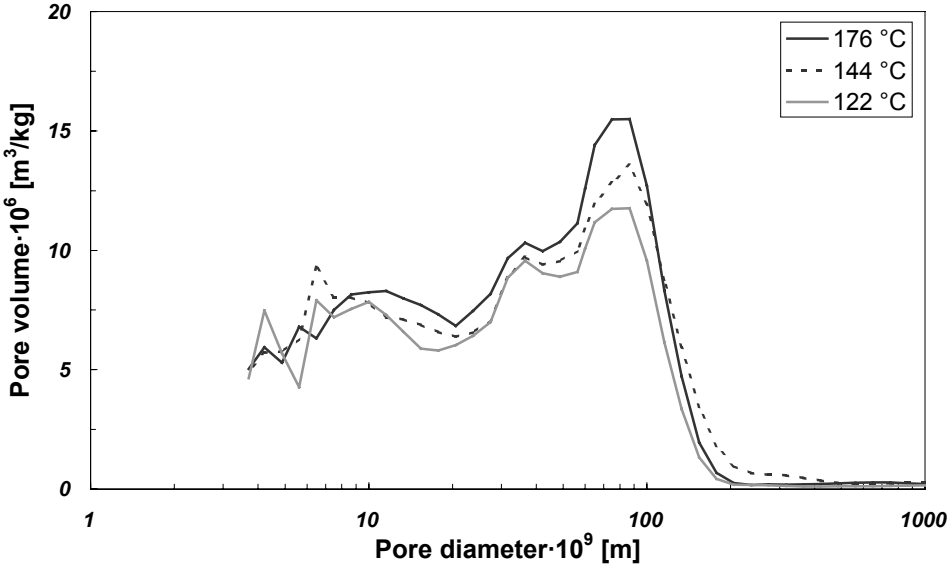

Figure 3.18. Pore volume distributions of washed FCC catalyst total product for three different air outlet temperatures, measured with mercury porosimetry.

As shown in figure 3.18, the pore volume distributions from mercury porosimetry show the increase of pore volume in the pore size range of 10^{-8} – 10^{-7} m diameter. These experiments were done with a constant feed flow and increasing air inlet and outlet temperature. This effect is also measured for a larger temperature difference, although the difference then results from a pore size range that shifted to a higher diameter ($6.0 \cdot 10^{-8}$ – $2.5 \cdot 10^{-7}$ m diameter). Because the pore volume distributions in the range of the smallest pores are almost identical and these small pores strongly determine the surface area, the total surface areas are comparable. The higher pore volume and a larger surface area results in a increase of the average pore diameter: about 10 and 23 % increasing the air outlet temperature 40 °C and 122 °C respectively.

The pore volume distributions for a constant air inlet temperature show a higher pore volume and surface area for the lower feed flow and air temperature, due to pores between $7 \cdot 10^{-9}$ – $1 \cdot 10^{-7}$ m diameter. The average pore diameter is 2 % higher for the lower feed flow. For a constant air outlet temperature the differences are small and no trend is observed.

Particle shape

The particle shape is in general spherical, although several deformed particles are present. The highest air outlet temperature results in many wrinkled particles, especially the larger ones. The lowest air outlet temperature results in much smoother particles, however several agglomerates have been found for these conditions. At high air outlet temperature, some particles broke and others show a large inner void or cracks in the surface. Various SEM visualisations of FCC catalyst are shown in figures 3.19 to 3.22.

Discussion

Although a wide range of spray drying conditions was applied, the macroscopic properties of FCC catalyst are not much influenced. The nozzle pressure mainly determines the mean particle diameter and the air temperature has no significant influence. The bulk density increases with decreasing mean particle diameter (increasing feed flow and nozzle pressure), which is probably due to the presence of more small particles. Increasing the air outlet temperature increases the pore volume: ca. 10 % for the total pore volume from incipient wetness impregnation. The micro-pore volume remains constant, while the results from the nitrogen and mercury analyses are different.

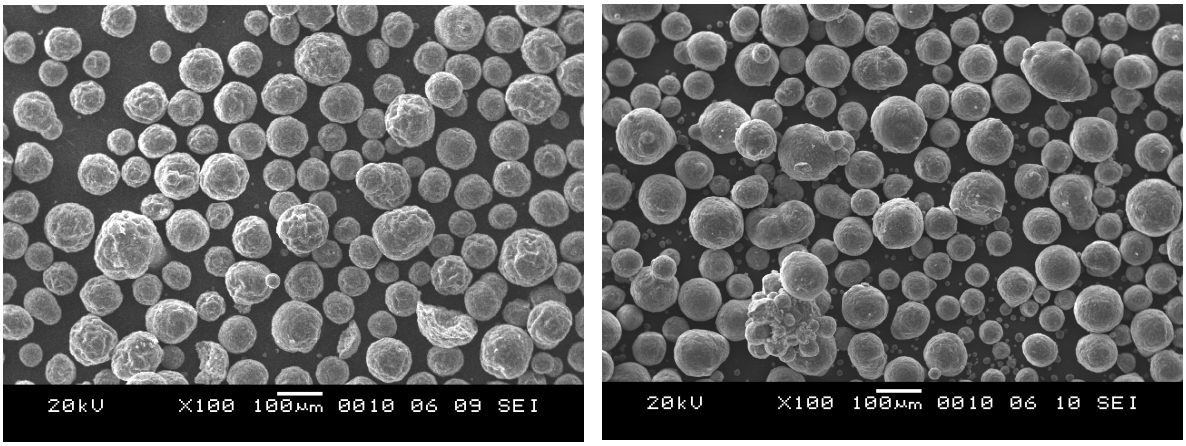

Figure 3.19. SEM scans of FCC catalyst from high (left) and low (right) air outlet temperatures.

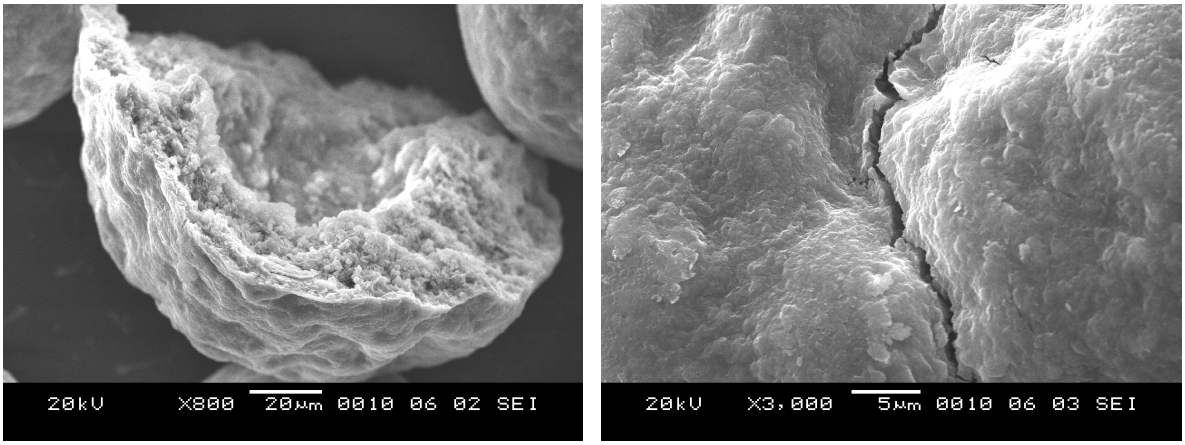

Figure 3.20. SEM scans of a broken, hollow particle (left) and a particle with surface crack (right).

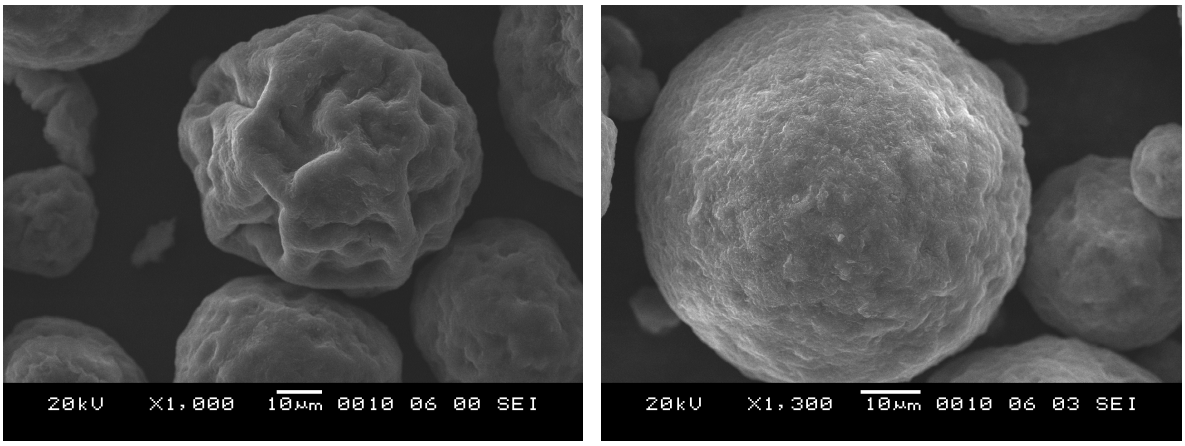

Figure 3.21. SEM scans of a wrinkled (left) and a smooth (right) FCC catalyst particle.

However, the increased pore volume and decreased bulk density indicate that the shrinkage is somewhat less for higher air temperatures.

Too high drying temperatures result in more broken and hollow particles, and cracks in the surface. Lower drying temperatures result in a smoother surface, although more agglomerates will be formed.

3.4.4 Effect of airflow

The influence of the airflow is studied by spray drying with an airflow of 1200 m^3/h and a constant feed flow of 50 kg/h. Higher airflows result in higher air velocities, lower outlet humidities, smaller temperature differences for equal heat transfer, and shorter residence times. The influence on the drying rate is, among others, dependent on the mixing behaviour of the process. For an ideally mixed process the outlet temperature and humidity determine the drying rate in the constant activity period. The drying rate will increase for higher airflows: for an equal air inlet temperature the air outlet temperature will be higher for constant feed flow, and for an equal air outlet temperature the outlet humidity will be lower.

The largest difference in the mass balances of the dry solids for these experiments was 7%. The tower-to-cyclone ratio for the higher airflow was 3.1 compared to 0.6 for the standard experiments. This is a logical result of the increased velocity near the exhaust pipe, which is directed downward. The dry solids contents only varied 2 %.

The d_p has not changed: differences of ca. $3 \cdot 10^{-6}$ m (5 %) are measured, both larger and smaller. The shape of the distribution for the higher airflow experiments all show an extra peak, which is probably caused by atomisation. The differences for the bulk density are within measuring accuracy.

Pore volume

The V_{wi} increased from $3.0 \cdot 10^4$ to $3.2 \cdot 10^4$ m^3/kg (7 %) for constant air inlet temperature. Measured differences for the V_{mipore} are within the accuracy. For a constant air inlet temperature, $V_{maporeN2}$ of the washed product increased 9 %, while the $V_{maporeN2}$ stayed constant for equal air outlet temperature condition. Differences measured with mercury porosimetry are within 6 %.

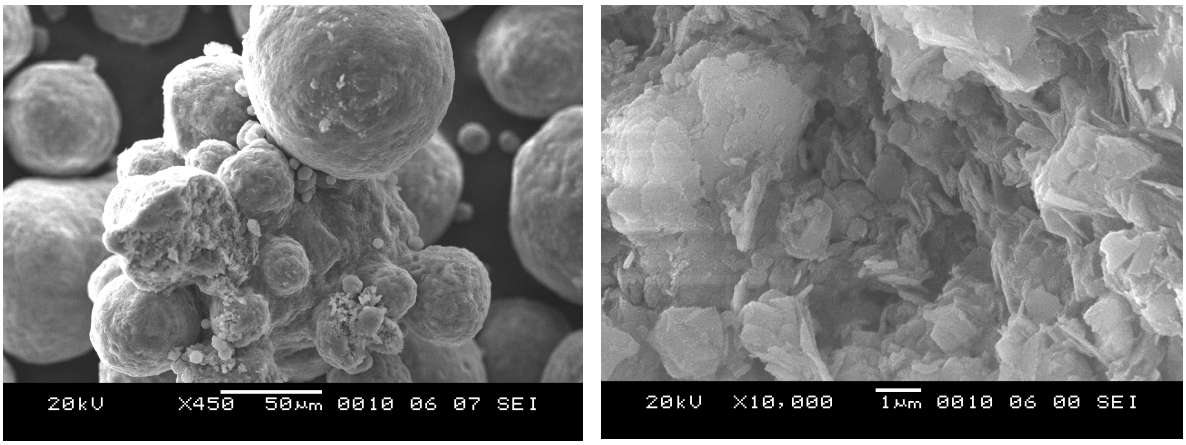

Figure 3.22. SEM scans of an agglomerate particle (left) and the interior of FCC catalyst (right).

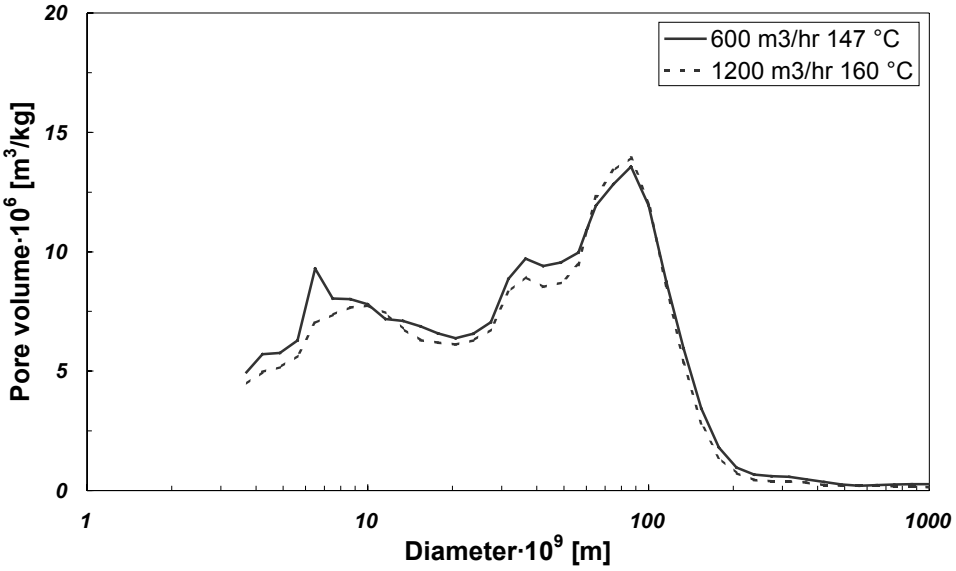

Figure 3.23. Pore volume distributions of washed FCC catalyst products at different airflows and comparable air outlet temperatures, measured with mercury porosimetry.

Surface area

The measured values for the A_{BET} varied within 3 %. Surface area from the t-plot analysis varied within 5 % and from the desorption isotherm within 7 %. The $A_{maporeHg}$ is ca. 6% lower for the higher airflow and is substantially lower than the results from nitrogen sorption.

Pore size and distribution

The nitrogen desorption isotherms show no large differences. The average pore diameter increased from $1.0 \cdot 10^{-8}$ to $1.1 \cdot 10^{-8}$ m. This is due to the increased total pore volume, which is an effect of the measurement technique.

The pore volume distributions from mercury porosimetry are depicted in figure 3.23. Although the outlet temperatures were different, the distributions are almost identical.

Particle shape

No SEM scans are made of samples from the higher airflow experiments.

Discussion

There is no influence found of the amount of airflow. The differences are ascribed to the accuracy of the measurements.

3.4.5 Effect of feed water content

Experiments have been done with feed water contents of 3.6, 4.6 and 7.3 kg_w/kg_s, i.e. 22, 18 and 12 wt.% solids respectively. Comparable drying conditions were obtained by atomising an equal flow rate of water at constant air inlet temperature. Hence, the feeds with higher water content have been atomised at lower pressures. The maximum solids accumulation for these experiments was 6 wt.% of the total solids rate. The tower-to-cyclone ratio was the smallest for the experiments with 12 wt.% dry solids. The final water content did not change more than 1 %.

In figures 3.24 and 3.25 the particle size distributions of the tower and cyclone product are given for different initial feed contents. The distributions have the same shape and the average particle diameter decreases 12 %, when the feed water content increases from 3.6 to 7.3 kg_w/kg_s. Although the initial droplets were larger, the low amount of solids results in smaller particles.

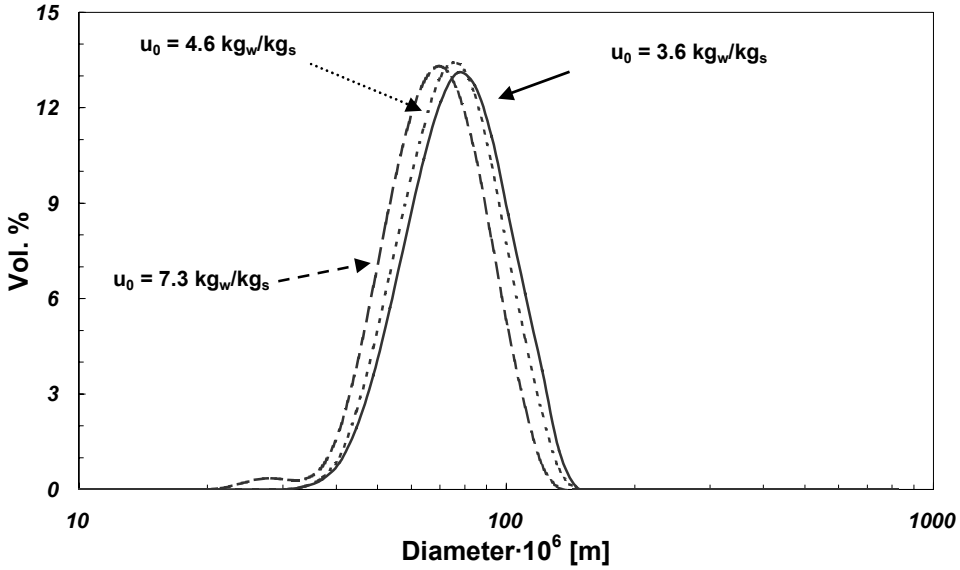

Figure 3.24. Particle size distribution of tower product FCC catalyst for three different feed water contents at comparable spray drying conditions.

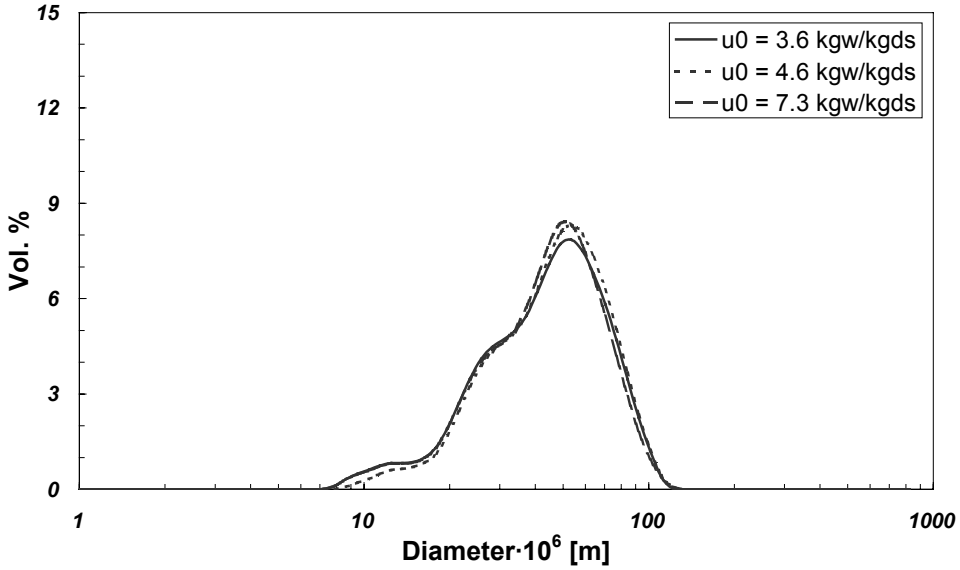

Figure 3.25. Particle size distribution of cyclone product FCC catalyst for three different feed water contents at comparable spray drying conditions.

The differences for the bulk density are within 2 %.

Pore volume

The V_{wi} of both the washed and unwashed product decrease ca. 6 % with increasing feed water content. This result is not in agreement with the decrease of the bulk density, however the differences are small. The V_{mipore} of the washed samples was equal for all feed water contents, about $7.3 \cdot 10^{-5}$ m³/kg.

The $V_{maporeN2}$ of the washed samples are $1.0 \cdot 10^{-4}$, $9.8 \cdot 10^{-5}$, and $8.6 \cdot 10^{-5}$ m³/kg for feed water contents of 3.6, 4.6, and 7.3 kg_w/kg_s respectively. The $V_{maporeHg}$ decreases with increasing initial water content from $2.4 \cdot 10^{-4}$ to $2.1 \cdot 10^{-4}$ m³/kg (13 %), which is comparable to the result from nitrogen desorption.

Surface area

The A_{BET} of the washed samples are $2.47 \cdot 10^5$, $2.41 \cdot 10^5$ and $2.36 \cdot 10^5$ m²/kg for increasing feed water contents. The $A_{maporeN2t}$ are $8.6 \cdot 10^4$ m²/kg for the two lowest feed water contents and is $7.6 \cdot 10^4$ m²/kg (i.e. 13% lower) for a feed water content of 7.3 kg_w/kg_s. The results for the $A_{maporeN2d}$ are comparable. The surface areas from mercury porosimetry are lower and decrease with increasing feed water content. The measured values are $5.3 \cdot 10^4$, $4.9 \cdot 10^4$ and $4.4 \cdot 10^4$ m²/kg respectively.

Pore size and distribution

The pore volume distributions have the same shape, as shown in figure 3.26. The pore volume slightly decreased with increasing feed water content. The average pore diameters were all approx. $1.1 \cdot 10^{-8}$ m. The results of the mercury porosimetry are comparable, as shown in figure 3.27. The shape of the pore volume and surface area distributions are identical and the differences small. The increased pore volume resulted mainly from pores between $6 \cdot 10^{-9}$ and $6 \cdot 10^{-8}$ nm diameter. The average pore diameter is between $1.8 \cdot 10^{-8}$ and $1.9 \cdot 10^{-8}$ m.

Particle shape

No SEM scans have been made.

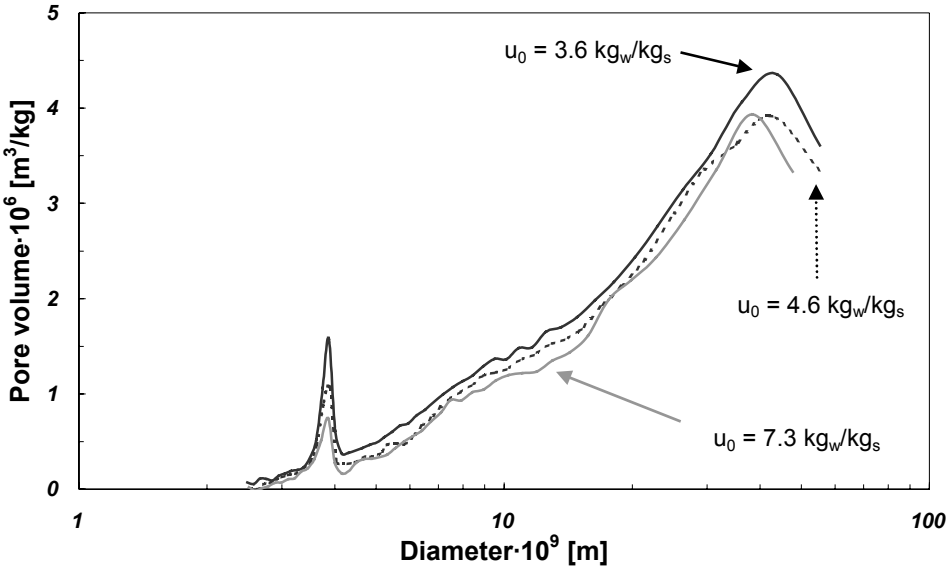

Figure 3.26. Pore volume distribution of unwashed FCC catalyst for different initial water contents at comparable spray drying conditions, measured with N_2-desorption.

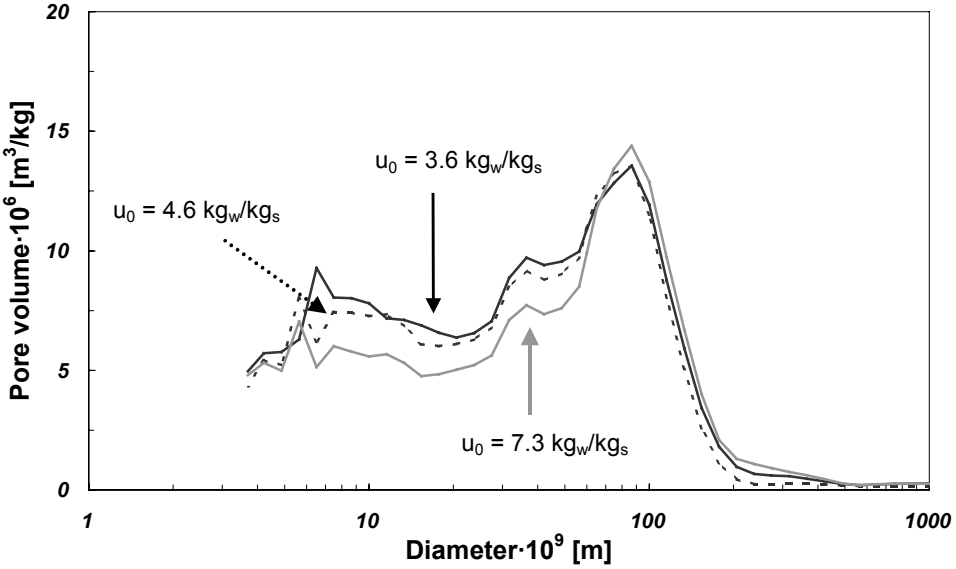

Figure 3.27. Pore volume distributions of washed FCC catalyst for different initial water contents, measured with mercury porosimetry.

Discussion

Changing the feed water content and maintaining comparable spray drying conditions results mainly in smaller particles. The pore volume and surface area seems to decrease slightly for a higher water content.

3.4.6 Calculation of shrinkage-coefficients and particle properties

The shrinkage-coefficient and particle properties are calculated with the experimental results for a constant feed flow and for different feed water contents. The skeletal density equals $2.44 \cdot 10^3$ kg/m^3 (chapter 2) and is used to calculate the porosity from the pore volume.

Increasing the air outlet temperature with 40 °C for a constant feed flow, increased the porosity by ca. 8 % and the corresponding shrinkage-coefficient decreased only 1 %, having an almost constant value of 0.93. The calculated particle density decreased from $1.53 \cdot 10^3$ to $1.45 \cdot 10^3$ kg/m^3 (5 %), while the measured ρ_{bulk} decreased 3 %. To compensate this result, the bed porosity had to decrease from 0.32 to 0.30 m^3/m^3. The calculated initial droplet diameter varied between $1.25 \cdot 10^{-4}$ and $1.27 \cdot 10^{-4}$ m.

The experiments with a feed flow of 50 kg/h and air outlet temperatures of 106 and 228 °C had porosities of 0.43 and 0.46 m^3/m^3 respectively. The calculated shrinkage-coefficients were 0.90 and 0.91. The particle density decreased 5 %: from $1.39 \cdot 10^3$ to $1.32 \cdot 10^3$ kg/m^3. Because ρ_{bulk} decreased 8 %, the calculated bed porosity increased from 0.31 to 0.38 m^3/m^3. The calculated droplet diameters were $1.31 \cdot 10^{-4}$ and $1.42 \cdot 10^{-4}$ m, mainly due to the difference in measured particle diameter.

The difference in porosities for the experiments with different feed water contents was very small (3 %). This resulted in an increasing shrinkage-coefficient with increasing feed water content, not illogically. The shrinkage-coefficients were 0.93, 0.94 and 0.97 for initial water content of 3.6, 4.6 and 7.3 kg_w/kg_s respectively. In figure 3.28, the calculated mean droplet diameters for different initial water contents are presented together with the measured mean particle diameters. The coefficient of determination (R^2) of the power-law fit for the droplet size equals 0.89.

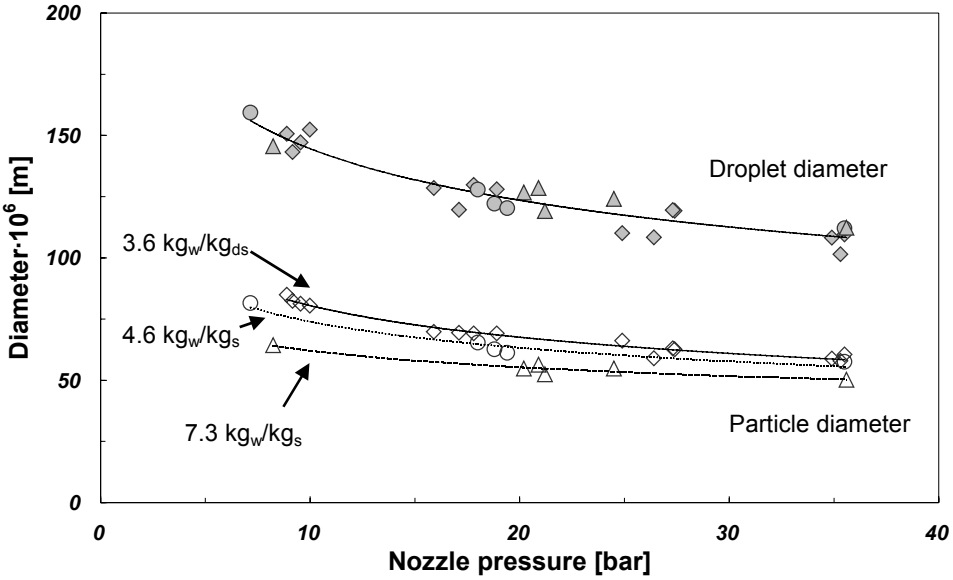

Figure 3.28. Measured mean particle diameter and calculated mean droplet diameter for different feed water contents.

3.4.7 General discussion

The pore volumes measured with mercury intrusion are always higher than the values from nitrogen desorption analysis. This indicates that a substantial volume is located in pores with relative large pore diameter ($> 2 \cdot 10^{-7}$ m).

The presence of the salts causes differences, probably via a dehydration and hydration mechanism. The pore size distribution results show small differences, which are more likely due to differences of the batch than to process conditions.

3.5 Conclusions

FCC catalyst has been spray dried at a wide range of process conditions. The physical properties are not much influenced by the drying conditions.

Too high drying temperatures will result in more broken and hollow particles, and cracks in the surface. Lower drying temperatures will result in a smoother surface, although more agglomerates will be formed. The air outlet temperature has the largest influence on the FCC catalyst properties. The mean particle size and particle size distribution are determined by the nozzle configuration, the feed flow rate and the feed water content. The viscosity of the feed is not studied explicitly.

A batch ageing time of several hours has a small effect on the FCC catalyst properties. However, the higher viscosity of the feed does affect the uniformity of the shrinkage and

probably induces wrinkling of the catalyst surface, which is unfavourable for attrition resistance. The surface wrinkling is observed more for larger particles, thus smaller (and denser) particles are favourable for attrition resistance. Although the influence is small, it appears that the batch ageing time results in smaller micro-pores and larger macro-pores, due to the growth and agglomeration of the binder primary particles.

These results are both favourable and unfavourable for FCC catalyst manufacturers. The spray drying process can be energetically optimised to have the maximum production choosing a high air inlet temperature at maximum airflow and high feed flow to obtain low air outlet temperatures and high humidities. The feed water content should be as low as possible to benefit the production rate and minimise the energy needed for evaporation per kilo FCC catalyst. The other side of the medal is that the studied FCC catalyst properties cannot be tuned with spray drying conditions. Alternatives to influence the FCC catalyst properties are to change the formulation or to search for components with different properties. An example of the latter is the use of meso-porous zeolites, such as MCM-22.

The presence of salts complicates the microscopic analysis of FCC catalyst. If the macroscopic properties are (more) important, washing can be omitted to allow faster comparison of results. However, to obtain knowledge about the microscopic properties, FCC catalyst should be washed properly to remove all salts.

It would be interesting to study the attrition resistance and cracking characteristics.

Notation

Roman

A	surface are	[m^2]
d	diameter	[m]
G	flow rate	[kg/s]
P	pressure	[bar]
S	shrinkage-coefficient	[-]
u	water content	[kg_w/kg_s]
V	volume	[m^3]

Greek

ε	porosity	[m^3/m^3]
ρ	density	[kg/m^3]

Subscript

n	nozzle
p	particle
s	solid
w	water
o	initial

References

Andersson, S.I. and Myrstad, T., 1998, Evaluation of Residue FCC Catalysts, Applied Catalysis A: General, 170, 59-71.

Andrieu, J., Dessalces, G., Joly-Vuillemin, C., Reymond, J.P. and Kolenda, F., 1992, Spray drying as a shaping technique for catalyst production, in: Drying '92 Proceedings of the International Drying Symposium, Ed. Mujumdar, A.S., Elsevier, Amsterdam, The Netherlands, 533-542.

Barrett, E.P., Joyner, L.G. and Halenda, P.P., 1951, Journal of the American Chemical Society, 73, 373.

Bergna, H. E., 1989, Attrition-resistant porous particles produced by spray drying, Characterization and catalyst development: an interactive approach, Ed. Bradley, S.A., Gattuso, M.J. and Bertolacini,R.J., ACS Symposium Series 411, chapter 7, Washington D.C., USA.

Brait, A., Seshan, K. and Lercher, J.A., 1998, Evaluation of commercial FCC catalysts for hydrocarbon conversion I. Physicochemical characterization and n-hexane conversion, Applied Catalysis A: General, 169, 299-313.

Brinker, C.J. and Scherer, G.W., 1990, Sol-gel science: the physics and chemistry of sol-gel processing, London Academic Press, London, UK.

Brunauer, S., Emmett, P.H. and Teller, E., 1938, Journal of the American Chemical Society, 60, 309.

Crosby, E.J. and Marshall, W.R. Jr., 1958, Effects of drying conditions on the properties of spray-dried particles, Chemical Engineering Progress, 54, 7, 56-63.

Doehne, E., 1994, In situ dynamics of sodium sulphate hydration and dehydration in stone pores: observations at high magnification using the environmental scanning electron microscope, in: III international symposium on the conservation of monuments in the Mediterranean basin, Eds. Fassina, V., Ott, H. and Zezza, F, Venice, Italy.

Gregg, S.J. and Sing, K.S.W., 1982, Adsorption, surface area and porosity, 2nd edition, Academic Press, London, UK.

Harkins, W.D. and Jura, G., 1944, Journal of the American Chemical Society, 66, 1366.

Johnson, M.F.L., 1978, Journal of Catalysis, 52, 425-431.

Kerkhof, P.J.A.M., 1975, A quantative study of the effect of process variables on the retention of volatile trace components in drying, Ph.D. thesis, Eindhoven University of Technology, Eindhoven, The Netherlands.

Kieviet, F.G. , 1997, Modelling quality in spray drying, Ph.D. thesis, Eindhoven University of Technology, Eindhoven, The Netherlands.

Lebeis, E.H. and Burtis, T.A., 1955, Effect of drying conditions on drying rate and physical properties of a porous solid, American Institute of Chemical Engineers Journal, 1, 3, 329-334.

Leofanti, G., Padovan, M., Tozzola, G. and Venturelli, B., 1998, Surface area and pore texture of catalysts, Catalysis Today, 41, 207-219.

Magee, J.S. and Blazek, J.J., 1976, Preparation and performance of zeolites cracking catalyst, in: Zeolite Chemistry and Catalysis, ed. Rabo, J.A., ACS Monograph, No. 171, American Chemical Society, Washington, D.C., USA, 615-679.

Masters, K., 1985, Spray drying handbook, Longman Scientific & Technical, Essex, UK.

Meenan, P., Roberts, K.J., Knight, P.C. and Yuregir, K., 1997, The influence of spray drying conditions on the particle properties of recrystallized burkeite ($Na_2CO_3 \cdot (Na_2SO_4)_2$), Powder Technology, 90, 125-130.

Meerdink, G. and Riet, K. van 't, 1995, Prediction of product quality during spray drying, Transactions of the Institution of Chemical Engineers, 73, C, 165-170.

Pedersen, L.A., Lowe, J.A. and Matocha, C.K. Sr., 1989, Attrition- and metal-resistant fluid cracking catalyst prepared with alumina powder in the matrix, in: Characterization and catalyst development: an interactive approach, Ed. Bradley, S.A., Gattuso, M.J. and Bertolacini, R.J., ACS Symposium Series 411, Chapter 38, 414-429, Washington D.C., USA.

Sullivan, E.C., 1995, Binder kinetics and FCC catalyst microstructure, Ph.D. thesis, University of Wisconsin-Madison, Wisconsin, USA.

Trullinger, C., 1997, Controlling atomization in your spray dryer, Powder and Bulk Engineering, 4, 87-94.

Woltermann, G.M., Magee, J.S. and Griffith, S.D., 1993, Commercial preparation and characterization of FCC catalysts, in: Fluid Catalytic Cracking: Science and Technology, Ed. Magee, J.S. and Mitchell, M.M.Jr., Elsevier, Amsterdam, The Netherlands.

Chapter 4

Modelling droplets of particulate slurries: drying behaviour and morphology

ABSTRACT

A model is presented that describes the mass and heat transport for spray drying of particulate slurries during shrinkage. The model discerns an initial stage in which the solid particles move according to Brownian motion and a successive stage in which the solid particles form a compressible crust. The capillary pressure in the pores at the surface controls the shrinkage of the crust. The compressive behaviour of the crust is described with a constitutive equation. The influence of the material parameters and process conditions on the transport coefficients, shrinkage and morphology is studied. Both the compressive behaviour and the particle size determine the amount of shrinkage. The spray drying conditions have a smaller influence. A comparison is made with experimentally spray dried fluid catalytic cracking catalyst and literature data. Various morphological developments during spray drying are predicted and the model shows reasonable agreement with results for titanium oxide. The results for FCC catalyst indicate that either the crust is very deformable and the particles have contact at higher water contents or the transition from the Brownian motion regime to the cake compression regime is quite smooth.

4.1 Introduction

Spray drying is a continuous industrial process to produce powders with specific properties, such as particle size distribution, bulk density and moisture content. The drying process involves simultaneous mass, heat and momentum transfer. The variety of the nature of spray dried materials is large and each material has its own characteristic drying behaviour and product properties. This study is focused on the drying behaviour of slurry feeds, which contain insoluble particles.

After atomisation of the liquid feed, heat is transferred from the drying air to the droplet and water evaporates from the surface. If the water activity remains near unity, the temperature of the droplet changes until the flux of energy transferred to the droplet equals the flux leaving the droplet in the form of latent heat of evaporated water. This pseudo-equilibrium stage is defined as the constant activity period (CAP). Although it is often referred to as the constant rate period, the drying rate is not constant due to the decreasing surface area (Kerkhof, 1975). The CAP ends when the flux of water at the evaporating surface starts to decrease due to decreasing surface water activity.

For soluble materials, such as sodium sulphate, it has been found that both the CAP and shrinkage stop when a crust is formed at the surface of the droplet (Ranz, 1952; Charlesworth, 1960; Miura, 1972; Audu, 1975; Toei, 1982; Cheong, 1986; and Ali, 1989). For insoluble materials the influence of the crust (and its formation) on transport properties is still not completely understood. The formation and compression of the crust and the influence on the drying kinetics will be very much material dependent. For some insoluble materials it has been found that droplets exhibit evaporation rates corresponding to that of pure water until a solid structure has been formed and shrinkage stops (Ranz, 1952; Lebeis, 1955; and Miura, 1972). The analysis that partially wetted surfaces are able to maintain a drying rate equal to that of pure water, indicates that the CAP could proceed after shrinkage has stopped (Schlünder, 1988).

The spray drying of ceramic materials often results in hollow, “mushroom”- or “doughnut”-shaped particles (Crosby, 1958; Lukasiewicz, 1989; and Walton, 2000). Recently, spray drying of sol-gel precursors has been investigated and the importance is shown of the state of aggregation-coagulation on properties such as density and attrition

resistance (Sizgek, 1998; Denny, 1998). Spray drying of well-dispersed sols of very small particles (ca. 10^{-8} m) resulted in hollow or "doughnut"-shaped granules, while spray drying of coagulated aggregates (diameter up to $5 \cdot 10^{-5}$ m) resulted in solid particles with low density and poor attrition resistance. Solid granules with high density and low porosity have been found if aggregated micron-sized particles were spray dried. Other authors report that (solid) particles are drawn inward by surface tension and a crust is formed during spray drying (Liang, 2001; Minoshima, 2001).

In earlier work, it is shown that the description of diffusion of micron-sized particles with Brownian motion results in very steep concentration gradients at the surface (Sanden, 2000). This indicates that in a very early stage of the spray drying process a crust is already formed. Experiments with fluid catalytic cracking (FCC) catalyst, which consists of micron-sized particles and a smaller binder material, resulted in low porosity granules, hence a large amount of shrinkage. This is indicative for a deformable crust during the spray drying process.

Several approaches incorporate shrinkage and elastic behaviour of a material in the drying model, however these models do not couple the stresses to the transport coefficient (e.g. Jomaa, 1991; Ketelaars, 1992).

Scherer wrote an extensive review on the drying of gels and included the development of pressure and stress distribution in the drying body (Scherer, 1990).

Liang *et al.* analysed the CAP in spray drying of slurries (Liang, 2001). They described the flow of water using Darcy's law and a concentration dependent capillary pressure as the driving force. However, the capillary pressure exists only at the liquid-gas interface and does not apply to the interior of the material, where there is no interface present. In addition, there was no resistance to deformation taken into account. A minimum porosity was always attained and depended only on the packing of the primary particles.

Brown *et al.* have described the consolidation of aggregated alumina suspensions on basis of a two-phase fluid description (Brown, 2002). The concentration has been related to the compressive pressure in the network. The network was assumed to shrink until the capillary pressure balanced the network compressive pressure. The drying has been analysed at different suspension pH's and external conditions. The presented mechanism is also applied in this spray drying model.

In spray drying practice, often relative high water contents are needed to pump the feed to the spray dryer. The models found in literature do not incorporate the description of drying at high water contents, where the solid particles have no contact. It is the aim to develop a two-phase fluid model that describes the spray drying of slurries containing insoluble particles from the initial stage until the droplet stops shrinking. The knowledge of cake filtration theory is applied and the emphasis is laid on the development of the morphology in relation with the compressive behaviour and the transport properties, as well as with the influence of spray drying process conditions.

4.2 Theory

4.2.1 Development of the model

The system is assumed to consist of a liquid phase and a solid phase (two phase-fluid). The particulate particles are referred to as primary particles. In a spray drying process, the droplets are usually so small that temperature gradients in the droplets can be neglected. Because of numerical convenience, a heat transport equation is incorporated in the model. Diffusion equations, transformed to solid material basis, have been used to describe the mass and heat transport (Van der Lijn, 1976).

At high water content, the primary particles move through Brownian motion and the diffusion coefficient is described with the Stokes-Einstein equation. At a certain concentration, the particles make contact and a crust is being formed, which is compressed upon further shrinkage. The formation and compression of the crust is described with the behaviour of a cake during filtration. Therefore, the terms cake and crust are both used. Darcy's law for fluid flow through porous media is incorporated in the diffusion equation for consistency with the Brownian motion diffusion. The gradient in pressure, the driving force for transport, is coupled to the concentration via a constitutive equation. The apparent diffusion coefficient depends on the compression parameters and permeability of the cake. The extent to which the cake is compressed is determined by the capillary pressure at the surface or by the maximum packing fraction of the primary particles.

First, the governing mass transport equations are described in respectively the Brownian motion regime and cake compression regime. Then the mathematical

framework is given, in which the equations are transformed to solid material basis and the appropriate initial and boundary conditions are given. Finally, the properties of spray dried granules are related to the final water content.

4.2.1.1 Brownian motion regime

At low solids concentrations, thus high water contents, the primary particles move freely in the liquid. The movement of particles, with a size much larger than the solvent molecules, is described with Brownian motion. The mass flux with respect to the solids velocity (i.e. the reference velocity), j_w^s, is given by:

$$j_w^s = \rho_w\left(v_w - v_s\right) = -\frac{D_{ws}}{(1-\varepsilon)}\left(\frac{\partial \rho_w}{\partial r}\right)_t \tag{4.1}$$

in which ρ_w is the water concentration, v_w the velocity of water and v_s of solids with respect to a fixed co-ordinate, D_{ws} the binary diffusion coefficient, ε the volume fraction water and r the space co-ordinate in a fixed frame.

The diffusion coefficient of the solid particles in water, D_{ws}, is calculated with the Stokes-Einstein equation:

$$D_{ws} = \frac{k_B T}{6\pi\eta_{eff} r_s} \tag{4.2}$$

in which k_B is the Boltzmann constant, T the temperature, η_{eff} the effective liquid viscosity and r_s the radius of the primary particle.

At somewhat higher solids concentrations, the particles will experience the influence of other particles. This effect is incorporated into the effective viscosity, which is described with the Krieger-Dougherty equation (Krieger, 1972):

$$\eta_{eff} = \eta_w\left[1 - \frac{\varepsilon_s}{\varepsilon_s^{\max}}\right]^{-[\eta]\varepsilon_s^{\max}} \tag{4.3}$$

in which η_w is the viscosity of pure water, ε_s the volume fraction solids (solidosity), ε_s^{max} the maximum volume fraction solids and $[\eta]$ the intrinsic viscosity of water.

The effective viscosity is calculated using the temperature dependent water viscosity and an intrinsic viscosity of 2.5. The maximum volume fraction solids is equal to 0.64, which is discussed further on.

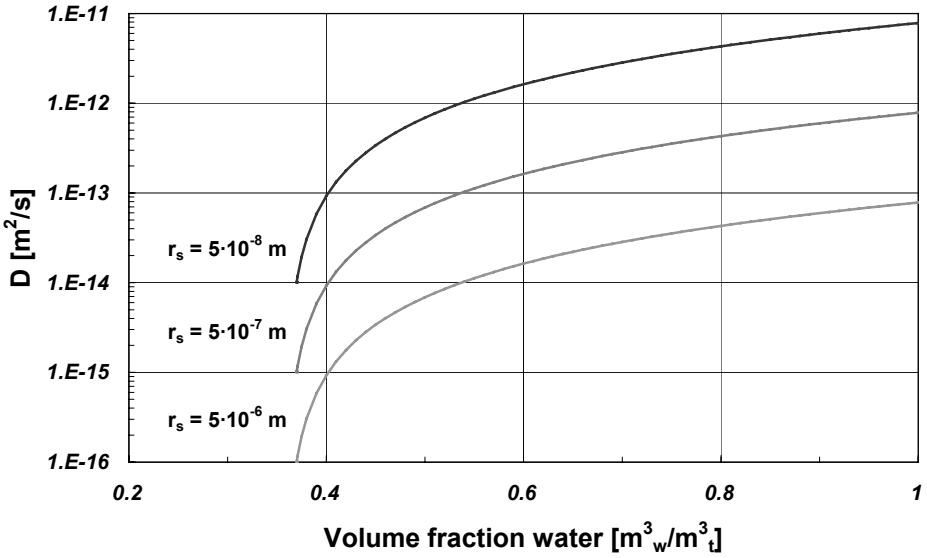

Figure 4.1. Stokes-Einstein diffusion coefficient as function of the volume fraction water for three different particle sizes.

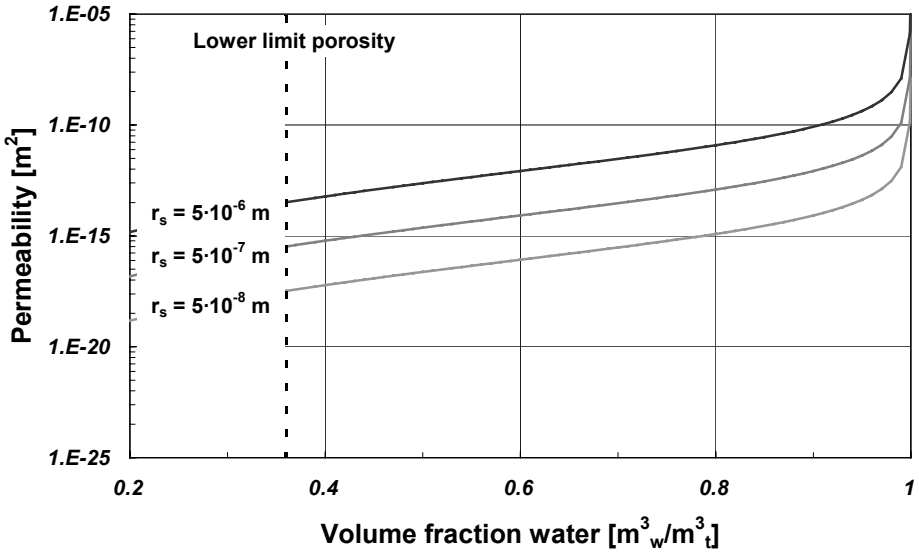

Figure 4.2. Permeability as function of volume fraction water for three different particle diameters.

Figure 4.1 gives the diffusion coefficient as function of the volume fraction water for three different particle sizes. The diffusion coefficient decreases with decreasing volume fraction water and is inversely proportional to the particle size. The diffusion coefficient increases with temperature, also partly due to the temperature dependency of the viscosity of water. The Brownian motion regime is assumed to stop when the primary particles touch each other and the cake formation starts.

4.2.1.2 Cake compression regime

In the cake compression regime, the transport is described analogously to filtration theory. When pressure is applied to a solid-liquid system, the pressure is transferred to the solid and liquid phase in the system. A force balance over a section of the material, neglecting inertial and acceleration forces, is given by:

$$\left(\frac{\partial P_l}{\partial r}\right)+\left(\frac{\partial P_s}{\partial r}\right)=0 \tag{4.4}$$

in which P_l is the liquid, or hydraulic, pressure and P_s the solids, or compressive, pressure. The pressure gradient in the liquid causes a flow, which obeys Darcy's law. The mass flux of water with respect to the solids velocity is:

$$j_w^s=\rho_w\left(v_w-v_s\right)=-\rho_w\frac{B_0}{\eta_w}\left(\frac{\partial P_l}{\partial r}\right) \tag{4.5}$$

in which B_0 is the permeability.

Because the cake is compressible, the pores remain completely filled with water and the permeability equals the intrinsic permeability. The permeability is calculated with the Carman-Kozeny equation:

$$B_0=\frac{4r_s^2}{75\tau^2}\frac{\varepsilon^3}{(1-\varepsilon)^2} \tag{4.6}$$

in which τ is the tortuosity.

The concept of tortuosity is a source of confusion in literature, as tortuosity, τ, and the tortuosity factor, τ^2, are often mixed up. The tortuosity is defined as the ratio of the average covered distance to the length of the porous medium along the axis of transport (Epstein, 1989). It is plausible to assume that the tortuosity depends on the morphology

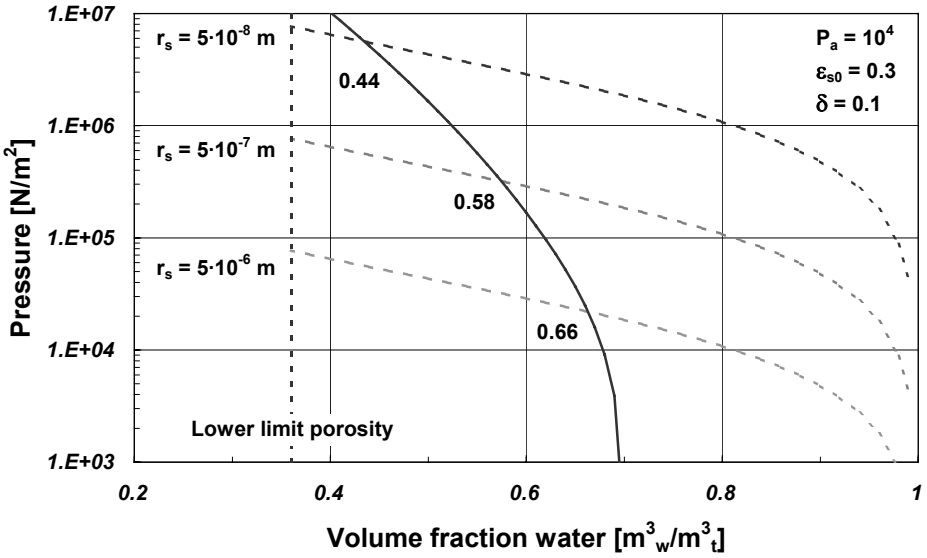

Figure 4.3. Compressive pressure (solid line) and capillary pressure (dotted lines) as function of volume fraction water for three different particle sizes at standard values. Values at cross-points represent the minimum surface porosities.

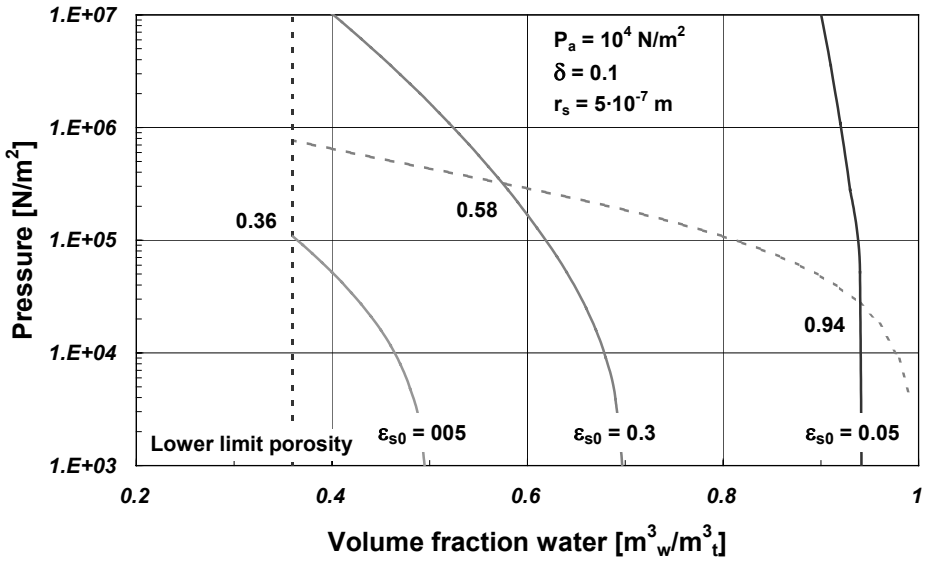

Figure 4.4. Compressive pressure (solid lines) and capillary pressure (dotted line) as function of volume fraction water for various null-stress volume fractions solids, ε_{sc}, at standard conditions. Values at cross-points represent the minimum surface porosities.

of the porous medium. The tortuosity factor, τ^2, depends on the porosity via (Marshall, 1957; Wesselingh, 1995):

$$\tau^2 = \varepsilon^{-1.5} \tag{4.7}$$

The permeability is given as function of volume fraction water for different particles sizes in figure 4.2.

At the surface pores are formed and the pore size decreases during compaction of the cake. The capillary pressure, which results from curvature of the liquid-vapour interface in the pores, supplies the compressive pressure for the cake at the surface. The maximum capillary pressure, P_c^{max}, is related to the particle size and porosity by (White, 1982):

$$P_c^{\max} = -\frac{3\sigma_{LV}\cos(\vartheta)}{r_s}\frac{(1-\varepsilon)}{\varepsilon} \tag{4.8}$$

in which σ_{LV} is the liquid-vapour surface tension and ϑ the contact angle. During drying it is assumed that the particles remain covered with a thin liquid film, thus the contact angle equals zero.

The compressive pressure is related to the volume fraction water by a constitutive equation. It is assumed that the deformation instantaneously follows the (applied) pressure. An empirical relation that can be used for many materials reads (Shirato, 1970; Leu, 1986; and Tiller, 1998):

$$\varepsilon_s = \varepsilon_{so}\left(1+\frac{P_s}{P_a}\right)^{\delta} \tag{4.9}$$

in which ε_{so} is the null-stress volume fraction solids, P_a the compressive modulus and δ the compressibility index. The null-stress volume fraction solids is the volume fraction of the primary particles at which compressive pressure equals zero. At this volume fraction, the particles just make contact and the cake compression regime begins. Incompressible materials have a value of $\delta = 0$, and more compressible materials have values of about $\delta = 0.5$ (Tiller, 1998). The constitutive equation is applied to a maximum solidosity, ε_s^{max}, at which it is assumed that the validity ends or where the parameters change substantially because of different mechanisms and forces in the compression. The solidosity of a random close packing of spherical particles may vary between 0.47 – 0.64 (Cumberland, 1987). The value of ε_s^{max} is taken equal to 0.64. It has generally been found that if the

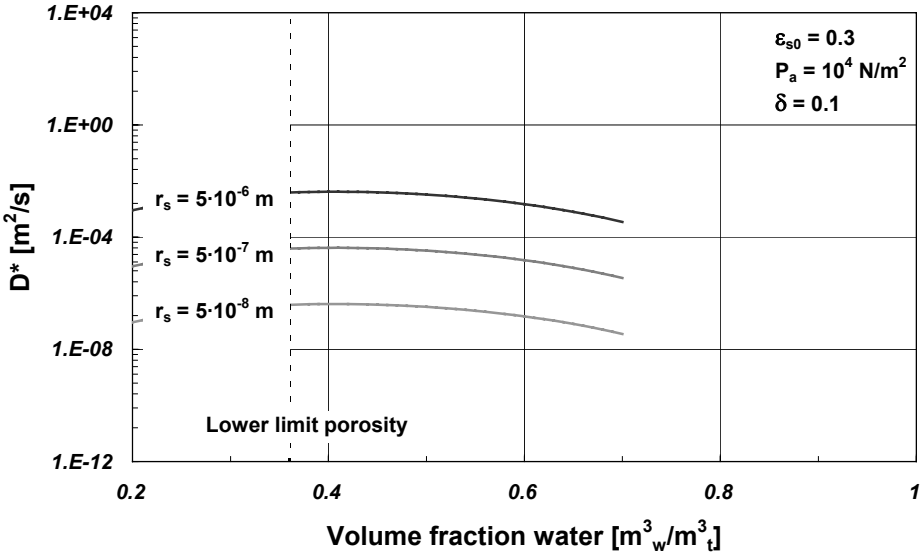

Figure 4.5. The apparent diffusion coefficient as function of volume fraction water for three different particle sizes and standard values.

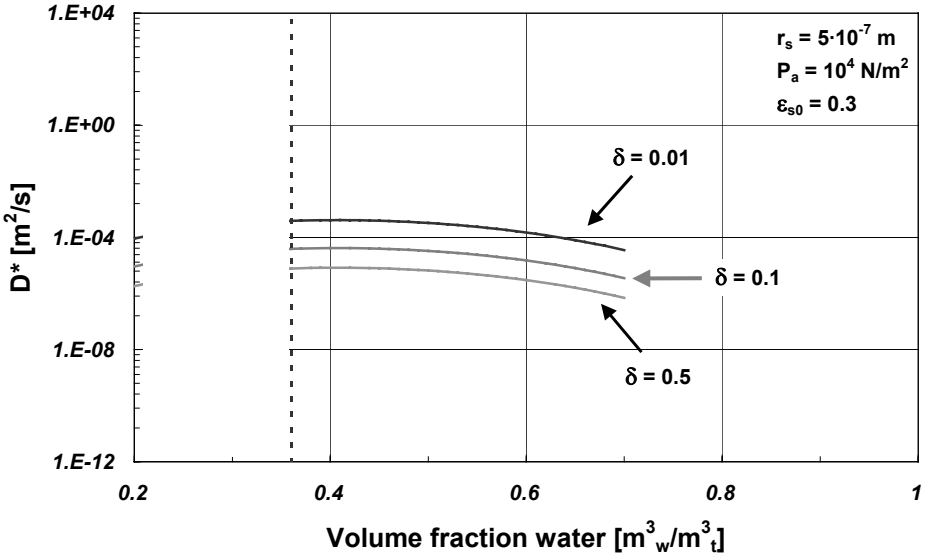

Figure 4.6. The apparent diffusion coefficient as function of the volume fraction water for three compressibility indices and standard values.

particle size decreases, friction, adhesion, and other surface forces become increasingly important for the volume fraction of the packing. When these factors contribute to bridging and arching the solidosity will decrease. In addition, irregularity of particle shape decreases the solidosity. However, a particle size distribution will increase the solidosity, because smaller particles fill the voids between the larger particles.

At the surface, the actual compressive pressure is determined by the volume fraction water and the constitutive equation. The capillary pressure is a measure for the maximum compressive pressure of the cake. The compressive pressure increases until the maximum capillary pressure balances it or until the maximum solidosity is reached. In figure 4.3 an example is given of the compressive pressure as function of volume fraction water (see also §*4.4.1.1*). In addition, the (negative) capillary pressure is shown for several particle sizes. A cross-point on the chart indicates the minimum possible surface porosity. It is assumed that when the surface reaches this value, the cake compression is at its maximum and the droplet stops shrinking. Hence, a smaller primary particle size results in a lower minimum porosity at the surface, for constant parameters of the constitutive equation. The influence of the material properties can be explained with equation 4.9. At an equal compressive pressure, a lower surface porosity is obtained for more compressible materials, i.e. materials with a higher compressibility index, δ, and/or a lower compressive modulus, P_a. In addition, a lower null-stress volume fraction solids results in a higher minimum surface porosity, as shown in figure 4.4.

The transport of water in the cake depends on the gradient in hydraulic pressure, which is related to the gradient in porosity via:

$$\left(\frac{\partial P_l}{\partial \rho_w}\right) = -\frac{1}{d_w}\left(\frac{\partial P_s}{\partial \varepsilon}\right) = \frac{P_a}{d_w \delta (1-\varepsilon)}\left(\frac{(1-\varepsilon)}{\varepsilon_{s0}}\right)^{\frac{1}{\delta}} \tag{4.10}$$

in which d_w is the density of water.

The combination of equations (4.1), (4.5), (4.6), (4.7) and (4.10) results in the apparent diffusion coefficient, D_{ws}*:

$$D_{ws}^{*} = \frac{4 r_s^2 P_a}{75 \delta \eta_w} \frac{\varepsilon^{5.5}}{(1-\varepsilon)^2}\left(\frac{(1-\varepsilon)}{\varepsilon_{s0}}\right)^{\frac{1}{\delta}} \tag{4.11}$$

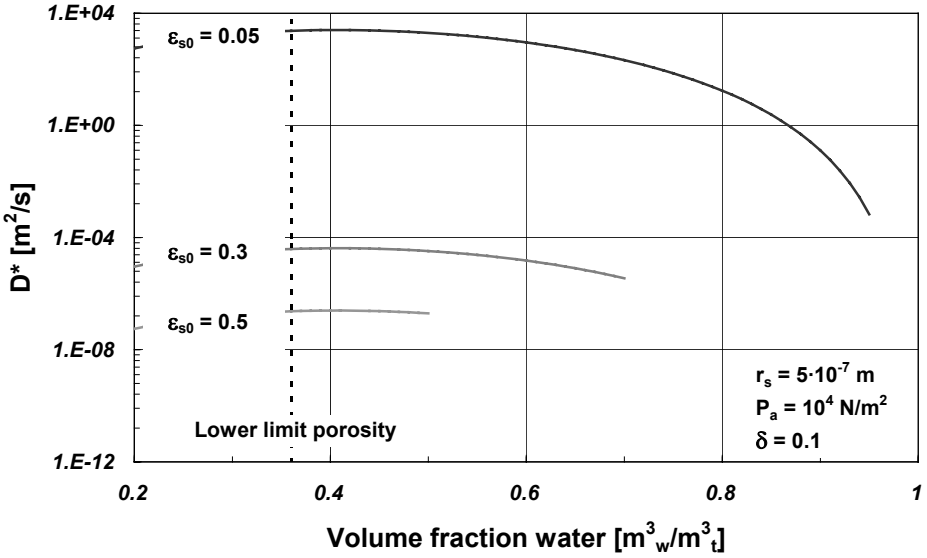

Figure 4.7. The apparent diffusion coefficient as function of volume fraction water for three null-stress volume fractions solids and standard values.

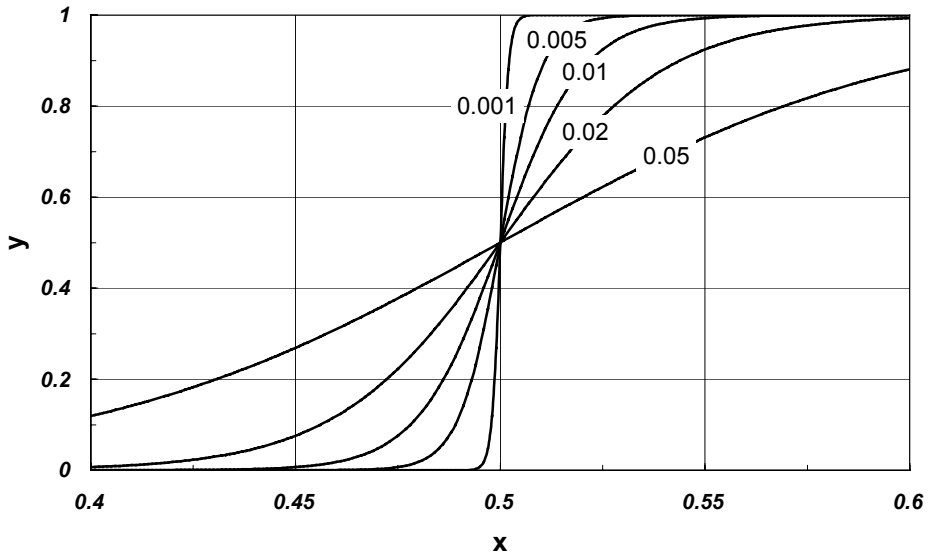

Figure 4.8. Transition values y as function of x calculated with equation (4.27) for different transition factors x_1.

In figure 4.5, the apparent diffusion coefficient is given as function of the volume fraction water for three particle sizes. The diffusion coefficient increases with increasing particle size, due to the increased permeability. The influence of the compressibility index δ and the null-stress volume fraction solids ε_{so} is shown in figures 4.6 and 4.7 respectively. The compressive modulus P_a is proportional with the apparent diffusion coefficient.

When the cake cannot be compressed any further, the meniscus of the liquid will probably retreat into the pores and a gaseous phase replaces the liquid. This complicates the transport processes and the compression of the cake, hence the model is limited to this point.

4.2.2. Mathematical framework

It is assumed that the air in the spray dryer is ideally mixed: the droplets experience a constant air temperature and humidity during the drying process. In addition, the momentum transfer between the droplets and the air is neglected. The mass and heat transfer coefficients for the film layer have been calculated with Sh = Nu = 2, which is accurate enough for small droplets (Wijlhuizen, 1979). The model is described with two continuity equations, one for mass (water) and one for energy. An important assumption is that shrinkage is ideal. The equations for the solid material are then directly coupled to the equations for water via the conservation balance:

$$\frac{\rho_w}{d_w} + \frac{\rho_s}{d_s} = 1 \tag{4.12}$$

in which d_s is the true density of the solids.
The volume average velocity v^v in the liquid equals zero:

$$v^v = \frac{n_w}{d_w} + \frac{n_s}{d_s} = 0 \tag{4.13}$$

in which n_i is the flux of species i.

The equations have been transformed to solid material basis (Van der Lijn, 1976). The transformed space co-ordinate, σ, is defined as:

$$\sigma \equiv \int_0^r \rho_s r^2 dr \tag{4.14}$$

The mass density of water based on solid material u_w is:

$$u_w \equiv \frac{\rho_w}{\rho_s} \tag{4.15}$$

4.2.2.1 Continuity equations

The transformed equation of continuity for water is given by:

$$\left(\frac{\partial u_w}{\partial t}\right)_\sigma = -\left(\frac{\partial}{\partial \sigma} r^2 j_w^s\right)_t \tag{4.16}$$

The equation for energy is given by:

$$C_{pw} T\left(\frac{\partial u_w}{\partial t}\right)_\sigma + \left(C_{ps} + u_w C_{pw}\right)\left(\frac{\partial T}{\partial t}\right)_\sigma = -\left(\frac{\partial}{\partial \sigma} r^2 q^s\right)_t \tag{4.17}$$

in which C_{pi} is the heat capacity of species i and q^s the heat flux with respect to the solids velocity.

4.2.2.2 Flux equations

The flux of water with respect to the solids velocity reads:

$$j_w^s = -r^2 \rho_s^2 D_{ws}^* \left(\frac{\partial u_w}{\partial \sigma}\right)_t \tag{4.18}$$

The heat flux is given by:

$$q^s = -r^2 \rho_s \left[\rho_s D_{ws}^* C_{pw} T\left(\frac{\partial u_w}{\partial \sigma}\right)_t + \lambda\left(\frac{\partial T}{\partial \sigma}\right)_t\right] \tag{4.19}$$

in which λ is the thermal conductivity. The diffusion coefficient and thermal conductivity (can) vary with the temperature and concentration.

4.2.2.3 Initial and boundary conditions

The initial conditions, with the dimensionless space-coordinate, are:

$$t = 0 \quad 0 \le \sigma' = \frac{\sigma}{\sigma_{\max}} \le 1 \quad u_w = u_{w0} \quad T = T_0 \tag{4.20}$$

The boundary conditions at the centre of the droplet read:

$$\begin{gathered} t > 0 \quad \sigma' = 0 \quad \left(\frac{\partial u_w}{\partial \sigma'}\right)_t = 0 \quad \left(\frac{\partial T}{\partial \sigma'}\right)_t = 0 \\ or \quad j_w^s = 0 \qquad q^s = 0 \end{gathered} \tag{4.21}$$

At the surface the mass transport through the film layer is described with Stefan-diffusion: water vapour diffuses through a stagnant layer of air under its own concentration gradient. The properties of the film are averaged with bulk and surface properties. The boundary condition for mass transfer is (e.g. Kerkhof and Schoeber, 1974 and Krischer, 1978):

$$t > 0 \quad \sigma' = 1$$
$$-r^2 \frac{\rho_s^2 D_{ws}^*}{\sigma_{\max}} \left(\frac{\partial u_w}{\partial \sigma'} \right)_t = k_f \rho_f \ln\left(\frac{1 + H_i}{1 + H_\infty} \right) \tag{4.22}$$

in which k_f is the mass transfer coefficient based on film conditions, H_i the humidity of the air at the interface and H_∞ the humidity of the bulk.

The boundary condition for heat transfer is given by:

$$-r^2 \frac{\rho_s}{\sigma_{\max}} \left\{ \rho_s D_{ws}^* C_{pw} T \left(\frac{\partial u_w}{\partial \sigma'} \right)_t + \lambda \left(\frac{\partial T}{\partial \sigma'} \right)_t \right\} =$$
$$\alpha_f (T_\infty - T_i) - k_f \rho_f \ln\left(\frac{1 + H_i}{1 + H_\infty} \right) \left((C_{pv} - C_{pw}) T + \Delta H_o \right) \tag{4.23}$$

in which α_f is the heat transfer coefficient, and ΔH_o the heat of evaporation.

4.2.3 Final granule properties

If the primary particles are inert and non-porous, the average properties of the granules can be related to the initial water content and the average water content, $\langle u_w \rangle$. Then, the final granule properties can be calculated with the average final water content.

The relative granule size is given by:

$$\frac{r_p}{r_{po}} = \left(\frac{\langle u_w \rangle d_s + d_w}{u_{wo} d_s + d_w} \right)^{\frac{1}{3}} \tag{4.24}$$

The porosity of the dried granule is given by:

$$\varepsilon_p = \frac{1}{1 + \dfrac{d_w}{\langle u_w \rangle d_s}} \tag{4.25}$$

The particle density of the dried granule is:

$$\rho_p = d_s(1-\langle\varepsilon\rangle) = \frac{1}{\frac{1}{d_s}+\frac{\langle u_w\rangle}{d_w}} \tag{4.26}$$

4.3 Numerical method and programming

The model has been programmed on a Borland Delphi® 5.0 platform using the D03PCF partial differential equation (PDE) solver from the numeric algorithm group® (NAG, 1998). D03PCF integrates a system of linear or non-linear parabolic PDEs in one space variable. The spatial discretisation is performed using finite differences, and the method of lines is employed to reduce the PDEs to a system of ordinary differential equations. The resulting system is solved using a backward differentiation formula method. The used grid is refined towards the surface and consists of 201 points.

Because of the discontinuity of the diffusion coefficients at the transition point of the regimes, the diffusion coefficients of equations 4.2 and 4.11 are coupled via:

$$\gamma = \frac{D_1 - D_2}{1+\exp\left(\frac{x-x_0}{x_1}\right)} + D_2 \tag{4.27}$$

in which D_i are the diffusion coefficients of the two regimes, x_0 is the transition value at which γ has exactly the averaged value $(D_1 + D_2)/2$ and x_1 is the factor that determines the start of the transition. Values of γ for $x_0 = 0.5$, $D_1 = 0$, $D_2 = 1$, and different values of factor x_1 are given in figure 4.8. The factor x_1 is taken 0.005 for the calculations and can be regarded as the factor of smoothness for the transition: if x_1 is equal to zero the transition is abrupt, and if x_1 is infinite, γ equals the average value (in this case 0.5).

4.4 Results and discussion

4.4.1 Simulations of spray drying droplets of particulate slurries

4.4.1.1 Standard conditions and values

The standard conditions and values are summarised in table 4.1. The true density of the solid particles is 2500 kg/m^3. To allow easy comparison between the figures, the concentrations are converted to the volume fractions.

The concentration profiles for the standard conditions and values are shown in figure 4.9. The temperature profiles for the first 0.04 s are shown in figure 4.10. Initially, the water concentration decreases sharply at the surface until the value is reached, where the cake starts to form: (1- ε_{so}). During further drying, the cake thickens and becomes more compact. The high apparent diffusion coefficient results in a flat concentration profile in the cake. It can be observed that the water concentration in the cake decreases faster in the early stage of the cake compression. The process of thickening and compacting continues until the minimum surface porosity is reached. The average porosity is 0.72 and the particle density is 708 kg/m^3.

It is plausible that from this point the liquid starts to retreat into the pores and the transport mechanism changes. If the droplet does not further deform the final granule becomes hollow. In that case a gas phase must enter or arise in the droplet. This could be caused by transport via a larger pore (network) or by boiling of the liquid. If the cake deforms the final granule might still be spherical with a surface that has wrinkles and/or cracks, or the granule can have a shrivelled, fractured or "doughnut"-like shape.

Table 4.1. Standard conditions and values for the simulation parameters.

Parameter	*Value*	*Parameter*	*Value*
Air temperature	120 °C	Particle radius	$5 \cdot 10^{-7}$ m
Air humidity	0.060 kg_w/kg_{da}	Porosity limit	0.36 m^3_w/m^3_t
Initial water content (ε_o)	1.5 kg_w/kg_s (0.78 m^3_w/m^3_t)	Null-stress volume fraction solids, ε_{so}	0.30 m^3_s/m^3_t
Droplet temperature	25 °C	Compressive modulus, P_a	10000 N/m^2
Droplet diameter	$100 \cdot 10^{-6}$ m	Compressibility index, δ	0.1

4.4.1.2 Effect of primary particle size

The primary particle radius is varied between $5 \cdot 10^{-8}$ – $5 \cdot 10^{-6}$ m. The time until the minimum surface porosity was reached for a feed with a primary particle radius of $5 \cdot 10^{-6}$ m was less than 0.05 s. The internal water concentration then equals the initial water concentration and towards the surface, in a region estimated smaller than $2 \cdot 10^{-7}$ m, the water concentration profile increases and sharply decreases. Due to the assumption of

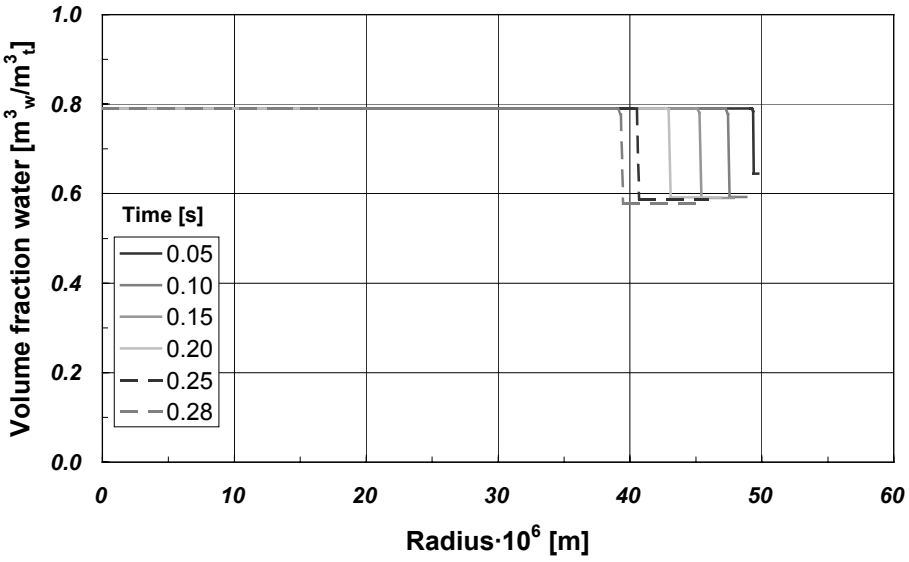

Figure 4.9. Water concentration profiles for standard values and conditions.

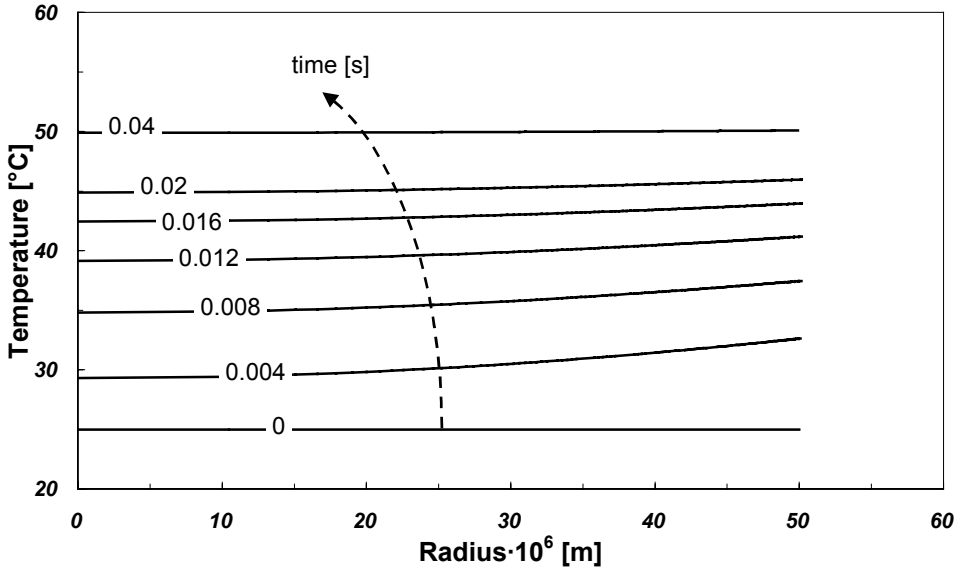

Figure 4.10. Temperature profiles at standard values and conditions.

ideal mixing of the air in the spray drier, the droplets experience a relative high humidity in the beginning of the drying process, hence the initial condensation. Figure 4.3 shows that the solidosity at the cross-point for this primary particle size (0.34) is slightly lower than the null-stress solidosity (0.30). Therefore, the minimum surface porosity is reached just after the start of the cake formation. This result is in agreement with the production of low density and high porosity particles from spray drying large, aggregated primary particles (Denny, 1998).

The water concentration profiles for a particle radius of $5 \cdot 10^{-8}$ m are depicted in figure 4.11. The higher maximum capillary pressure from the particle size allows the cake to be compressed until the capillary pressure balances the compressive pressure. The dried granules have a low porosity (0.44) and hence a high density (1400 kg/m^3). This result is different from the hollow and "doughnut" shaped particles from well-dispersed sols of small particles (Sizgek, 1998). Although smaller primary particles generate larger capillary pressures, the particle interactions might be such that the cake behaviour becomes incompressible and the granules become hollow or fractured.

4.4.1.3. Effect of cake compressibility

For a particular water concentration, the compressive pressure of the cake is given by the null-stress volume fraction solids, ε_{so}, the compressibility index, δ, and the compressive modulus, P_a. If the two other parameters are kept constant, the compressive pressure for a particular water concentration decreases with increasing null-stress volume fraction solids, increasing compressibility index and decreasing compressive modulus. A lower compressive pressure results in a lower minimum surface porosity for a constant capillary pressure. When the minimum surface porosity is lower, the granules shrink more, and the granules have a higher density and lower average porosity.

The null-stress volume fraction solids determines the volume fraction water where the particles are assumed to make contact and start to form a cake. If this value is lower than the initial solidosity, the particles make contact from the beginning and the cake would already be under pressure. For standard values and a null-stress volume fraction solids of 0.05, the capillary pressure is lower than the initial compressive pressure and the calculation stops immediately. For a null-stress volume fraction solids of 0.5 the cake

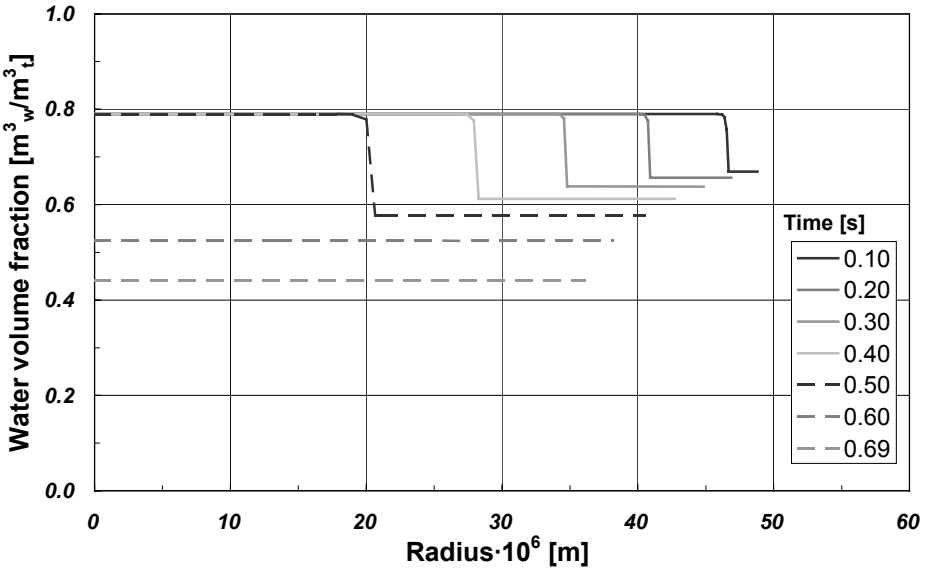

Figure 4.11. Water concentration profiles for a particle radius of $5 \cdot 10^{-8}$ m at standard drying conditions.

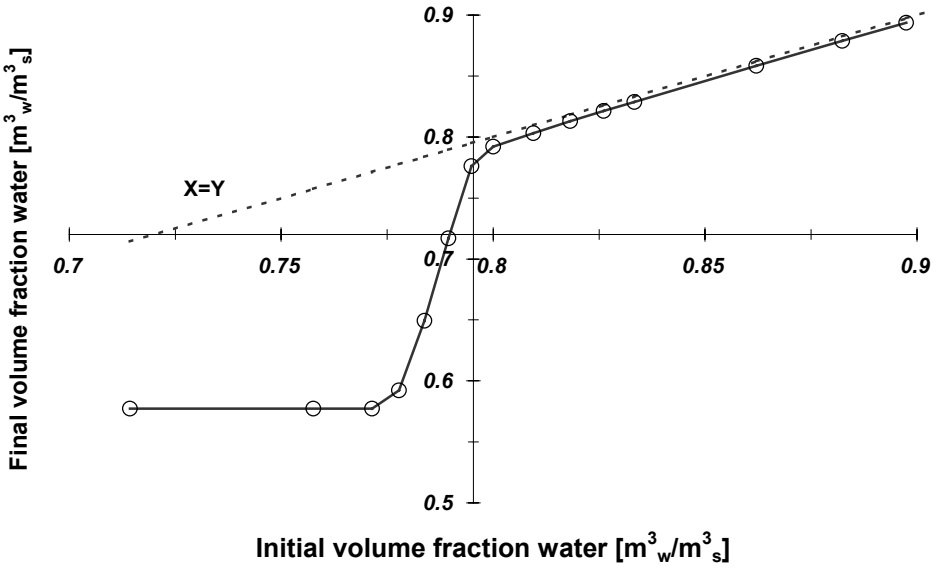

Figure 4.12. The final volume fraction water (porosity) as function of the initial volume fraction water.

reaches the porosity limit after a very short time. This is caused by both the small difference between the null-stress volume fraction solids and the solidosity limit and by the fast compaction of the cake. A compressive modulus of 1000 N/m^2 results in a solid granule, and the profiles are like shown in figure 4.11. The average porosity (0.44) equals the minimum surface porosity, which is higher than the porosity limit. The uniform porosity of the granule is a result of the high apparent diffusion coefficient in the cake. A lower compressibility index results in a short shrinkage, and for a compressibility index larger than 0.2, the droplet solidifies to the maximum packing fraction.

4.4.1.4. Effect of feed water content

When the water content of the feed is increased, more water has to evaporate before the particles make contact and cake formation begins. However, because of the low values of the Stokes-Einstein diffusion coefficient, the concentration gradient at the surface is steep and the formation of the cake always starts in a very early stage of the drying process. During the cake compression process, the cake thickness grows, the cake is compressed and water flows through the cake to the surface. In the core of the droplet, the water content is still equal to the initial water content and, since the evaporation flux is constant, a higher initial water content results in a slower rate of cake thickening. Simultaneously, the water content in the cake decreases until the minimum surface porosity is reached. In figure 4.12, the volume fraction water at the end of the shrinking period (the final volume fraction water) is shown as function of the initial volume fraction water. For initial volume fractions larger than 0.8 m^3_w/m^3_t (ca. 1.6 kg_w/kg_s), the minimum surface porosity is reached just after the start of the cake formation and the final volume fraction approximates the initial value. For initial water volume fractions smaller than 0.77 m^3_w/m^3_t (ca. 1.3 kg_w/kg_s), the cake thickens until the centre of the droplet is reached. In these cases, the capillary pressure controls the shrinkage. So, a lower feed water content results in denser and less porous granules. The situation in which the initial water volume fraction is lower than the null-stress volume fraction water, is not realistic and therefore not studied.

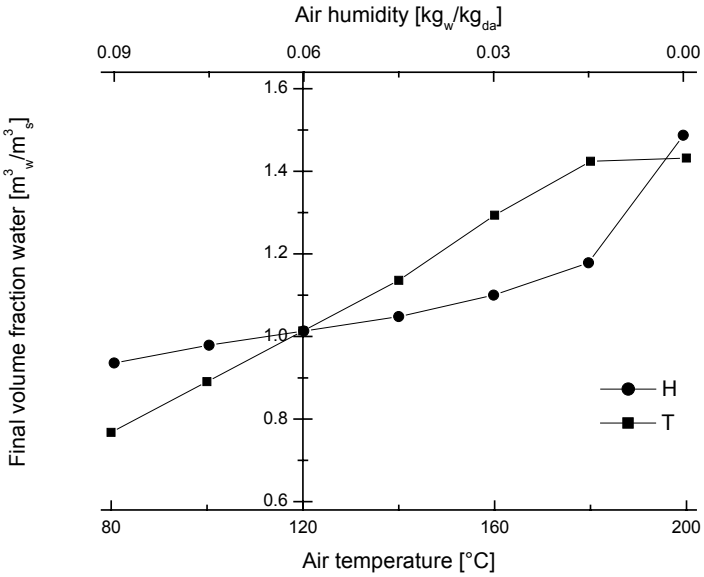

Figure 4.13. Final volume fraction water (porosity) as function of the air temperature and humidity. Note the reverse axis of the humidity.

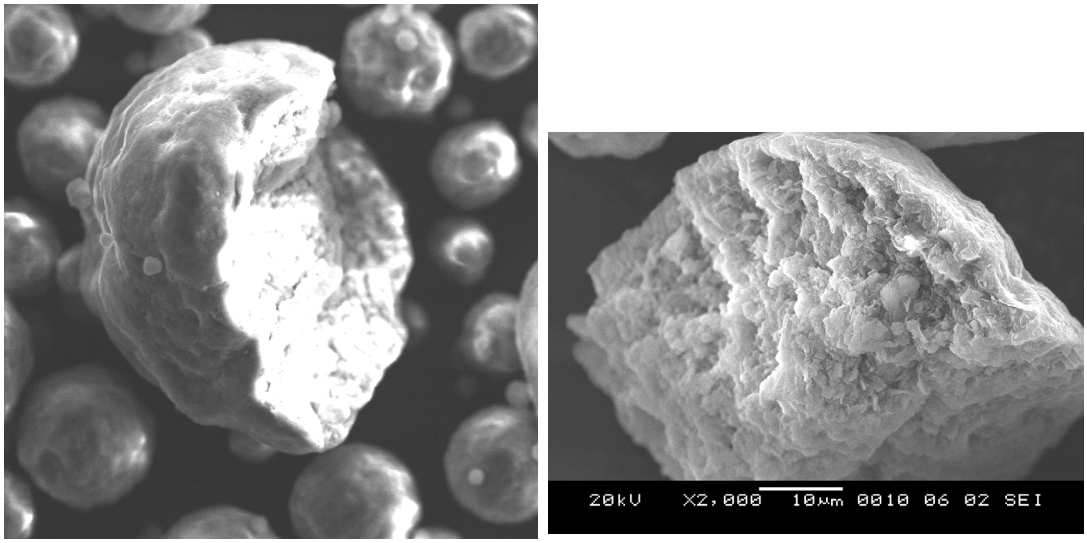

Figure 4.14. SEM scans of the interior of FCC catalyst.

4.4.1.5 Effect of initial droplet diameter

The droplet diameter influences the mass and heat transfer coefficients in the film via the Sherwood and Nusselt correlations. In addition, it determines the surface area available for evaporation. Although in the CAP the absolute drying rate is proportional to the diameter of the droplet, the large specific surface area of smaller droplets results in shorter drying times. However, the drying process on a reduced time-scale, t/R_o^2, remains identical (Kerkhof, 1975). Therefore, the final granules have the same average density and porosity. A larger droplet diameter does result in a larger granule size and a longer drying time.

4.4.1.6 Effect of air conditions

The influence of air conditions in a spray drying process is rather complicated due to the interdependency of the variables. For example, a higher air temperature increases the drying flux and hence the humidity. The influence of the air temperature and humidity can be studied independently with the model. The drying flux increases with increasing air temperature and decreasing air humidity. A higher flux results in a more rapidly decrease of the (surface) water concentration. The surface tension decreases with increasing temperature. A lower surface tension results in a lower capillary pressure. Therefore, for both a higher temperature and lower humidity, the minimum surface porosity is reached at a higher average water content and the granules will have a higher porosity and lower density. The results of the studied temperatures and humidities are depicted in figure 4.13.

4.4.2 Comparison with experimental data

4.4.2.1 FCC catalyst

A typical FCC catalyst formulation is spray dried at different spray drying conditions, which is described in chapter 3. As discussed in *§4.4.1.4*, the initial water content has a large influence on the amount of shrinkage: high feed water contents are unfavourable for shrinkage. Therefore, the simulations are focused on the results from the experiments with a feed water content of 7.3 kg_w/kg_s. Some (essential) process conditions and

measured properties of the experiments are given in table 4.2. Most of the formed granules were spherical and SEM photos of broken particles show a solid interior (figure 4.14). The differences in powder properties are very small and the measured porosity is equal for the three samples. This shows that even the feed with the highest water content has shrunk to a solid granule. To simulate this drying behaviour, a compressible cake is required. Therefore, the following parameters are used in the simulation. The constitutive parameters have been chosen comparable to Mierlo sludge: ε_{s0} =0.12, δ =0.5, and P_a = 1000 N/m^2 (La Heij, 1994). The null-stress solidosity, ε_{s0}, is taken equal to the solidosity of the most concentrated FCC catalyst feed. The droplet radius is $1.5 \cdot 10^{-6}$ m, the primary particle radius, r_s, is taken equal to $5 \cdot 10^{-7}$ m. With these parameters, the simulations for the lowest feed water contents (3.6 and 4.6 kg_w/kg_s) result in solidified granules with final porosities of 0.37. However, the final porosity for the feed with 7.3 kg_w/kg_s is higher than the measured FCC catalyst porosity: 0.75 compared to 0.38 measured.

Changing the compressibility index and the compressive modulus, for ε_{s0} = 0.12, did not result in complete solidification. When the null-stress volume fraction solids is taken 0.10, the simulation continues until the particle solidifies and the final porosity becomes 0.37. Probably the interaction between the primary particles (i.e. cake formation) starts at a higher water content, which is related to the attractive and repulsive forces on (colloidal) particles. In addition, it implies that Brownian motion might not occur at all or only for a much smaller concentration regime. Unfortunately, the cake compression behaviour is not studied experimentally.

The transition from the Brownian motion regime to the cake compression regime can also be considered. A less sharply defined transition can be illustrated with the x_1 parameter from equation 2.47 (see figure 4.8). The effect on the transport properties is found in a more gradual increase of the apparent diffusion coefficient, which results in flatter gradients and prolonged shrinkage. The water volume fraction profiles, calculated with x_1 = 0.02 and initial constitutive parameter values as mentioned above, are shown in figure 4.15.

Table 4.2. Process conditions and measured properties of spray dried FCC catalyst.

Process conditions		*81202_34*	*81221_12*	*81218_12*
Feed water content	[kg_w/kg_s]	3.6	4.6	7.3
Feed flow	[kg_t/hr]	50	48	46
Nozzle pressure	[bar]	26	18	21
Air outlet temperature	[°C]	144	142	143
Air outlet humidity	[kg_w/kg_{da}]	0.018	0.021	0.025
Air flow	[kg/s]	0.176	0.176	0.180
Powder properties				
Average diameter $\cdot 10^6$	[m]	59	65	53
Bulk density	[kg/m^3]	1100	1084	1073
Porosity	[-]	0.39	0.38	0.38

Another explanation is that the small binder particles, with a diameter of ca. 10^{-8} m (see also chapter 3), generate larger capillary pressures. The larger pressure allows the cake to compress further. However, using a particle diameter of 10^{-8} m does not result in a solidified particle.

4.4.2.2 Morphology of spray dried materials

In literature, the morphology of spray dried materials is categorised into crystalline, skin forming and agglomerate. The morphology of agglomerate particles is compared to the simulation results. Especially the study of single droplet drying has given direct insight in the drying kinetics and behaviour of various materials. The observation that droplets containing insoluble particles have evaporation rates of pure water and shrink until a solid structure is formed, corresponds to simulation of drying of materials with a high deformability, of which the cake penetrates until the centre is reached (Ranz, 1952; Lebeis, 1955; and Miura, 1972). It is often assumed that the CAP stops when a crust is formed. However, the presented model shows that a crust can be formed and thicken during the CAP as long as the minimum surface porosity is not reached.

The bulk of spray dried agglomerate particles has a spherical, solid and regular structure (Walton, 2000). The porous structure of the packed primary particles contributes to a low mass transfer resistance, which is in agreement with the high values

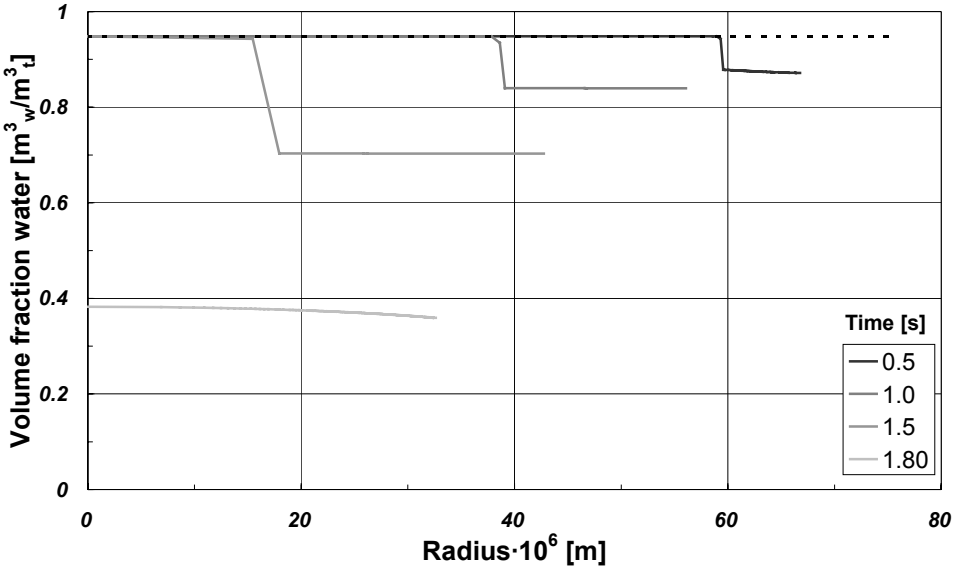

Figure 4.15. Water concentration profiles for FCC catalyst with x_i = 0.02 and the process conditions of experiment *81218_12*.

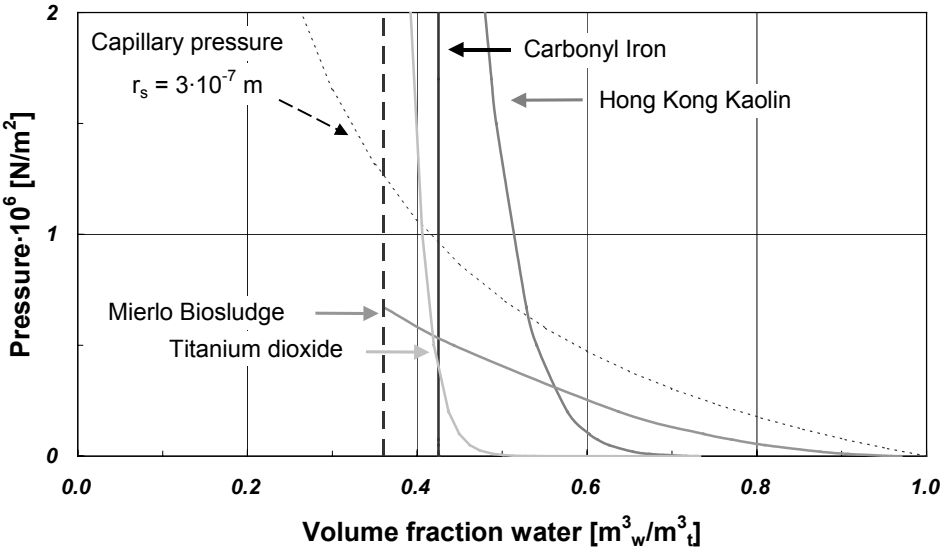

Figure 4.16. Capillary pressure (dotted line) and compressive pressures (solid lines) for several materials (used data from Tiller, 1998 and Reichmann, 2001).

of the apparent diffusion coefficient (figure 4.5). Probably, the formed crust is deformable and the droplet solidifies completely.

The early onset of the cake formation may attribute to the mechanism of incomplete atomisation: the droplet forms a crust before a spherical shape is obtained, which results in irregularly shaped granules (Walton, 2000).

Spray drying very dilute slurries of attapulgus clay slip (6 wt.% solids in the feed) at different conditions resulted in collapsed particles with comparable crust thickness (Crosby, 1958). The model shows that for high initial water contents, the formation of the crust is in the beginning of the drying process. Even if the crust is moderately deformable, the crust thickens, but the surface soon reaches its minimum porosity and stops shrinking.

The observation that spray drying primary particle sizes, much larger than 10^{-6} m, results in solid granules is in contradiction to the simulations with larger particle size, and the difference can only be explained if the material is very compressible (Denny, 1998).

Drying single droplets containing colloidal carbon particles (particle size < 10^{-6} m) resulted in spherical and hollow granules (Walton, 2000). The formation of the bubble occurred after the majority of the water had evaporated from the droplet. In some other cases particles with blowholes were formed. This could be an effect of the shrinkage resistance of the crust, when the minimum surface porosity is reached. The crust may deform locally as a result from tangential stress and the surface would show craters or wrinkles. Also an internally nucleated bubble that expands could rupture the crust. Cycles of inflation, rupture and shrivelling have also been reported (Hecht, 2001).

4.4.2.3 Cake compression behaviour

The cake compression behaviour of materials can be classified into three categories, 1) incompressible, 2) moderately compactable and 3) highly compactable. Examples of materials and their constitutive equation values are given in table 4.3 (Tiller, 1998; Reichmann, 2001). For the materials, the compressive pressure and the capillary pressure are given as function of the water concentration in figure 4.16. For incompressible materials, such as carbonyl iron, the water concentration is independent of the applied

stress. Highly compactable materials, such as Mierlo sludge, are able to compact to a water concentration much lower than the null-stress porosity (1- ε_{so}). Flocculated particles have lower null-stress solidosities than dispersed solid particles, because of the high porosity of the flocks. These flocculated systems are normally very compactable. It is also suggested that the compressibility index decreases with increasing null-stress solidosity (Tiller, 1998).

Simulation of spray drying carbonyl iron with standard conditions and values results in large granules with very low density and high porosity. The volume fraction water at the surface decreases sharply to the null-stress water concentration and shrinkage stops immediately. Moderately compactable Hong Kong Kaolin forms a cake, which penetrates into the centre of the droplet. The droplet dries until the minimum surface porosity is reached, and shows no concentration gradient. The highly compactable Mierlo Sludge shows total absence of water concentration gradients. The initial volume fraction solids (0.79) is higher than the null-stress volume fraction solids, thus the particles initially make contact. In addition, the capillary pressure remains higher than the compressive pressure and the cake compacts until the porosity limit of 0.36.

Table 4.3. Values for the constitutive equation for different materials (Tiller, 1998).

Material/ Parameter	*Incompressible Carbonyl Iron*	*Moderately compactable Hong Kong Kaolin*	*Highly compactable Mierlo Sludge*	*Titanium dioxide*
ε_{so}	0.575	0.27	0.03	0.267
δ	0.001	0.09	0.47	0.033
P_a	∞ (10^9)	1370	1000	$3 \cdot 10^{-5}$

The influence of the feed concentration and air outlet temperature is studied for titanium dioxide. This was the only material of which pictures of spray dried material, primary particle size and constitutive equation parameters have been found in literature (Walton, 2000; and Reichmann, 2001). The primary particle diameter was $6.1 \cdot 10^{-7}$ m and the values of the constitutive equation parameters are given in table 4.3. The compressive and capillary pressures as function of water concentration are shown in figure 4.16. The sharp rise in the compressive pressure is due to the low compressibility

index (Reichmann, 2001). Pictures 36 and 114 in (Walton, 2000) show solid particles with a nearly spherical shape and an irregular surface. It is also mentioned that the particles have a cohesive flow behaviour and showed agglomeration. This is probably caused by surface properties, which are not included in this model. Information about the spray drying conditions is limited to the flow- and atomisation-type, the feed concentration and air inlet temperature. Therefore, standard spray drying conditions are applied in the simulations. The feed concentration has a large influence on the particle properties. For a feed concentration of 50 wt.% solids (u_o = 1 kg_w/kg_s), the particles become solid when the surface water concentration reaches the minimum surface porosity, while for lower feed concentrations the surface reaches the minimum porosity before the cake extends to the centre of the droplet. Decreasing the air temperature to 100 °C results in solid granules for a feed concentration of 44.4 wt.% (u_o = 1.25 kg_w/kg_s). For a feed of 40 wt.% solids (u_o = 1.5 kg_w/kg_s) and an air temperature of 80 °C, the cake still does not reach the centre. This example demonstrates on one hand that increasing the feed concentration results in more dense particles, and on the other hand that changing process conditions can be used to influence granule properties. In figure 4.17 the water concentration profiles are shown for a droplet with 44.4 wt.% initial solids concentration and an air temperature of 100 °C.

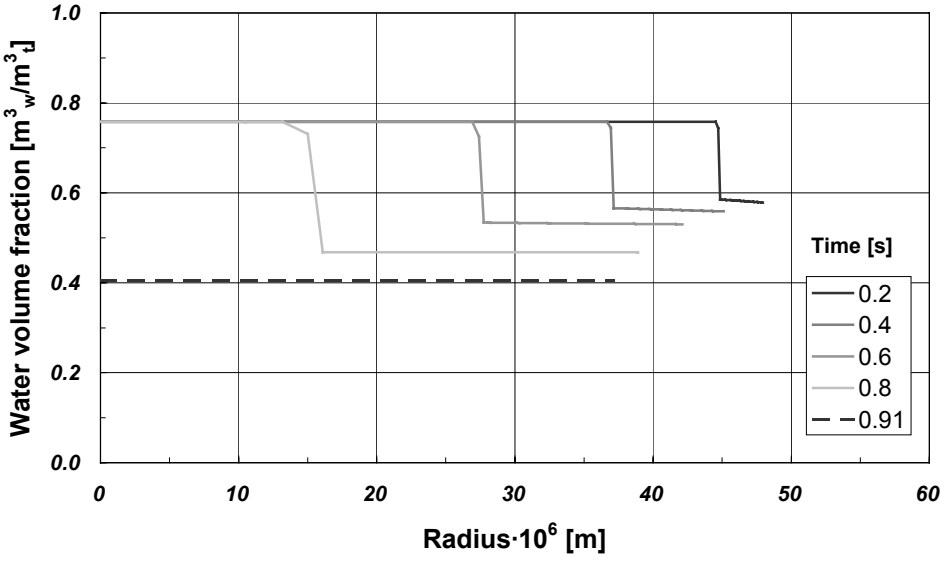

Figure 4.17. Water concentration profiles for TiO_2 with 44.4 wt.% initial solids content and an air outlet temperature of 100 °C.

4.5 Conclusions

The presented model for spray drying particulate slurries predicts concentration and temperature profiles. The development of the concentration profiles depends on material properties and spray drying process conditions. The material properties are the compression behaviour of the solid material (cake) and primary particle size. The process conditions are air temperature and humidity. The material properties and the process conditions all influence the amount of shrinkage. The mechanical behaviour of the cake has a strong influence on the amount of shrinkage: more compressible cakes show more shrinkage for equal drying conditions. The apparent diffusion coefficient in the cake has very high values and results in a flat concentration profile in the cake. The final granule properties size, density and porosity are determined by the amount of shrinkage.

The properties of spray dried FCC catalyst can only be simulated if the cake formation starts at a lower solids concentration than the initial concentration. This strongly indicates that the Brownian motion regime is very limited or that the contact between the solid particles occurs at relatively low volume fraction solids. The latter could be an effect of the binder material.

The model predicts various morphologies that are reported in literature, although verification is difficult due to lack of precise information. The relation between primary particle size and cake compression behaviour might explain the differences between the model and literature data.

To obtain dense and low porous granules, it is very important to prepare a slurry with a low water content. In addition, decreasing the drying flux results in granules with higher density and lower porosity.

It is recommended to perform filtration experiments and spray drying or single droplet drying experiments to further explore and validate the presented model. For manufacturers, the use of filtration experiments can assist in scale-up and design or might even replace expensive trial runs.

Notation

Roman

B_o	Permeability	[m^2]
C_p	Heat capacity	[J/kgK]
d_i	True mass density	[kg_i/m_i^3]
D_{ij}	Diffusion coefficient	[m^2/s]
H	Humidity	[kg_w/kg_{da}]
j_i	Mass flux of component i	[kg_i/m^2s]
k	Mass transfer coefficient	[m/s]
k_B	Boltzmann constant	[J/K]
n_i	Mass flux of component i	[kg_i/m^2s]
P_a	Compressive modulus	[N/m^2]
P_c	Capillary pressure	[N/m^2]
P_l	Hydraulic pressure	[N/m^2]
P_s	Compressive pressure	[N/m^2]
q	Heat flux	[J/m^2s]
r	Space co-ordinate	[m]
r_i	Radius	[m]
t	Time	[s]
T	Temperature	[°C]
u	Transformed water density	[kg_w/kg_s]
v	Mass averaged velocity	[m/s]
v^v	Volume averaged velocity	[m/s]
v_i	Velocity	[m/s]

Greek

α	Heat transfer coefficient	[W/m^2K]
β	Compressibility index	[-]
ε	Porosity	[-]
ε_s	Volume fraction solids	[m_s^3/m_t^3]
η	Viscosity	[N/m^2 s]
ϑ	Contact angle	[rad]
λ	Heat conductivity	[W/mK]
ρ_i	Mass density	[kg_i/m_t^3]
ρ_t	Mixture mass density	[kg_t/m_t^3]
σ	Transformed space co-ordinate	[kg_s]
σ_{LV}	Surface tension	[J/m^2]
τ	Tortuosity	[-]
ω_i	Mass fraction	[-]

Subscripts

c	Critical
da	Dry air
eff	Effective
i	Interface
max	Maximum
s	Solid material
t	Total
w	Water
o	Initial, null-stress or saturated value
∞	Bulk or infinite value

Superscripts

v	With respect to volume averaged velocity
s	With respect to the solid material velocity
*	Apparent value

References

Ali, H.H., Mumford, C.J., Jeffreys, G.V. and Bains, G.S., 1989, A study of evaporation from, and drying of, single droplets, Proceedings of the 6th International Drying Symposium 1988, 378-385.

Audu, T.O.K. and Jeffreys, G.V., 1975, The drying of drops of particulate slurries, Transactions of the Institution of Chemical Engineers, 53, 165-172.

Brown, L.A., Zukoski, C.F. and White, L.R., 2002, Consolidation during drying of aggregated suspensions, American Institute of Chemical Engineers Journal, 48, 3, 492-502.

Charlesworth, D.H. and Marshall, W.R. Jr., 1960, Evaporation from drops containing dissolved solids, American Institute of Chemical Engineers Journal, 6, 1, 9-23.

Cheong, H.W., Jeffreys, G.V. and Mumford, C.J., 1986, A receding interface model for the drying of slurry droplets, American Institute of Chemical Engineers Journal, 32, 8, 1334-1346.

Crosby, E.J. and Marshall, W.R. Jr., 1958, Effects of drying conditions on the properties of spray-dried particles, Chemical Engineering Progress, 54, 7, 56-63.

Cumberland, D. J. and Crawford, R. J., 1987, The packing of particles, Elsevier, Amsterdam, The Netherlands.

Denny, P.J. and Handley, T.T.J., 1998, The effect of gel precursor structures on the properties of spray dried particles, Proceedings of the World Congress on Particle Technology 3, Brighton, England, Paper 192.

Epstein, N., 1989, On tortuosity and the tortuosity factor in flow and diffusion through porous media, Chemical Engineering Science, 44, 3, 777-779.

Hecht, J.P. and King, C.J., 2000, Spray drying: influence of developing drop morphology on drying rates and retention of volatile substances. 1. single-drop experiments, Industrial & Engineering Chemistry Research, 39, 1756-1765.

Hoffman, T.W. and Ross, L.L., 1972, A theoretical investigation of the effect of mass transfer on heat transfer to an evaporating droplet, International Journal of Heat and Mass Transfer, 15, 599-617.

Jomaa, W. and Puiggali, J.-R., 1991, Drying of shrinking materials: modelling with shrinkage velocity, Drying Technology, 9, 5, 1271-1293.

Kerkhof, P.J.A.M. and Schoeber, W.J.A.H., 1974, Theoretical modelling of the drying behaviour of droplets in spray dryers, Advances in preconcentration and dehydration of foods, Ed. A. Spicer, Applied Science Publishers Ltd., London, England, 349-397.

Kerkhof, P.J.A.M., 1975, A quantative study of the effect of process variables on the retention of volatile trace components in drying, Ph.D. thesis, Eindhoven University of Technology, Eindhoven, The Netherlands.

Ketelaars, A.A.J., Jomaa, W., Puiggali, J.-R. and Coumans, W.J., 1992, Drying shrinkage and stresses, Proceedings of the 8th International Drying Symposium Drying '92, Elsevier Science, Amsterdam, The Netherlands, 293-303.

Krieger, I.M., 1972, Rheology of monodisperse lattices, Advances in Colloid and Interface Science, 3, 111-136.

Krischer, O. und Kast, W., 1978, Trocknungstechnik, Erster Band, Die wissenschaftlichen Grundlagen der Trocknungstechnik, Springer-Verlag, Berlin, Germany.

La Heij, E.J., 1994, An analysis of sludge filtration and expression, Ph.D. thesis, Eindhoven University of Technology, Eindhoven, The Netherlands.

Lebeis, E.H. and Burtis, T.A., 1955, Effect of drying conditions on drying rate and physical properties of a porous solid, American Institute of Chemical Engineers Journal, 1, 3, 329-334.

Leofanti, G., Padovan, M., Tozzola, G. and Venturelli,B., 1998, Surface area and pore texture of catalysts, Catalysis Today, 41, 207-219.

Leu, W., 1986, Principles of compressible cake filtration, Encyclopedia of Fluid Dynamics, Vol. 5, Slurry Flow Technology, Chapter 21, ed. Cheremisineff, N.P., Gulf Publishing Company, Houston, USA.

Liang, H., Shinohara, K., Minoshima, H. and Matsushima, K., 2001, Analysis of constant rate period of spray drying of slurry, Chemical Engineering Science, 56, 2205-2213.

Lijn, J. van der, 1976, The 'constant rate period' during the drying of shrinking spheres, Chemical Engineering Science, 31, 929-935.

Lukasiewicz, S.J., 1989, Spray drying ceramic powders, Journal of the American Ceramic Society, 72, 4, 617-624.

Marshall, T.J., 1957, Permeability and the size distribution of pores, Nature, 180, 664-665.

Minoshima, H., Matsushima, K., Liang, H. and Shinohara, K., 2001, Basic model of spray drying granulation, Journal of Chemical Engineering of Japan, 34 ,4, 472-478.

Miura, K., Atarashiya, K., Ouchi, I. and Ohtani, S., 1972, Experimental study of drying characteristics of single drops containing solids, Heat Transfer-Japanese Research, 1, 2, 11-17.

NAG, 1998, The NAG Fortran Library Manual – Mark 18, software edition 2.1, July 27th 1998, D03PCF.

Ranz, W.E. and Marshall, W.R. Jr., 1952, Evaporation from drops, Chemical Engineering Progress, 48, 4, 141-180.

Reichmann, B. and Tomas, J., 2001, Expression behaviour of fine particle suspensions and the consolidated cake strength, Powder Technology, 121, 182-189.

Sanden, S.C.T. van der, Coumans, W.J. and Kerkhof, P.J.A.M., 2000, Shrinkage behaviour of FCC catalyst droplets in a spray drying process, Proceedings of the 12th International Drying Symposium IDS2000, Paper No. 393, Elsevier Science, Amsterdam, The Netherlands.

Scherer, G.W., 1990, Theory of drying, Journal of the American Ceramic Society, 73, 1, 3-14.

Schlünder, E.-U., 1988, On the mechanism of the constant drying rate period and its relevance to diffusion controlled catalytic gas phase reactions, Chemical Engineering Science, 43, 10, 2685-2688.

Shirato, M., Kato, H., Kobayashi, K. and Sakazaki, H., 1970, Analysis of settling of thick slurries due to consolidation, Journal of Chemical Engineering of Japan, 3, 1, 98-104.

Sizgek, E., Bartlett, J.R. and Brungs, M.P., 1998, Production of titanate microspheres by sol-gel and spray drying, Journal of Sol-Gel Science and Technology, 13, 1011-1016.

Tiller, F.M. and Kwon, J.H., 1998, Role of porosity in filtration: XIII. Behavior of highly compactable cakes, American Institute of Chemical Engineers Journal, 44, 10, 2159-2167.

Toei, R. and Furuta, T., 1982, Drying of a droplet in a non-supported state, American Institute of Chemical Engineers Symposium Series, 78, 218, 101-110.

Walton, D.E., 2000, The morphology of spray-dried particles. A qualitative view, Drying Technology, 18, 9, 1943-1986.

Wesselingh, J.A., Vonk, P. and Kraaijeveld, G., 1995, Exploring the Maxwell-Stefan description of ion exchange, Chemical Engineering Journal, 57, 75-89.

White, L.R., 1982, Capillary rise in powders, Journal of Colloid and Interface Science, 90, 2, 536-538.

Chapter 5
Modelling binder segregation during spray drying of slurries

ABSTRACT

A model is presented that describes binder segregation during shrinkage in a spray drying process of particulate slurries. A binary liquid of water and binder is transported through the pores of a compressible solid crust. The capillary pressure in the pores at the surface controls the shrinkage of the crust. The deformation behaviour and the permeability properties of the cake are included. The transport of binder in water is described with diffusion.

The influence of spray drying conditions and material properties on the segregation of the binder are studied numerically and a comparison is made with literature. The model indicates the importance of the diffusion coefficient of the binder on the amount of segregation. However, the amount of shrinkage of the droplet is controlled by the cake compression parameters.

5.1 Introduction

Spray drying is a widely used process to produce powders with specific properties such as particle size, density and water content. Particulate materials can be spray dried to obtain (composite) granules. Often a binder is added to the slurry feed, which prevents disintegration, increases strength or supplies properties needed for further processing.

During spray drying the binder can be transported with water to the surface and form an enriched shell. Such a shell results in higher breakage strength and larger attrition resistance of catalysts (Jothimurugesan, 2000; Pham, 2000; and Bergna, 1989).

Baklouti *et al.* measured the distribution of polyvinyl alcohol (PVA) binder during spray drying of alumina (Baklouti, 1998). Pictures of granules were taken with an optical microscope and the binder was visualised with pyrolysis. A heuristic model estimated the shell thickness and the amount of binder in the shell. The model under-predicted the measured shell thickness. For a higher initial water content the amount of binder in the shell increased, up to 70 % of the initial binder content.

Zhang *et al.* developed a model for spray drying flocculated slurries with binder (Zhang, 1998). The binder transport has been described with a diffusion and convection model, in which the solid particles are evenly distributed during drying. The model has been validated with spray drying alumina with PVA as binder material. The binder distribution is measured with a liquid immersion technique combined with a laser microscope. The model and experimental results agree. The binder concentration in the centre is constant and is increased in a region of $5 \cdot 10^{-6}$ and $9 \cdot 10^{-6}$ m from the surface (49 and 66 vol.% of the granules). The segregation increases with increasing initial binder concentration and with increasing granule size.

Mandanas *et al.* used thermo-gravimetric analysis to evaluate micro structural development and PVA binder distribution during drying of alumina (Mandanas, 2000). Binder segregation is only found for the suspension with low initial solids and high PVA concentration. They propose that PVA forms a network at the surface that stops shrinkage. Higher initial water concentrations result in a longer constant rate period and more evaporation of water before the PVA network stops the shrinkage. At higher initial solids concentrations, the solids form a network through which the binder must diffuse,

which slows down the distribution. Drying of a suspension with an emulsion of relative large particle size results in a constant distribution. This is attributed to transport resistance due to the large size of the emulsion droplets.

Minoshima *et al.* proposed a spray drying granulation model for a hollow granule (Minoshima, 2001). The granule strength is calculated from the thickness of the formed shell. The solid particles have no motion and concentrate at the surface when water evaporates. The surface tension draws the particles under the surface and the granule becomes solid or hollow, depending on the properties of the shell. The transport in the incompressible shell is modelled as a filtration process using Darcy's law.

Meerdink *et al.* measured and modelled the segregation of sucrose in an aqueous solution of sodium caseinate and sucrose. The model has been used to predict segregation in spray drying (Meerdink, 1995). The model is based on the Maxwell-Stefan multi-component diffusion equations. It is found that segregation takes place mainly in the first stage of the drying process. The model predicts less segregation for spray drying compared to layer drying. The amount of segregation is less for lower initial water content, which is explained with the concentration dependent diffusion coefficient.

The models reported in literature either describe binder segregation without concentration gradients for the solid material (Zhang, 1998) or describe the transport of solid material with a diffusion process (Meerdink, 1995). The aim is to develop a model to describe binder segregation for spray drying particulate particles. The diffusive transport of binder in the liquid is combined with a cake compression model for the solid material. The influence of material properties and spray drying conditions on the segregation of binder and development of the solid structure is studied. The model is based on the cake compression model proposed in chapter 4 and is extended with diffusive transport of the binder in the binary liquid. An essential difference is the absence of a Brownian motion region. The model is restricted to the shrinking period.

After description of the material and the assumptions, the mass transfer equations are derived and coupled to the conservation equation for the solid material. The transport equations are rewritten to solid material basis to prevent moving of the surface through the space-grid during shrinkage (Van der Lijn, 1976). Although in a spray drying process

temperature gradients in the droplets are usually negligible, the heat transport equation is incorporated, because it simplified the numerical programming.

5.2 Theory

5.2.1 Material description

The material to be dried consists of water with suspended particulates (solid particles) and binder particles. Because the model is limited to the shrinking period, there is no gas phase present and the material is described with a two fluid phase model. The solid phase consists of solid particles with a diameter of about a micrometer. The liquid phase is a binary mixture of water and binder particles. The binder particles are considered as the liquid phase because the particles are so small (diameter $\approx 10^{-8}$ m) that they are transported with water. The solid particles form a porous network, a cake or crust, which compacts during drying. Therefore, the solid phase is also referred to as a cake, which is saturated with the binary liquid. For fluid catalytic cracking (FCC) catalysts, the binder material is often included in the matrix, and the zeolite is considered separately. Here the cake includes the zeolite and parts of the matrix, and the binder is considered separately. A schematic representation of a droplet is given in figure 5.1.

The volume fractions ϕ are given by:

$$\phi_w + \phi_b + \phi_s = \phi_l + \phi_s = 1 \tag{5.1}$$

in which ϕ_w is the volume fraction water, ϕ_b the volume fraction binder, ϕ_s the volume fraction cake and ϕ_l the volume fraction liquid.

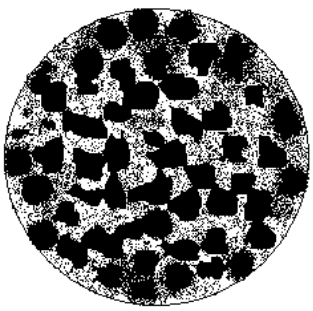

Figure 5.1. Schematic representation of droplet containing large solid particles and small binder particles.

5.2.2 Spray dried granule properties

The definition of the properties of spray dried granules is also somewhat different. The porosity of a granule equals the volume fraction of voids after spray drying. Therefore the porosity is assumed equal to the volume fraction water at the moment shrinkage stops. The solidosity is defined as the sum of the volume fractions of cake and binder.

The volume fractions of the cake ϕ_s and binder ϕ_b have both a maximum value of 0.64, based on the total volume and the liquid volume respectively. This is the maximum packing fraction for a randomly packed bed of uniform spheres (Cumberland, 1987).

5.2.3 Model description

The model combines two transport processes: 1) the transport of the binary liquid in the pores of the cake and 2) the diffusion of binder in the liquid. The model is limited to the shrinking period because the presence of a gas phase in the material complicates both the mechanical behaviour of the matrix and the transport mechanisms. The transport of the binary liquid is described with Darcy' law. The binder particles in the liquid move according to Brownian motion and the diffusion coefficient is described with the Stokes-Einstein equation. During evaporation, pores are formed at the surface of the cake. The meniscus of the liquid results in a capillary pressure that compresses the cake (solids pressure). The pressure is transferred into the cake and results in a gradient that transports the liquid to the surface. The compressive behaviour is described with a constitutive equation. The shrinkage is assumed to stop when the maximum capillary pressure balances the solids compressive pressure. In addition, shrinkage is assumed to stop if either of the volume fractions of the solids (cake) or binder reaches the maximum value at the surface.

At that moment, a substantial amount of water might be present and various scenarios for further drying are possible. If the droplet stops shrinking, the pores could be emptied and a hollow granule results. The crust could also break or a crack may arise in the surface, allowing a gas phase to enter. Boiling phenomena inside the liquid could occur when the particle temperature increases. The pressure of the gas can inflate or disintegrate the particle. Shrinkage could also continue, and the granules may end up with a shrivelled-, doughnut- or pear-shape (e.g. Walton, 2000). These deformations

depend at least for a certain amount on the rheological behaviour of the crust with the binder and the developing strains and stresses during further drying.

5.2.4 Assumptions

- The air is ideally mixed in the spray dryer.
- The influence of the momentum transfer between droplet and air is neglected.
- The Fourier law for heat flux holds and heat sources (e.g. chemical reactions) are neglected.
- The droplet remains spherical and shrinks ideally: there is no gas phase present.
- The water and binder mixture behaves like an incompressible, isotropic Newtonian liquid.
- The influence of binder volume fraction on the viscosity of the liquid can be described with an effective viscosity.
- Gravitational and acceleration forces in the momentum balance are neglected.
- The solid particles initially have contact.
- The compression of the cake is instantaneously followed by a change in pressure (there are no time effects).
- The particulate particles are inert and have a certain diameter and density. For composite materials, the effective diameter and density can be used.
- There is a no-slip condition at the interface between the cake and the liquid.
- The thermodynamic interaction between binder particles and water is ideal: the thermodynamic parameter matrix equals the unity matrix.

5.2.5 Mass transport equations

5.2.5.1 Momentum balance for the liquid phase

The mass transport equations are derived from a species momentum balance for a binary mixture in an inert pore, analogous to the derivation of the velocity profile model (Kerkhof, 2001). The velocity profile model shows the importance of the radial distribution of the pore velocities and a diffusion-averaging factor g'_D is introduced. This factor is the ratio between the averaged velocity difference and difference in averaged velocities. In the momentum balance, the driving force is balanced by the friction

between the components in the liquid and between the component and the pore wall (i.e. the cake wall).

For an isotherm, binary liquid in an inert, straight pore the momentum balance for component *i* is given by:

$$c'_i\left(\frac{d\mu_i}{dz}\right)_T = -c'_t\,RTg'_D\,\frac{x'_i\,x'_j}{Đ_{ij}}(\overline{u}_i-\overline{u}_j)-c'_t\,RT\beta_{is}(\overline{u}_i-u_s) \tag{5.2}$$

in which c_i is the concentration of species i, μ the chemical potential, c_t the total concentration, z is the axial co-ordinate of the straight pore, R the gas constant, T the temperature, x_i the mol fraction and $Đ_{ij}$ the binary diffusion coefficient. $\overline{u}_i$ is the velocity of species i, averaged over the cross-section of the pore. β_{is} is the wall-friction factor. The prime, ', indicates that parameters are based on the liquid volume. The velocity of the wall, u_s, is introduced because the cake moves as the droplet shrinks. The wall friction factor, β_{is}, is defined in accordance with the binary friction model (Kerkhof, 2001):

$$\beta_{is} = \frac{\phi'_i\,\kappa_i}{B_\circ} = \frac{\eta'_i}{c'_t\,RTB_\circ} \tag{5.3}$$

in which κ_i is the frictional viscosity coefficient of species i, $B_\circ$ the permeability, and η'_i are the partial viscosities of species i.

For an ideal liquid mixture, the thermodynamic parameter is one and the left-hand side of equation 5.2 is given by:

$$c'_i\left(\frac{d\mu_i}{dz}\right)_T = c'_i\left(\frac{d\mu_i}{dz}\right)_{TP} + \phi'_i\left(\frac{dP_l}{dz}\right)_T = c'_t\,RT\left(\frac{dx'_i}{dz}\right)_{TP} + \phi'_i\left(\frac{dP_l}{dz}\right)_T \tag{5.4}$$

in which P_l is the liquid pressure.

The combination of equations 5.2 and 5.4 results in the basic momentum balance equations. The balance for water is:

$$c'_t\,RT\left(\frac{dx'_w}{dz}\right)_{TP} + \phi'_w\left(\frac{dP_l}{dz}\right)_T = -c'_t\,RTg'_D\,\frac{x'_w\,x'_b}{Đ_{wb}}\left(\overline{u}_w-\overline{u}_b\right)-\frac{\eta'_w}{B_\circ}\left(\overline{u}_w-u_s\right) \tag{5.5}$$

and for binder:

$$c'_t\,RT\left(\frac{dx'_b}{dz}\right)_{TP} + \phi'_b\left(\frac{dP_l}{dz}\right)_T = -c'_t\,RTg'_D\,\frac{x'_w\,x'_b}{Đ_{wb}}\left(\overline{u}_b-\overline{u}_w\right)-\frac{\eta'_b}{B_\circ}\left(\overline{u}_b-u_s\right) \tag{5.6}$$

In these equations, the velocities are based the axial direction of the straight pore. However, pores are tortuous and the equations are rewritten to a new co-ordinate, *r*, and (superficial) velocity, *v*. The tortuosity, τ, is defined as the ratio of the average length of a tortuous pore, *z*, to the length of the matrix along the major flow or diffusion axis, *r* (Epstein, 1989):

$$dr = \frac{dz}{\tau} \tag{5.7}$$

The superficial velocity is related to the pore velocity by:

$$v_i = \frac{\tau \overline{u}_i}{\phi_l} \tag{5.8}$$

The equation are then given by:

$$c'_t RT\left(\frac{dx'_w}{dr}\right)_{TP} + \phi'_w\left(\frac{dP_l}{dr}\right)_T = -c'_t RTg'_D \frac{x'_w x'_b \tau^2}{\mathcal{D}_{wb}\phi_l}\left(v_w - v_b\right) - \frac{\eta'_w \tau^2}{B_o \phi_l}\left(v_w - v_s\right) \tag{5.9}$$

and:

$$c'_t RT\left(\frac{dx'_b}{dr}\right)_{TP} + \phi'_b\left(\frac{dP_l}{dr}\right)_T = -c'_t RTg'_D \frac{x'_w x'_b \tau^2}{\mathcal{D}_{wb}\phi_l}\left(v_b - v_w\right) - \frac{\eta'_b \tau^2}{B_o \phi_l}\left(v_b - v_s\right) \tag{5.10}$$

In appendix E, the consistency of these equations with Fick's and Darcy's law in the limit situations is illustrated.

5.2.5.2 Coupling equation for the matrix

A force balance over a part of the matrix, neglecting inertial and acceleration forces, is given by:

$$\left(\frac{\partial P_l}{\partial r}\right) + \left(\frac{\partial P_s}{\partial r}\right) = 0 \tag{5.11}$$

in which P_s is the solids or compressive pressure. For an instantaneous deformation of the cake, there is an equilibrium between the volume fraction and the pressure of the solid phase, which is given by a constitutive equation (Shirato, 1970; and Leu, 1986). For now, a function γ is defined that relates the pressure gradient to the volume fraction gradient:

$$\frac{dP_s}{dr} = \frac{dP_s}{d\phi_s}\frac{d\phi_s}{dr} = \gamma \frac{d\phi_s}{dr} \tag{5.12}$$

The capillary pressure at the surface of the cake originates from the curvature of the meniscus at the gas-liquid interface in the pores. The maximum capillary pressure, P_c^{max}, is related to the cake particle size, r_s, and cake volume fraction by (White, 1986):

$$P_c^{\max} = -\frac{3\sigma_{LV}\cos(\vartheta)}{r_s}\frac{\phi_s}{(1-\phi_s)} \tag{5.13}$$

in which σ_{LV} is the liquid-vapour surface tension and ϑ the contact angle. During drying it is assumed that the solid particles remain covered with a liquid film, thus the contact angle equals zero.

When water evaporates, the curvature of the meniscus increases, and with it the capillary pressure. The change is assumed to be followed instantaneously by that in the volume fraction cake, which is compacted. The compaction continues until the maximum capillary pressure balances the compressive pressure. The actual compressive pressure at the surface is determined by the volume fraction of the cake and the constitutive equation and will determine the curvature of the meniscus at the interface in the pore.

Addition of equations 5.9 and 5.10 couples the equations to the cake:

$$\left(\frac{dP_l}{dr}\right)_T = -\gamma\left(\frac{d\phi_s}{dr}\right)_T = -\frac{c'_t RT\tau^2}{\phi_l}\left[\frac{\eta'_w}{B_\circ}(v_w - v_s) + \frac{\eta'_b}{B_\circ}(v_b - v_s)\right] \tag{5.14}$$

5.2.5.3 Flux equations

The concentrations in the pore volume are rewritten to the total volume using:

$$c'_i = c_i / \phi_l \tag{5.15}$$

and

$$c'_t = (c_w + c_b)/\phi_l \tag{5.16}$$

Rewriting equations 5.9 and 5.14 results in the two final equations that describe the mass transport of water and binder:

$$\begin{aligned}&\left(\frac{c_b RT}{(c_w+c_b)} + c_w\overline{V}_w^2\gamma\right)\left(\frac{dc_w}{dr}\right)_T + \left(\frac{c_w RT}{(c_w+c_b)} + c_w\overline{V}_w\overline{V}_b\gamma\right)\left(\frac{dc_b}{dr}\right)_T = \\ &-\left(\frac{c_b g'_D RT\tau^2}{(c_w+c_b)\mathcal{D}_{wb}\phi_l} + \frac{\eta'_w\tau^2}{c_w B_\circ}\left(1+\frac{\phi_w}{\phi_s}\right)\right)J_w^v - \left(-\frac{c_w g'_D RT\tau^2}{(c_w+c_b)\mathcal{D}_{wb}\phi_l} + \frac{\eta'_w\phi_b\tau^2}{c_b B_\circ\phi_s}\right)J_b^v\end{aligned} \tag{5.17}$$

and

$$\gamma\overline{V}_w\left(\frac{dc_w}{dr}\right)_T+\gamma\overline{V}_b\left(\frac{dc_b}{dr}\right)_T= \\ -\left(\frac{\tau^2}{c_wB_\circ\phi_l}\left(\eta'_w\left(1+\frac{\phi_w}{\phi_s}\right)+\frac{\eta'_b\,\phi_w}{\phi_s}\right)\right)J_w^v-\left(\frac{\tau^2}{c_bB_\circ\phi_l}\left(\frac{\eta'_w\,\phi_b}{\phi_s}+\eta'_b\left(1+\frac{\phi_b}{\phi_s}\right)\right)\right)J_b^v \tag{5.18}$$

in which $\overline{V}_i$ is the molar volume of species *i*, and J_i^v is the flux of species *i* with respect to the volume average velocity v^v.

These equations can be expressed in matrix formulation as:

$$\left(J^v\right)=-[B]^{-1}[P]\left(\frac{dc}{dr}\right)=-[E]\left(\frac{dc}{dr}\right) \tag{5.19}$$

The elements of *[P]* are:

$$P_{ww}=\frac{c_bRT}{(c_w+c_b)}+c_w\overline{V}_w^2\gamma \tag{5.20}$$

$$P_{wb}=\frac{c_wRT}{(c_w+c_b)}+c_w\overline{V}_w\overline{V}_b\gamma \tag{5.21}$$

$$P_{bw}=\gamma\overline{V}_w \tag{5.22}$$

$$P_{bb}=\gamma\overline{V}_b \tag{5.23}$$

The elements of *[B]* are:

$$B_{ww}=\frac{c_bg'_DRT\tau^2}{(c_w+c_b)Đ_{wb}\phi_l}+\frac{\eta'_w\,\tau^2}{c_wB_\circ}\left(1+\frac{\phi_w}{\phi_s}\right) \tag{5.24}$$

$$B_{wb}=-\frac{c_wg'_DRT\tau^2}{(c_w+c_b)Đ_{wb}\phi_l}+\frac{\eta'_w\,\phi_b\tau^2}{c_bB_\circ\phi_s} \tag{5.25}$$

$$B_{bw}=\frac{\tau^2}{c_wB_\circ\phi_l}\left(\eta'_w\left(1+\frac{\phi_w}{\phi_s}\right)+\frac{\eta'_b\,\phi_w}{\phi_s}\right) \tag{5.26}$$

$$B_{bb}=\frac{\tau^2}{c_bB_\circ\phi_l}\left(\frac{\eta'_w\,\phi_b}{\phi_s}+\eta'_b\left(1+\frac{\phi_b}{\phi_s}\right)\right) \tag{5.27}$$

5.2.5.4 Parameters

The diffusion coefficient of the binder in the liquid is calculated with the Stokes-Einstein diffusion coefficient, $Đ_{wb}$:

$$Đ_{wb} = \frac{k_B T}{6\pi\eta'_l r_b} \tag{5.28}$$

in which k_B is the Boltzmann constant, and r_b the radius of the binder particles.

The effective viscosity of the liquid in the pore, η'_l, increases with the volume fraction binder and is described with the Krieger-Dougherty equation (Krieger, 1972):

$$\eta'_l = \eta'_w \left(1 - \frac{\phi'_b}{\phi'^{\max}_b}\right)^{-[\eta]\phi'^{\max}_b} \tag{5.29}$$

in which η'_w is the viscosity of pure water and $[\eta]$ the intrinsic viscosity, which has a value of 2.5. The partial viscosities are calculated from the liquid viscosity and the fractional viscosity coefficients (Kerkhof, 1996):

$$\eta'_l = \eta'_w + \eta'_b = c'_t RT\left(\kappa_w \phi'_w + \kappa_b \phi'_b\right) \tag{5.30}$$

The viscosities are given as function of binder volume fraction in the liquid in figure 5.2.

The tortuosity factor, τ^2, is taken a function of the volume fraction liquid (Wesselingh, 1995; Marshall, 1957):

$$\tau^2 = \phi_l^{-1.5} \tag{5.31}$$

The effective liquid viscosity accounts for the influence of the vicinity of binder particles on the diffusion coefficient. The diffusion coefficient also depends on the volume fraction liquid, which becomes clear if the diffusion coefficient is written as an effective diffusion coefficient:

$$Đ_{wb,eff} = \frac{Đ_{wb}\phi_l}{\tau^2} = Đ_{wb}\phi_l^{2.5} = Đ_{wb}(1-\phi_s)^{2.5} \tag{5.32}$$

The diffusion-averaging factor, g'_D, is defined as (Kerkhof, 2001):

$$g'_D = \frac{1}{h} - \varphi \tag{5.33}$$

with

$$\varphi = \frac{Đ_{wb}}{c'_t RT x'_w x'_b} \frac{\eta'_w \eta'_b}{\eta'_l B_\circ} \tag{5.34}$$

and

$$h = 1 - \frac{2}{\omega R} \frac{I_1(\omega R)}{I_\circ(\omega R)} \tag{5.35}$$

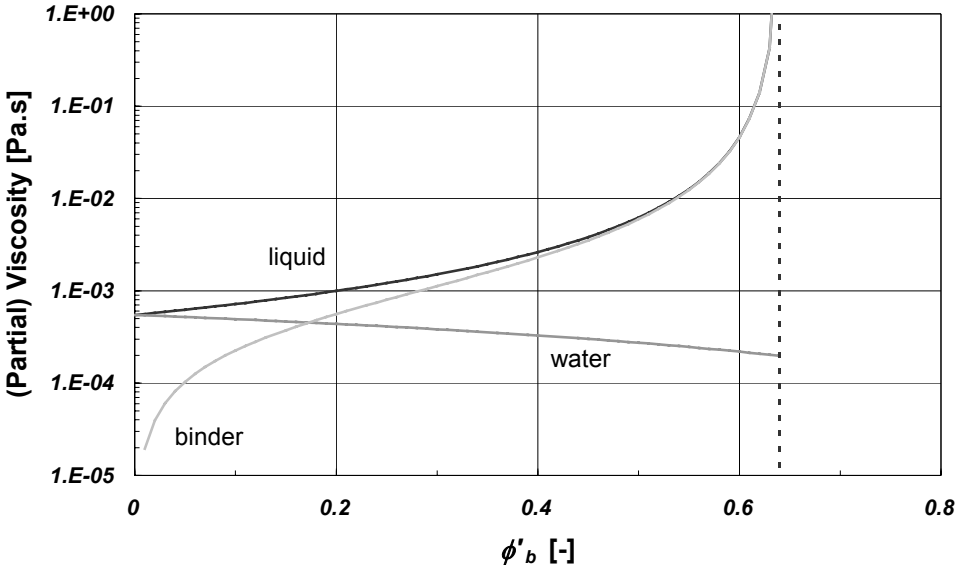

Figure 5.2. Liquid viscosity and partial viscosities of water and binder as function of volume fraction binder in the liquid.

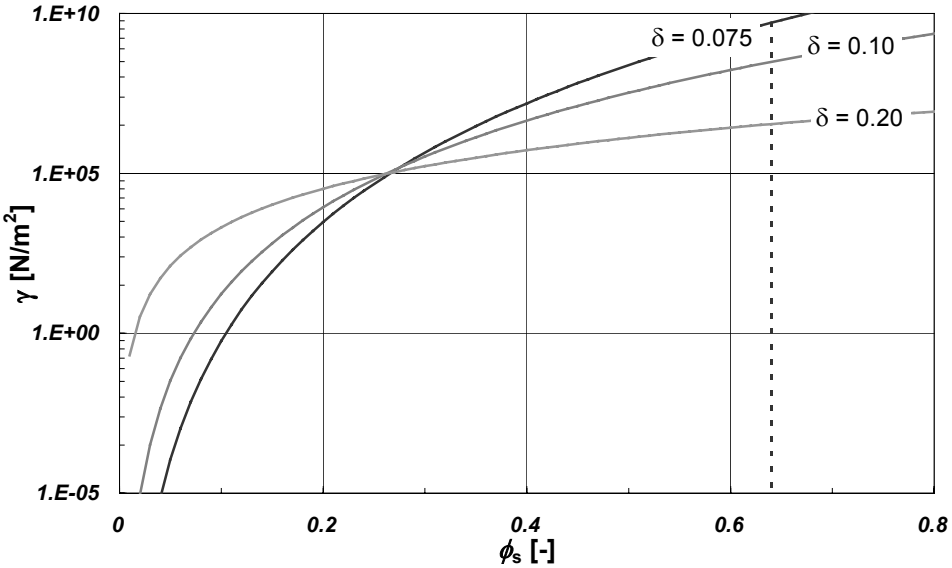

Figure 5.3. Function γ as function of volume fraction matrix for three different compressibility indices.

For circular capillaries the root ωR is given by:

$$\omega R = \sqrt{\frac{8}{\varphi}} \tag{5.36}$$

and I_i are modified Bessel functions of the first kind of the i^{th} order.

A constitutive equation that applies well for different materials is given by (see e.g. Shirato, 1970; Leu, 1986; and Tiller, 1998;):

$$\phi_s = \phi_{s0}\left(1 + \frac{P_s}{P_a}\right)^{\delta} \tag{5.37}$$

The function γ of equation 5.12 is then given by:

$$\gamma = \frac{dP_s}{d\phi_s} = \frac{P_a}{\delta\phi_{s0}}\left(\frac{\phi_s}{\phi_{s0}}\right)^{\frac{1-\delta}{\delta}} \tag{5.38}$$

In figure 5.3 values of the function γ are given as function of the volume fraction solids for different compressibility indices. The null-stress volume fraction solids, ϕ_{s0}, represents the matrix volume fraction at which the solids pressure equals zero. In the model the null-stress volume fraction solids is not related to the initial water content.

The permeability is defined by equation 5.6 and equals:

$$B_0 \equiv \frac{r_h^2}{8} \tag{5.39}$$

in which r_h is the hydraulic radius of the pores in the cake.

The hydraulic radius of the pores depends on the cake particle size and volume fraction, and is taken equal to the hydraulic radius for a packed bed of uniform sizes spheres:

$$r_h = \frac{2r_s(1-\phi_s)}{3\phi_s} \tag{5.40}$$

The thermal conductivity of the two-phase fluid, λ, is a mass averaged value.

5.2.6 Mathematical framework

Because the air is ideally mixed, a droplet experiences identical air conditions during the drying process: the boundary conditions for heat and mass transport through the film layer are constant. The heat and mass transfer coefficients for the film layer are calculated

with average film conditions and Nu = Sh = 2, which is accurate for small droplets (Wijlhuizen, 1979). The model is described with the continuity equations for energy, water and binder.

The transformed space co-ordinate, σ, is defined as:

$$\sigma = \int_{0}^{r} \phi_s r^2 dr \tag{5.41}$$

The transformed concentrations, u_i, are defined as:

$$u_w = \frac{c_w}{\phi_s} \tag{5.42}$$

and

$$u_b = \frac{c_b}{\phi_s} \tag{5.43}$$

The solid phase volume fraction is related to the transformed concentrations by:

$$\phi_s = \frac{1}{1 + u_w \overline{V}_w + u_b \overline{V}_b} \tag{5.44}$$

The volume average velocity equals:

$$v^v = \phi_w v_w + \phi_b v_b + \phi_s v_s = 0 \tag{5.45}$$

5.2.6.1. Continuity equations

The transformed continuity equation for water reads:

$$\left(\frac{\partial u_w}{\partial t}\right)_\sigma = -\left(\frac{\partial}{\partial \sigma} r^2 J_w^s\right)_t \tag{5.46}$$

in which, J_w^s, is flux of water with respect to the solids velocity in transformed co-ordinates.

The equation for the binder is given by:

$$\left(\frac{\partial u_b}{\partial t}\right)_\sigma = -\left(\frac{\partial}{\partial \sigma} r^2 J_b^s\right)_t \tag{5.47}$$

The transformed energy conservation balance is:

$$C_{pw} T\left(\frac{\partial u_w}{\partial t}\right)_\sigma + C_{pb} T\left(\frac{\partial u_b}{\partial t}\right)_\sigma + \left(u_w C_{pw} + u_b C_{pb} + \frac{C_{ps}}{\overline{V}_s}\right)\left(\frac{\partial T}{\partial t}\right)_\sigma = -\left(\frac{\partial}{\partial \sigma} r^2 q^s\right) \tag{5.48}$$

in which C_{pi} is the heat capacity of species i and q^s the heat flux with respect to the solids velocity.

5.2.6.2 Transformed flux equations

The flux of water with respect to the solids velocity in transformed co-ordinates is:

$$J_w^s = -A\left(\frac{\partial u_w}{\partial \sigma}\right)_t - B\left(\frac{\partial u_b}{\partial \sigma}\right)_t \tag{5.49}$$

The flux of binder with respect to the solids velocity is:

$$J_b^s = -C\left(\frac{\partial u_w}{\partial \sigma}\right)_t - D\left(\frac{\partial u_b}{\partial \sigma}\right)_t \tag{5.50}$$

The heat flux is given by:

$$q^s = J_w^s C_{pw} T + J_b^s C_{pb} T - r^2 \phi_s \lambda \left(\frac{\partial T}{\partial \sigma}\right)_t \tag{5.51}$$

In which:

$$A = r^2 c_s \overline{V}_s \left(\left(1 - c_b \overline{V}_b\right)\left(\left(1 - c_w \overline{V}_w\right)E_{ww} - c_b \overline{V}_w E_{wb}\right) + c_w \overline{V}_b \left(\left(1 - c_w \overline{V}_w\right)E_{bw} - c_b \overline{V}_w E_{bb}\right)\right) \tag{5.52}$$

$$B = r^2 c_s \overline{V}_s \left(-\left(1 - c_b \overline{V}_b\right)\left(c_w \overline{V}_b E_{ww} - \left(1 - c_b \overline{V}_b\right)E_{wb}\right) - c_w \overline{V}_b \left(c_w \overline{V}_b E_{bw} - \left(1 - c_b \overline{V}_b\right)E_{bb}\right)\right) \tag{5.53}$$

$$C = r^2 c_s \overline{V}_s \left(c_b \overline{V}_w \left(\left(1 - c_w \overline{V}_w\right)E_{ww} - c_b \overline{V}_w E_{wb}\right) + \left(1 - c_w \overline{V}_w\right)\left(\left(1 - c_w \overline{V}_w\right)E_{bw} - c_b \overline{V}_w E_{bb}\right)\right) \tag{5.54}$$

$$D = r^2 c_s \overline{V}_s \left(-c_b \overline{V}_w \left(c_w \overline{V}_b E_{ww} - \left(1 - c_b \overline{V}_b\right)E_{wb}\right) - \left(1 - c_w \overline{V}_w\right)\left(c_w \overline{V}_b E_{bw} - \left(1 - c_b \overline{V}_b\right)E_{bb}\right)\right) \tag{5.55}$$

The elements of *[E]* are defined in equation 5.19.

5.2.6.3 Initial and boundary conditions

The initial conditions in transformed co-ordinates are:

$$t = 0 \quad 0 \le \sigma' = \frac{\sigma}{\sigma_0} \le 1 \qquad u_w = u_{w0} \quad u_b = u_{b0} \quad T = T_0 \tag{5.56}$$

The boundary conditions at the centre of the droplet read:

$$\begin{aligned} t > 0 \quad \sigma' = 0 \qquad & \frac{\partial u_w}{\partial \sigma} = 0 \quad \frac{\partial u_b}{\partial \sigma} = 0 \quad \frac{\partial T}{\partial \sigma} = 0 \\ \textit{or} \quad & J_w^s = 0 \quad J_b^s = 0 \quad q^s = 0 \end{aligned} \tag{5.57}$$

In the film near the surface the water vapour transport is described with Stefan-diffusion, and the film properties are averaged with bulk and surface properties. At the surface the boundary conditions are given by (e.g. Kerkhof and Schoeber, 1974; Krischer, 1978):

$$\begin{aligned} &t > 0 \quad \sigma' = 1 \\ &J_w^s = k_f \rho_f \ln\left(\frac{1+H_i}{1+H_\infty}\right) \\ &J_b^s = 0 \\ &q^s = \alpha_f (T_\infty - T) - k_f \rho_f \ln\left(\frac{1+H_i}{1+H_\infty}\right)\left((C_{pv} - C_{pw})T + \Delta H_o\right) \end{aligned} \tag{5.58}$$

in which α_f is the heat transfer coefficient, k_f is the mass transfer coefficient, H the humidity and ΔH_o the heat of evaporation.

5.2.7 Segregation

The segregation is described with a segregation factor (SF). The SF is defined as the volume fraction of the binder that is present in certain volume fraction of the particle at the end of the shrinkage period. The SF50 is defined as the binder fraction in the *outer* 50 volume percent of the granule. The SF10 is the binder fraction in the *outer* 10 volume percent. To determine the final granule properties it is assumed that all the residual water evaporates during further drying. In addition, the layer thickness is calculated in which the binder concentration substantially increases. The final granule properties are characterised by an average porosity and average density, which are calculated with the initial water content and the final water content (see chapter 4).

5.3 Numerical method and programming

The model has been programmed on a Borland Delphi® 5.0 platform using the D03PCF partial differential equation (PDE) solver from the numeric algorithm group (NAG, 1998). D03PCF integrates a system of linear or non-linear parabolic PDEs in one space variable. The spatial discretisation is performed using finite differences, and the method of lines is employed to reduce the PDEs to a system of ordinary differential equations. The resulting system is solved using a backward differentiation formula method. The used grid is refined towards the surface and consists of 51 points.

5.4 Results and discussion

To facilitate comparison of the results, the concentrations of the components are presented as volume fractions. The initial volume fraction is shown as a dotted line. The concentration profiles are shown every 0.2 s. In addition, the final concentration profile is shown at the time when the shrinkage period is assumed to end.

The parameters that have been varied are: the binder particle size, the matrix particle size, the cake compressibility (i.e. constitutive equation parameters), the initial water content, the initial binder content, the initial droplet diameter and the air temperature and humidity. The range of the parameters and the results are summarised in table 5.3.

5.4.1 Standard conditions and values

The standard conditions and values are summarised in table 5.1. The initial composition and spray drying conditions are comparable to the experiments with FCC catalyst (described in chapter 3). Unfortunately, the amount of segregation is not measured and the results of this work are not validated with measurements of FCC catalyst.

The temperature gradients in the droplet can be neglected (chapter 4, figure 4.10). The concentration profiles of water, binder and cake for the standard conditions and values are shown in figures 5.4 – 5.6. The development of the concentration profiles shows the effect of the two transport mechanisms. The binder concentration increases at the surface, while in the interior the volume fraction binder remains approximately constant. The concentration gradient near the surface results in counter diffusion into the droplet. However, the rate of diffusion is much smaller than the transport with the liquid to the surface. The ratio of the volume fraction binder to water in the centre of the droplet slightly increases. This is due to the higher partial viscosity of water at low concentrations, as shown in figure 5.2. At higher volume fractions binder, the lower diffusion coefficient decreases the rate of counter diffusion, resulting in increasing gradients towards the surface in time.

During shrinkage the cake compacts, the solids pressure increases and is transferred on the network throughout the droplet. Figure 5.6 shows that at the surface the cake volume fraction increases and then the pressure transfer results in an almost linear

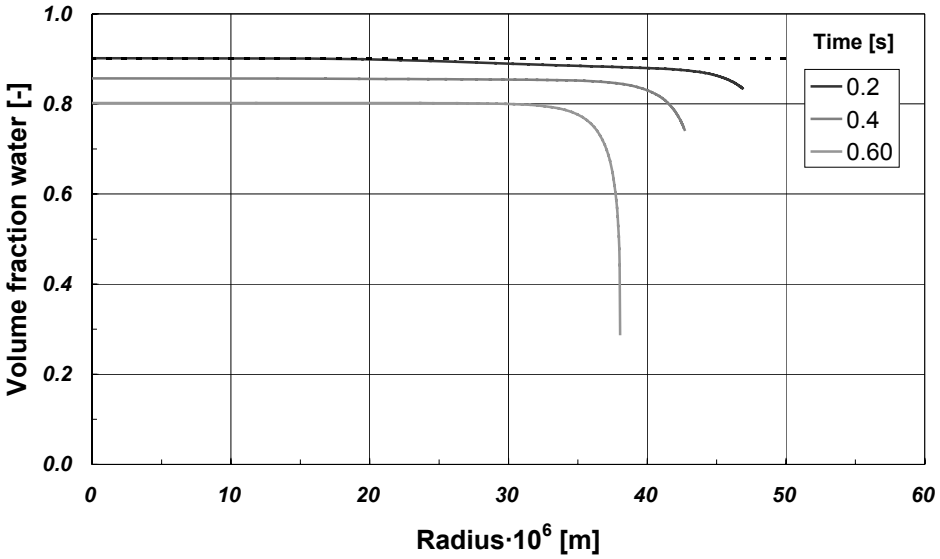

Figure 5.4. Water concentration profiles for standard values and conditions.

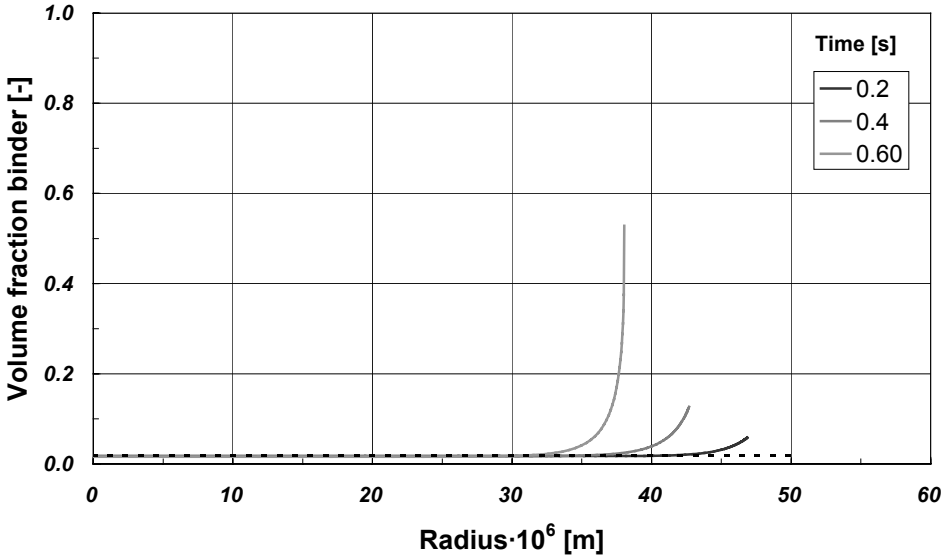

Figure 5.5. Binder concentration profiles for standard values and conditions.

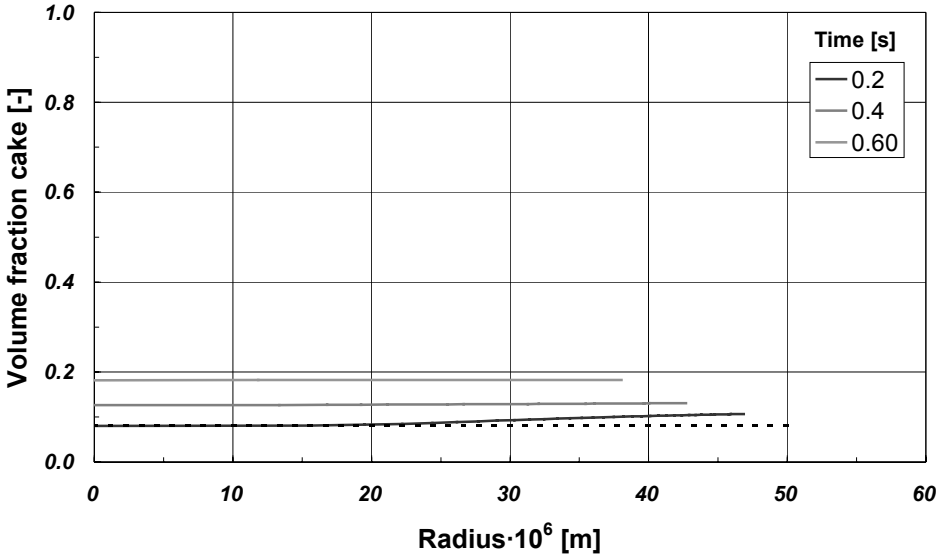

Figure 5.6. Cake concentration profiles for standard conditions and values.

decrease of the volume fraction into the interior. The flattening of the concentration profiles for higher volume fractions of the cake is illustrated by the increasing value of the function γ (see figure 5.2).

Shrinkage stops when the volume fraction binder reaches the maximum volume fraction at the surface. Then, approximately 80 vol.% of the binder is transported into the outer 50 vol.% of the granule (SF50 = 0.8) and about 44 vol.% is present in the outer 10 vol.% (SF10 = 0.44). The layer, in which the binder concentration is more than twice the initial value, has a thickness of ca. $3.5 \cdot 10^{-6}$ m.

The porosity of the dried granule is equal to 0.78 and the particle density equal to 600 kg/m^3.

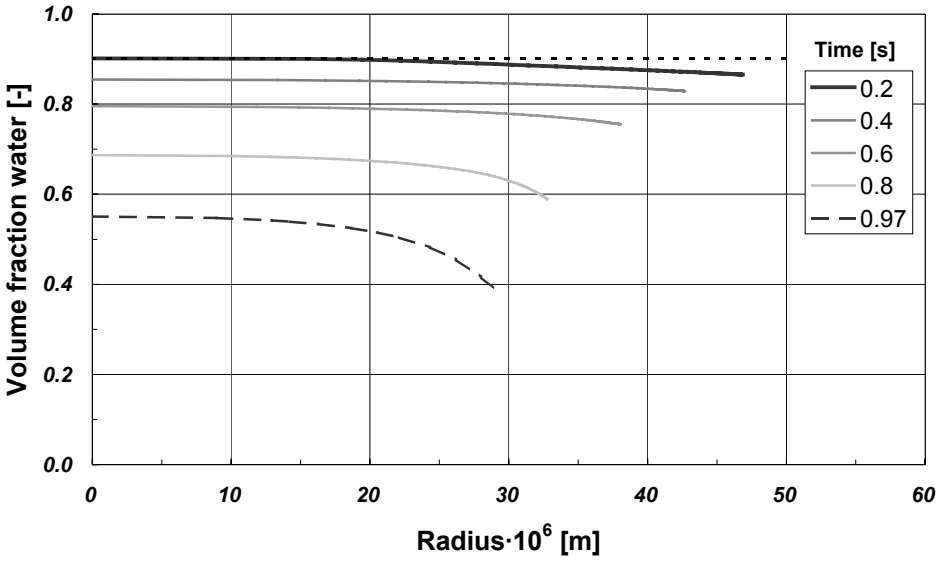

Figure 5.7. Water concentration profiles for a binder particle size of 10^{-9} m and standard values and conditions.

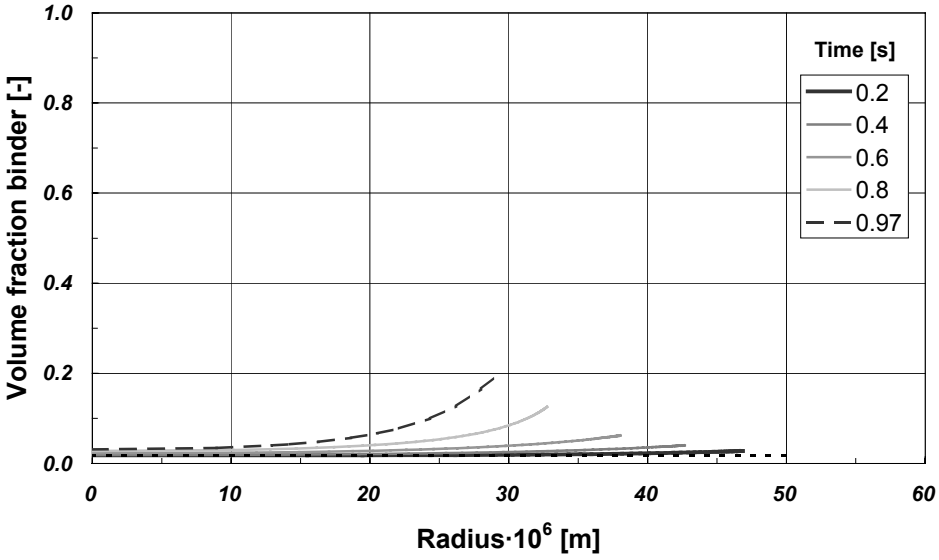

Figure 5.8. Binder concentration profiles for a binder particle size of 10^{-9} m and standard values and conditions.

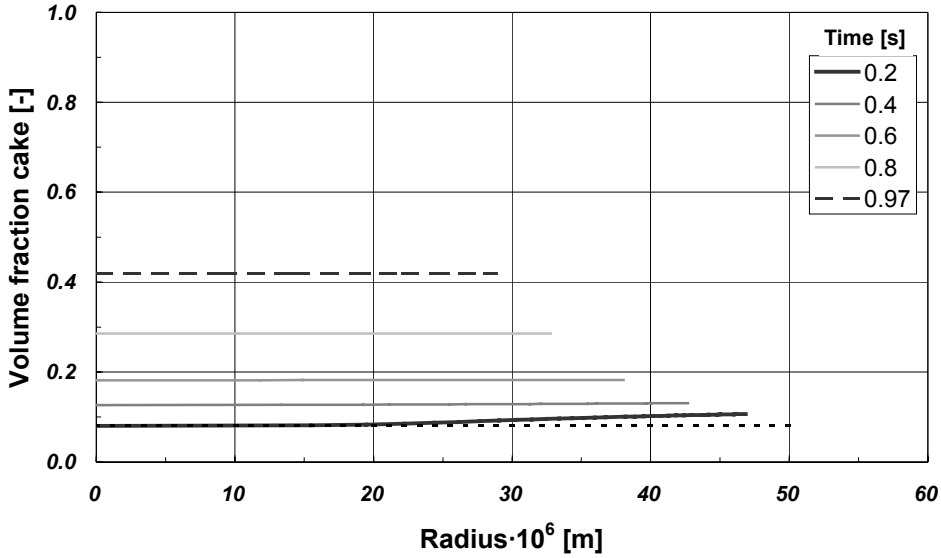

Figure 5.9. Cake concentration profiles for a binder particle size of 10^{-9} m and standard conditions and values.

Table 5.1. Standard conditions and values for the simulation parameters.

Parameter	*Value*	*Parameter*	*Value*
Air temperature	120 °C	Matrix particle diameter	10^{-6} m
Air humidity	0.060 kg_w/kg_{da}	Binder true density	2200 kg/m^3
Initial water content	4.0 kg_w/kg_s	Matrix true density	2800 kg/m^3
Initial binder content	0.175 kg_b/kg_s	Null-stress volume fraction matrix, ϕ_{so}	0.30 m_s^3/m_t^3
Droplet temperature	25 °C	Compressive modulus, P_a	10000 N/m^2
Droplet diameter	10^{-4} m	Compressibility index, δ	0.1
Binder particle diameter	10^{-8} m		

5.4.2 Effect of binder particle size

The binder particle diameter is varied between 10^{-9} – 10^{-7} m. The diffusion coefficient for the binder particles in water is inverse proportional to the particle size and varies between ca. 10^{-9} and 10^{-11} m^2/s for an infinitely diluted suspension.

A larger particle size gives a lower diffusion coefficient, which results in steeper gradients near the surface and the maximum volume fraction binder is reached in less

time (0.18 s). The development of the cake concentration profiles is equal to the standard conditions. For these conditions, the binder segregation was much less (see table 5.3).

The concentration profiles for binder particles of 10^{-9} m diameter are shown in figures 5.7 – 5.9. The higher diffusion coefficient results in less steep binder profiles. The initial development of the cake concentration profiles is not influenced by the binder particle size. After 0.97 s, the capillary pressure balances the solids pressure and shrinkage stops. The average volume fraction of the solid phase is equal to 0.42. The higher diffusivity results in less segregation, as reported in table 5.3.

In practice, many different binder materials are used. The studied range of particle diameter covers a reasonable range of diffusivities for different applied materials. However, one should bear in mind that the concentration dependency of the diffusion coefficient might be quite different.

5.4.3 Effect of cake particle size

The cake particle size influences both the permeability of the formed cake and the maximum capillary pressure. The cake particle diameter was varied between 10^{-7} – 10^{-5} m. The permeability of the cake increases with increasing particle size.

The higher permeability for a diameter of 10^{-5} m results in flat cake concentration profiles throughout the entire droplet. The binder concentration profiles are not influenced by the cake particle size. Therefore, the shrinkage time and the segregation factors are the same.

The concentration profiles for a cake particle size of 10^{-7} m are shown in figures 5.10 – 5.12. The permeability is lower and the cake concentration profiles are steeper towards the surface, while the interior remains unchanged. The water profiles show a double slope, showing the effect of the friction with the binder and the cake wall. The binder concentration profiles are also steeper near the surface. This is caused by the higher volume fraction of the cake near the surface, which decreases the effective diffusion coefficient (equation 5.32). The shrinkage stops after 0.53 s, when the binder reaches the maximum concentration. The segregation factors are smaller than for standard conditions, due to the shorter time.

In case of a matrix particle size of 10^{-7} m and a binder particle size of 10^{-9} m, the cake compacts until the maximum volume fraction of the cake at the surface is 0.64. The capillary pressure is high enough for complete solidification. The binder and cake concentration profiles are flat throughout the droplet. The initial steep gradient of the cake volume fraction flattens for higher values. The volume fraction binder does not reach the maximum value, which is due to the smaller particle size and higher diffusivity. The binder size has no noticeable effect on the (initial) development of the cake concentration profiles.

5.4.4 Effect of cake compressibility

The constitutive equation parameters determine the solids pressure as function of the volume fraction of the solid phase. In addition, the parameters determine the behaviour of the pressure transfer onto the solids network, which influences the development of the cake concentration profiles. Because the simulation with a binder particle diameter of 10^{-9} m illustrates the mechanism of cake compaction better, simulations for the cake compressibility are done with this particle diameter.

5.4.4.1 Effect of null-stress volume fraction solids

A lower null-stress volume fraction solids increases both the initial solids pressure and the value of function γ. For a null-stress volume fraction solids of 0.5, the concentration profiles were similar to those of a cake particle size of 10^{-7} m (figures 5.10 – 5.12), although the segregation factors are somewhat higher. This is caused by an increase in droplet temperature at the end of the simulation with the cake particle diameter of 10^{-7} m. The higher temperature causes the diffusion coefficient to increase and the amount of segregation becomes less.

If the null-stress volume fraction solids is 0.1, the cake concentration profiles become flat because the values of the function γ increase. The maximum capillary pressure balances the compressive pressure at a lower cake volume fraction. This results in less shrinkage than for standard conditions and values. There is no influence on the development of the binder profiles and segregation is less because of the shorter shrinkage time (0.37 s).

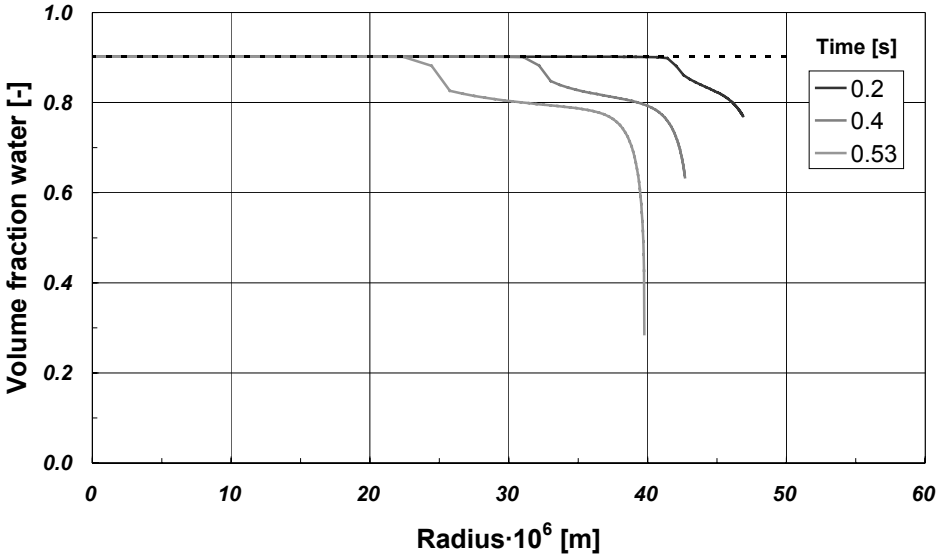

Figure 5.10. Water concentration profiles for a matrix particle size of 10^{-7} m and standard conditions and values.

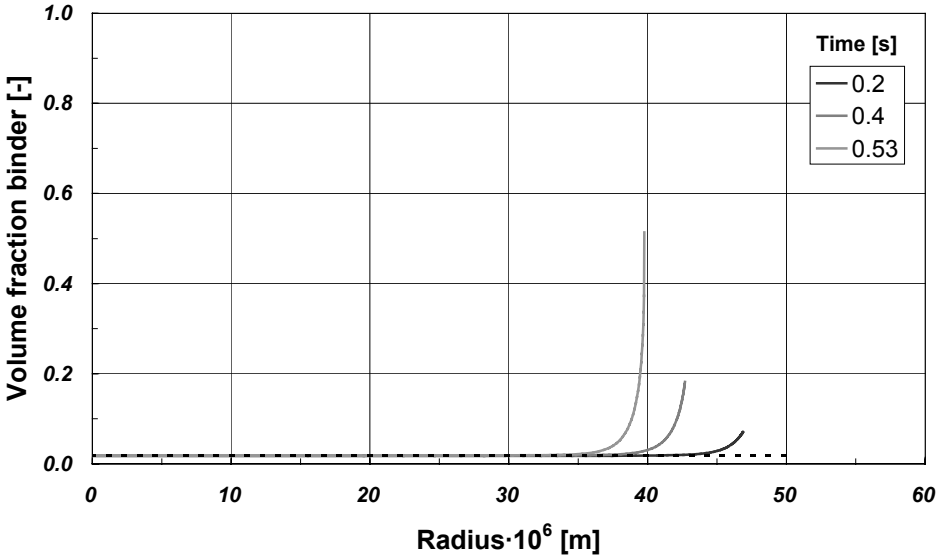

Figure 5.11. Binder concentration profiles for a matrix particle size of 10^{-7} m and standard conditions and values.

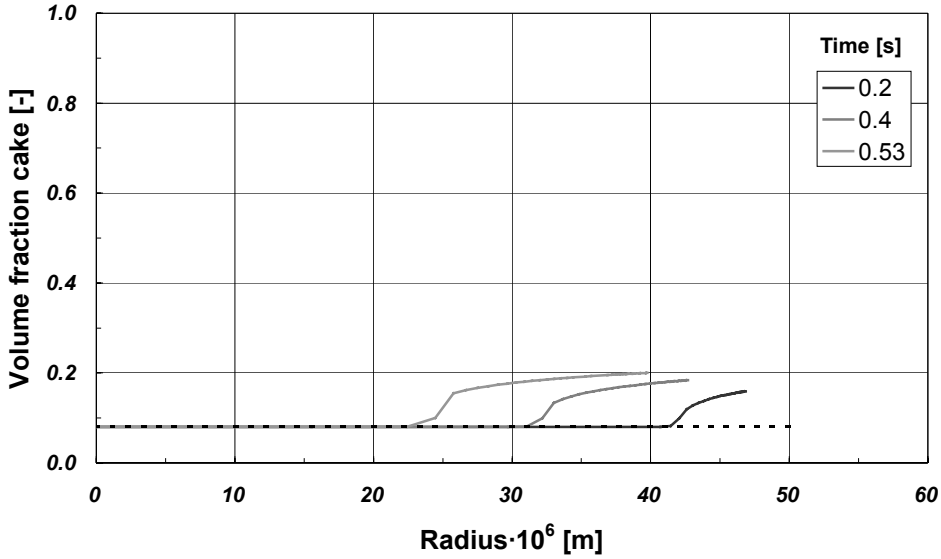

Figure 5.12. Cake concentration profiles for a matrix particle size of 10^{-7} m and standard value and conditions.

5.4.4.2 Effect of compressibility index

The influence of the compressibility index on function γ is shown in figure 5.3. For a lower compressibility index, the value of the function γ is lower for the initial volume fraction solids. Results for a compressibility index of 0.075 and a binder particle diameter of 10^{-9} m are given in figures 5.13 – 5.15. The results show initial steep cake concentration profiles, which flatten due to the increased value of γ with increasing volume fraction. The shrinkage stops when the maximum capillary pressure balances the compressive pressure. The segregation is somewhat less than for a compressibility index of 0.1, due to the equilibrium value of the compressive pressure.

For a higher compressibility index, the argumentation is reverse: the cake concentration profiles show no gradients. The binder profiles are comparable to standard conditions with a binder particle diameter of 10^{-9} m. The volume fraction binder increases until the maximum volume fraction is reached at the surface. The segregation factors are somewhat smaller, due to the shorter shrinking period.

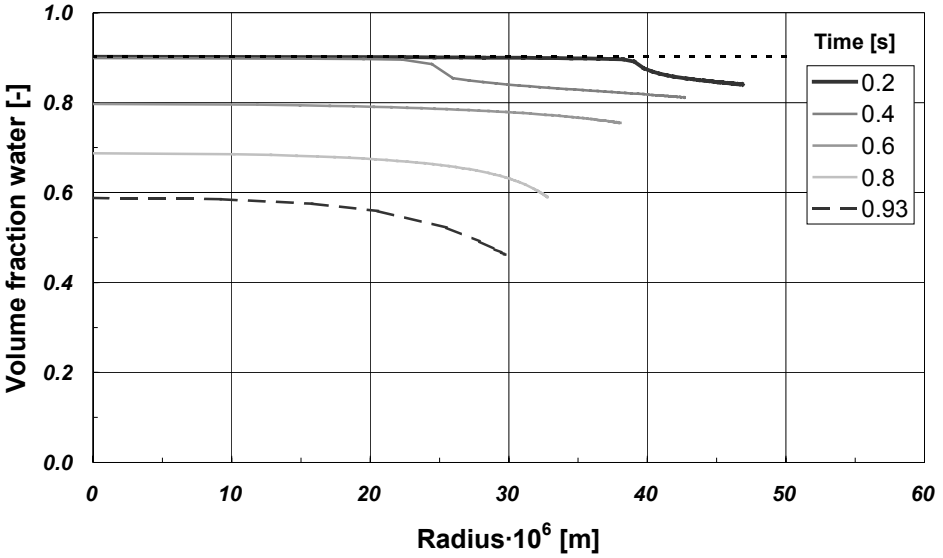

Figure 5.13. Water concentration profiles for a compressibility index of 0.075 and a binder particle size of 10^{-9} m.

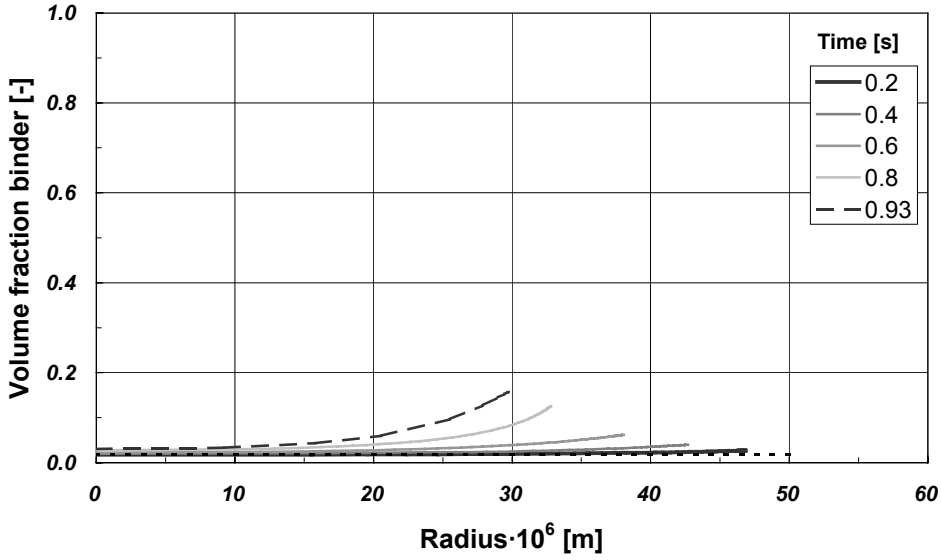

Figure 5.14. Binder concentration profiles for a compressibility index of 0.075 and a binder particle size of 10^{-9} m.

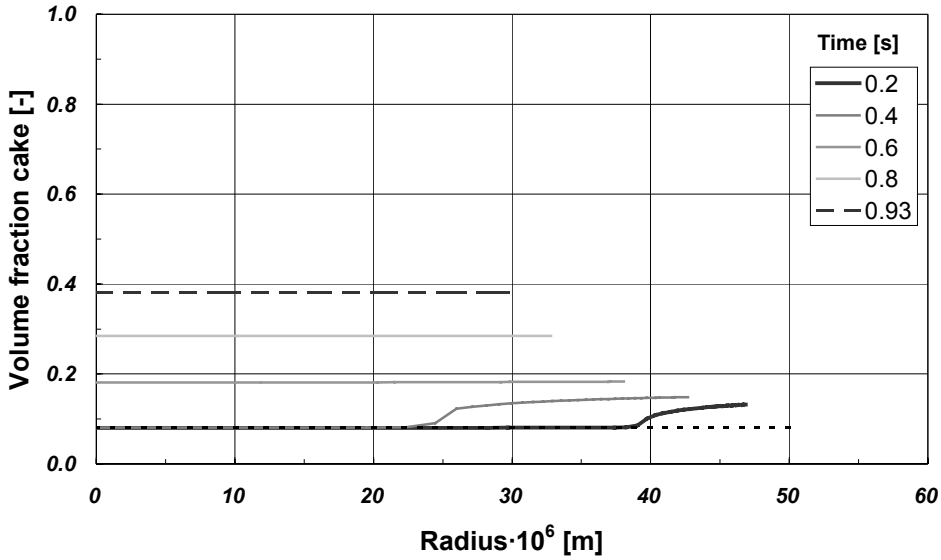

Figure 5.15. Cake concentration profiles for a compressibility index of 0.075 and a binder particle size of 10^{-9} m.

5.4.4.3 Effect of compressive modulus

The effect of the compressive modulus is comparable to the effect of the compressibility index. A higher modulus results in flat cake concentration profiles and a binder profile development comparable to the simulation with standard conditions and a binder particle diameter of 10^{-9} m. A higher compressive pressure, which is linearly related to the compressive modulus, equals the maximum capillary pressure at a lower volume fraction of the cake. Hence, shrinkage stops earlier and the segregation is less.

A lower compressive modulus results in cake concentration profiles similar to the simulation with a cake particle diameter of 10^{-7} m (figure 5.12). However, the shrinkage time is longer and the cake concentration profiles flatten at higher volume fractions, which is caused by the increase of the value of γ. The shrinkage continues until the maximum volume fraction binder is reached and the shrinkage time is somewhat shorter than for a binder particle size of 10^{-9} m. The segregation is higher, due to the lower binder diffusivity as result of the increased volume fraction solids.

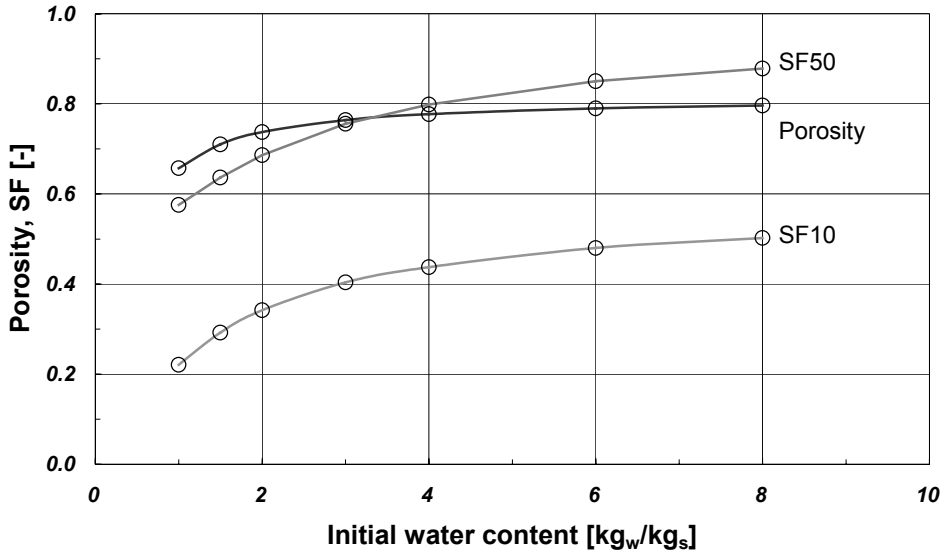

Figure 5.16. Porosity and segregation factors as function of initial water content for standard values and conditions.

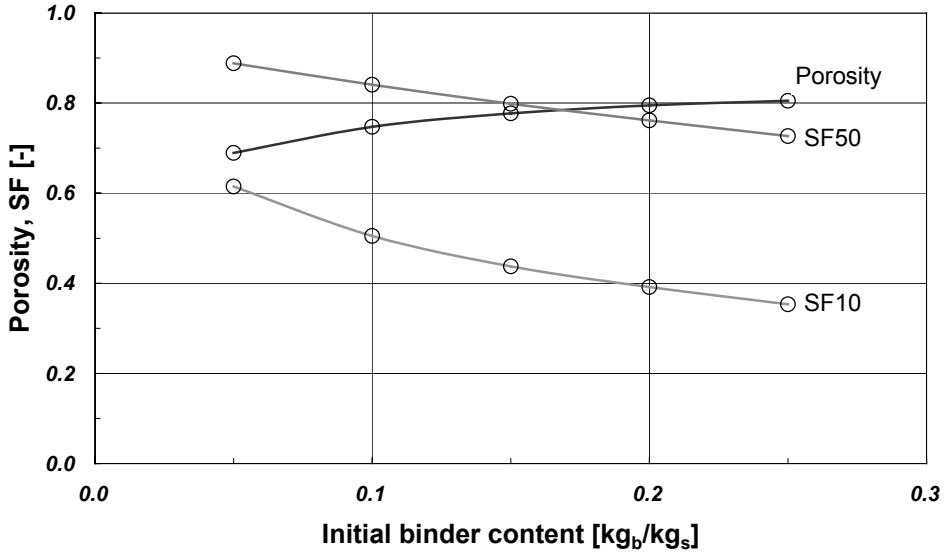

Figure 5.17. Final porosity and segregation factors as function of initial binder content for standard conditions and values.

It can be concluded that the compressibility behaviour of the cake mainly influences the development of the cake and water concentration profiles. There is no large effect on the development of the binder concentration profiles. The segregation factor is influenced (indirectly) by the shrinking time and increases with respectively increasing null-stress volume fraction solids, increasing compressibility index and decreasing compressive modulus.

5.4.5 Effect of initial water content

As mentioned before, the null-stress volume fraction solids is not related to the initial water content. In figure 5.16, the final porosities and segregation factors are given as function of the initial water content. Changing the initial water content changes the initial volume fractions of the components. Decreasing the initial water content increases the (initial) cake volume fraction and hence the value of γ, resulting in flatter cake concentration profiles. Lower initial water contents decrease the (initial) binder diffusion coefficient. This results in steeper gradients of the binder concentration profiles, which is most clearly near the surface. The maximum volume fraction binder is reached earlier. Because the initial volume fraction water is lower, the final granules have a lower porosity and higher density compared to the standard initial water content. The segregation for lower initial water contents is less, mainly caused by the shorter drying times. This result is in agreement with literature (Baklouti, 1998; Meerdink, 1995). The results for higher initial water contents are exactly opposite.

5.4.6 Effect of initial binder content

The initial binder content is varied between 5 – 25 wt.% of the total solids (including binder). The standard value is 15 wt.% (0.175 kg_b/kg_s) and a summary of the results in given in figure 5.17. The corresponding initial binder volume fractions vary between 0.5 – 3.5 vol.% on total volume and between 0.6 – 3.6 vol.% on liquid volume basis. The effect on the initial volume fractions water and cake is less than 2 vol.% compared to the standard values. Lower initial binder volume fractions result in a higher diffusivity, which flattens the binder profiles. Hence, the shrinkage period was prolonged if the maximum volume fraction binder stops the shrinkage. The initial binder content has a small

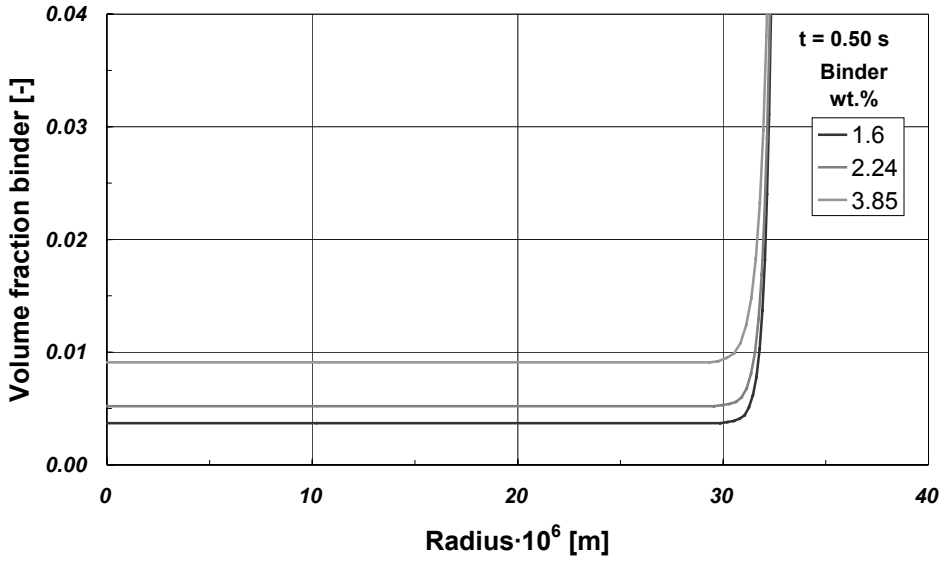

Figure 5.18. Binder concentration profiles for different initial binder concentrations. Data from simulation of spray drying alumina with polyvinyl alcohol as binder.

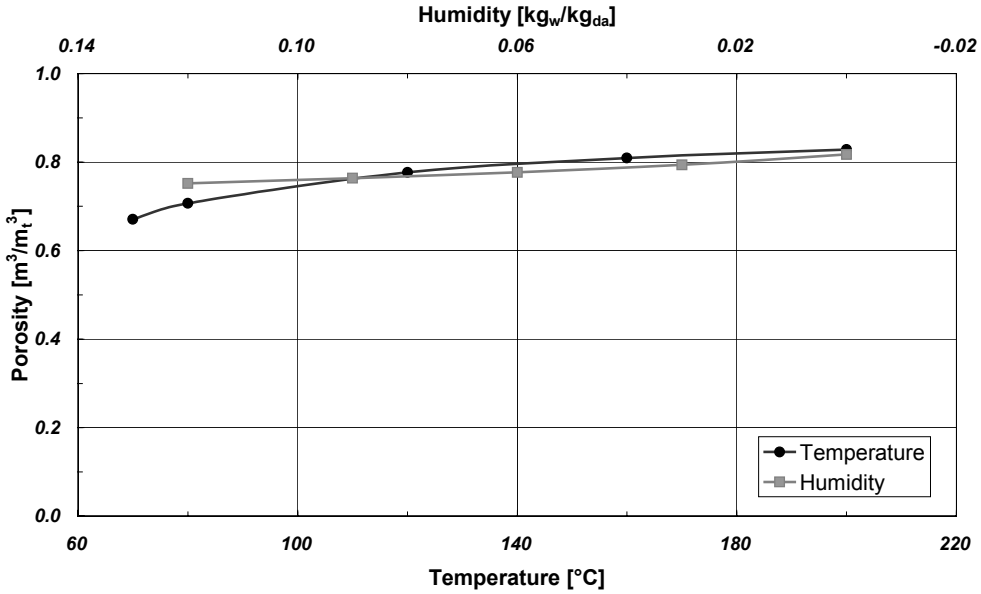

Figure 5.19. Final porosity as function of temperature and humidity for standard values and conditions.

influence on the cake concentration profiles: the profiles are slightly less steep. Due to the small volume fraction of binder, the viscosity of the liquid, hence the friction with the cake wall is almost identical as for standard values. The prolonged shrinking time for smaller initial binder content resulted in more segregation.

Increasing the initial binder content results in opposite effects.

In literature, it is mentioned that the amount of binder at the surface increased with increasing initial binder content. In figure 5.18, the results are shown for simulations with the PVA diffusion coefficient from Zhang *et al.* (Zhang, 1998). Simulations show a higher segregation factor for a lower initial binder content, although the absolute amount of binder at the surface increases with the initial binder content. This is not caused by more segregation, but due to the initial amount of binder. The data used for the simulations, other than the standard values, is summarised in table 5.2.

Table 5.2. Changed parameters for the simulation with literature data.

Parameter	*Value*	*Parameter*	*Value*
Alumina density	3990 kg/m^3	Droplet diameter	$8.0 \cdot 10^{-5}$ m
Air temperature	95 °C	Binder particle size	$1 \cdot 10^{-9}$ m
Initial water content	0.6667 kg_w/kg_s	Compressibility index	0.5

5.4.7 Effect of initial droplet diameter

The droplet diameter determines the surface area available for evaporation and influences the external mass and heat transfer coefficients via the Sherwood and Nusselt correlations. However, in the constant activity period (CAP) the absolute drying rate is proportional to the diameter of the droplet. The reduced drying time (= t/R_o^2) of the process remains identical for different droplet sizes (Meerdink, 1995; Kerkhof, 1975). Therefore, the droplet size does not influence the development of the concentration profiles during the CAP. For the standard conditions and values, the shrinkage period stops just after the end of the CAP, when the droplet temperature started to rise. Therefore, the segregation factors, the dried granules density and porosity are the same for all diameters.

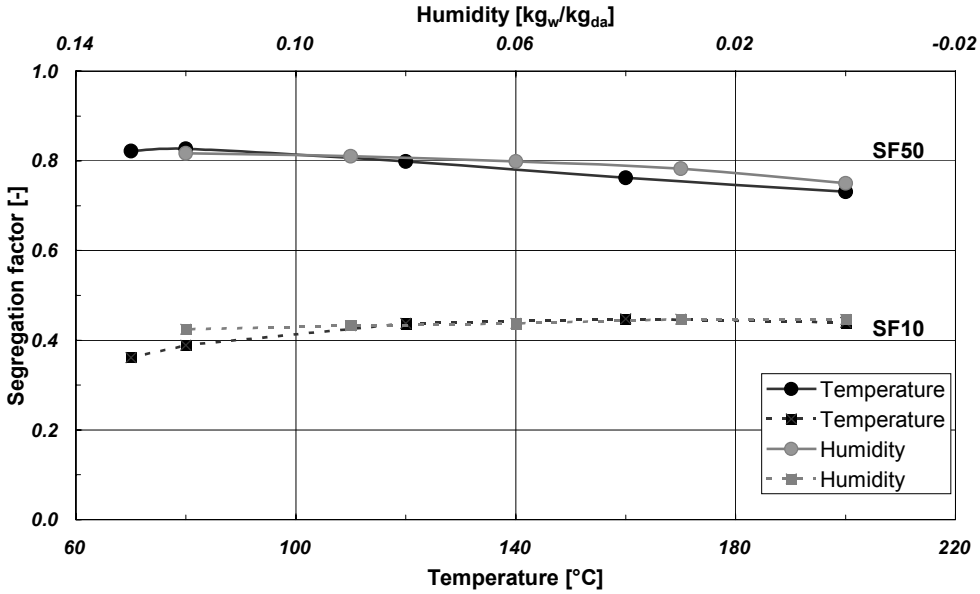

Figure 5.20. Segregation factors as function of temperature and humidity for standard values and conditions.

Table 5.3. Summary of simulation results.

Simulation parameters	*SF50 (-)*	*SF10 (-)*	*Porosity (-)*	*Density (kg/m^3)*
Standard	0.80	0.44	0.78	600
$d_{pb} = 10^{-7}$ m	0.58	0.24	0.88	312
$d_{pb} = 10^{-9}$ m	0.70	0.19	0.49	1376
$d_{ps} = 10^{-5}$ m	0.80	0.44	0.78	601
$d_{ps} = 10^{-7}$ m	0.74	0.43	0.80	562
$\phi_{so} = 0.2^{I}$	0.63	0.15	0.68	862
$\phi_{so} = 0.5^{I}$	0.74	0.26	0.53	1274
$\delta = 0.075^{I}$	0.69	0.18	0.53	1254
$\delta = 0.2^{I}$	0.74	0.25	0.51	1309
$P_a = 100$ N/m^2 (^{I})	0.74	0.26	0.53	1278
$P_a = 10^6$ N/m^2(^{I})	0.66	0.16	0.63	1003

^{I}: simulations done with binder particle diameter of = 10^{-9} m.

This result is in contradiction with measurements of PVA as binder, where more segregation was found for larger granules (Zhang, 1998). This could be due to segregation after shrinkage has stopped. However, it is found that segregation mainly occurs in the initial stage of the drying process (Meerdink, 1995).

5.4.8 Effect of air conditions

The influence of the air conditions is rather complicated due to the interdependency of the process variables. It is not the aim of this study to describe the relations between process variables and drying conditions extensively. However, in a simplified view on process conditions, an increase of the air temperature and a decrease of the air humidity result in higher drying fluxes. Although these parameters influence each other, the parameters are studied separately with the model.

Higher air temperatures increase the heat flux to the droplet surface and result in a higher wet-bulb, or pseudo-equilibrium, temperature. The surface water vapour pressure, the film layer temperature, and the drying flux increase. At a higher temperature, the diffusion coefficient of the binder is also higher. The surface tension of water is lower, which results in a lower capillary pressure.

If the humidity of the air is lower, the driving force for mass transfer becomes higher. This increases the latent heat flux and results in a lower wet-bulb temperature. The lower temperature gives a lower binder diffusivity and higher surface tension.

Without further going into details, higher drying fluxes result in steeper water concentration profiles near the surface. The binder reaches the maximum volume fraction after a shorter period and more binder accumulated in the outer volume of the droplet. The SF10 increases, while the SF50 decreases, compared to the standard conditions. The effects on the segregation factors and dried granule porosity are shown in figures 5.19 and 5.20. In addition, the shorter shrinkage time resulted in a higher porosity and lower density for the granules.

5.4 Conclusions

The presented model describes both the binder distribution and cake compression during the shrinking stage of spray drying. Two transport mechanisms are combined and result in binder transport with the liquid towards the surface and counter diffusion to the centre. The effects of material and process conditions on segregation are described and insight is gained in the contributions of the mechanisms to binder and matrix segregation. The diffusion coefficient of the binder has the largest influence on binder segregation. In the model the diffusion coefficient is mainly determined by the binder particle size and depends on the liquid viscosity. If segregation is of considerable importance, it is necessary to have a reliable value of the binder diffusion coefficient. The compression behaviour of the cake is important for the amount of shrinkage, hence for the final granule morphology.

The results from literature indicate that after shrinkage has stopped segregation still can occur. This is plausible since the binder particles can move in the liquid. It is also interesting and useful to study the deformation behaviour of a matrix, which is filled with binder.

Notation

Roman

B_o	Permeability	[m^2]
c	Concentration	[mol/m^3]
C_p	Heat capacity	[J/kgK]
D_{ij}	Diffusion coefficient	[m^2/s]
g'_D	diffusion averaging factor	[-]
h	function (see eqn. 5.35)	[-]
H	Humidity	[kg_w/kg_{da}]
I	Modified Bessel function	
J_i	Molar flux	[$kmol_i/m^2$ s]
k	Mass transfer coefficient	[m/s]
k_B	Boltzmann constant	[J/K]
n_i	Mass flux of component i	[kg_i/m^2s]
P_a	Compressive modulus	[N/m^2]
P_c	Capillary pressure	[N/m^2]
P_l	Liquid or hydraulic pressure	[N/m^2]
P_s	Solids or compressive pressure	[N/m^2]
q	Heat flux	[J/m^2s]
r	Space co-ordinate	[m]
r_b	radius of binder particle	[m]
r_h	Hydraulic radius	[m]
r_s	Radius of solid particle	[m]
R	Gas constant	[kJ/kmol K]
t	Time	[s]
T	Temperature	[°C]
u	Transformed concentration	[kmol/kmol]
u	velocity (see eqn. 5.2,5.5,5.6,5.8)	[m/s]
v	Velocity	[m/s]

v^v	Volume averaged velocity	[m/s]
$\overline{V}$	specific molar volume	[m³/kmol]
x	mole fraction	[-]
z	co-ordinate	[m]

Greek

α	Heat transfer coefficient	[W/m²K]
β	Wall-friction factor	[s/m²]
γ	Function defined in eqn. 5.12	[N/m²]
δ	Compressibility index	[-]
η	(Partial) Viscosity	[N/m² s]
$[\eta]$	Intrinsic viscosity	[N/m² s]
ϑ	Contact angle	[rad]
φ	modulus (see eqn. 5.34)	[-]
κ	Frictional viscosity coefficient	[s]
λ	Heat conductivity	[W/m K]
μ	Chemical potential	[J/mol]
ωR	Root (see eqn. 5.35)	[m⁻¹]
ϕ	Volume fraction	[-]
σ	Transformed space co-ordinate	[kg_s]
σ_{LV}	Surface tension	[J/m²]
τ	Tortuosity	[-]

Subscripts

b	Binder
da	Dry air
eff	Effective
f	Film
i	Interface
l	Liquid
s	Solid material or cake
w	Water
o	Initial, null-stress or saturated value
∞	Bulk or infinite value

Superscripts

max	Maximum value
v	With respect to the volume averaged velocity
s	With respect to the solid material velocity

References

Baklouti, S., Chartier, T. and Baumard, J.F., 1998, Binder distribution in spray-dried alumina agglomerates, Journal of the European Ceramic Society, 18, 2117-2121.

Bergna, H. E., 1989, Attrition-resistant porous particles produced by spray drying, Characterization and catalyst development: an interactive approach, Ed. Bradley, S.A., Gattuso, M.J. and Bertolacini,R.J., ACS Symposium Series 411, chapter 7, Washington D.C., USA.

Cumberland, D. J. and Crawford, R. J., 1987, The packing of particles, Elsevier, Amsterdam, The Netherlands.

Epstein, N., 1989, On tortuosity and the tortuosity factor in flow and diffusion through porous media, Chemical Engineering Science, 44, 3, 777-779.

Jothimurugesan, K., Goodwin Jr., J.G., Gangwal, S.K. and Spivey, J.J., 2000, Development of Fe Fisher-Tropsch catalysts for slurry bubble column reactors, Catalysis Today, 58, 335-344.

Kerkhof, P.J.A.M., Schoeber, W.J.A.H., 1974, Theoretical modelling of the drying behaviour of droplets in spray dryers, Advances in preconcentration and dehydration of foods, Ed. A. Spicer, Applied Science Publishers Ltd., London, England, 349-397.

Kerkhof, P.J.A.M., 1975, A quantative study of the effect of process variables on the retention of volatile trace components in drying, Ph.D. thesis, Eindhoven University of Technology, Eindhoven, The Netherlands.

Kerkhof, P.J.A.M., 1996, A modified Maxwell-Stefan model for transport through inert membranes: the binary friction model, The Chemical Engineering Journal, 64, 319-343.

Kerkhof, P.J.A.M., Geboers, M.A.M. and Ptasinksi, K.J., 2001, On the isothermal binary mass transport in a single pore, Chemical Engineering Journal, 83, 107-121.

Krieger, I.M., 1972, Rheology of monodisperse lattices, Advances in Colloid and Interface Science, 3, 111-136.

Krischer, O. und Kast, W., 1978, Trocknungstechnik, Erster Band, Die wissenschaftlichen Grundlagen der Trocknungstechnik, Springer-Verlag, Berlin, Germany.

Leu, W., 1986, Principles of compressible cake filtration, Encyclopedia of Fluid Dynamics, Vol. 5, Slurry Flow Technology, Chapter 21, ed. Cheremisineff, N.P., Gulf Publishing Company, Houston, USA.

Lijn, J. van der, 1976, The 'constant rate period' during the drying of shrinking spheres, Chemical Engineering Science, 31, 929-935.

Mandanas, M.M. and Messing, G.L., 2000, Thermogravimetric analysis of organic binder segregation during drying of particulate suspensions, Thermochimica Acta, 363, 37-45.

Marshall, T.J., 1957, Permeability and the size distribution of pores, Nature, 180, 664-665.

Meerdink, G., Riet, K. van 't, 1995, Modeling segregation of solute material during drying of liquid foods, American Institute of Chemical Engineers Journal, 41, 3, 732-736.

Minoshima, H., Matsushima, K., Liang, H. and Shinohara, K., 2001, Basic model of spray drying granulation, Journal of Chemical Engineering of Japan, 34, 4, 472-478.

Pham, H.N., Viergutz, A., Gormley, R.J. and Datye, A.K., 2000, Improving the attrition resistance of slurry phase heterogeneous catalysts, Powder Technology, 110, 196-203.

Shirato, M., Kato, H., Kobayashi, K. and Sakazaki, H., 1970, Analysis of settling of thick slurries due to consolidation, Journal of Chemical Engineering of Japan, 3, 1, 98-104.

Tiller, F.M. and Kwon, J.H., 1998, Role of porosity in filtration: XIII. Behavior of highly compactable cakes, American Institute of Chemical Engineers Journal, 44, 10, 2159-2167.

Walton, D.E., 2000, The morphology of spray-dried particles. A qualitative view, Drying Technology, 18, 9, 1943-1986.

Wesselingh, J.A., Vonk, P. and Kraaijeveld, G., 1995, Exploring the Maxwell-Stefan description of ion exchange, Chemical Engineering Journal, 57, 75-89.

White, L.R., 1982, Capillary rise in powders, Journal of Colloid and Interface Science, 90, 2, 536-538.

Wijlhuizen, A.E., Kerkhof, P.J.A.M. and Bruin, S., 1979, Chemical Engineering Science, 34, 651-660.

Zhang, Y., Tang, X., Uchida, N. and Uematsu, K., 1998, Binder surface segregation during spray drying of ceramic slurry, Journal of Material Research, 13, 7, 1881-1887.

Chapter 6
Evaluation

The central question that initiated this research was how spray drying conditions influence fluid catalytic cracking (FCC) catalyst properties. In order to give an answer to this question some fundamental aspects of spray drying FCC catalyst have been studied. The drying behaviour of FCC catalyst has been studied on a laboratory scale and spray drying experiments have been done on a pilot-plant scale. In addition, novel models have been developed that describe the spray drying of a slurry droplet and the binder segregation within the droplet.

Conclusions

The study of the drying kinetics provided insight in the phenomenological aspects of the drying process and gave rules to predict the sorption isotherm and diffusion coefficient with the properties of the single components. The shrinkage behaviour during spray drying is probably exemplary: FCC catalyst shrinks uniformly until the shrinkage limit is reached and then stops shrinking. The major part of the drying process is in the 'constant activity period', although the silica binder influences the 'activity'. The formation of small pores at the interface decreases the activity and hence the drying rate is slightly decreased. The transition to the 'falling rate period' depends on the initial drying rate for layer drying experiments, though may coincide with the shrinkage limit in the spray drying process. When shrinkage has stopped, the liquid probably retreats in the pores, leaving the surface dry. This process takes place in the 'falling rate period' and can be described with the penetration period and the regular regime.

The experiments with the pilot-scale spray drier showed that the influence of the drying conditions on the studied properties is small. The largest influence is found on the morphology of the particles, as cracks manifest and particles break for high drying rates and wrinkles and agglomerates appear for very low drying rates. Using high drying rates increases the pore volume and surface area only a few percent. The particle size distribution is mainly controlled with the nozzle configuration and the solids content of the feed. The time between preparation and spray drying of the feed has two effects on

the FCC catalyst. A short time will decrease the amount of wrinkled surfaces, which is very likely positive for the attrition resistance. On the other hand, waiting a longer time increases the binder particle size and results in more segregation at the surface, which is also positive for the attrition resistance. This subject would be interesting for further study.

For the design of a spray drying process to manufacture FCC catalysts, the 'falling rate period' may not be so important. When shrinkage has stopped and the surface is dry, the particles will not be sticky and the morphology of the FCC catalyst is already largely determined. However, it is not quite certain how the binder segregates after the shrinkage has stopped.

The models, which describe the spray drying of slurries with and without binder material, gave insight in a possible mechanism for crust formation and compaction during spray drying. In addition, the segregation of binder is described for a deformable crust. The main conclusion is that to be able to control the segregation, one should control the binder diffusion. It will be of interest to refine these models by comparison to more detailed experimental measurements, and to investigate the applicability in practice.

Recommendations

The recommendations from this work are classified in two categories: 1) more spray drying, and 2) validation of the models.

- It is recommended to study the attrition resistance of FCC catalyst, not only because of the importance of this property. It could also be combined with the second category, due to the influence of binder segregation. The binder segregation could be measured with one of the techniques mentioned in chapter 5.
- The influence of the formulation or composition on the FCC catalyst properties is another subject that is interesting for manufacturers. This would also attribute to the window of design.
- The presented models are also applicable to other materials than FCC catalyst and it is interesting to combine cake filtration experiments with spray drying experiments.
- Cake filtration experiments with a material that consists of large and small particles (such as the FCC catalyst) would give valuable information about the compressive behaviour of such a cake. This is also interesting for ceramic materials.

Appendix A

Sorption isotherm equation and parameters

The used equation to fit the sorption isotherm is:

$$a_w = a + \frac{b}{\pi}\left(\arctan\left(\frac{u-c}{d}\right)+\frac{\pi}{2}\right) \tag{A.1}$$

In table A.1 the parameters of the single components for different temperatures are given.

Table A.1: Sorption-isotherm fit parameters.

Material	*T [°C]*	R^2	*a*	*b*	*c*	*d*
Zeolite	30	0.985	-5.36E-2	1.17	2.29E-1	1.70E-2
	45	0.973	-2.89E-3	1.31	2.42E-1	1.47E-2
	70	0.992	-9.68E-4	1.13	2.18E-1	1.33E-2
Clay	30	0.993	-2.27E-1	1.17	7.97E-3	4.44E-3
	45	0.989	-2.15E-1	1.21	8.08E-3	4.83E-3
	70	0.995	-1.84E-1	1.14	6.56E-3	3.12E-3
Alumina	30	0.972	-4.91E-1	1.66	1.30E-2	1.42E-1
	45	0.973	-3.74E-1	1.31	6.94E-2	7.20E-2
	70	0.990	-3.73E-1	1.50	1.17E-1	1.05E-2
Silica	30	0.996	-2.34E –1	1.15	1.59E-1	1.12E-1
	45	0.994	-2.46E-1	1.15	1.48E-1	1.11E-1
	70	0.996	-3.46E-1	1.31	1.18E-1	1.28E-1
FCC catalyst	30	0.996	-2.39E-1	1.23	1.18E-1	7.19E-2
	45	0.996	-2.17E-1	1.23	1.22E-1	6.80E-2
	70	0.995	-1.32 E-1	1.09	9.95E-2	3.67E-2

Appendix B

Figures for drying kinetics of FCC catalyst

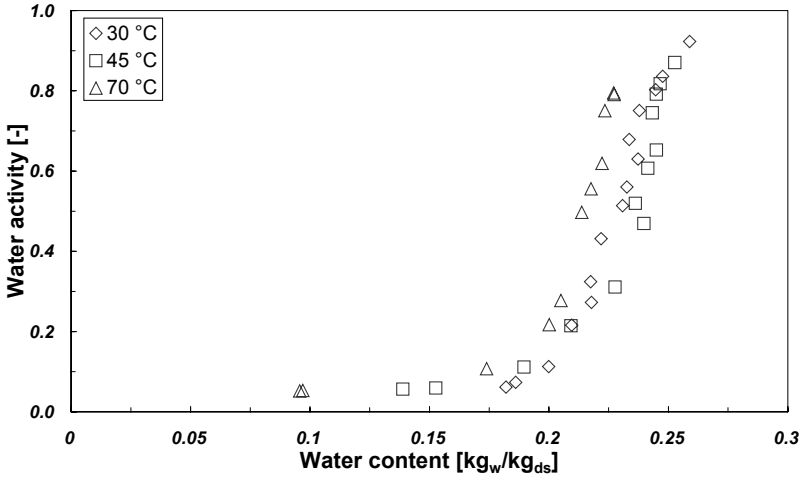

Figure B1. Desorption isotherms of zeolite Y at 30, 45 and 70 °C.

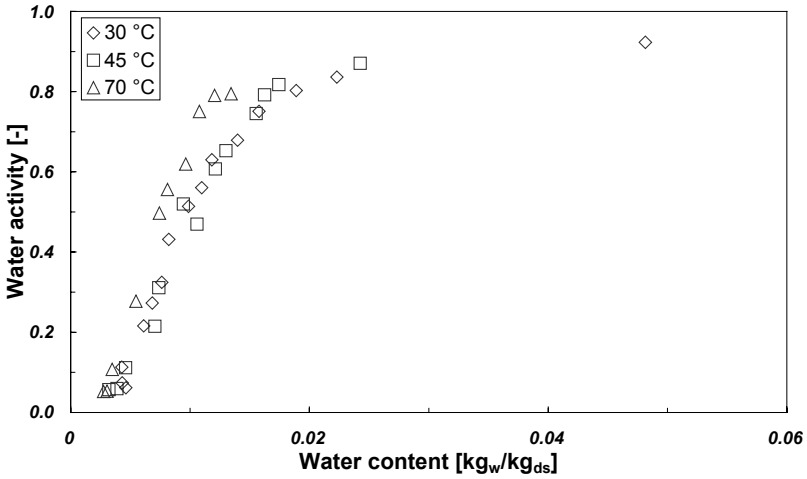

Figure B2. Desorption isotherms of clay at 30, 45 and 70 °C.

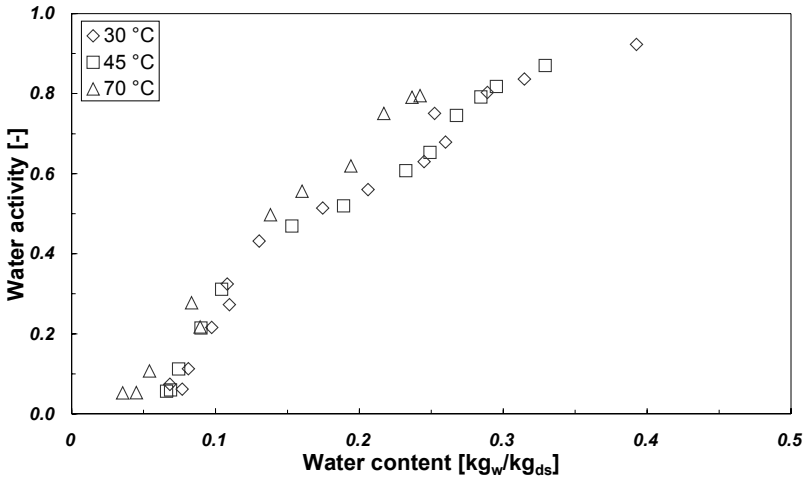

Figure B3. Desorption isotherms of alumina at 30, 45 and 70

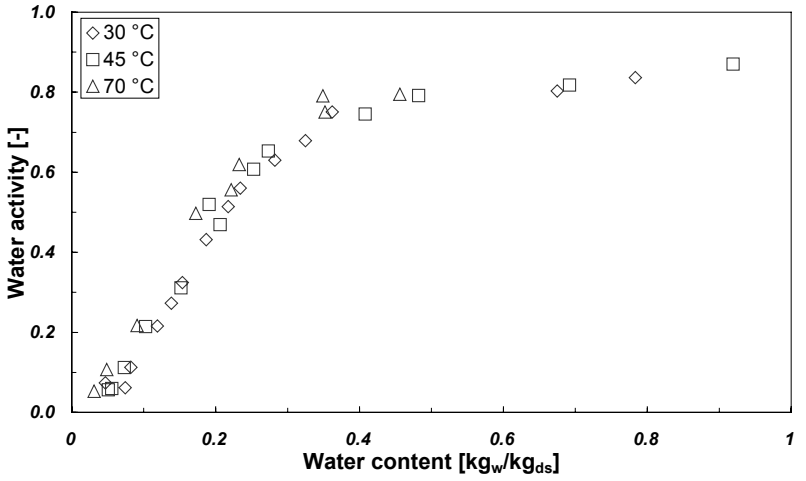

Figure B4. Desorption isotherms of silica at 30, 45 and 70 °C.

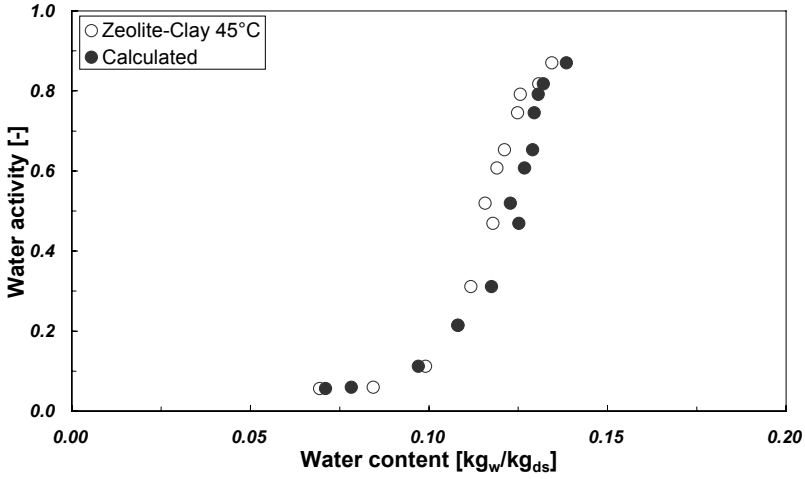

Figure B5. Measured and calculated sorption isotherm of a 1:1 zeolite clay mixture at 45 °C.

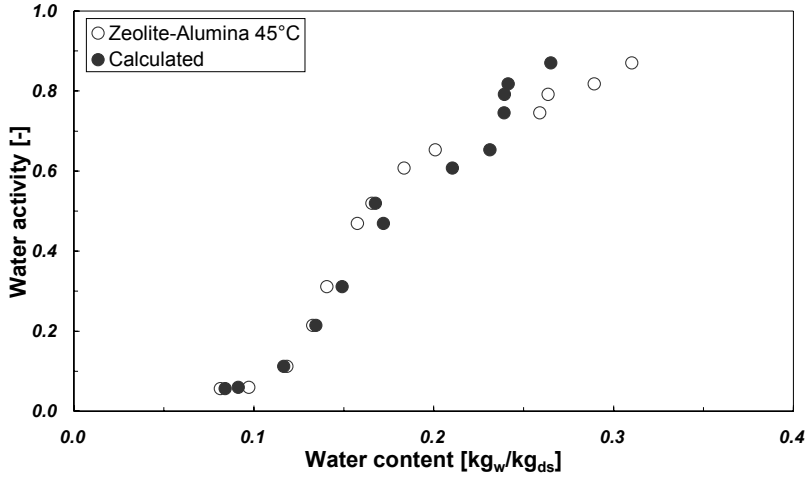

Figure B6. Measured and calculated desorption isotherm of a 1:1 zeolite alumina mixture at 45 °C.

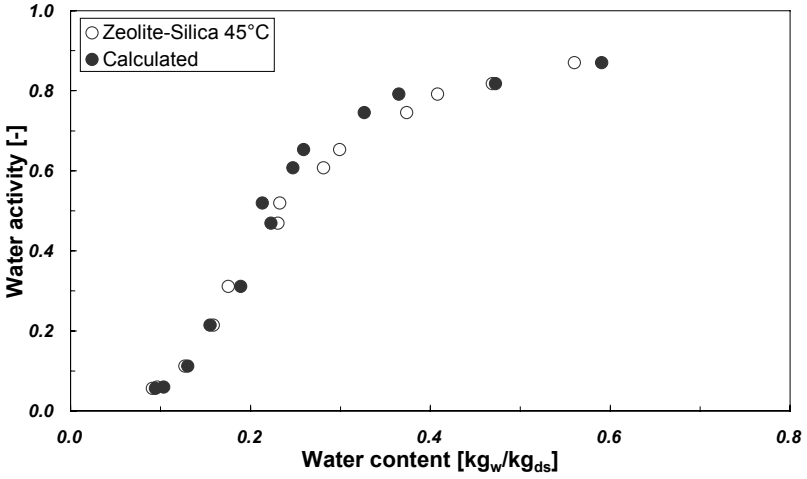

Figure B7. Measured and calculated desorption isotherm of a 1:1 zeolite silica mixture at 45 °C.

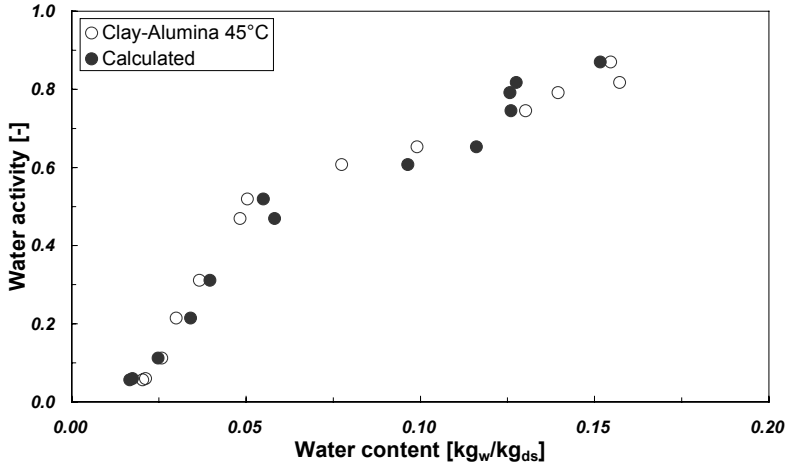

Figure B8. Measured and calculated desorption isotherm of a 1:1 clay alumina mixture at 45 °C.

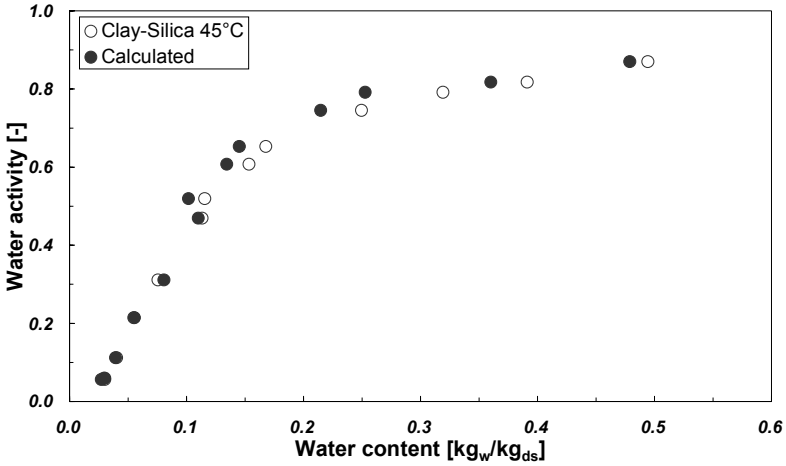

Figure B9. Measured and predicted desorption isotherm of a 1:1 clay silica mixture at 45 °C.

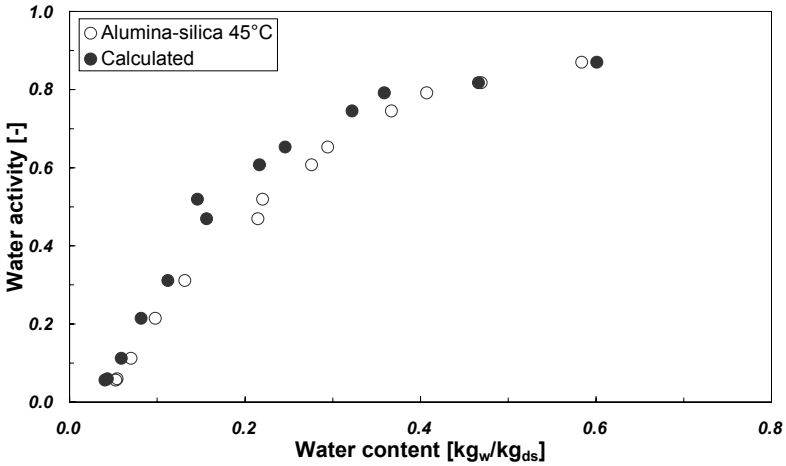

Figure B10. Measured and calculated desorption isotherm of a 1:1 alumina silica mixture at 45 C.

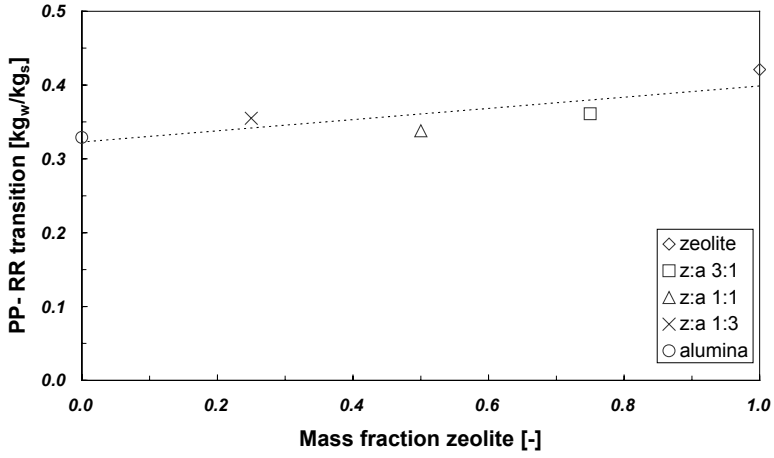

Figure B11. Water content at PP-RR transitions of zeolite – alumina mixtures and single components at sample temperature of 45 °C.

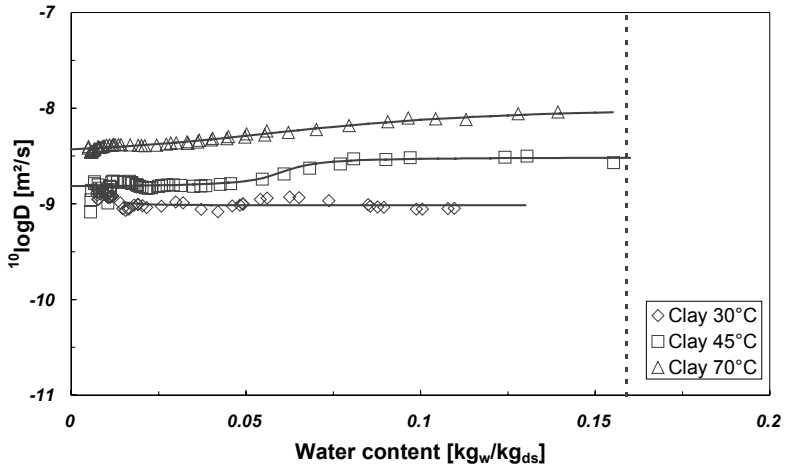

Figure B12. Diffusion coefficient of water in clay for different sample temperatures.

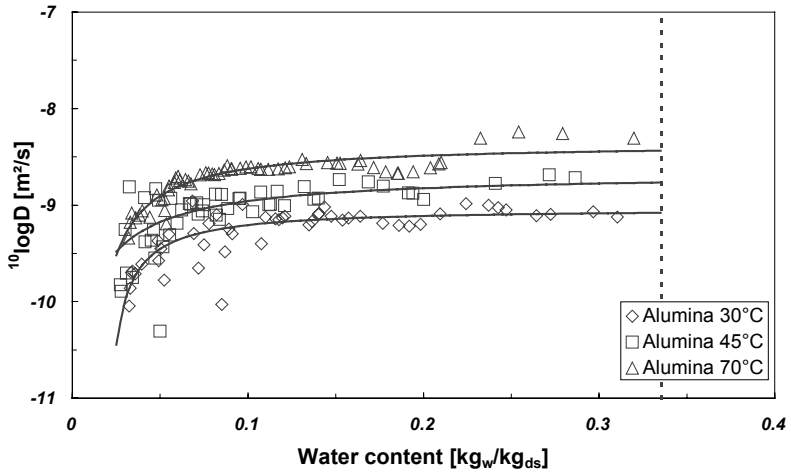

Figure B13. Diffusion coefficient of water in alumina for different sample temperatures.

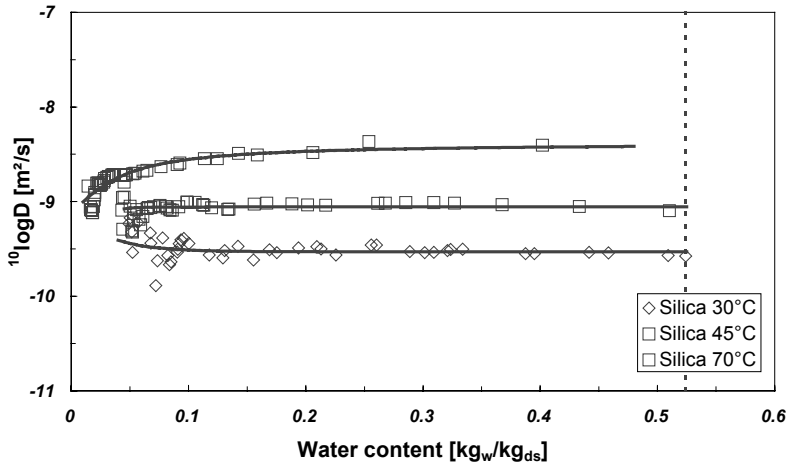

Figure B14. Diffusion coefficient of water in silica for different sample temperatures.

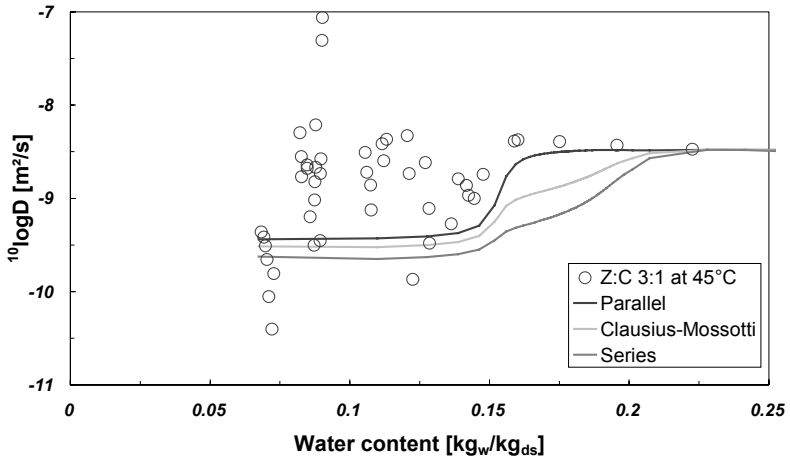

Figure B15. Diffusion coefficient of water in a 3:1 zeolite – clay mixture at 45 °C and predicted values from the series, parallel and Clausius-Mossotti models.

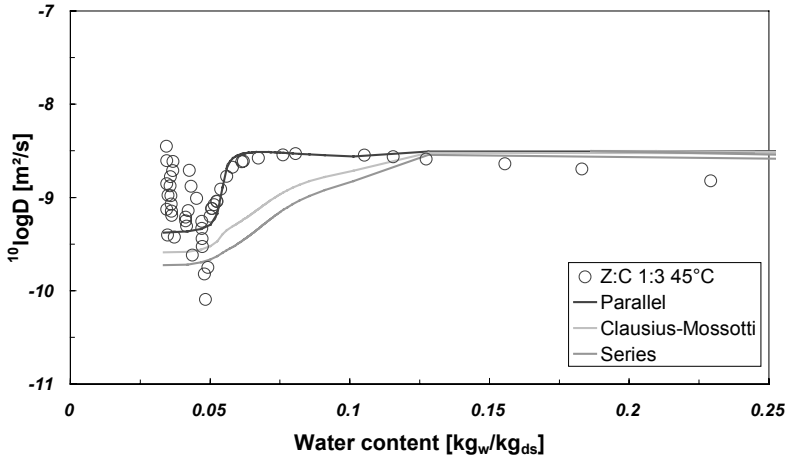

Figure B16. Diffusion coefficient of water in a 1:3 zeolite – clay mixture at 45 °C and predicted values from the series, parallel and Clausius-Mossotti models.

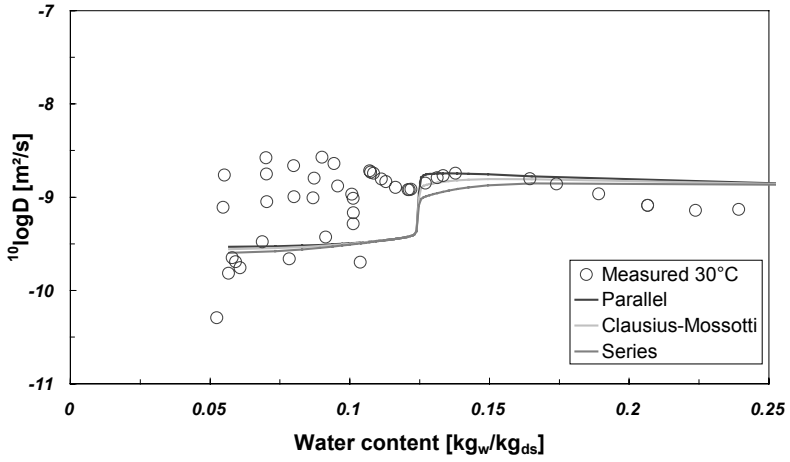

Figure B17. Diffusion coefficient of water at 30 °C in a 1:1 zeolite – clay mixture and predicted values from the series, parallel and Clausius-Mossotti models.

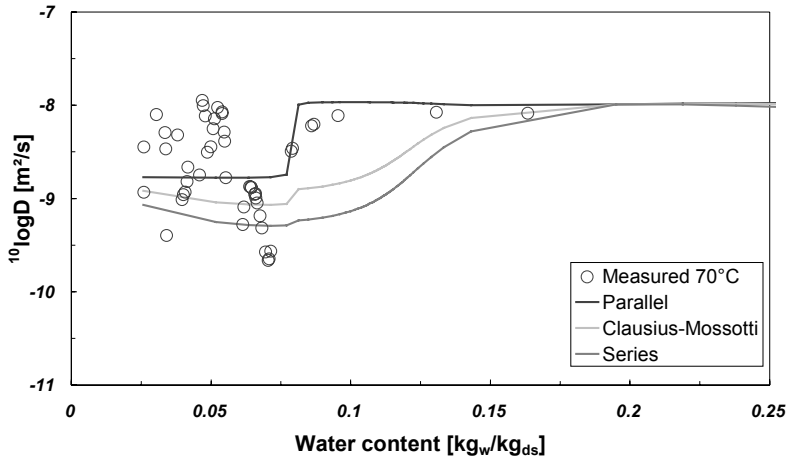

Figure B18. Diffusion coefficient of water at 70 °C in a 1:1 zeolite = clay mixture and predicted values from the series, parallel and Clausius-Mossotti models.

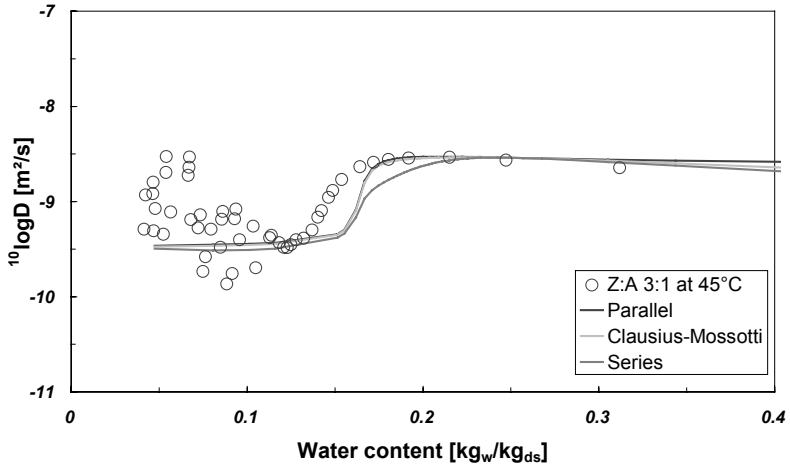

Figure B19. Diffusion coefficient of water at 45 °C in a 3:1 zeolite – alumina mixture and predicted values from the series, parallel and Clausius-Mossotti models.

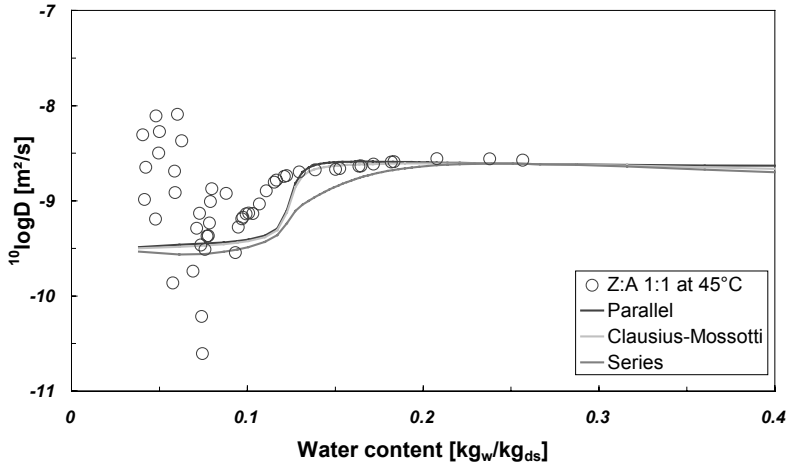

Figure B20. Diffusion coefficient of water at 45 °C in a 1:1 zeolite – alumina mixture and predicted values from the series, parallel and Clausius-Mossotti models.

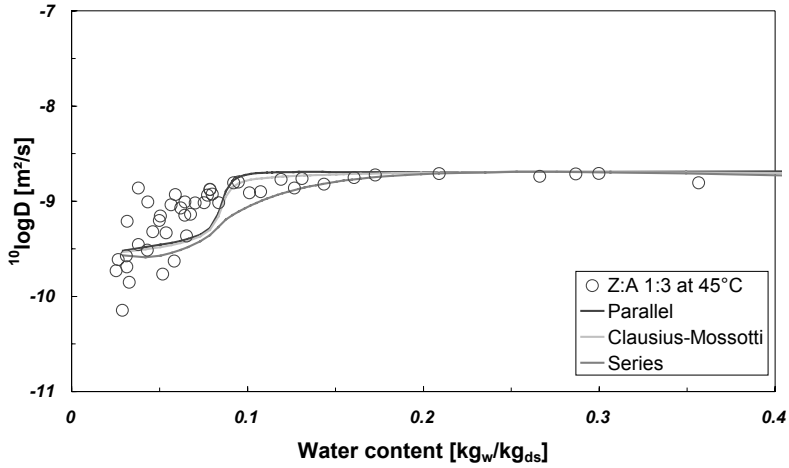

Figure B21. Diffusion coefficient of water at 45 °C in a 1:3 zeolite – alumina mixture and predicted values from the series, parallel and Clausius-Mossotti models.

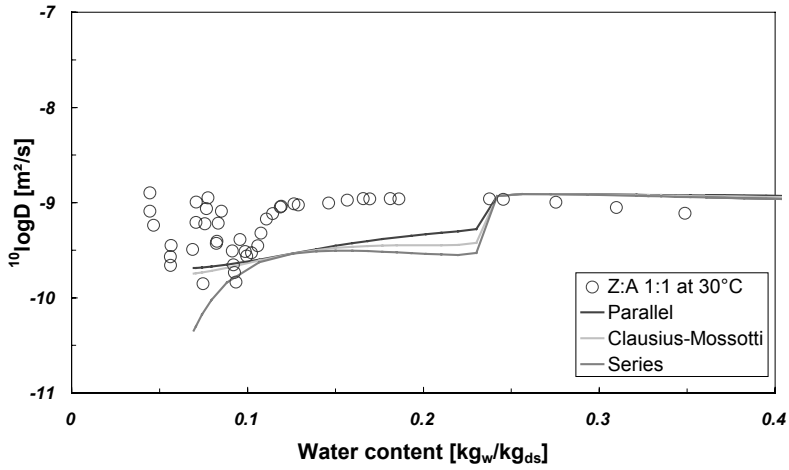

Figure B22. Diffusion coefficient of water at 30 °C in a 1:1 zeolite – alumina mixture and predicted values from the series, parallel and Clausius-Mossotti models.

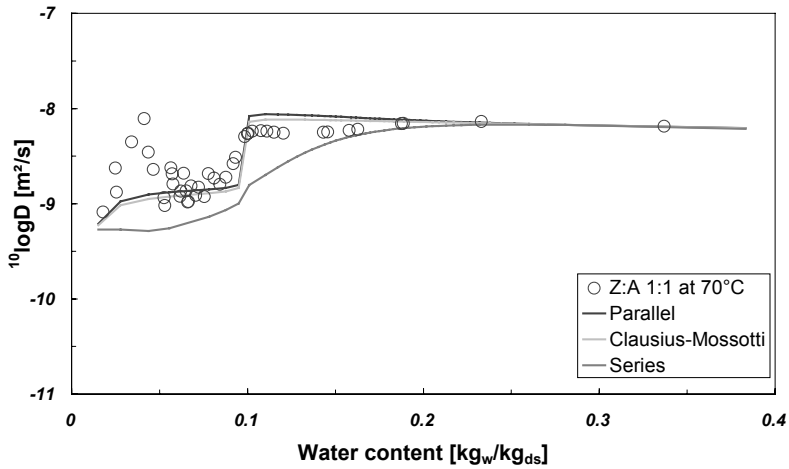

Figure B23. Diffusion coefficient of water in a 1:1 zeolite – alumina mixture at 70 °C and predicted values from the series, parallel and Clausius-Mossotti models.

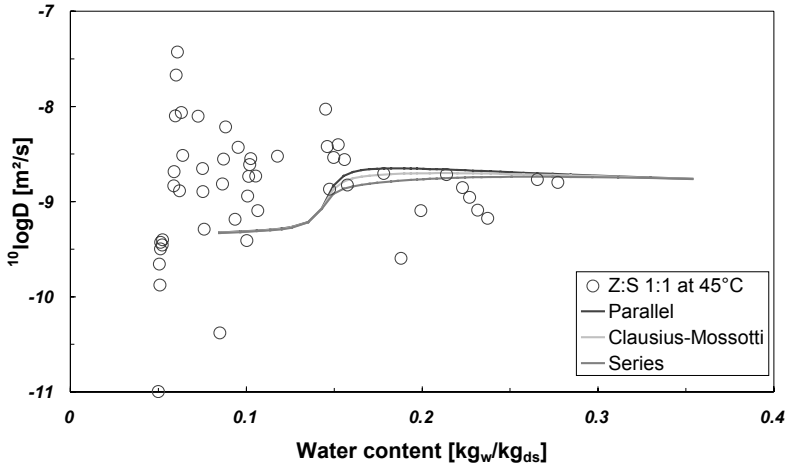

Figure B24. Diffusion coefficient of water in a 1:1 zeolite – silica mixture at 45 °C and predicted values from the series, parallel and Clausius-Mossotti models.

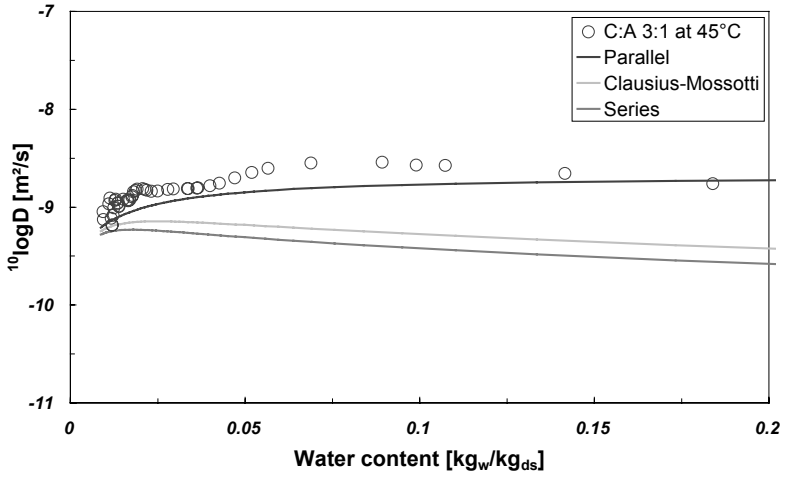

Figure B25. Diffusion coefficient of water in a 3:1 clay – alumina mixture at 45 °C and predicted values from the series, parallel and Clausius-Mossotti models.

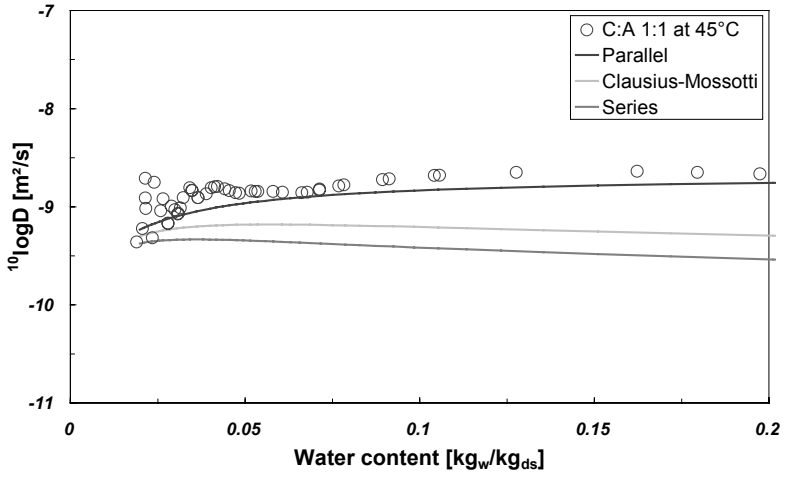

Figure B26. Diffusion coefficient of water in a 1:1 clay – alumina mixture at 45 °C and predicted values from the series, parallel and Clausius-Mossotti models.

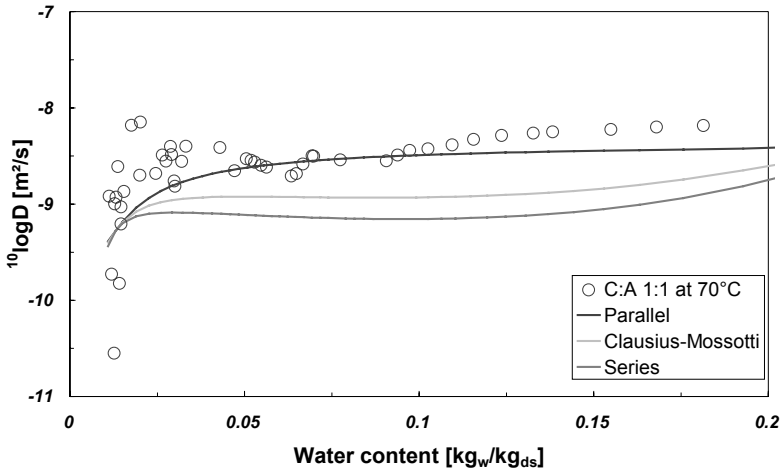

Figure B27. Diffusion coefficient of water in a 1:1 clay – alumina mixture at 70 °C and predicted values from the series, parallel and Clausius-Mossotti models.

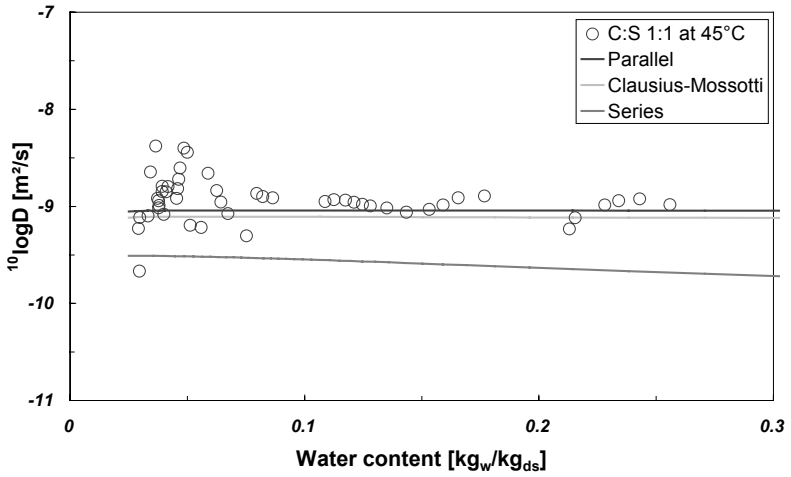

Figure B28. Diffusion coefficient of water in a 1:1 clay – silica mixture at 45°C and predicted values from the series, parallel and Clausius-Mossotti models.

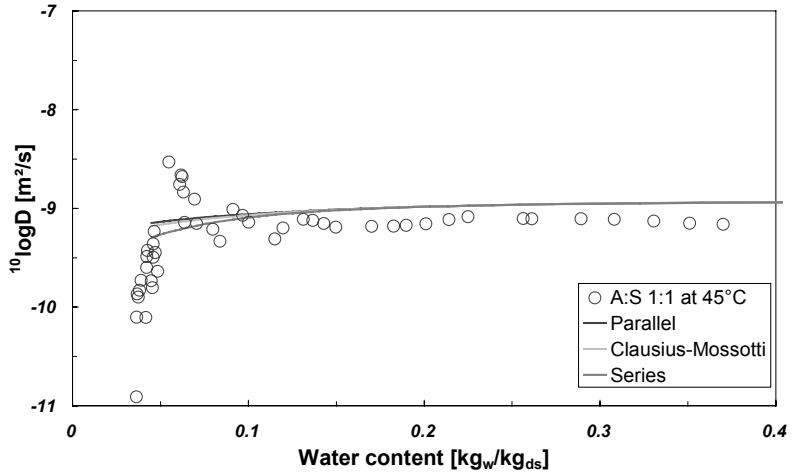

Figure B29. Diffusion coefficient of water in a 1:1 alumina – silica mixture at 45°C and predicted values from the series, parallel and Clausius-Mossotti models.

Appendix C

Diffusion coefficients equations and parameters

The diffusion coefficients are fitted with the equations:

$$^{10}\log D = a + b\exp\left(-\frac{u}{c}\right) \tag{C.1}$$

and

$$^{10}\log D = a + \frac{b}{\pi}\left(\arctan\left(\frac{u-c}{d}\right) + \frac{\pi}{2}\right) \tag{C.2}$$

The parameters to fit the diffusion coefficients are:

Material	*T [°C]*	*Eqn.*	R^2	*A*	*b*	*c*	*d*
Zeolite	30	(C.2)	0.475	-9.62	8.66E-1	2.36E-1	2.83E-4
	45	(C.2)	0.349	-9.47	1.026	2.03E-1	5.20E-3
	70	(C.2)	0.384	-8.79	8.36E-1	1.55E-1	5.77E-4
Clay	30	(C.1)	0.607	-9.01	6.26E-1	4.88E-2	-
	45	(C.2)	0.924	-8.82	3.12E-1	6.35E-2	7.46E-3
	70	(C.2)	0.974	-8.58	6.40E-1	5.73E-2	5.26E-2
Alumina	30	(C.2)	0.634	-2.45E1	1.54E1	1.47E-2	3.03E-3
	45	(C.2)	0.241	-2.12E1	1.25E1	-1.53E-2	8.32E-3
	70	(C.2)	0.831	-2.14E1	1.31E1	3.52E-3	6.14E-3
Silica	30	(C.1)	0.038	-9.53	4.36E-1	3.13E-1	-
	45	(C.2)	0.852	-1.13E1	2.25	3.63E-2	2.70E-4
	70	(C.2)	0.754	-9.28	1.44	1.23E-3	3.99E-2
FCC catalyst	30	(C.2)	0.325	-9.50	3.95E-1	7.47E-2	1.85E-3
	45	(C.2)	0.742	-9.39	7.01E-1	5.31E-2	1.16E-2
	70	(C.2)	0.780	-9.34	1.05	3.74E-2	2.02E-2

Appendix D

Spray drying process conditions and measured FCC catalyst properties

Commentary

Numbers that have a shaded background result from an experimental error.

Experiment	units	**Reference**	**Ageing**	**Duplo**	**Nozzle**	**Nozzle**	**Air T**	**Air T**	**Air T**	**Air T**	**Air T**
Reference number		00419_12	00419_34	00420_12	00425_12	00425_34	00501_12	00501_34	81029_34	81029_56	81029_78
Catalyst composition											
Zeolite	wt.%	23%	23%	23%	24%	24%	24%	24%	24%	24%	24%
Clay	wt.%	47%	47%	47%	47%	47%	47%	47%	47%	47%	47%
Alumina	wt.%	14%	14%	14%	14%	14%	14%	14%	15%	15%	15%
Silica	wt.%	16%	16%	16%	16%	16%	16%	16%	14%	14%	14%
Feed composition											
Water content	kgw/kgs	3.63	3.63	3.61	3.59	3.59	3.58	3.58	3.72	3.72	3.72
Dry solids content	wt.%	21.6%	21.6%	21.7%	21.8%	21.8%	21.8%	21.8%	21.2%	21.2%	21.2%
Spray drying conditions											
Batch ageing time	min.	45	210	45	45	90	45	75	40	50	60
Feed flow	kg/hr	50	50	50	50	50	50	50	15.9	24.9	35.3
Nozzle pressure	bar	19.4	19.0	17.6	25.5	38.9	27.0	26.5	16	16	16
Feed temperature	°C										
Feed density	kg/m3	1160	1170	1165	1170	1180	1160	1170	23	23	22
Ambient temperature	°C	23	23	23	23	23	23	23	565	565	583
Air flow	m3/hr	642	643	651	643	643	586	696	393	389	384
Air inlet temperature	°C	358	358	358	357	357	497	220	6.7	6.7	6.7
Air inlet humidity	gw/kgda	5.9	5.9	5.7	7.3	7.3	7.5	7.5	176	160	147
Air outlet temperature	°C	167	168	166	169	165	228	106			
Air outlet humidity	gw/kgda	38.4	40.3	37.3	61.3	64.4	54.0	44.0	3.61	3.30	4.19
Tower product flow	kg/hr	3.87	3.90	2.75	3.56	2.03	4.52	2.86	5.48	6.67	9.49
Cyclone product flow	kg/hr	7.03	7.25	8.28	6.38	8.52	6.77	7.57			
Product properties									0.956	0.953	0.939
Tower dry solids content	kgds/kgt	0.963	0.964	0.956	0.956	0.954	0.964	0.932	0.968	0.952	0.95
Cyclone dry solids content	kgds/kgt	0.971	0.972	0.970	0.967	0.969	0.979	0.944	0.046	0.049	0.065
Tower water content	kgw/kgs	0.039	0.037	0.046	0.046	0.048	0.038	0.073	0.033	0.050	0.053
Cyclone water content	kgw/kgs	0.030	0.029	0.031	0.035	0.032	0.021	0.060	89	83	75
Tower mean particle size	µm	89	91	98	96	77	93	120	23	21	19
Standard deviation	µm	23	23	23	24	18	27	79	58	49	47
Cyclone mean particle size	µm	67	66	72	69	55	60	67	23	22	22
Standard deviation	µm	22	23	23	23	20	27	28	70	66	58
Total mean particle size	µm	69	71	74	71	57	82	74	27	32	26
Standard deviation	µm	25	28	25	25	22	30	28			
Washed mean particle size	µm	70	71		73	60	76	72	1048	1061	1054
Tower bulk density	kgs/m3	1037	990	1026	1040	1028	975	1060	1096	1098	1108
Cyclone bulk density	kgs/m3	1097	1061	1092	1092	1080	1044	1132	1069		
Total bulk density	kgs/m3										
Incipient wetness impregnation pore volume									0.29	0.26	0.29
Tower product	ml/g	0.21	0.21	0.21	0.21	0.22	0.22	0.23	0.27	0.28	0.27
Cyclone product	ml/g	0.18	0.19	0.19	0.18	0.18	0.19	0.21	0.33		
Total product washed	ml/g	0.33	0.35		0.32	0.33	0.35	0.31			
Nitrogen adsorption micro-pore volume									0.054	0.053	
Tower product	ml/g	0.056	0.057	0.057	0.055	0.052	0.063	0.047	0.055		
Cyclone product	ml/g	0.057	0.057	0.054	0.054	0.059	0.064	0.048	0.050	0.046	0.045
Total product	ml/g									0.070	
Total product washed	ml/g	0.071	0.073		0.074	0.090	0.073	0.073			
Total product washed	ml/g				0.075		0.074	0.072			
Nitrogen desorption macro-pore volume									0.058	0.056	
Tower product	ml/g	0.075	0.112	0.077	0.088	0.092	0.064	0.037	0.055		
Cyclone product	ml/g	0.039	0.063	0.089	0.049	0.060	0.056	0.037	0.058	0.051	0.047
Total product	ml/g									0.18	
Total product washed	ml/g	0.104	0.114		0.099	0.062	0.104	0.100			
Total product washed	ml/g				0.108		0.130	0.113			
Mercury intrusion meso- and macro-pore volume										0.27	
Total product washed	ml/g	0.26	0.32		0.25	0.29	0.29	0.25		0.25	
" " < 1000nm	ml/g	0.24	0.30		0.22	0.25	0.27	0.23			
BET surface area									139	139	
Tower product	m2/g	144	148	150	145	135	178	118	141		
Cyclone product	m2/g	135	148	138	138	120	167	116	130	122	114
Total product	m2/g									241	
Total product washed	m2/g	226	250		249	224	247	249			
Total product washed	m2/g				237		239	226			
T-plot surface area									22	23	
Tower product	m2/g	23	24	26	27	22	42	18	21		
Cyclone product	m2/g	14	27	21	22	19	30	13	23	23	17
Total product	m2/g									89	
Total product washed	m2/g	90	92		88	29	88	90			
Total product washed	m2/g				73		78	71			
Desorption surface area									22	20	
Tower product	m2/g	23	28	25	25	23	32	16	21		
Cyclone product	m2/g	17	25	24	19	21	25	14	21	19	15
Total product	m2/g									87	
Total product washed	m2/g	89	91		86	177	89	90			
Total product washed	m2/g				43		53	44			
Mercury surface area											
Total product washed	m2/g	67	84		54	63	63	66		53	
" " < 1000nm	m2/g	62	79		49	56	58	61			
Nitrogen desorption average pore size										11	11
Tower product	nm	13	16	12	14	16	8.0	10		11	
Cyclone product	nm	9.0	10	15	10	11	10	12		11	10
Total product	nm									8.4	
Total product washed	nm	4.6	5.0		4.5	8.5	4.7	4.5			
Total product washed	nm				5.9		6.7	6.4			
Mercury intrusion average pore size											
Total product washed	nm	25	24		34	42	26	23		19	
" " < 1000nm	nm	17	16		20	20	20	17			

Experiment	units	**Air T**	**Air T**	**Air T**	**Air T**	**Air T**	**Air T**	**Air T**	**Air T**	**Air T**	**Air T**
Reference number		81125_12	81125_34	81125_56	81130-1,2	81130-3,4	81130-5,6	81202-1,2	81202-3,4	81202-5,6	81202-7,8
Catalyst composition											
Zeolite	wt.%	24%	24%	24%	24%	24%	24%	23%	23%	23%	23%
Clay	wt.%	47%	47%	47%	47%	47%	47%	47%	47%	47%	47%
Alumina	wt.%	15%	15%	15%	15%	15%	15%	15%	15%	15%	15%
Silica	wt.%	14%	14%	14%	14%	14%	14%	14%	14%	14%	14%
Feed composition											
Water content	kgw/kgs	3.61	3.61	3.61	3.59	3.59	3.59	3.59	3.59	3.59	3.59
Dry solids content	wt.%	21.7%	21.7%	21.7%	21.8%	21.8%	21.8%	21.8%	21.8%	21.8%	21.8%
Spray drying conditions											
Batch ageing time	min.										
Feed flow	kg/hr	30	40	50	30	70	80	60	50	40	30
Nozzle pressure	bar	8.89	18.9	27.4	9.54	50.8	58.6	34.9	26.4	17.1	9.16
Feed temperature	°C	14	14	14	12	12	12	15	15	15	15
Feed density	kg/m3										
Ambient temperature	°C	23	23	22	21	21	21	22	22	23	24
Air flow	m3/hr	632	638	648	581	626	637	642	633	630	602
Air inlet temperature	°C	332	331	332	393	393	393	363	363	363	363
Air inlet humidity	gw/kgda	9.1	9.1	9.1	8.2	8.2	8.2	6.6	6.6	6.6	6.6
Air outlet temperature	°C	159	149	138	184	142	129	135	144	156	172
Air outlet humidity	gw/kgda										
Tower product flow	kg/hr	3.00	3.60	3.97	3.90	6.22	7.09	4.88	3.87	3.32	2.53
Cyclone product flow	kg/hr	3.98	5.76	7.51	3.53	9.76	11.40	8.93	7.53	5.90	3.56
Product properties											
Tower dry solids content	kgds/kgt	0.955	0.955	0.949	0.963	0.945	0.937	0.938	0.942	0.9474	0.947
Cyclone dry solids content	kgds/kgt	0.965	0.964	0.961	0.972	0.956	0.952	0.951	0.958	0.963	0.968
Tower water content	kgw/kgs	0.047	0.047	0.054	0.038	0.058	0.067	0.066	0.062	0.056	0.056
Cyclone water content	kgw/kgs	0.036	0.037	0.041	0.029	0.046	0.050	0.052	0.044	0.038	0.033
Tower mean particle size	µm	99	90	83	95	66	69	77	76	88	102
Standard deviation	µm	25	23	22	26	19	20	21	21	23	21
Cyclone mean particle size	µm	71	58	55	67	43	38	50	50	55	63
Standard deviation	µm	26	22	23	26	20	21	22	22	24	22
Total mean particle size	µm	85	69	63	81	53	51	59	59	69	83
Standard deviation	µm	29	26	26	29	23	25	24	25	27	33
Washed mean particle size	µm										
Tower bulk density	kgs/m3	1061	1066	1069	1030	1072	1100	1073	1056	1043	1024
Cyclone bulk density	kgs/m3	1089	1099	1111	1066	1108	1119	1097	1100	1085	1071
Total bulk density	kgs/m3		1087							1095	
Incipient wetness impregnation pore volume											
Tower product	ml/g	0.27	0.26	0.25	0.28	0.26	0.28	0.27	0.28	0.29	0.29
Cyclone product	ml/g	0.26	0.26	0.23	0.26	0.25	0.26	0.25	0.26	0.27	0.26
Total product washed	ml/g				0.36		0.32		0.32		
Nitrogen adsorption micro-pore volume											
Tower product	ml/g		0.050		0.053		0.040		0.043	0.046	
Cyclone product	ml/g		0.039				0.044		0.043	0.043	
Total product	ml/g	0.050	0.040	0.044	0.053	0.042	0.039	0.044	0.045	0.048	0.048
Total product washed	ml/g				0.073		0.088		0.074		
Total product washed	ml/g										
Nitrogen desorption macro-pore volume											
Tower product	ml/g		0.057		0.068		0.046		0.054	0.055	
Cyclone product	ml/g		0.053				0.047		0.051	0.056	
Total product	ml/g	0.050	0.048	0.046	0.066	0.043	0.044	0.046	0.050	0.055	0.061
Total product washed	ml/g				0.19		0.14		0.19		
Total product washed	ml/g										
Mercury intrusion meso- and macro-pore volume											
Total product washed	ml/g				0.26		0.30		0.27		
" " < 1000nm	ml/g				0.25		0.22		0.24		
BET surface area											
Tower product	m2/g		133		145		105		114	122	
Cyclone product	m2/g		102						111	112	
Total product	m2/g	128	102	118	143	103	99	111	115	116	130
Total product washed	m2/g				253		209		247		
Total product washed	m2/g										
T-plot surface area											
Tower product	m2/g		25		30		19		21	23	
Cyclone product	m2/g		19				18		18	20	
Total product	m2/g	21	16	22	29	13	14	15	20	12	25
Total product washed	m2/g				95		19		87		
Total product washed	m2/g										
Desorption surface area											
Tower product	m2/g		22		27		16		20	21	
Cyclone product	m2/g		18				15		17	19	
Total product	m2/g	20	15	18	25	15	15	15	18	16	22
Total product washed	m2/g				94		85		87		
Total product washed	m2/g										
Mercury surface area											
Total product washed	m2/g										
" " < 1000nm	m2/g				55		49		53		
Nitrogen desorption average pore size											
Tower product	nm			10		10		12		11	11
Cyclone product	nm			12				12		12	12
Total product	nm	12	10	13	10	10	11	12	12	11	14
Total product washed	nm				8.3		6.5		8.6		
Total product washed	nm										
Mercury intrusion average pore size											
Total product washed	nm										
" " < 1000nm	nm				18		17		18		

Experiment	units	**Air T**	**Air T**	**Air T**	**Air T**	**Air T**	**Airflow**	**Airflow**	**Airflow**	**Airflow**	**U0**
Reference number		81202-9,10	81209-1,2	81209-3,4	81209-5,6	81209-7,8	81214-1,2	81214-3,4	81214-5,6	81214-7,8	81218-1,2
Catalyst composition											
Zeolite	wt.%	23%	24%	24%	24%	24%	24%	24%	24%	24%	24%
Clay	wt.%	47%	47%	47%	47%	47%	15%	47%	47%	47%	47%
Alumina	wt.%	15%	15%	15%	15%	15%	14%	15%	15%	15%	15%
Silica	wt.%	14%	14%	14%	14%	14%	47%	14%	14%	14%	14%
Feed composition											
Water content	kgw/kgs	3.59	3.61	3.61	3.61	3.61	3.59	3.59	3.59	3.59	7.32
Dry solids content	wt.%	21.8%	21.7%	21.7%	21.7%	21.7%	21.8%	21.8%	21.8%	21.8%	12.0%
Spray drying conditions											
Batch ageing time	min.										
Feed flow	kg/hr	70	50	40	30	60	50	50	50	50	46
Nozzle pressure	bar	46.5	27.3	17.8	9.98	35.5	25.5	26.6	26.35	26.2	21.2
Feed temperature	°C	15	18	18	18	18	22	22	22	22	23
Feed density	kg/m3										
Ambient temperature	°C	24	22	23	25	24	27	27	27	28	22
Air flow	m3/hr	630	656	665	658	678	1227	1216	1205	1201	648
Air inlet temperature	°C	363	302	302	302	332	251	276	302	326	363
Air inlet humidity	gw/kgda	6.6	7.7	7.7	7.7	7.7	10	10	10	10	9.4
Air outlet temperature	°C	129	122	131	144	118	136	147	160	177	143
Air outlet humidity	gw/kgda										
Tower product flow	kg/hr	6.23	6.72	4.71	3.90	5.47	8.88	9.06	8.80	8.44	1.59
Cyclone product flow	kg/hr	9.36	6.91	4.79	3.60	7.94	2.84	2.88	2.71	2.92	4.23
Product properties											
Tower dry solids content	kgds/kgt	0.934	0.928	0.935	0.946	0.923	0.939	0.939	0.947	0.952	0.93
Cyclone dry solids content	kgds/kgt	0.959	0.939	0.951	0.958	0.942	0.948	0.952	0.96	0.967	0.945
Tower water content	kgw/kgs	0.071	0.078	0.070	0.057	0.083	0.065	0.065	0.056	0.050	0.075
Cyclone water content	kgw/kgs	0.043	0.065	0.052	0.044	0.062	0.055	0.050	0.042	0.034	0.058
Tower mean particle size	µm	67	77	81	91	77	70	74	67	74	70
Standard deviation	µm	20	22	22	26	22	22	23	22	22	19
Cyclone mean particle size	µm	43	55	60	65	48	51	47	46	48	44
Standard deviation	µm	21	22	23	26	22	24	23	23	22	20
Total mean particle size	µm	55	63	69	81	60	64	65	61	65	53
Standard deviation	µm	25	23	25	30	26	24	25	23	24	23
Washed mean particle size	µm										
Tower bulk density	kgs/m3	1076	1070	1067	1075	1067	1095	1081	1070	1058	1043
Cyclone bulk density	kgs/m3	1111	1116	1105	1086	1115	1131	1123	1109	1100	1077
Total bulk density	kgs/m3			1107							
Incipient wetness impregnation pore volume											
Tower product	ml/g	0.27	0.26	0.26	0.27	0.25	0.22	0.23	0.23	0.25	0.26
Cyclone product	ml/g	0.24	0.26	0.23	0.24	0.23	0.24	0.24	0.24	0.26	0.25
Total product washed	ml/g		0.30		0.33				0.32		0.30
Nitrogen adsorption micro-pore volume											
Tower product	ml/g		0.036	0.040	0.042		0.042		0.043	0.046	0.036
Cyclone product	ml/g			0.042			0.041			0.042	0.039
Total product	ml/g	0.041	0.038	0.044	0.043	0.043	0.041		0.043	0.045	
Total product washed	ml/g		0.072		0.072						
Total product washed	ml/g										
Nitrogen desorption macro-pore volume											
Tower product	ml/g		0.041	0.045	0.054		0.041		0.059	0.062	0.041
Cyclone product	ml/g			0.049			0.048			0.065	0.046
Total product	ml/g	0.042	0.040	0.047	0.046	0.048	0.045		0.059	0.063	
Total product washed	ml/g		0.17		0.19						
Total product washed	ml/g										
Mercury intrusion meso- and macro-pore volume											
Total product washed	ml/g		0.23		0.25				0.24		0.24
" " < 1000nm	ml/g		0.21		0.24				0.22		0.21
BET surface area											
Tower product	m2/g		92	107	111		108		113	126	90
Cyclone product	m2/g			112			108			130	99
Total product	m2/g	100	91	116	113	112	108		113	127	96
Total product washed	m2/g		239		244						
Total product washed	m2/g										
T-plot surface area											
Tower product	m2/g		14	20	21		19		20	26	12
Cyclone product	m2/g			20			19			39	16
Total product	m2/g	12	10	21	21	19	19		20	29	
Total product washed	m2/g		83		89						
Total product washed	m2/g										
Desorption surface area											
Tower product	m2/g		13	17	20		14		21	22	13
Cyclone product	m2/g			17			16			27	15
Total product	m2/g	12	10	18	18	17	15		21	23	
Total product washed	m2/g		82		89						
Total product washed	m2/g										
Mercury surface area											
Total product washed	m2/g								48		44
" " < 1000nm	m2/g		50		55				48		44
Nitrogen desorption average pore size											
Tower product	nm			12	11	11		12		11	11
Cyclone product	nm				12			12			10
Total product	nm	11	14	16	10	10	11	12		11	11
Total product washed	nm		8.5		8.6						
Total product washed	nm										
Mercury intrusion average pore size											
Total product washed	nm										
" " < 1000nm	nm		17		17				19		19

Experiment	units	**U0**	**U0**	**U0**	**U0**	**U0**	**U0**	**U0**	**U0**	**U0**	**U0**
Reference number		81218-3,4	81218-5,6	81218-7,8	81218-9,10	81218-11,12	81221-1,2	81221-3,4	81221-5,6	81221-7,8	81221-9,10
Catalyst composition											
Zeolite	wt.%	24%	24%	24%	24%	24%	23%	23%	23%	23%	23%
Clay	wt.%	47%	47%	47%	47%	47%	48%	48%	48%	48%	48%
Alumina	wt.%	15%	15%	15%	15%	15%	15%	15%	15%	15%	15%
Silica	wt.%	14%	14%	14%	14%	14%	14%	14%	14%	14%	14%
Feed composition											
Water content	kgw/kgs	7.32	7.32	7.32	7.32	7.32	4.58	4.58	4.58	4.58	4.58
Dry solids content	wt.%	12.0%	12.0%	12.0%	12.0%	12.0%	17.9%	17.9%	17.9%	17.9%	17.9%
Spray drying conditions											
Batch ageing time	min.										
Feed flow	kg/hr	46	28	64	46	46	48	29	68	48	48
Nozzle pressure	bar	20.9	8.23	35.6	20.2	24.5	18	7.15	35.5	18.8	19.4
Feed temperature	°C	23	23	23	23	23	19	19	19	19	19
Feed density	kg/m3										
Ambient temperature	°C	24	24	23	23	24	20	22	23	22	23
Air flow	m3/hr	664	634	652	631	645	635	618	636	634	654
Air inlet temperature	°C	302	363	363	394	363	363	363	362	394	302
Air inlet humidity	gw/kgda	9.4	9.4	9.4	9.4	9.4	8.1	8.1	8.1	8.1	8.1
Air outlet temperature	°C	123	167	127	154	146	142	166	123	152	123
Air outlet humidity	gw/kgda										
Tower product flow	kg/hr	0.98	0.94	1.41	1.40	1.28	3.64	2.73	5.01	3.74	3.41
Cyclone product flow	kg/hr	3.84	2.31	5.10	4.21	4.33	5.18	2.74	7.20	5.56	5.63
Product properties											
Tower dry solids content	kgds/kgt	0.921	0.937	0.923	0.933	0.932	0.936	0.95	0.928	0.938	0.932
Cyclone dry solids content	kgds/kgt	0.942	0.957	0.942	0.954	0.953	0.948	0.961	0.942	0.955	0.946
Tower water content	kgw/kgs	0.086	0.067	0.083	0.072	0.073	0.068	0.053	0.078	0.066	0.073
Cyclone water content	kgw/kgs	0.062	0.045	0.062	0.048	0.049	0.055	0.041	0.062	0.047	0.057
Tower mean particle size	µm	88	89	70	73	77	82	96	73	80	78
Standard deviation	µm	28	22	17	19	19	22	25	20	20	21
Cyclone mean particle size	µm	48	54	45	49	45	55	67	47	51	51
Standard deviation	µm	20	23	20	21	21	23	25	20	22	22
Total mean particle size	µm	56	64	50	55	55	65	82	58	63	61
Standard deviation	µm	28	26	21	23	23	25	28	23	24	25
Washed mean particle size	µm										
Tower bulk density	kgs/m3	1058	1024	1064	1042	1042	1056	1032	1067	1046	1060
Cyclone bulk density	kgs/m3	1092	1063	1080	1068	1068	1084	1072	1099	1083	1101
Total bulk density	kgs/m3										
Incipient wetness impregnation pore volume											
Tower product	ml/g	0.26	0.25	0.29	0.25	0.26	0.27	0.27	0.26	0.28	0.26
Cyclone product	ml/g	0.24	0.26	0.28	0.20	0.25	0.24	0.25	0.27	0.25	0.24
Total product washed	ml/g						0.31				
Nitrogen adsorption micro-pore volume											
Tower product	ml/g	0.035			0.036	0.037	0.037			0.039	0.036
Cyclone product	ml/g				0.040	0.040	0.039			0.042	
Total product	ml/g				0.039	0.040				0.041	0.036
Total product washed	ml/g										
Total product washed	ml/g										
Nitrogen desorption macro-pore volume											
Tower product	ml/g	0.033			0.048	0.043	0.046			0.052	0.044
Cyclone product	ml/g				0.048	0.053	0.044			0.053	
Total product	ml/g				0.048	0.051				0.053	0.044
Total product washed	ml/g										
Total product washed	ml/g										
Mercury intrusion meso- and macro-pore volume											
Total product washed	ml/g						0.24				
" " < 1000nm	ml/g						0.22				
BET surface area											
Tower product	m2/g	94			98	97	94			106	98
Cyclone product	m2/g				105	104	101			110	
Total product	m2/g	94			103	102	98			109	98
Total product washed	m2/g										
Total product washed	m2/g										
T-plot surface area											
Tower product	m2/g	19			21	17	15			21	20
Cyclone product	m2/g				18	17	16			20	
Total product	m2/g				19	17				20	20
Total product washed	m2/g										
Total product washed	m2/g										
Desorption surface area											
Tower product	m2/g	11			17	16	15			19	17
Cyclone product	m2/g				17	15	15			18	
Total product	m2/g				17	15				18	17
Total product washed	m2/g										
Total product washed	m2/g										
Mercury surface area											
Total product washed	m2/g						49				
" " < 1000nm	m2/g						49				
Nitrogen desorption average pore size											
Tower product	nm	13	12			11	11	12			11
Cyclone product	nm	12				12	14	12			12
Total product	nm					11	13				12
Total product washed	nm										
Total product washed	nm										
Mercury intrusion average pore size											
Total product washed	nm										
" " < 1000nm	nm						18				

Appendix E

Analogy between the momentum balance equations and Fick's and Darcy's law

When the momentum balance equations are used in limit situations the equations should transform in either diffusion equations or Darcy's law. The momentum balance is given by equations 5.9 and 5.10 (using 5.3):

$$c'_t RT\left(\frac{dx'_1}{dz}\right)_{TP} + \phi'_1\left(\frac{dP_l}{dz}\right)_T = -c'_t RTg'_D \frac{x'_1 x'_2}{\mathcal{D}_{12}}\left(\overline{u}_1 - \overline{u}_2\right) - c'_t RT\beta_{1s}\left(\overline{u}_1 - u_s\right) \qquad \text{(E.1)}$$

and

$$c'_t RT\left(\frac{dx'_2}{dz}\right)_{TP} + \phi'_2\left(\frac{dP_l}{dz}\right)_T = -c'_t RTg'_D \frac{x'_1 x'_2}{\mathcal{D}_{12}}\left(\overline{u}_2 - \overline{u}_1\right) - c'_t RT\beta_{2s}\left(\overline{u}_2 - u_s\right) \qquad \text{(E.2)}$$

Limit situations

a) No wall-friction, infinite liquid

In case of no wall-friction the β_{is} are zero and the diffusion averaging factor, g'_D, goes to one. Then E.1 and E.2 are written:

$$c'_t RT\left(\frac{dx'_1}{dz}\right)_{TP} + \phi'_1\left(\frac{dP_l}{dz}\right)_T = -c'_t RT\frac{x'_1 x'_2}{\mathcal{D}_{12}}\left(\overline{u}_1 - \overline{u}_2\right) \qquad \text{(E.3)}$$

and

$$c'_t RT\left(\frac{dx'_2}{dz}\right)_{TP} + \phi'_2\left(\frac{dP_l}{dz}\right)_T = -c'_t RT\frac{x'_1 x'_2}{\mathcal{D}_{12}}\left(\overline{u}_2 - \overline{u}_1\right) \qquad \text{(E.4)}$$

Addition of these equations gives:

$$\frac{dP_l}{dz} = 0 \qquad \text{(E.5)}$$

So:

$$\left(\frac{dx'_1}{dz}\right)_{TP} = -\frac{x'_1 x'_2}{Đ_{12}}\left(\overline{u}_1 - \overline{u}_2\right) = -\frac{N'_1 x_2 - N'_2 x_1}{c_t Đ_{12}} \tag{E.6}$$

which results in:

$$N'_1 = N'_t x'_1 - Đ_{12} c'_t \frac{dx'_1}{dz} \tag{E.7}$$

Rewriting the mole fraction:

$$x'_1 = \frac{c'_1}{c'_t} = \frac{c'_1}{c'_1 + c'_2} \tag{E.8}$$

and using:

$$c'_1 \overline{V}_1 + c'_2 \overline{V}_2 = 1 \Rightarrow c'_t = c'_1\left(1 - \frac{\overline{V}_1}{\overline{V}_2}\right) + \frac{1}{\overline{V}_2} \tag{E.9}$$

and

$$J'^{v}_2 = -J'^{v}_1 \frac{\overline{V}_1}{\overline{V}_2} \tag{E.10}$$

results in Fick's law, realising that equation E.7 is not fixed to any co-ordinate.

b) Pure liquid without diffusion

The volume fraction of component 1 is one, and of component 2 zero. Then equation E.1 becomes:

$$\left(\frac{dP_l}{dz}\right)_T = -c'_t RT\beta_{1s}\left(\overline{u}_1 - u_s\right) = -\frac{\eta_1}{B_o}\left(\overline{u}_1 - u_s\right) \tag{E.11}$$

which is Darcy's law with:

$$B_o \equiv \frac{r_o^2}{8} \tag{E.12}$$

Woord van dank

Vanaf het moment dat ik met dit onderzoek startte tot aan de afronding, zijn er veel mensen geweest die, op welke wijze dan ook, geholpen hebben met de totstandkoming van de resultaten die gedeeltelijk beschreven staan in dit proefschrift. Al die mensen wil ik hier bedanken.

Piet Kerkhof en Jan Coumans: bedankt voor jullie vertrouwen en voor de (soms te) grote vrijheid. Piet, jou bedank ik speciaal voor de laatste anderhalf jaar waarin we hard gewerkt hebben om het ternair model kloppend te krijgen. Jan, bedankt voor de scherpe correcties, de discussies en voor de leerzame organisatie van IDS2000.

Ook de afstudeerders en stagiaires wil ik hier hartelijk danken voor hun inzet en de prettige samenwerking. Roger Goossens en Rob Gemen: bedankt voor jullie bijdragen aan de droogexperimenten. Met Jean Pierre Verbraak, Rogier Hooyschuur, Flavie Brion en Oscar van Vleuten zijn de sproeidroogexperimenten met kunst en vliegwerk gedaan.

Met het opstarten van de sproeidroogexperimenten in 1996 en de verhuizing in 1999-2000 zijn vele technici bezig geweest. Ik bedank Chris Luyk, Piet van Eeten, Henk Hermans, Frans van der Krieken, Toon Gevers, Jovita Moerel en Evert Ridderhof in het bijzonder en die ik ben vergeten ook.

Voor hulp bij de analyses wil ik Martin Otten, Ton Sommen en Henk Woestenberg bedanken. Voor de discussies in de vakgroep dank ik Gerben Mooiweer en Ton van der Zanden (met een Z).

Ook een woord van dank voor mijn sponsor Akzo-Nobel, en met name Edwin Berends en Erik La Heij, die naast het mij leren brouwen van de *strike*, de nodige materialen, analyses en discussies hebben verschaft.

Voor het lezen en corrigeren van het proefschrift bedank ik Kees van Weert en de kerncommissie. Martine de Rooy wil ik danken voor het maken van de omslag. Voor de hulp met (o.a.) de papierwinkel bedank ik Denise Tjallema.

Zo, nu we ongeveer iedereen hebben gehad die inhoudelijk heeft bijgedragen wil ik nu de mensen bedanken die voor het nodige vertier hebben gezorgd: Bram, Bart, Chris[2], Earl, Gwen, Fabrice, Frans, Frank, Jaco, Jasper, Jeroen, Joop, Joost, Maartje, Marcel, Martijn, Maurice, Peter, Rob, Rogerio, Roy, Tjerk, Vincent, Wil, Willem-Jan en Xiaojun.

Tot slot bedank ik mijn overige vrienden en familie voor hun steun en toeverlaat. Ik ga eindelijk weer tijd voor jullie vrijmaken en voor andere dingen.

Houdoe en bedankt allemaal!